UNIVERSITY OF BIRMINGHAM

POSITRON EMISSION PARTICLE TRACKING APPLIED TO SOLID-LIQUID MIXING IN MECHANICALLY AGITATED VESSELS

by

Antonio Guida

A thesis submitted to
The University of Birmingham
for the degree of
DOCTOR OF PHILOSOPHY

School of Chemical Engineering
College of Engineering and Physical Sciences
The University of Birmingham
April 2010

Dedicated to the memory of my father,

Paolo Guida, my foremost teacher

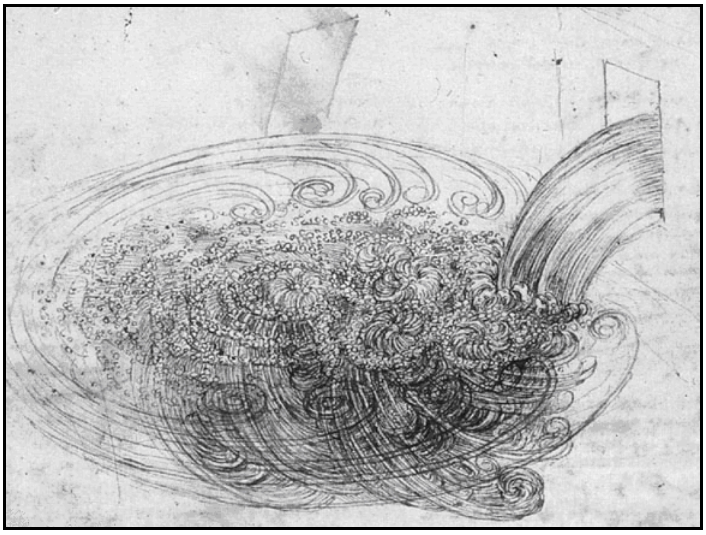

"Ricordati, quando commenti l'acque, d'allegar prima la sperienza e poi la ragione"

(Remember, when discoursing on the flow of water, to adduce first experience and then reason)

Leonardo da Vinci

[1493-1494; Ms H, f. 90r.]

Abstract

Mechanically agitated vessels are widely used for various mixing operations within a wide range of industries including the chemical, pharmaceutical, food and petroleum industries. They are used for liquid blending, solid-liquid mixing, gas dispersion in liquids, heat/mass transfer enhancement and chemical reaction. Mixing is intrinsically a Lagrangian process and, whilst Eulerian data are essential, Lagrangian information is necessary for its complete description. Possible approaches of generating Lagrangian data can, in principle, employ numerical simulations or experimental techniques based on Lagrangian tracking to provide the trajectories of fluid elements or solid particles. In this work a set of tools are developed for the analysis and theoretical validation of Lagrangian single and multi-phase flow data obtained from tracer trajectories in mechanically agitated vessels. Whilst theoretical procedures developed here exploit a large range of mathematical and statistical concepts with Shannon entropy being an example, the computational data analysis often involved handling and sequential processing of multidimensional matrices containing several millions of data points. Computational codes were developed for performing Lagrangian statistical data analysis, Lagrangian-Eulerian data conversion, Shannon entropy analysis, multi-phase mixing studies and detailed Eulerian multi-plane investigations. The implementation and power of these tools are demonstrated by analysing a wide range of measurements acquired using the technique of positron emission particle tracking (PEPT) during the mixing of Newtonian and non-Newtonian fluids, as well as the mixing of highly concentrated solid-liquid systems. These multi-phase suspensions included monodisperse, binary and polydisperse solid-liquid suspensions. Experimental measurements obtained in these systems are unique and valuable in their own right as, for the first time, it has been possible to determine the full 3D velocity and concentration fields of liquid and solid phases within opaque dense slurries of this type containing up to 40 wt% solids.

Acknowledgments

First and foremost, I would like to express my gratitude towards my supervisor Prof. Mostafa Barigou. It has been a privilege and great pleasure to work with him and Prof. Alvin W. Nienow not only for their constant guidance and valuable input throughout the course of this research, but also for their friendship.

I would like to thank Prof. David Parker, Dr Xianfeng Fan and Dr Thomas Leadbeater of the Positron Imaging Centre for their assistance with the PEPT experiments. I would also like to thank Dr Andy Ingram and Dr Serafim Bakalis from Chemical Engineering for several valuable suggestions during the early stages of this research, along with old colleagues Dr Fabio Chiti (now at Merck), Dr Luke Adams (now at Rolls Royce) and Dr Kenneth Chung (now at British Sugar) for the endless and constructive discussions on PEPT, PIV, MATLAB and CFD we have had.

I would like to thank Andrea Gabriele, Dr Mark Simmons and Dr Andreas Tsoligkas for their advice with PIV and PLIF experiments, Sala Odeen for his help in performing rheological measurements, and Shih Chi Chu for her guidance in using precision instrumentations. In addition, I genuinely appreciate the masterpieces produced by Robert Sharpe and Philip Harris from the Mechanical Engineering workshop team. I would also like to thank Lynn Draper and all other great people from the General Office for their friendship and continuous support. Financial support was provided by the Engineering and Physical Sciences Research Council (UK) through Grant GR/S70517/01 and is gratefully acknowledged.

I am also grateful to my managers Dr Gráinne Carpenter and Michelle Wise for their interest and encouragement, and for facilitating the completion of this work through their flexibility and time allowances during my first six months at UKAEA.

Finally, I would like to thank my family for their encouragement and infinite understanding over the years.

Table of Contents

List of Figures

List of Tables

Chapter I
Introduction

Among several definitions, Mixing can be defined as the reduction of inhomogeneity in order to achieve a desired process result (Paul *et al.*, 2004). The inhomogeneity can be one of concentration, phase, or temperature. Secondary effects, such as mass transfer, chemical reactions, and product properties are usually the critical objectives. Failure to provide the necessary mixing may result in severe manufacturing problems, ranging from costly corrections in the plant to complete failure of a process. The costs associated with these problems are usually far greater than the cost of adequately evaluating and solving the problem during process development (Smith, 1990). Due to their importance in the field of process industries, mixing operations have been for decades the subject of many investigations. Nevertheless, many aspects of mixing processes are yet to be properly understood.

Failure of a mixing process must not be associated only with insufficient mixing or low energy efficiency; there are a number of industrial applications where excessive mixing is not only wasteful of energy but also counter-productive (Nienow *et al.*, 1997). For example, in the mixing of biological materials, excessive power inputs or impeller speeds may damage mammalian cells or mycelia in agitated bioreactors (Nienow *et al.*, 1996; Jüsten *et al.*, 1996). Structured molecular forms of complex fluids, solutions or slurry can be permanently damaged by overmixing and the desired rheological characteristics of the product may never be obtained. In crystallization, the overall process may be affected by high mixer speeds which cause a significant increase in secondary nucleation and therefore crystal size smaller than desired.

The fundamental variables to identify in any mixing problem are the required degree of homogeneity, i.e. the length scale of mixing, and the time available to reach such level of mixing, i.e. the time scale (Kresta and Brodkey, 2004). These key variables are the result of a

set of fundamental phenomena which must be understood to address and resolve difficult mixing problems. These include the flow regime (laminar, transitional or turbulent), rheology of the fluid, different behaviour of the flow components in a multi-phase system and mixing at the molecular scale.

A wide range of mixing equipment is now available, with the current generation of equipment typically designed for a specific process result. The stirred vessel, however, is probably the most reviewed and commonly encountered mixing apparatus in the process industry. Mechanically agitated vessels are widely used for various operations within a wide range of industries including the chemical, pharmaceutical, food and petroleum industries. They are used for liquid blending, solid-liquid mixing, gas dispersion in liquids, heat/mass transfer enhancement and chemical reaction. The methods generally used for designing stirred vessels, however, tend to be based on a global 'black-box' approach, and a more detailed description of the internal flow structure has long been missing to enable the development of more rational rules for establishing process parameters and equipment design. The advent of powerful measurement and modelling techniques in recent years has reenergised interest in this field and more effort is increasingly being devoted to try and fully understand the mixing mechanisms on the basis of localised hydrodynamic approaches.

Several techniques have been developed over the years for obtaining qualitative and quantitative measurements of fluid flows. Laser Doppler velocimetry (LDV) and particle image velocimetry (PIV), which yield accurate velocity measurements at one or more points within the flow, have become the most employed to examine the complex nature of the flow fields in such stirred vessels (Kresta and Wood, 1993a; Baldi and Yianneskis, 2004). These techniques are based on image capturing, provided the equipment and fluids used are optically transparent. Unfortunately, this is a major limitation given that, in real mixing processes, fluids and multi-phase mixtures are usually partially or entirely opaque. Moreover, the inherent Eulerian nature of such measurements does not allow ready access to the Lagrangian character of the flow or the structures present.

Although Eulerian data are crucial, Lagrangian information is necessary for the whole description of the mixing phenomena. Various authors have shown that the Lagrangian description of mixing unravel precious information which is not obtainable by the Eulerian approach, both for laminar (Ottino, 1989) and turbulent (Toschi and Bodenschatz, 2009)

mixing. Fluid element transport has features which can be completely different from and complementary to those of the underlying velocity field. Examples of experimental Lagrangian tracking techniques are positron emission particle tracking (PEPT) and computer automated radioactive particle tracking (CARPT). Both allow non-invasive probing of opaque fluids and within opaque apparatus by using a single radioactive particle as flow tracer, which is tracked in 3D space and time to reveal its Lagrangian trajectory (Barigou, 2004; Doucet *et al.*, 2008).

Solid-liquid suspensions are ubiquitous in the industrial processes including the manufacture of fine chemicals, pharmaceuticals, polymers, food, personal/home care products, paper and pulp. Numerous difficult mixing problems are found with solid-liquid processing, some 80 % of products in the chemical industry, for example, being of this type (Shamlou, 1993). Previous research studies of solid-liquid suspensions have mainly been focused on the suspension of dense fine particles in turbulent Newtonian flows, and a number of empirical relationships and theoretical models for predicting the minimum impeller rotational speed for complete particle suspension have been proposed (Zwietering, 1958; Nienow, 1968; Molerus and Latzel, 1987a-b; Raghava Rao *et al.*, 1988; Geisler *et al.*, 1993; Mersmann *et al.*, 1998; Armenante *et al.*, 1998). Recently, Brujes *et al.* (1998) compiled most of the correlations published over the previous four decades, and tested them against experimental measurements obtained in baffled and unbaffled vessels containing suspensions of glass beads, resins particles or microcapsules. It emerges from such literature that the fundamental mechanisms which govern particle suspension and distribution within a stirred vessel are still not well understood.

The fluid-dynamic characterisation of mechanically agitated solid-liquid suspensions using the Lagrangian technique of positron emission particle tracking is the central objective of this work.

1-1 Objectives

The objectives of this study are:

- *Definition of a methodology for the analysis of Lagrangian data collected in mechanically agitated vessels using PEPT.* A detailed procedure will be delineated

for the analysis and validation of data obtained in single- and multi-phase stirred vessels from tracer trajectories by Lagrangian tracking. A Lagrangian-Eulerian analysis will be used to extract Eulerian information form the purely Lagrangian information contained in the tracer trajectory; and second a Lagrangian-statistical analysis will be used to obtain quantities only accessible via Lagrangian measurements.

- *Creation of a code for automated and fast analysis of PEPT data.* The structure of the computational code for extracting Eulerian information will be developed on the basis of a set of subroutines containing different algorithms aimed to progressively analyse the initial Lagrangian information and store important intermediate outputs. Due to the variety of mixing systems which can be examined, the code has to be flexible enabling key-parameters to be set and specific subroutines to be activated or deactivated as required.

- *Assessment of the influence of the position of the investigation plane in the study of a stirred single-phase turbulent system using an optical technique.* In order to study the nature of the cylindrical symmetry within a baffled mechanically agitated vessel, the effect of the azimuthal position of the measurement plane in a fully baffled stirred vessel will be investigated by PIV to assess the magnitude of the differences in the flow fields between different planes.

- *Assessment of the reliability of the PEPT technique for studying mixing systems.* Using identical equipment and fluid, three-dimensional Eulerian velocity measurements made by PEPT in a baffled stirred vessel will be compared directly with the above mentioned PIV measurements performed in multiple planes. The study aims to investigate possible minor local discrepancies and, whether significant, develop an understanding of the reasons of their existence.

- *Exploring the applicability of alternative mathematical and statistical tools for the analysis of Lagrangian data obtained in mechanically agitated vessels using PEPT.* A new methodology for quantifying the local and global mixing characteristics within a mechanically-agitated fluid batch system will be developed on the basis of Lagrangian tracking. The experimental component of this new methodology will involve the use of PEPT.

- *Fluid-dynamic characterisation of stirred monodisperse solid-liquid suspensions at varying solids concentration.* The mixing of moderately to highly concentrated suspensions of nearly monomodal coarse glass particles will be investigated using a PBT operating in both up-pumping and down-pumping modes; velocity and concentration fields obtained at different solids concentrations will be presented.
- *Fluid-dynamic characterisation of stirred binary solid-liquid suspensions at varying solids concentration.* The three-component flow field and spatial phase distribution of binary mixtures of glass particles suspended in water in a stirred vessel will be resolved using PEPT. Using a PBT pumping upwards rather than downwards, the experimental campaign will be repeated to compare the performance of these two different agitation modes in complex multi-phase systems.
- *Fluid-dynamic characterisation of stirred polydisperse solid-liquid suspensions at varying solids concentration.* On the basis of the experience gained with the investigations of simpler systems, complex solid-liquid systems where several particle-size fractions are dispersed in a liquid phase will be studied. Given that 3D velocity and concentration of every solid and liquid component will be fully mapped, a very large amount of unique experimental results will be obtained.

1-2 Thesis Layout

The present thesis is structured as follows. Subsequent to the present introducing section, a thorough review of existing literature on different aspects of fluid mixing in single- and multi-phase stirred tanks, an introduction to the Lagrangian approach for the study of mixing systems and a review of the available flow visualisation techniques are given in Chapter II.

The experimental procedures, apparatus and equipment used including the underlying theory are described in Chapter III. Here the methodology used as a basis for the code developed for the analysis of Lagrangian data is presented in detail. For clarity, sample results obtained analysing data extracted from the sets of experiments which are then fully examined in then subsequent chapters are also presented in this chapter.

A well-established optical imaging technique (PIV) is used in Chapter IV to assess the error

in the velocity measurements generated when in a baffled stirred vessel the axial symmetry is assumed. By using PEPT to probe an identical system, the data optically collected in multiple vertical planes are used again in Chapter V to provide a 3D comparison between PIV and PEPT. In the same chapter, PEPT data collected in a non-Newtonian fluid will be compared with those collected by another optical technique (PLIF).

A novel approach to the study of a long Lagrangian trajectory of a particle tracer is presented in Chapter VI. Statistical tools defined on the basis of Shannon Entropy, a quantity at the heart of the Information Theory, are employed to define new local mixing indices which expand the meanings of dispersion and mixing time.

Chapter VII is the first of three chapters presenting results on solid-liquid mixing. Details of materials, equipments, the experimental procedures and data analysis used are given in each of these three chapters. Whilst a full study of a monodisperse solid-liquid system using PEPT is presented in Chapter VII, binary suspensions are similarly investigated in Chapter VIII. Subsequently, a very large amount of experimental results obtained in a polydisperse system by PEPT are presented in Chapter IX in a compact form, where each of the five solid and one liquid component of the suspensions have been examined by PEPT at varying solids concentration.

Due to the large number of symbols used, for clarity purposes a separate notation section has been added at the end of each chapter. Please note that the same symbols may represent different quantities in different chapters, and vice versa. References, on the other hand, have been grouped at the end of the thesis as these are used throughput the thesis.

1-3 Publications arising from thesis

1-3.1 Journal Papers

Guida, A., Fan, X., Parker, D.J., Nienow, A.W. and Barigou, M. (2009), Positron Emission Particle Tracking in a mechanically agitated solid-liquid suspension of coarse particles, *Chemical Engineering Research and Design*, 87(4A), 421-429.

Guida, A., Nienow, A.W. and Barigou, M. (2010), PEPT measurements of solid-liquid flow field and spatial phase distribution in concentrated monodisperse stirred suspensions,

Chemical Engineering Science, 65(6), 1905-1914.

Guida, A., Nienow, A.W. and Barigou, M. (2010), The effects of the azimuthal position of the measurement plane on the flow parameters determined by PIV within a stirred vessel, *Chemical Engineering Science*, 65(8), 2454-2463.

Guida, A., Nienow, A.W. and Barigou, M. (2010), Shannon entropy for local and global description of mixing by Lagrangian particle tracking, *Chemical Engineering Science*, 65(10), 2865-2883.

Barigou, M., Chiti, F., Pianko-Oprych, P., **Guida, A.**, Adams, L., Fan, X., Parker, D.J. and Nienow, A.W. (2009), Using Positron Emission Particle Tracking (PEPT) to Study Mixing in Stirred Vessels: Validation and Tackling Unsolved Problems in Opaque Systems, *Journal of Chemical Engineering of Japan*, 42(11), 839-846.

1-3.2 International Conference Proceedings

Guida, A., Nienow, A.W., Parker, D.J. and Barigou, M. (2008), Eulerian description of solid liquid mixing in a stirred tank based on a Lagrangian observation by positron emission particle tracking, *Proceedings of 26th National Heat Transfer Conference*, Palermo, Italy, June 23-25.

Guida, A., Chiti, F., Nienow, A.W. and Barigou, M. (2008), Determination of velocity field and solids distribution in a stirred polydisperse system by positron emission particle tracking, *Proceedings of International Symposium on Mixing in Industrial Processes VI*, Niagara on the Lake, Niagara Falls, Ontario, Canada, August 17-21.

Guida, A., Nienow, A.W., Parker, D.J. and Barigou, M. (2008), Two-phase Positron Emission Particle Tracking in a mixing vessel containing a polydisperse slurry, *Proceedings of 11th International Conference on Multiphase Flow in Industrial Plants*, Palermo, Italy, September 7-10.

Guida, A., Nienow, A.W. and Barigou, M. (2009), Eulerian description of a stirred suspension using two-phase positron emission particle tracking, *Proceedings of 13th European Conference on Mixing*, London, UK, April 14-17.

Adams, L., Chiti, F., **Guida, A.**, Jaffer, S., Nienow, A.W. and Barigou, M. (2008), Positron

emission particle tracking inside caverns formed during mixing of an industrial slurry, *Proceedings of International Symposium on Mixing in Industrial Processes VI*, Niagara on the Lake, Niagara Falls, Ontario, Canada, August 17-21.

Barigou, M., Chiti, F., Pianko-Oprych, P., **Guida, A.**, Adams, L., Parker, D.J. and Nienow, A.W. (2008), Using Positron Emission Particle Tracking (PEPT) to Study Mixing in Stirred Vessels, *Proceedings of 2nd Asian Conference on Mixing*, Yonezawa, Japan, October 7-9.

Chapter II
Literature Review

Abstract

Mechanically agitated vessels are extensively used for various operations within a wide range of industries including the chemical, pharmaceutical, food and petroleum industries. They are used for liquid blending, solid-liquid mixing, gas dispersion in liquids, heat/mass transfer enhancement and chemical reaction. Starting from a brief general description of mixing principles, this literature survey gives an overview of applications and typical configurations of stirred vessels and agitators. On the basis of the dimensional analysis, a wide range of dimensionless parameters have been developed by scientists for the study of thermo-fluid-dynamics. Mixing phenomena may well be described by a variety of these and other purposely defined dimensionless quantities. Numbers describing flow regimes, classification of fluids, heat exchange properties, diffusion, power consumption, multiphase interaction and mixing effectiveness are reviewed here. Furthermore, industrial applications of solid-liquid mixing and specifically the stirring of dense particle suspensions are briefly discussed together with design issues and main physical phenomena involved. Finally, a review of the experimental techniques of most relevance to this work is given.

2-1 Mixing Systems

A wide range of mixing equipment is now available, with the current generation of equipment typically designed for a specific process result. The mechanically agitated vessel, however, is probably the most reviewed and commonly encountered mixing apparatus in the process industry.

2-2 Mechanically agitated vessels

Over 50% of the world's chemical production involves the use of mechanically agitated stirred vessels for manufacturing high-added-value products (Hemrajani and Tatterson, 2004). The fundamental mechanism for these vessels is the transfer of momentum to the material within the vessel via the physical movement of rotating impeller blades. Some common examples of the uses of stirred vessels are given below:

- Homogenisation/blending of miscible liquids, e.g. dilution and gasoline additives
- Emulsification of immiscible liquids, e.g. polymerisation and food additives
- Solid suspension in a liquid phase, e.g. catalysis, crystallisation and solvent extraction
- Gas dispersion in liquid, e.g., hydrogenation or oxidation reactions
- Heat transfer

The application at hand often dictates the choice of vessel size and geometry, impeller design, and number and type of baffles. Although unbaffled vessels are used in some applications such as high throughput experimentation reactors (Hall *et al.*, 2005a; Chung *et al.*, 2007), the majority of industrial stirred vessels which are used in the transitional and turbulent flow regimes are equipped with baffles. When operating at these flow regimes, four longitudinal baffles (of width ~ $T/10$) are usually installed to prevent solid body rotation of the fluid, otherwise termed as fluid swirl, and to promote axial mixing between top and bottom part of the vessel.

For a standard vertical cylindrical vessels equipped with one impeller, the generally adopted notation is summarised in **Figure 2.1**. In the case where fluid is filled to a height, H, larger than the tank diameter, T, multiple coaxial impellers may be installed.

2-2.1 Impeller choice and resulting flow pattern

In a baffled vessel with standard configuration (i.e. $H = T$, $D = 0.33\text{-}0.5\ T$ and $C = 0.25\text{-}0.33\ T$) operating with Newtonian fluids in the turbulent region, the typical primary flow patterns to be expected are illustrated in **Figure 2.2**. Of course, the velocities at any point will be three-dimensional and unsteady (Edwards *et al.*, 1997). In a vessel with radial flow pattern, the strongly swirling flow is discharged radially from the impeller and separated into two streams at the vessel walls, forming upper and lower circulation loops. Whereas in an axial flow field the strong downward impeller discharge impinges on the vessel bottom and rises along the vessel wall, which aids the suspension of solid particles before finally returning back into the impeller, forming one large circulation loop.

The type of impeller has a significant impact on the flow pattern and mixing effectiveness, hence it should be carefully chosen based on the type of process. Down-pumping axial flow impellers, such as marine propellers (**Figure 2.3d)** and hydrofoil impellers (**Figure 2.3e)**, are most used for the suspension of solid particles. The simplest radial flow impellers on the other hand, are flat paddles and the Rushton Disc Turbine (RDT), shown in **Figure 2.3a-b**. When used for gas dispersion purposes, the RDT suffers from a significant drop in power draw upon gassing, which is attributed to the formation of cavities behind the impeller blades.

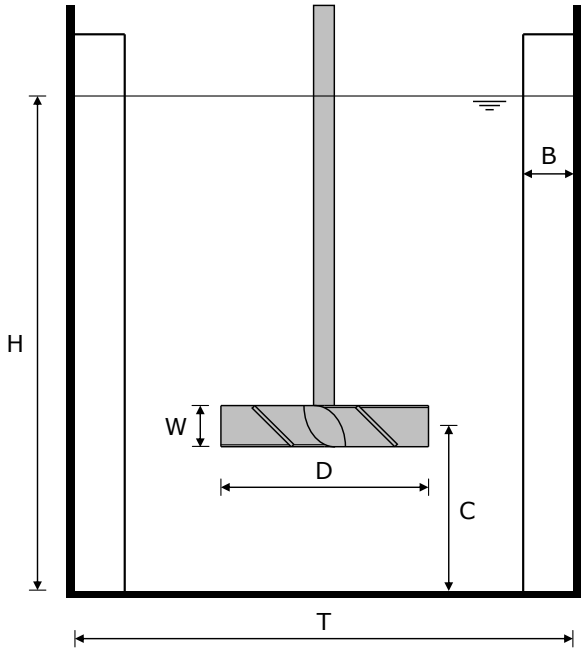

Figure 2.1. Standard nomenclature for a mechanically agitated vessel.

As a result, radial flow impellers with more complicated designs have been introduced such as the Smith turbine, depicted in **Figure 2.3c,** where the impeller blades are curved to prevent cavity formation; this in turn provides a better gas dispersion and improved gas holdup compared to the standard RDT.

If the blades of a flat paddle impeller are pitched at an angle to the vertical, the direction of

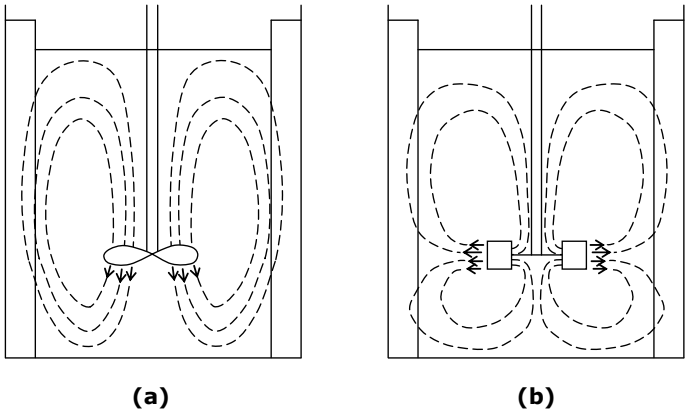

Figure 2.2. Typical flow pattern expected for a fully baffled vessel with (a) axial flow and (b) radial flow impeller (Edwards *et al.*, 1997).

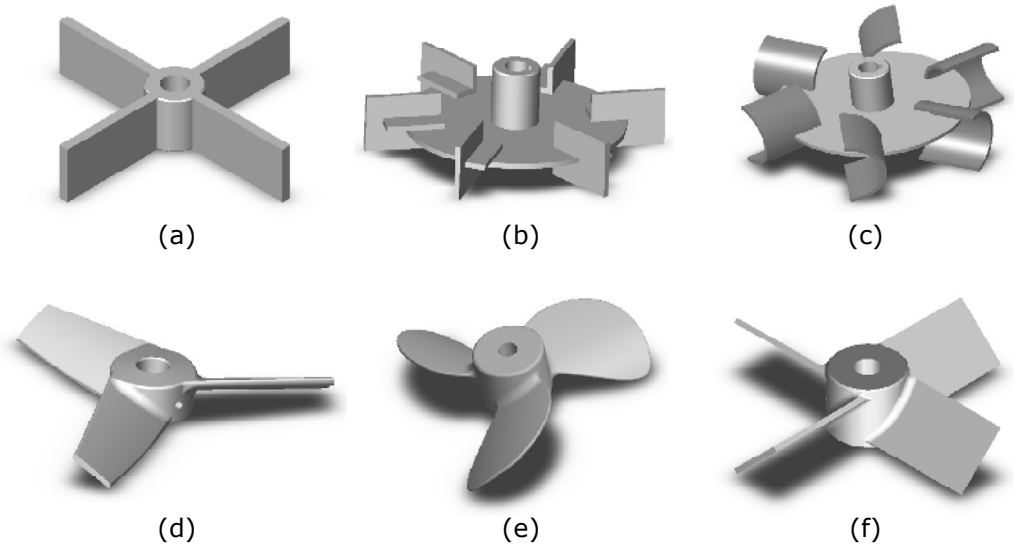

Figure 2.3. Examples of radial flow impellers, (a) flat paddle impeller, (c) Rushton disc turbine, (c) Smith turbine; axial flow impellers, (d) hydrofoil impeller (e) marine propeller; mixed flow impeller, (f) pitched blade turbine.

flow in the impeller discharge can be altered. An example of impellers of this type is the Pitched Blade Turbine (PBT), as shown in **Figure 2.3f**. The blades may be pitched at any angle between 10º and 90º but the most commonly adopted inclination is 45º. If the angle of the blade pushes the fluid downwards as the PBT is rotated, the flow is said to be in the down pumping mode, i.e. PBTD, and usually displays the characteristic of an axial impeller as shown in **Figure 2.2a**. When the blade pushes the fluid upwards, either by reversing the direction of rotation or by rotating the blades, the flow is in the up-pumping mode, i.e. PBTU. Generally, power consumption and pumping effectiveness appear to be more favourable for a down-pumping PBT in single-phase systems (Aubin *et al.*, 2004).

Nevertheless, the PBTU mode has been proven to be very effective for gas dispersion and energy dissipation (Bujalski *et al.*, 1990; Gabriele *et al.*, 2009). The flow is discharged in both axial and radial directions in low to medium viscosity fluids as shown by Hall *et al.* (2005b) and Chung (2008); hence it is sometimes termed mixed flow. In the high transition to turbulent regime, these authors found that the mixed flow generated from PBTU produced a very strong lower circulation loop; such flow in the clockwise direction induced an upper circulation loop, but of a much weaker strength. However, if the impeller D/T ratio is raised above 0.55, the PBTU will become a radial flow impeller as centrifugal forces become dominant (Hemrajani and Tatterson, 2004).

The need to properly design or optimise these processes has motivated numerous studies aiming to develop a deep understanding of the complex local hydrodynamics inside stirred vessels. As a consequence, a number of impeller designs have been produced over the years, agitators which are often purposely designed for the application at hand. A detailed summary which describes the impellers commonly used in liquids of different ranges of viscosity and the resulting flow patterns can be found in Zlokarnik (2001).

2-3 Dimensionless analysis

The Buckingham π theorem is a fundamental theorem in dimensional analysis. The theorem provides a method for computing sets of dimensionless parameters from the variables involved in physical problem, even if the correlating equations are unknown. Although, the 'method of dimensions' was first proposed by Lord Rayleigh in his book 'The Theory of

Sound' (1877), Buckingham (1914) created a solid theoretical basis on the concept of rank used in Matrix Algebra. However, the choice of dimensionless parameters is not unique: Buckingham's theorem only provides a way of generating sets of dimensionless parameters, and not the most 'physically meaningful' dimensionless numbers. The most common dimensionless numbers used for mixing studies are discussed in the following subsections.

2-3.1 Flow regime

In fluid mechanics, the Reynolds number Re is a dimensionless number that gives a measure of the ratio of inertial forces to viscous forces and consequently quantifies the relative importance of these two types of forces for given flow conditions. Traditionally defined as

$$\mathrm{Re} = \frac{\rho u L}{\mu} = \frac{u L}{\nu} \tag{2.1}$$

where u is the mean fluid velocity, L is a characteristic lengths (e.g., pipe diameter), ρ is the density of the fluid and μ and ν are the fluid dynamic and kinematic viscosity, respectively. For mixing studies in stirred vessels, the impeller Reynolds number, Re_{imp}, usually replaces the classic definition of the Reynolds number, namely

$$\mathrm{Re}_{imp} = \frac{D^2 N}{\nu} \tag{2.2}$$

which is justified by the fact that the impeller tip speed is proportional to ND. Impeller Reynolds number is generally used to characterize different flow regimes in mechanically agitated vessels.

For heat transfer studies in multi-phase systems, the Nusselt number is the dimensionless ratio of convective to conductive heat transfer across interface; that is

$$\mathrm{Nu} = \frac{hL}{k} \tag{2.3}$$

where h is the convective heat transfer coefficient, k the conductivity of the fluid and L is a characteristic length. The conductive component is measured under the same conditions as the heat convection but with a (hypothetically) stagnant fluid. A Nusselt number close to unity, namely convection and conduction of similar magnitude, is characteristic of 'slug flow'

or laminar flow. A larger Nusselt number corresponds to more active convection, with turbulent flow typically in the range Nu = 100-1000 (Incropera and DeWitt, 1996).

The Froude number compares inertia and gravitational forces. It is used to quantify the influence of gravity on fluid motion. Froude number is originally defined as a speed ratio, that is

$$\mathrm{Fr} = \frac{u}{c} \tag{2.4}$$

where u is a characteristic velocity, and c is a characteristic water wave propagation velocity. The Froude number is thus the hydrodynamic equivalent to the Mach number.

For shallow water with uniform depth d_w, for example tidal waves and hydraulic jump phenomena, the characteristic velocity u is the average flow velocity, averaged over the cross-section perpendicular to the flow direction. The wave velocity, c, is equal to the square root of gravitational acceleration g, times the depth d_w, thus

$$\mathrm{Fr} = \frac{u}{\sqrt{g d_w}} \tag{2.5}$$

For ease of calculations, an alternate definition of Fr is used in fluid mechanics, namely

$$\mathrm{Fr} = \frac{u^2}{g d_w} \tag{2.6}$$

where each of the terms on the right have been squared. In the particular case of mixing vessels, the Froude number governs the formation of surface vortices (Edwards *et al.*, 1997), and its expression is given by

$$\mathrm{Fr} = \frac{N^2 D}{g} \tag{2.7}$$

which, similarly to Re_{imp}, is justified by the fact that the impeller tip speed is proportional to ND. Whilst this dimensionless number is usually important only in situations where gross vortexing exists, it can be neglected if the Reynolds number is less than about 300 (Skelland, 1967). For higher Reynolds numbers the Froude number effects can be eliminated by the use

of baffles, an eccentric shaft (Hall *et al.*, 2004; Galletti and Brunazzi, 2008) or square tanks (Kresta *et al.*, 2006).

2-3.2 Power consumption

In a stirred tank mixing system, one of the most important measurements that can be made is that of the power draw of the system, as many scale-up empirical and semi-empirical rules depend heavily on the specific power input (Brown *et al.*, 2004). The power draw, *P*, of an impeller is characterized by its dimensionless power number, Po, expressed by

$$\mathrm{Po} = \frac{P}{\rho\ N^3 D^5} \tag{2.8}$$

All the energy supplied to the fluid by the agitation system must eventually be dissipated as heat, so one possible method of measuring the power draw is to insulate the system and measure the temperature rise over time. In practice, however, this is extremely difficult to do accurately, due to problems with the effectiveness of the insulation and with the fluid physical properties being a function of temperature. Another frequently employed method involves the measurements of torque and rotational speed of the impeller.

Using the Buckingham π theorem, it can be shown that for geometrically similar systems (i.e., scaled apparatus) the power number can be reduced to a function of Re_{imp} and Fr (Edwards *et al.*, 1997), i.e.,

$$\mathrm{Po} \cong f(\mathrm{Re}_{imp}, \mathrm{Fr}) \tag{2.9}$$

When the influence of Froude number can be neglected, for example when using baffles, the power requirement of the impeller under these conditions will only depend upon the Reynolds number and Eq. (2.9) becomes

$$\mathrm{Po} \cong f(\mathrm{Re}_{imp}) \tag{2.10}$$

Nevertheless, presently, Po cannot be accurately predicted by a correlation or computational fluid dynamics (CFD) simulations (Ciofalo *et al.*, 1996; Brucato *et al.*, 1998); it is usually calculated from experimental power draw data.

According to Hemrajani and Tatterson (2004), Po remains constant throughout the turbulent

regime ($Re_{imp} > 10^4$) and hence independent of liquid viscosity. However in the laminar regime ($Re_{imp} < 10$), Po is inversely proportional to the impeller Reynolds number, Re_{imp}. Po varies with Re_{imp} for flow throughout the transition regime ($10 < Re_{imp} < 10^4$). In a fully baffled vessel under single phase turbulent mixing conditions, Po is ~ 5 and ~ 1.7 for RDT and 45° PBT ($D = 0.33T$) impellers respectively (Nienow, 1997a).

2-3.3 Single- or Multi-phase Fluid

The Prandtl number, Pr, is a dimensionless number approximating the ratio between the viscous diffusion rate and the thermal diffusion rate. Whilst viscous diffusion rate or momentum diffusivity is represented by the kinematic viscosity, ν, the thermal diffusivity, α, is defined as

$$\alpha = \frac{k}{\rho c_p} \tag{2.11}$$

where the k, ρ and c_p are the conductivity, density and specific heat of the fluid. On the basis of their physical meaning and given that both kinematic viscosity and thermal diffusivity have the dimensions of a surface propagation velocity, i.e. $m^2\ s^{-1}$, the Prandtl number is defined as

$$\mathrm{Pr} = \frac{\nu}{\alpha} \tag{2.12}$$

When Pr is small, the heat diffuses rapidly compared to the velocity (momentum). On the contrary, for high values of ν/α, the momentum diffusion rate produces a much more significant effect than the thermal diffusivity.

An alternative definition of the Prandtl number takes into account momentum and thermal eddy diffusivities, and it is usually called turbulent Prandtl number (Incropera and DeWitt, 1996). Such a dimensionless parameter is of more complicated derivation and it is usually used in CFD studies (Sahu and Joshi, 1995).

Sometimes referred to as the inertial parameter, the Stokes number, St, is an index of the *impactability* of a particle within a flowing fluid (McNaught and Wilkinson, 1997). This dimensionless number governs the behaviour of particles suspended in a fluid flow, and is usually defined as the ratio of the product of the bulk velocity of the fluid, u, and the

relaxation time of the particle, τ_p, to a characteristic dimension of the obstacle, d; namely

$$\mathrm{St} = \frac{\tau_p u}{d} \tag{2.13}$$

On the basis of this definition, the Stokes number can be interpreted as a ratio of distances, where $\tau_p u$ is the stopping distance of the particle, i.e., the viscous damping of the particle inertia, and d is a characteristic length of an obstacle. Alternatively, St can be imagined as the ratio of the particle response time (to adjust to changes in flow velocity or direction), τ_p, to the fluid response time to an external disturbance, d/u. For mixing studies d can be replaced by the diameter of the agitator.

Whilst for St » 1 the particle will continue in a straight line impacting on an obstacle as the fluid turns around it, for St « 1, particles will follow the fluid streamlines closely. For particle tracking studies where particle tracer and fluid have different density, the Stokes number is a very useful tool to assess the reliability of the flow following process (Fangary *et al.*, 2000; Fishwick *et al.*, 2003). Studies of the influence of large-scale vortex structures on the particle dispersion process have also benefited from the use of this dimensionless number (Tang *et al.*, 1992).

2-3.4 Capacity, effectiveness and efficiency

The pumping capacity, Q, which is described as the nominal volumetric flow rate of fluid passing through the planes surrounding the impeller as it rotates, is often reported in terms of the pumping or flow number, Fl. The flow number is a dimensionless parameter used to measure impeller pumping effectiveness, and is usually defined as the normalised volumetric discharge, i.e.,

$$\mathrm{Fl} = \frac{Q}{ND^3} \tag{2.14}$$

The plane of measurement depends on the direction of major flow discharge, so that the discharge flow, Q, is traditionally measured as shown in **Figure 2.4a** and **b** for a radial and an axial flow impeller, respectively. A detailed discussion on the validity of these traditional definitions and the three-dimensional aspect of this quantity is given in Chapter IV.

Mavros and Baudou (1997) defined a dimensionless agitation index, I_g, in order to determine

the effectiveness of an impeller to induce flow in a vessel. The index I_g is calculated using the resultant mean velocity vector module, u_{ij}, of the three time-averaged velocity components at each measuring point (ij) in the investigated vertical plane. On the basis of the measurement resolution, the velocity value obtained at a point is extended to a small surrounding volume, V_{ij}, where the velocity is assumed to be uniformly equal to the measured value u_{ij}. Therefore, the volume weighted average velocity for the entire tank can be obtain as

$$\bar{u} = \frac{\sum_i \sum_j V_{ij} u_{ij}}{\sum_i \sum_j V_{ij}} = \frac{\sum_i \sum_j V_{ij} u_{ij}}{V_T} \tag{2.15}$$

where V_T is the total volume of the working fluid. An agitation index, I_g, is obtained by normalising the volume-weighted average velocity with the impeller tip sped u_{tip}, that is

$$I_g = 100 \frac{\bar{u}}{u_{tip}} \ [\%] \tag{2.16}$$

which represents the global mean velocity expressed as a percentage of the tip velocity. Given that the primary function of an agitator is to induce flow inside a vessel, the agitator index I_g is a measure of the impeller effectiveness as high values of I_g correspond to high

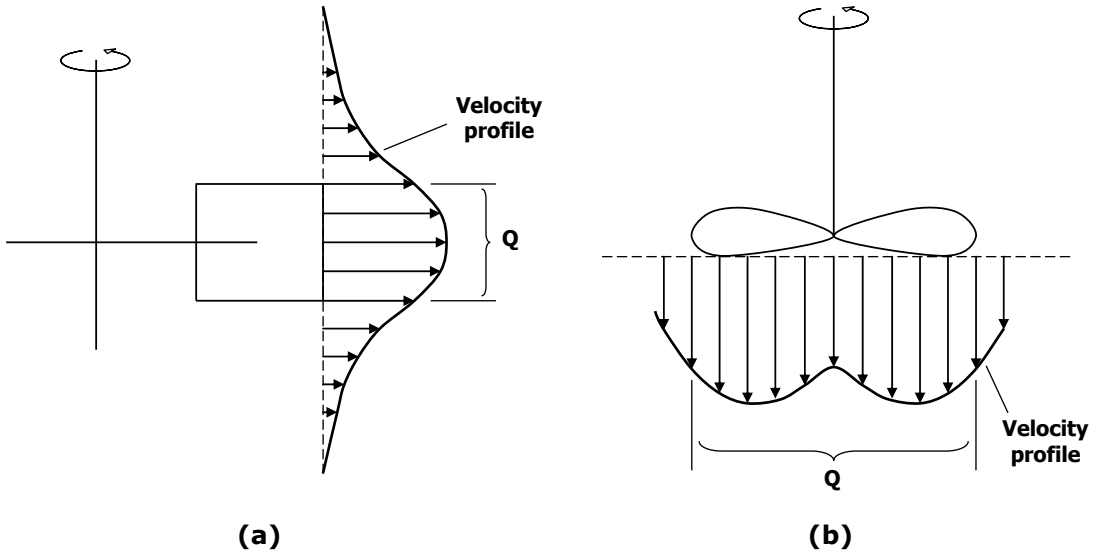

Figure 2.4. Traditional definitions of flow rate, Q, for determining the flow number for (a) radial flow agitators and (b) axial flow agitators (Nienow, 1997a).

induced velocities inside the vessel. The usefulness of this agitation index lies in its ability to differentiate among several possible alternatives, either in terms of type of agitator or in terms of their placement in the vessel (Aubin *et al.*, 2004). The determination of such an index is based on measurements performed in a single 2D plane (Aubin *et al.*, 2004); such a practice, however, appears to be unreliable for describing impeller effectiveness as it can vary by up to 50% between measurement planes, as shown in Chapter IV.

Based on considerations of hydraulic pumping efficiency and the ratio of gain in enthalpy to the power input, P, by the impeller, Bakker and Van den Akker (1990) defined the dimensionless pumping efficiency as

$$\eta = \frac{\mathrm{Fl}^3}{\mathrm{Po}}\left(\frac{D}{T}\right)^4 \tag{2.17}$$

This dimensionless parameter can also be used to compare impellers having different D/T geometrical ratios. Using the expressions in Eqs. (2.8) and (2.14), Eq. (2.17) becomes

$$\eta = \frac{Q^3\rho}{PT^4} \tag{2.18}$$

As a consequence, if Q and P are actually measured, the pumping efficiency can be obtained directly so that any error in the assumption of constant Fl and Po can be eliminated (Jaworski *et al.*, 1996).

Mixing systems often involves two or more miscible fluids which are blended to provide a desired degree of uniformity. The time taken to reach this degree of homogeneity, θ_m, is called the blend time, macroscale mixing time or, simply, mixing time. The impeller rotational speed is generally used to make θ_m a dimensionless number, so that, the parameter $N\theta_m$ corresponds to the number of revolutions necessary to reach the desired degree of homogeneity. The value of this important dimensionless parameter, which is often obtained by measurements, is dependent on impeller and vessel geometry. A number of techniques are available for its measurement, such as dye injection and acid-base colorization-decolorization (Cronin *et al.*, 1994). A novel methodology for measuring mixing time is presented in Chapter VI.

Several design correlations available in the literature, for example Grenville and Nienow

(2004) proposed that

$$N\theta_m = 5.2Po^{-1/3}\frac{T^{1.5}H^{0.5}}{D^2} \tag{2.19}$$

This correlation was obtained empirically through measurements executed in cylindrical vessels with diameters in the range 0.30-2.97m. A similar correlation was obtained by Kresta *et al.* (2006) in unbaffled square tanks where the vessel fill height, H, was set equal to the width of the tank, T_s, that is

$$N\theta_m = 6.0Po^{-1/3}\frac{T_s^2}{D^2} \tag{2.20}$$

The author concluded that the square tank is a less efficient mixing geometry than the cylindrical tank as the correlation constant for cylindrical tanks, 5.2 in Eq. (2.19), must be increased to 6.0 for square tanks.

2-4 Solid-liquid mixing

In operations such as crystallization or solid-catalysed liquid reactions, it is necessary to suspend solid particles in a relatively low viscosity liquid (Nienow *et al.*, 1997). This can be achieved in stirred vessels where the agitator is used to prevent sedimentation of the solids and to provide conditions suitable for good liquid-solid mass transfer, heat transfer and/or chemical reaction. Where agitation is not sufficient or interrupted, the relative densities of the solid and liquid phases determine the tendency of the particles to settle out or float to the surface. These floating solids include solids that are less dense than the liquid, dense solids with trapped gas, and solids that are difficult to wet.

Sometimes, solid-liquid mixing operations are performed in the presence of gas bubbles. The introduction of the gaseous phase in these systems, which are referred to as gassed suspensions, may occur, directly as in solid-catalyzed hydrogenation reactions, entrained inadvertently or deliberately from the headspace, or evolved as in an evaporative crystallization or as a gaseous reaction product (Atiemo-Obeng *et al.*, 2004). Suspensions in the absence of gas bubbles are usually known as ungassed suspensions.

At the opposite extreme, other solid-liquid operations involve the dispersion of very fine particles into a highly viscous fluid where the interfacial phenomena dominate the dispersion process, for example, the old practice of incorporating carbon black into rubber (Parkinson, 1951). In this case, the product is usually stable, highly viscous and may well exhibit complex rheology. Such processes generally do not involve heat/mass transfer or chemical reactions.

The branch of solid liquid mixing which studies suspensions of solids in low viscosity liquids is the most relevant to the present work. In Chapters VII, VIII and IX, detailed hydrodynamic and phase dispersion experimental studies in such systems will be presented.

2-4.1 Solid-liquid process design

The desired process results for solid-liquid mixing vary from process to process. Therefore it is essential to consider and understand, early in the process development stage, all the relevant physical and chemical phenomena involved in the mixing operation. Typical tasks involved in the design of solid-liquid mixing process are

- achieving and maintaining off-bottom suspension of solids;
- achieving and maintaining uniform solids concentration throughout the tank of interest particularly for slurry catalyst reactors and for feeding downstream equipment;
- controlling mass transfer for solids dissolution;
- maintaining the required slurry composition on discharge;
- avoiding plugged nozzles during tank draining with solids present;
- controlling abrasion due to particle-particle and impeller-particle interactions.

Some other difficult design problems that have not yet been completely resolved include non-wetting, clumping, or floating solids (Khazam and Kresta, 2008; 2009). Other mixing effects concerning solids in suspension include agglomeration, fouling, and scaling. These problems, however, can be reduced with good mixing designs (Paul *et al.*, 2004).

2-4.2 Particle distribution

When suspending dense solid particles in relatively low viscosity Newtonian fluids, the input

energy is transferred through the agitator to the fluid to create a turbulent flow field in which solid particles are lifted from the vessel base and subsequently dispersed and distributed throughout the liquid.

In mechanically agitated vessels, the degree of solids suspension is generally classified into four levels: non-progressive fillets mode, complete on-bottom motion, just complete suspension, and uniform suspension (Nienow, 1997b). The four suspension modes are illustrated in **Figure 2.1**. In non-progressive fillets mode, a small proportion of particles is allowed to collect in relatively stagnant regions where fillets are formed, i.e., a loose aggregation of particles in corners or other parts of the tank bottom. This condition may offer advantages from a practical point of view because of the very large saving in power consumption compared with that required for complete suspension. This power saving may offset the loss of active solids (Nienow, 1997b).

The complete on-bottom motion state is characterised by the complete motion of all particles around the bottom of the vessel. Although in motion, some particles are in constant contact with the base of the vessel, so that only a partial surface area of particles is available for chemical reaction or heat/mass transfer. Nevertheless, this suspension mode excludes the formation of fillets and is sufficient for the dissolution of highly soluble solids (Atiemo-Obeng *et al.*, 2004).

The accepted definition of the just complete suspension mode is based on a criterion suggested by Zwietering, (1958) which postulates that particles are 'just suspended' when no

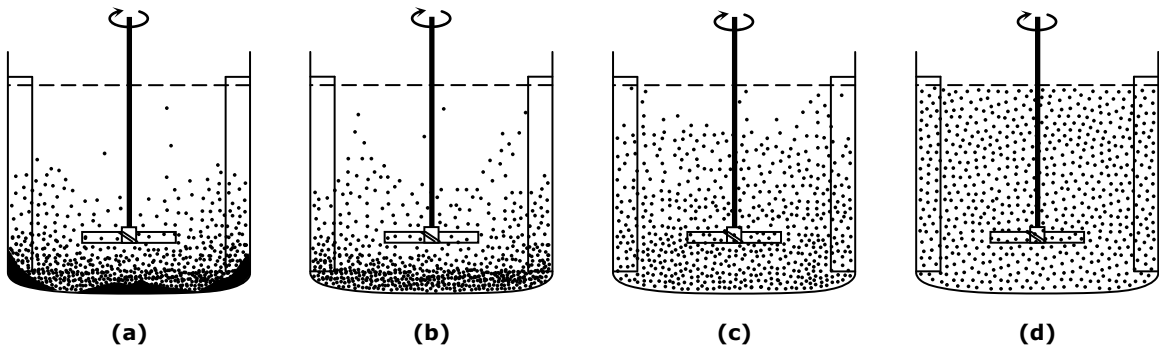

Figure 2.5. Degrees of solid suspension (Nienow, 1997b): (a) non- progressive fillets mode; (b) complete on-bottom motion; (c) just complete suspension; (d) uniform suspension.

particle remains on the tank base for more than 1-2 s. It must be noted that, at this condition, the solid distribution throughout the system may be extremely non-uniform, especially when the aspect ratio H/T is higher than 1. Much of the work in the literature pertaining to particle suspension is related to the minimum agitator speed or specific power required to achieve this condition (Nienow, 1997b). A number of empirical relationships and theoretical models for predicting the minimum impeller rotational speed for complete particle suspension have been proposed (Zwietering, 1958; Nienow, 1968; Molerus and Latzel, 1987a-b; Raghava Rao *et al.*, 1988; Geisler *et al.*, 1993; Mersmann *et al.*, 1998; Aremante *et al.*, 1998). Recently, Brujes *et al.* (1998) compiled most of the correlations published over the previous four decades, and tested them against experimental measurements obtained in baffled and unbaffled vessels containing suspensions of glass beads, resins particles or microcapsules. It emerges from such literature that the fundamental mechanisms which govern particle suspension and distribution within a stirred vessel are still not well understood.

Uniform suspension corresponds to the state of solid distribution at which particle concentration and particle size distribution are practically uniform throughout the vessel; any further increase in the rotational speed of the impeller does not significantly enhance the solids distribution in the system. In practical terms, a phase distribution can already be considered uniform when the standard deviation of the local volume concentration of each particle size fraction, measured at different points in the system, is < 5 % of the mean solid volume concentration (Brown *et al.*, 2004). This condition is particularly desirable when a continuous and representative flow of solids from the system is required or a uniform concentration of solids must be achieved, e.g, in crystallization.

2-5 Experimental measurement techniques

A large number of experimental methods have been employed over the years to quantify mixing processes. The experimental techniques of most relevance to this work are the optical techniques of LDV and PIV for single point and planar flow field investigations, PLIF for quantifying tracer local concentration, and the Lagrangian tracking techniques of PEPT and CARPT. As a consequence, the following review is focused on these five methods. A thorough review of available experimental techniques for the analysis of different aspect of mixing in stirred vessels can be found in Mavros (2001) and Brown *et al.*, 2004.

2-5.1 Laser Doppler velocimetry

Laser Doppler velocimetry (LDV) is a non-intrusive optical measurement technique for investigating velocities at a point in a liquid flow. The technique can be used in any liquid flow with optical access to the measurement point provided that micron-sized seeding particles are present.

The measurements are performed at the intersection of two coherent laser beams, as shown in **Figure 2.6**. The two laser beams having wavelength, λ, generate an interference fringe pattern of alternating light and dark planes. The fringe spacing, d_f, is a geometric function of λ and the angle ϕ (Papadopoulos and Arik, 2004), that is

$$d_f = \frac{\lambda}{2\sin\phi} \tag{2.21}$$

Each particle going through the measuring region moves through the fringe pattern, creating a scattered light signal (burst). The light scattered by particles, as they go through the measuring volume, is collected by the receiving optics system and sent to the photodetector. The frequency of the burst signal or Doppler frequency, f_D, is the inverse of the time required to cross a pair of consecutive fringes; thus

$$u = f_D d_f \tag{2.22}$$

Note that a pair of beams can only detect one velocity component at a time, i.e. the vertical

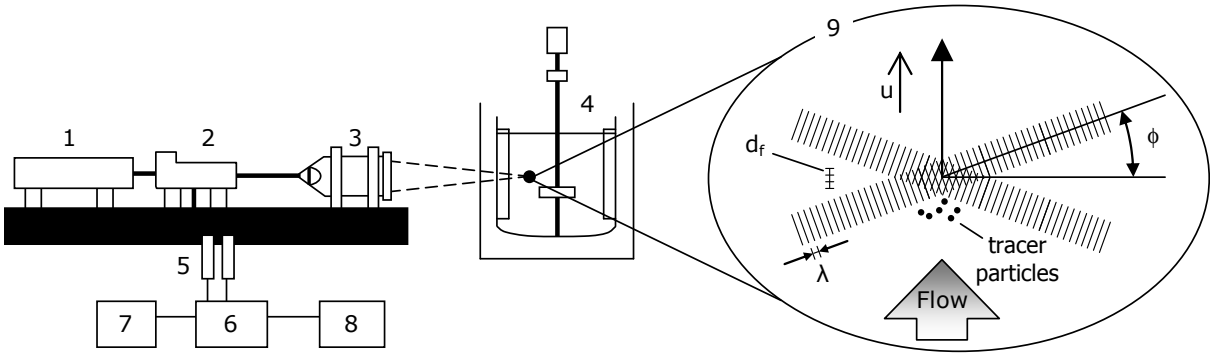

Figure 2.6. Typical LDV experimental set-up: 1 laser; 2 fiber-optical module; 3 transmitting/receiving optics; 4 stirred vessel; 5 photomultipliers; 6 flow velocity analyser; 7 oscilloscope; 8 computer; 9 intersection of the two coherent laser beams.

component for the schematic illustration in **Figure 2.6**. By combining two or three sets of double beams, it is possible to determine at the same time two or three velocity vector components (Mavros *et al.*, 1996; 1998). Also, by installing the optical equipment on a traversing system, which allows the beam intersection to be located at various places inside the stirred vessel, velocities can accurately be determined at various points (Armenante *et al.*, 1997).

LDV can either be performed on forward- or back-scattered light. Data obtained from forward scattering LDV have a better signal-to-noise ratio, which benefits the measurement of high speed flows and flows with very low turbulence intensities as the turbulent fluctuations can be drowned out by noise. The simplicity of back scattering LDV, where all units are contained within a common housing, makes it the favourable choice for the average user since it saves the time required to align separate units.

An example of the application of the LDV technique to a stirred vessel is given by Yianneskis & Whitelaw (1993), the authors carried out angle resolved measurements around the blades of a RDT. In a similar way, by using LDV and PIV, angle resolved measurements were obtained on a small scale vessel (T = 100 mm) by Baldi and Yianneskis (2003). Using a refractive index matched system, Haam *et al.* (2000) applied LDV to a very dilute solid-liquid system; the solid component used was made by nearly-spherical poly(methyl methacrylate) particles.

The use of transparent fluids is an essential prerequisite for the application of the LDV technique. Unfortunately, this is a major limitation given that, in real mixing processes, fluids are usually partially or entirely opaque. In such situations, it is necessary to perform the measurements in transparent model fluids with similar rheological properties (Chandrasekaran *et al.*, 1997). However, such model fluids are not always available.

2-5.2 Particle image velocimetry

Particle image velocimetry is a non-intrusive optical Eulerian technique based on images of tracer ‘seeding’ particles suspended in the flow. Principles of PIV can be found in many pubblications, including Lourenco *et al.* (1989), Adrian (1991), and Willert and Gharib (1991). Various aspects of PIV are also discussed in details in a more recent book by Raffel *et al.* (1998). This technique is based on the measurement of the displacement of tracer

particles suspended in the transparent fluid which is illuminated by a pulsing thin plane of laser light. In order to obtain an accurate instantaneous flow velocity, the time between exposures should be small compared to the time scales in the flow; and the spatial resolution of the PIV sensor should be small compared to the length scales of the flow (Atiemo-Obeng *et al.*, 2004).

Among the various flow visualisation techniques, PIV has probably become the most employed to examine the complex nature of the flow fields in stirred vessels, provided the equipment and fluids used are optically transparent. Astonishingly foreseen by Leonardo Da Vinci who used to throw pollen grains to follow the vortices on water streams, the basic principles of PIV originated in the 1930s, and it was not until the 1980's that the roots of modern PIV were developed (Chang *et al.*, 1985a; 1985b).

A PIV measurement system typically consists of several sub-systems. As shown in **Figure 2.7**, the main component of a PIV setup includes a laser emitting unit which illuminates a cross-section of the seeded flow field, a recording camera located perpendicular to the light sheet and a data processor to analyse the images for displacement information.

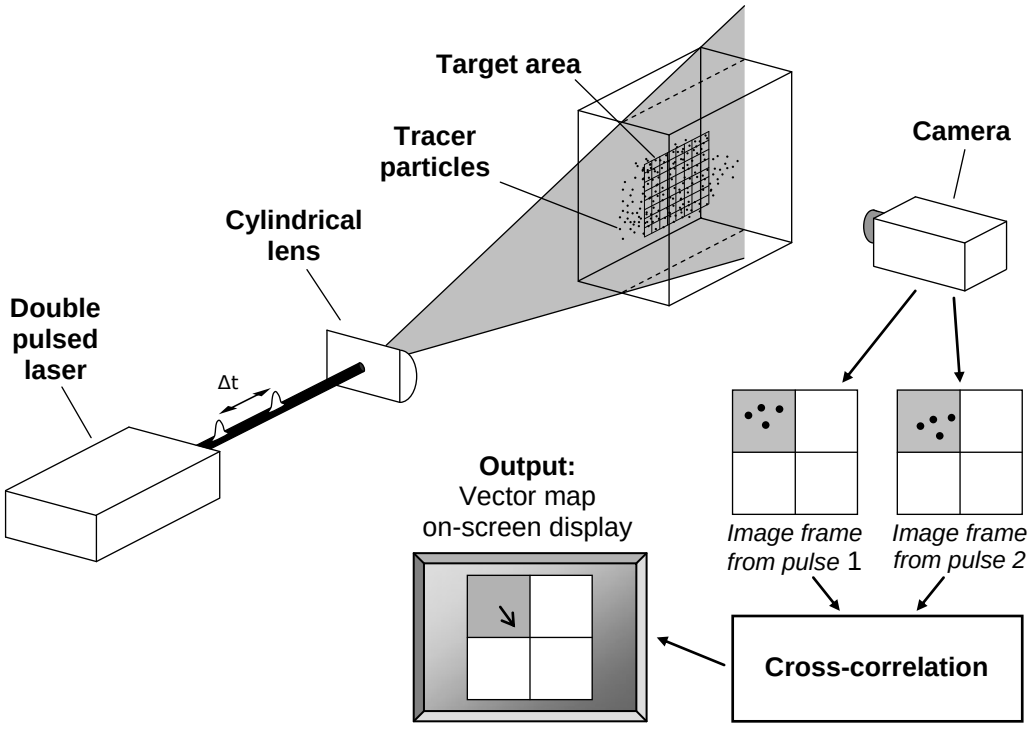

Figure 2.7. Simplified set-up of a typical positron image velocimetry system.

Tracer particles are added to the volume of interest prior to experiments in which they are to be illuminated by a pulse of laser light twice within a short controlled time interval. The laser is converted into a thin sheet via a cylindrical lens. The light scattered by the particles is recorded via charge-coupled device (CCD) camera on two separate frames, as employed in Chapter IV, or via double exposure on a single frame of silver halide photographic film, as used in earlier PIV systems. Tracer particle displacement is obtained via cross-correlation for the two-frames method or via autocorrelation for the single-frame method.

2-5.3 Planar laser induced fluorescence

A very powerful technique, which allows mapping of concentration as a function of time over a full plane of the flow, is planar laser induced fluorescence (PLIF). It provides a full plane of instantaneous concentration data in a transparent system and can be very valuable where the intermittency of concentration at the visible scales of motion must be understood. It has been applied successfully to several low Reynolds number mixing devices to elucidate mixing structures (Adams and Barigou, 2007; Alvarez-Hernández *et al.*, 2002). Examples of images captured using the PLIF technique are presented in **Figure 2.8**.

The technique exploits chemical substances which become fluorescent when excited by a

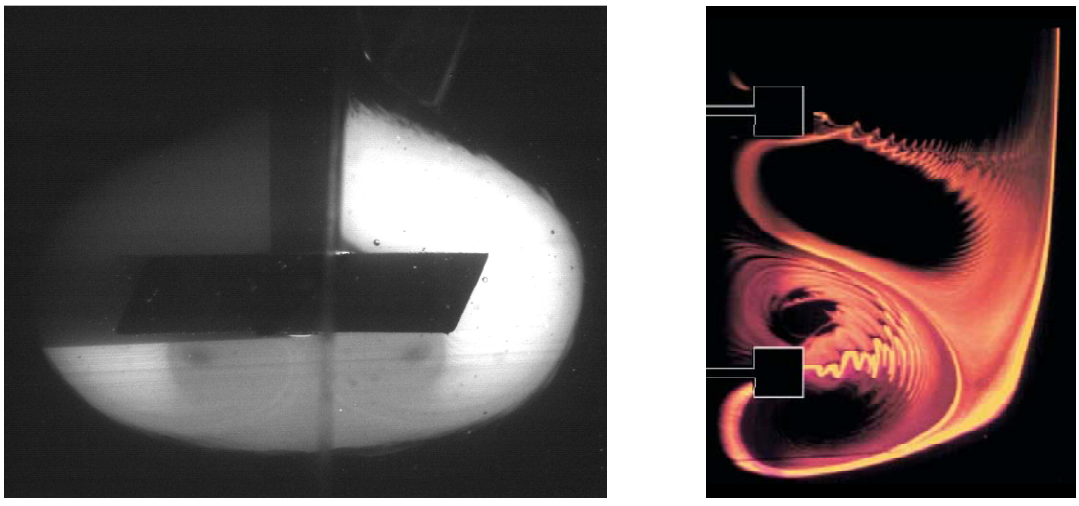

(a) **(b)**

Figure 2.8. Examples of PLIF images: (a) formation of cavern around the impeller in a yield-stress non-Newtonian fluid at Re_{imp} ~ 7.5 (Adams and Barigou, 2007); (b) oscillatory structure in a multi-impeller agitated vessel containing a Newtonian fluid at Re_{imp} ~ 40 (Alvarez-Hernández *et al.*, 2002).

light source with a particular wave length. Several substances of this kind exist and fluorescein and rhodamine B are two examples. The phenomenon was initially denominated phototropism; however, the current term is 'photochromism' and the dyes are named photochromic dyes (Mavros, 2001). When a laser beam illuminates a planar slice of the system, the fluorescent dye, already fully dispersed in the fluid, is excited becoming fluorescent. The signal is usually captured by a CCD camera and timing electronics is often used to synchronize pulsed light sources with intensified cameras. Quantitative analysis of the images can be done by converting light intensity to dye concentration at each pixel of data (Kresta and Brodkey, 2004).

2-5.4 Computer automated radioactive particle tracking

In a similar way to positron emission particle tracking, the technique of computer automated radioactive tracking (CARPT) is a Lagrangian technique which uses a radioactively labelled particle tracer. The detection system consists of an array of 8 to 16 Sodium Iodide (NaI-Tl) detectors, as shown in **Figure 2.9**, that record the number of disintegration events coming from the source within the domain during a specific dwell time, typically 5-10 ms (Doucet *et al.*, 2008a). This setup allows system with large dimensions to be investigated since the

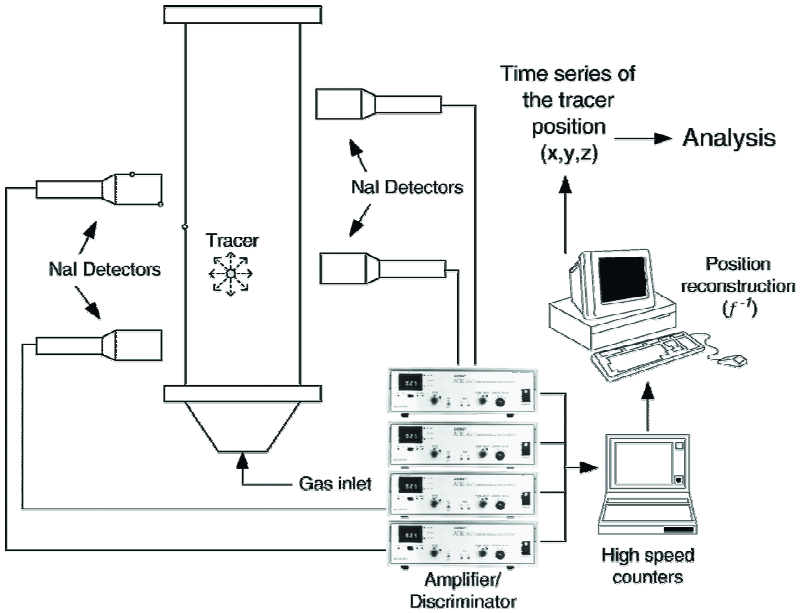

Figure 2.9. Application of CARPT to the study of multiphase reactors (Doucet *et al.*, 2008a).

detectors can be positioned individually around the system (Cassanello *et al.*, 1995, Larachi *et al.*, 1996; Limtrakul *et al.*, 2005).

Prior to an experiment, the tracer is positioned in a number of specific positions in order to calibrate the signal obtained by the discriminators (**Figure 2.9**). The reconstruction of the tracer position by using the measurements obtained from the multiple detectors surrounding the system is referred to as the inverse map problem (Larachi *et al.*, 1994; 1995). Such an analytical process must take into account several factors and the geometry of the system must be known *a priori*. Geometrical anisotropy induced by the boundaries as well as the solid angle with each detector must be well accounted for since the quality of the map depends essentially on the level of precision with which these two quantities can be predicted.

2-5.5 Positron emission particle tracking

Over the last 20 years, Positron Emission Tomography (PET) has developed as one of the most powerful and efficient imaging techniques in medicine. It is used to determine the distribution of metabolic fluids, whose molecules are labelled with a positron-emitter radionuclide, to identify functional disorders or the growth of cancers. By simultaneously detecting the pair of back-to-back gamma rays generated when a positron annihilates with an electron, a line passing close to the source is identified, and by detecting all γ-ray pairs emerging from different parts of the system and using tomographic image reconstruction methods, the distribution of the metabolic fluid can be mapped. The use of PET for engineering processes was pioneered at the University of Birmingham (UK), where the related technique of positron emission particle tracking (PEPT), whereby a single tracer particle can be tracked at high speed within operating equipment, was also developed (Parker *et al.*, 1993).

Originally, PEPT was performed using a pair of multiwire detectors, but more recently it has been using a pair of digital gamma camera heads. In 1999 the Positron Imaging Centre acquired a medical PET/SPECT scanner (ADAC Laboratories) which has been rebuilt in a flexible geometry for use in PEPT investigations. Fast moving tracer particles can now be rapidly and accurately located.

As mentioned above technique of positron emission particle tracking involves a positron camera, a radioactively-labelled particle tracer and a location algorithm for computing the

tracer location. The positron camera uses two position-sensitive detectors between which the system under study is mounted, as shown in **Figure 2.10**. The Birmingham positron camera comprises two gamma camera-heads working in coincidence, mounted on a motorised gantry which allows their rotation about a horizontal axis (Parker *et al.*, 2002). Each detector contains a single sodium iodide crystal optically coupled to an array of photomultiplier tubes.

The positron-emitting radioactive tracer is introduced into the flow (**Figure 2.10**). Once emitted from the nucleus, a positron annihilates with an electron, releasing energy in the form of two back-to-back collinear 511 keV γ-quanta. Each detector captures incident γ-rays over a large rectangular active area, the two incident γ-rays produce scintillations in the crystals within the detectors, the related photomultipliers generate positional signals and the two 2D centroids are then obtained.

Using a small number of annihilation events (theoretically only two), the position of the positron-emitting particle can be located at the intersection of the photon-trajectories. The location algorithm calculates the time-space location of the radioactive tracer minimising the sum of perpendicular distances from a generic point to the various photon-trajectories (Parker *et al.*, 1993). PEPT data are provided in the form of a text file including four columns representing the location time, *t*, and the three Cartesian coordinates, *x*, *y* and *z*, of the radioactive tracer. These data can also be converted to give an Eulerian description of the flow.

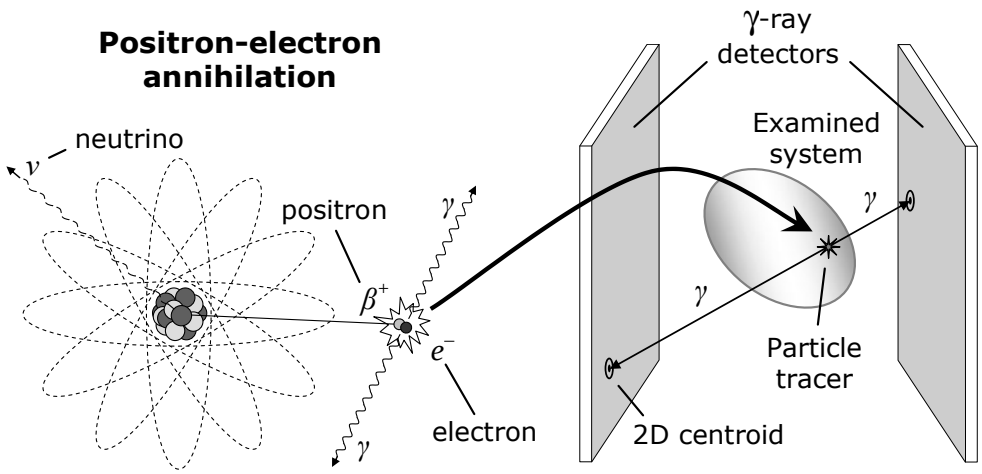

Figure 2.10. Schematic illustration of positron annihilation and gamma ray detection by the PEPT camera.

PEPT has been used in recent years to study flow in a variety of situations. For example, Fangary *et al.* (2000) used PEPT data to obtain the particle Trajectory Length Distribution in a mechanically agitated non-Newtonian fluid and estimate fluid circulation; the variance in location of a delimited sample of PEPT locations after a given period of time was analysed by Martin *et al.* (2007) to obtain an indication of phase dispersion in a ribbon bladed mixer. PEPT was recently used to study solid-liquid flows in pipes (Eesa and Barigou, 2008; 2009) and in stirred vessels (Barigou *et al.*, 2009) thus obtaining the full velocity field and spatial distribution of both phases. Other experimental data generated by PEPT in different types of powder mixers, includes the single blade (Laurent and Bridgwater, 2002), the high shear (Kuo *et al.*, 2004), the ploughshare (Broadbent *et al.*, 1993; Jones and Bridgwater, 1998; Forrest *et al.*, 2003), and the planetary (Hiseman *et al.*, 2002). Recent works have also successfully applied this technique to obtain the flow field in a V-blender for different fill levels (Kuo *et al.*, 2005).

The technique is particularly useful for the study of multiphase flows, to map the flow of fluids and particles, where one component can be labelled and its behaviour observed (Parker *et al.*, 2002; Barigou, 2004). A more detailed description of the technique and related data analysis is provided in Chapter III.

2-6 Conclusions

This chapter provides a general description of mixing principles, typical configurations of mechanically agitated vessels, agitators, solid-liquid systems and relevant experimental techniques. Nevertheless, due to the different nature of some the following chapters, additional literature review, state of the art, drawbacks of experimental techniques, and discussions on research needs relevant to each particular study are often presented in the introducing section of the following chapters.

Notation

Roman letters

B	Baffle width	m
c	Characteristic fluid wave propagation velocity	m s^{-1}
C	Impeller off-bottom clearance	m
c_p	Specific heat of the fluid	J kg^{-1} K^{-1}
d	Characteristic length of an obstacle in the flow	m
D	Impeller diameter	m
d_f	Distance between fringes	m
d_w	Uniform fluid depth	m
f_D	Doppler frequency	s^{-1}
Fl	Flow number	-
Fr	Froude number	-
g	Gravitational acceleration	m s^{-2}
h	Convective heat transfer coefficient	W m^{-2} K^{-1}
H	Vessel fill height	m
i j	Radial and axial position indices	-
I_g	Agitation index	-
k	Conductivity of the fluid	W m^{-1} K^{-1}
L	Characteristic length	m
N	Impeller rotational speed	s^{-1}
Nu	Nusselt number	-
P	Power draw	W
Po	Power number	-
Pr	Prandtl number	-
Q	Impeller pumping rate	kg m^{-3}
Re	Reynolds number	-
Re_{imp}	Impeller Reynolds number	-
St	Stokes number	-
t	Time	s
T	Vessel diameter	m
T_s	Width of square vessel	m

u	Velocity	m s^{-1}
$\bar{u}$	Volume weighted average Eulerian velocity	m s^{-1}
u_{ij}	Eulerian velocity measured in *ij*	m s^{-1}
u_{tip}	Impeller tip speed	m s^{-1}
V_{ij}	Volume of surrounding the measuring point *ij*	m^3
V_T	Total fluid volume in the vessel	m^3
W	Impeller height	m
$x\ y\ z$	Cartesian coordinates	m

Greek letters

α	Thermal diffusivity of the fluid	m^2 s^{-1}
η	Pumping efficiency	-
θ_m	Macroscale mixing time	s
λ	Laser wavelength	m
μ	Dynamic viscosity of the fluid	Pa s
ν	Kinematic viscosity of the fluid	m^2 s^{-1}
ρ	Density of the fluid	kg m^{-3}
τ_p	Particle relaxation time	s
ϕ	Laser beam crossing angle	rad

Abbreviations

CARPT	Computer automated radioactive tracking
CCD	Charge-coupled device
CFD	Computational fluid dynamics
LDV	Laser Doppler velocimetry
PBT	Pitched blade turbine
PBTD	Down-pumping PBT
PBTU	Up-pumping PBT
PEPT	Positron emission particle tracking
PIV	Particle image velocimetry
PLIF	Planar laser induced fluorescence
RTD	Rushton disk turbine

Chapter III
Experimental and Theoretical Procedures

Abstract

Mixing is intrinsically a Lagrangian process and, whilst Eulerian data are essential, Lagrangian information is necessary for its complete description. Possible approaches of generating Lagrangian data can, in principle, employ numerical simulations or experimental techniques based on Lagrangian tracking to provide the trajectories of fluid elements or solid particles. Following a description of the experimental technique and equipment used, this chapter presents a set of tools developed for the analysis and theoretical validation of Lagrangian multi-phase flow data obtained from tracer trajectories in mechanically agitated vessels. The implementation and power of these tools are demonstrated by analysing a wide range of sample measurements acquired using the technique of positron emission particle tracking (PEPT) during the mixing of Newtonian and non-Newtonian fluids, as well as the mixing of highly concentrated solid-liquid suspensions. The sample results are extracted from the various studies following this chapter.

3-1 Introduction

Mixing is intrinsically a Lagrangian process and, although Eulerian data are essential, a Lagrangian study is necessary for its complete description. The Lagrangian approach has been used to describe laminar mixing properties using the dynamical system viewpoint and chaos theory (Aref, 1984; Ottino, 1989). These authors' works, in particular, have shown that fluid element transport has features which can be completely different from and complementary to those of the underlying velocity field. Aref (1984), for instance, showed through an idealised model that a simple velocity field could induce very complex fluid trajectories leading to the creation of large internal surfaces, which is conducive to good mixing. Rubinovitch and Mann (1983a-b) studied the flow of inter-connected volumes, representing the movement of particles by a Markov chain. Information on the probability of visiting a volume and total residence time in the specific volumes could be obtained. This conceptual approach has not been exploited in the analysis of real systems such as stirred vessels, however. On the other hand, applying the Lagrangian approach to turbulent flows, Toschi and Bodenschatz (2009) concluded that the Lagrangian description of turbulence is characterized by conceptual simplicity and immediate connection with dispersion and mixing.

Possible approaches of generating Lagrangian data can in principle employ numerical simulations or 'non-intrusive' experimental techniques based on Lagrangian tracking to provide the trajectories of fluid elements or solid particles in a flow system. For example, by numerically simulating the paths taken by 100 000 particles released at three different points, LaRoche (2005) studied the effect of the position of the feed point on the mixing efficiency inside a stirred vessel. The different behaviour in the suspension of three sizes of heavy particles within a mixing vessel was recently simulated by Lavezzo *et al.* (2009) employing Lagrangian particle tracking and direct numerical simulation of turbulence. Experimental techniques which are effective in providing Lagrangian data in flow systems, however, have been rare. A three-dimensional particle tracking technique based on images of turbulent flow captured in a stirred vessel by two synchronised video cameras was developed by Wittmer *et al.* (1998). This technique, however, suffered from drawbacks including the large size of the particle tracer, the low frequency of data acquisition, and the fluid and vessel had to be optically transparent. Rammohan *et al.* (2001) developed a more sophisticated computer automated radioactive particle tracking (CARPT) technique based on gamma-ray emissions. Despite the experimental difficulties encountered, these authors and others have shown that

the analysis of Lagrangian data obtained from a single particle trajectory unravel precious mixing information which is not measurable by Eulerian observations (Villermaux, 1996; Wittmer *et al.*, 1998; Rammohan *et al.*, 2001; Doucet *et al.*, 2008b).

3-2 Data collection

As introduced in Chapter II, the Lagrangian tracking approach is based on the study of data obtained following the long-term trajectory of a particle tracer either numerically or experimentally. Therefore, the starting point is the knowledge of the position of the particle tracer in space at multiple instants which can be expressed by the four time-space arrays $[t_k]$, $[x_k]$, $[y_k]$, $[z_k]$ where k is a location counter. It must be stressed that obtaining accurate data of this kind is not a trivial matter. Positron emission particle tracking (PEPT) is probably the only experimental technique which can currently provide Lagrangian data with a high time-space resolution in both single-phase and highly concentrated multi-phase opaque flows (Pianko-Oprych *et al.*, 2009; Guida *et al.*, 2010).

3-2.1 Experimental particle tracking by PEPT

Positron emission particle tracking allows non-invasive probing of opaque fluids and within opaque apparatus by using a single small sub-millimetre positron-emitting particle as flow tracer, which is accurately tracked in 3D space and time to reveal its Lagrangian trajectory (Barigou, 2004; Parker *et al.*, 2008). Being able to examine flow phenomena in three dimensions that could not be observed as effectively by using other techniques, PEPT is particularly useful for the study of multi-phase or multi-component flows, where one component can be selectively labelled and its behaviour observed (Fangary *et al.*, 2000; 2002; Guida *et al.*, 2009).

The technique of Positron emission particle tracking primarily involves the use of a labelled particle tracer, a positron camera and a location algorithm for computing the tracer location. The tracer particle is labelled with a positron-emitting nuclide and the radio isotopes usually used are ^{18}F, ^{61}Cu and ^{66}Ga. Isotope ^{18}F has a half-life of 109 min, and is produced from either purified water or solid materials under direct bombardment with high energy (33 MeV) ^{3}He beams via the reactions

$$^{16}\mathrm{O}(^{3}\mathrm{He}, p)^{18}\mathrm{F} \quad \text{or} \quad ^{16}\mathrm{O}(^{3}\mathrm{He}, p)^{18}\mathrm{Ne} \rightarrow ^{18}\mathrm{F} \tag{3.1}$$

The ^{3}He nuclei are accelerated in situ by using a cyclotron. Similarly, the reaction

$$^{60}\mathrm{Ni}(d, n)^{61}\mathrm{Cu} \tag{3.2}$$

is induced to produce ^{61}Cu, having a half-life of 3.3 h, by irradiating natural nickel with deuterons. The gallium radionuclide ^{66}Ga has a half-life of 9.3 h and is produced from zinc foils via the reaction

$$^{66}\mathrm{Zn}(p, n)^{66}\mathrm{Ga} \tag{3.3}$$

The separation of trace amounts of copper (gallium) radioisotopes from nickel (zinc) foils is conducted by Cation Chromatography. The techniques currently employed for particle labelling are Surface Modification (Fan *et al.*, 2006a), Direct Irradiation and Ion-Exchange (Fan *et al.*, 2006b).

A positron emitted by the particle tracer rapidly annihilates with an electron emitting a pair of almost collinear 511 keV γ-quanta in opposite directions. The detection in coincidence of these two γ-rays by the positron camera is the first step in locating the tracer. The positron camera, shown in **Figure 3.1**, consists of two γ-camera heads working in coincidence and mounted on a motorised gantry which allows their rotation about a horizontal axis. Each head contains a single sodium iodide crystal optically coupled to an array of photomultiplier tubes (Parker *et al.*, 2002). When a positron-electron annihilation occurs the γ-rays emitted produce two coincident scintillations in the crystals, the related photomultipliers generate positional signals and two 2D centroids are calculated by the detection software (**Figure 3.2**). The joining line is the photon-trajectory related to the annihilation event. With a small number of annihilation events (theoretically only two) the position of a single positron-emitting particle can be located at the intersection of the photon-trajectories.

The location algorithm, which is used offline, calculates the time-space location of the tracer minimising the sum of perpendicular distances from a generic point to the various photon-trajectories (Parker *et al.*, 1993). Moreover, it discards iteratively the corrupt events caused by Compton scattering, the radioactive background or if the two detected γ-rays were not in fact a pair of 511 keV photons originating from the same positron-electron annihilation event.

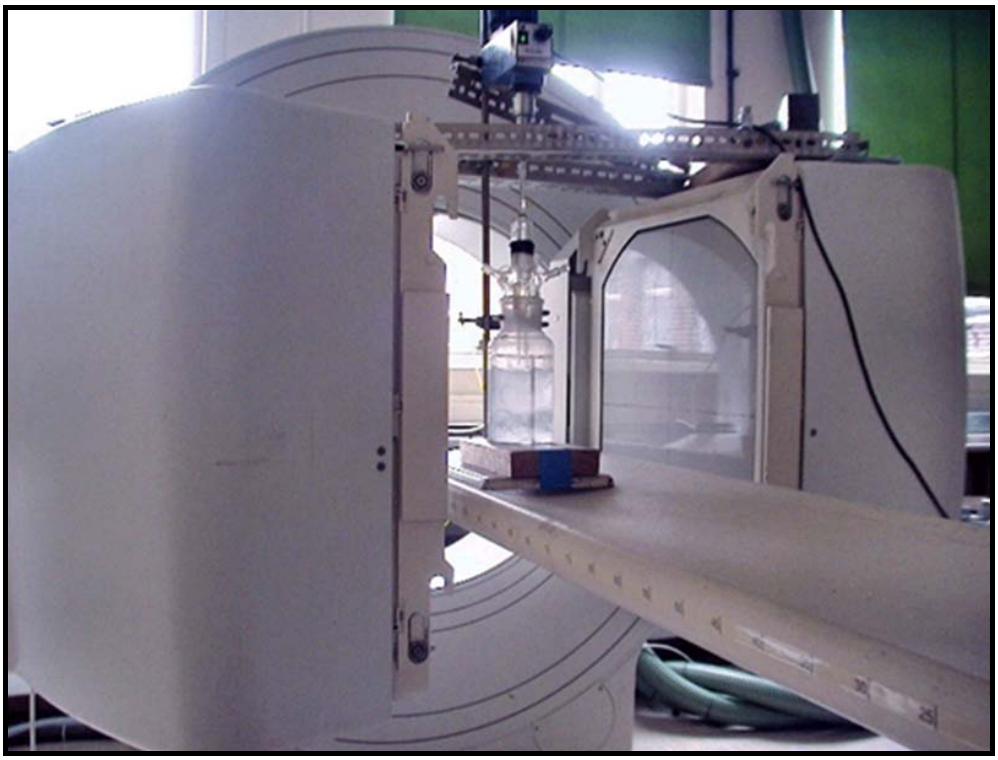

Figure 3.1. The Birmingham positron camera.

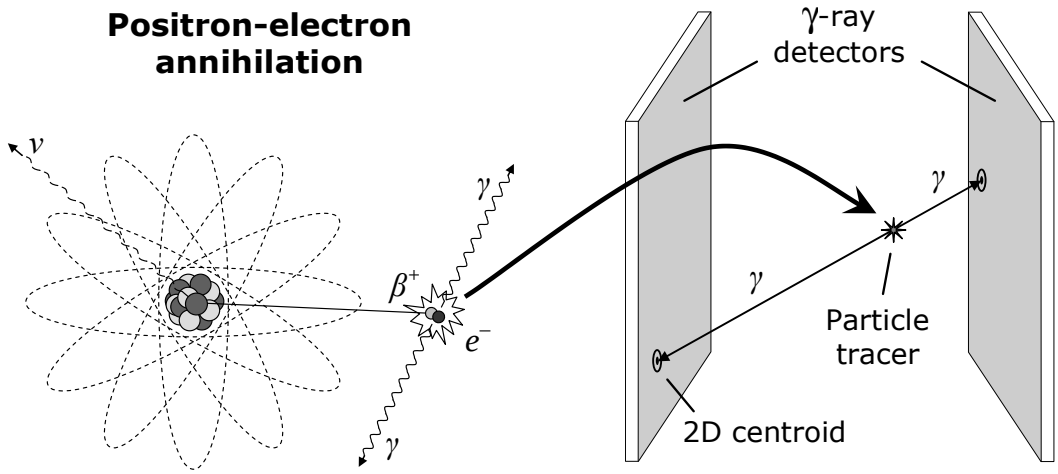

Figure 3.2. Schematic illustration of positron annihilation and gamma rays detection by the positron camera.

The major limitations of the PEPT technique are currently due to the positron-emitting particle tracer. Tracer dimensions, density, mechanical resistance and radioactivity content are probably the four major factors which determine the quality of the flow data obtainable. The ideal radioactive particle tracer has exactly the same density of the tracked fluid, negligible dimensions, high mechanical resistance, and is capable of carrying high amounts of a positron-emitting nuclide (e.g., ^{18}F).

In this work, the density of the tracer used to track the liquid phase was generally higher than the density of the liquid phase (water). Therefore, the resin tracer was usually made neutrally buoyant by adding NaCl to the water so that the density of the fluid matched that of the tracer.

The resin tracer currently used for liquid tracking has usually a diameter of 250-600 μm. This determines the flow-dynamic resolution as the tracer cannot be representative of the liquid system when flow structures smaller than its own size are taken into considerations. Although, the use of interest areas which are generally ~ 1000 times larger than the dimensions of the particle tracer, effectively mitigates the negative effect of large particle tracers, it reduces the spatial resolution of the flow velocity maps. As discussed in the following sections, the verification of the ergodicity condition and mass continuity, and the comparison between results obtained by PEPT and other Eulerian well-established techniques are tools that can be used to assess the quality of PEPT data.

When the multi-phase system studied is characterised by a very high solid concentration, the mechanical resistance of the particle tracer becomes a major challenge. The disintegration or partitioning of the particle tracer usually causes the immediate failure of the experiment. In this work, where turbulent solid-liquid systems were investigated, the current mechanical performance of the particle tracer allowed experiments to be performed with a solid concentration up to 40 wt%.

The current radioactivity content of a typical PEPT tracer used in this work to track the liquid phase was generally high enough to allow collection of experimental data for more than six consecutive hours. Higher radioactivity content would certainly be beneficial for the experimental investigations; it could allow shorter experiments to be performed while maintaining a high resolution, enable higher resolution using the same PEPT runtime, or enable longer experiments which are useful to investigate complex systems in detail or time-dependent long-term behaviour.

3-2.2 Mixing systems examined

A broad set of PEPT experiments were conducted on single-phase and solid-liquid systems in fully-baffled flat-base cylindrical vessels having a diameter T varying in the range 150-290 mm (**Figure 3.3**). Newtonian and non-Newtonian single-phase fluids were employed to study turbulent and laminar mixing including cavern formation, using neutrally-buoyant particle tracers. Nearly-monomodal and nearly-spherical glass beads with a diameter d in the range 1 to 3.3 mm were used to make monodisperse, binary and polydisperse slurries for analysis by PEPT. The suspending medium was usually an aqueous NaCl solution. The mean solid mass concentration, X, was varied in the range 0 to 40 wt%. The level of the single-phase fluid or solid-liquid suspension in the tank was kept at $H = T$ for all the experiments. Solid-liquid mixing experiments were conducted at the minimum rotational speed for particle suspension, N_{js}, determined experimentally according to the well-known Zwietering criterion, i.e. no particle should remain stationary on the base of the vessel for longer than 1-2 s (Zwietering, 1958). The agitator used was a 6-blade 45° pitched blade turbine (PBT) pumping downwards (PBTD) or upwards (PBTU). Its diameter, D, was varied in the range 0.33-0.55 T and its off-bottom clearance was set at 0.25 T or 0.33 T.

In a multi-phase system the flow behaviour of the different phases is expected to be different; therefore, each phase component is tracked separately. In a monodisperse suspension, where the number of components is equal to the number of phases (solid and liquid), two sets of

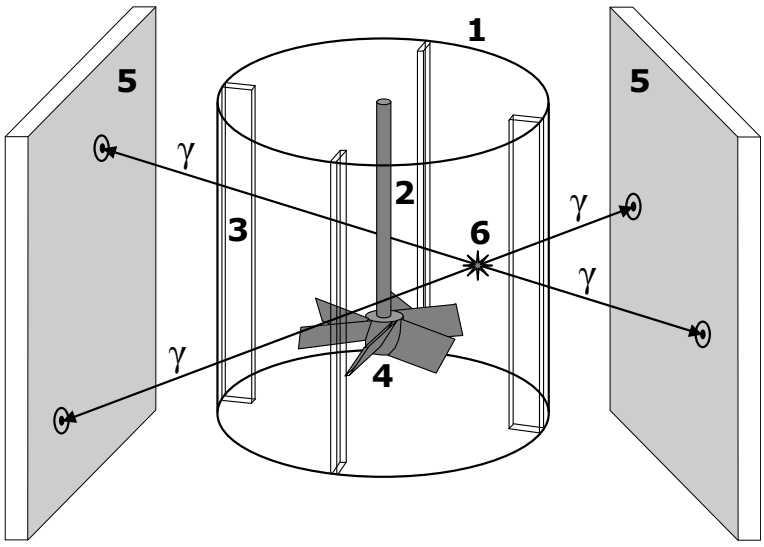

Figure 3.3. Experimental PEPT set-up: 1 tank; 2 shaft; 3 baffle; 4 impeller; 5 γ-ray detectors; 6 PEPT tracer.

trajectory data are required to describe the suspension. Similarly, for a binary suspension with two particle size fractions, three separate sets of trajectory data describing the three components are required, i.e. one liquid phase component and two solid phase components. More generally, a polydisperse suspension consisting of n_s different size fractions of particles requires $n_s + 1$ separate trackings.

3-2.3 Selective labelling in multi-component systems

As explained above, in the case of a multi-component system, the full three-dimensional trajectory of each component must be resolved separately. Currently, PEPT can most accurately track only one particle at a time. For this reason, PEPT multi-component investigations consisted of multiple successive and distinct experiments: two for a monodisperse suspension, three for a binary suspension and $n_s + 1$ for a polydisperse suspension.

Resin tracers radioactively labelled with ^{18}F by Ion Exchange are usually employed to track the liquid phase. They can be as small as 250 μm and have a density slightly higher than water. The resin particle tracer is made neutrally buoyant by using an aqueous NaCl solution whose salt concentration is adjusted so that its density matches that of the tracer. Each solid component is tracked using a representative glass bead of the examined particle size fraction which is directly irradiated by means of a cyclotron and, therefore, enriched in ^{18}F via the nuclear reaction in Eq. (3.1).

3-3 Lagrangian-Eulerian analysis

Two kinds of data analysis are presented in this chapter: first, a Lagrangian-Eulerian analysis used to extract Eulerian information from the purely Lagrangian information contained in the tracer trajectory; and second, a Lagrangian-statistical analysis exploiting concepts such as circulation time, trajectory length distribution and Poincaré maps obtainable only when Lagrangian data are available. The structure of the computational code developed for extracting Eulerian information consists of a set of subroutines containing different algorithms created to progressively analyse the initial Lagrangian data and store important intermediate outputs. Due to the varied nature of the mixing systems examined, the code had

to be flexible enabling key-parameters to be set and specific subroutines to be activated or deactivated as required.

3-3.1 Direct trajectory visualisation

The conversion of the input file in four numerical arrays $[t_k]$, $[x_k]$, $[y_k]$, $[z_k]$, where k is the location counter, is the first step in the data analysis. Plotting values of the spatial coordinates x, y and z, in 3D space generates images similar to those in **Figure 3.4** which show the extent of the regions visited by the tracer. In **Figure 3.4a**, where the neutrally-buoyant particle is tracking a single-phase in turbulent flow ($Re_{imp} \sim 40000$), the entire volume is covered very rapidly. The complexity of the trajectory also gives a visual impression of the quality of fluid mixing inside the vessel. In the mixing of viscoplastic fluids which exhibit an apparent yield stress the impeller creates a cavern within which fluid is in flow, but in the bulk where the shear stresses are below the yield stress the fluid is stagnant (Adams and Barigou, 2007). In this case, the particle tracer visits only a portion of the vessel volume delineating the boundaries of the cavern formed (**Figure 3.4b**), which allows an accurate estimation of the

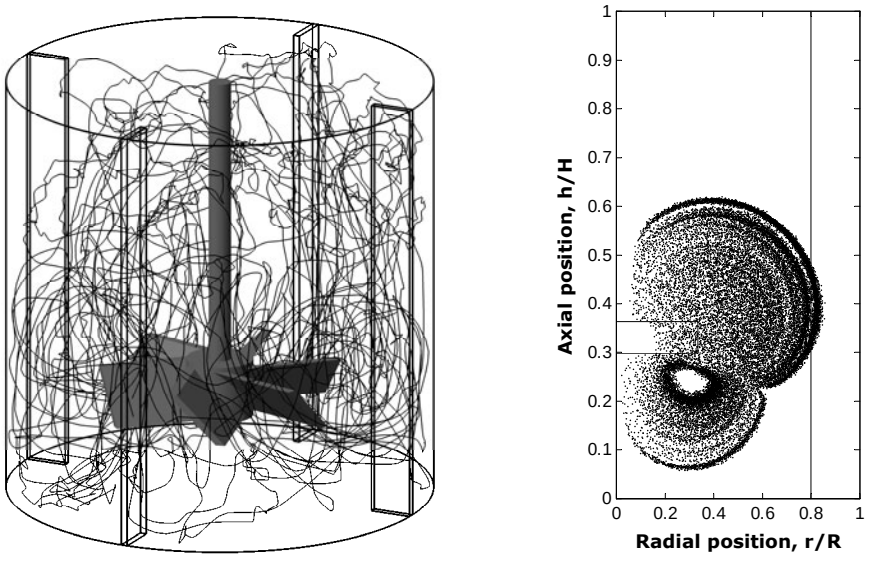

Figure 3.4. Lagrangian tracking: (a) fluid trajectory in a turbulent system; (b) cavern visualisation in laminar flow of a viscoplastic fluid with an apparent yield stress – figure shows the locus of tracer locations within cavern.

cavern volume and gives a detailed description of the flow field within, information which has hitherto been impossible to obtain in opaque fluids.

3-3.2 PEPT Location filter

A basic step in the analysis of PEPT data is the elimination of the occasionally corrupt locations not discarded by the initial PEPT reconstruction algorithm, which may be caused by spurious radioactivity from the surroundings, scattering phenomena or a too short time interval between two consecutive positron emissions. To efficiently remove such corrupt locations, a filter function needs to operate locally taking into account the probability of tracer detection and local flow velocity.

The three-dimensional flow field in a mixing vessel is very complex and is often characterised by high local velocity gradients. Assuming a constant frequency of acquisition of the 3D locations of the positron-emitting particle tracer, an acceleration of the tracer creates a dilation of the curvilinear distance separating two consecutively detected locations along the trajectory; therefore, in the presence of a high velocity the density of tracer detections along the trajectory would be reduced. However, the frequency of data acquisition is not constant as the probability of its detection varies with its 3D location. **Figure 3.5a** is a two-dimensional illustration of how the location of the tracer can affect the probability of detection. Knowledge of the density of tracer detections along the trajectory can be employed to realise a filter function which efficiently identifies and discards occasionally corrupt locations.

The probability of tracer detection can be assumed – to a first approximation – to be proportional to the geometric efficiency of detection which can be calculated through geometric considerations. Such an approximation is reasonable since other factors (or their variation with tracer position) affecting the detection ability and accuracy of PEPT are of a secondary order compared to the geometric efficiency (or its variation with tracer position), including the possibility that two decay events occur in the same time window, the range of the positron in the matter before annihilation with an electron, the fact that the γ-rays are not exactly 180^o apart (±0.5^o), photon absorption/scattering phenomena and the angle at which the γ-rays pass through the crystal inside the detector.

The infinitesimal probability that one γ-ray will travel inside the solid angle, $d\Omega$, subtended at the source by an infinitesimal area of a detector can be expressed by normalising this angle by

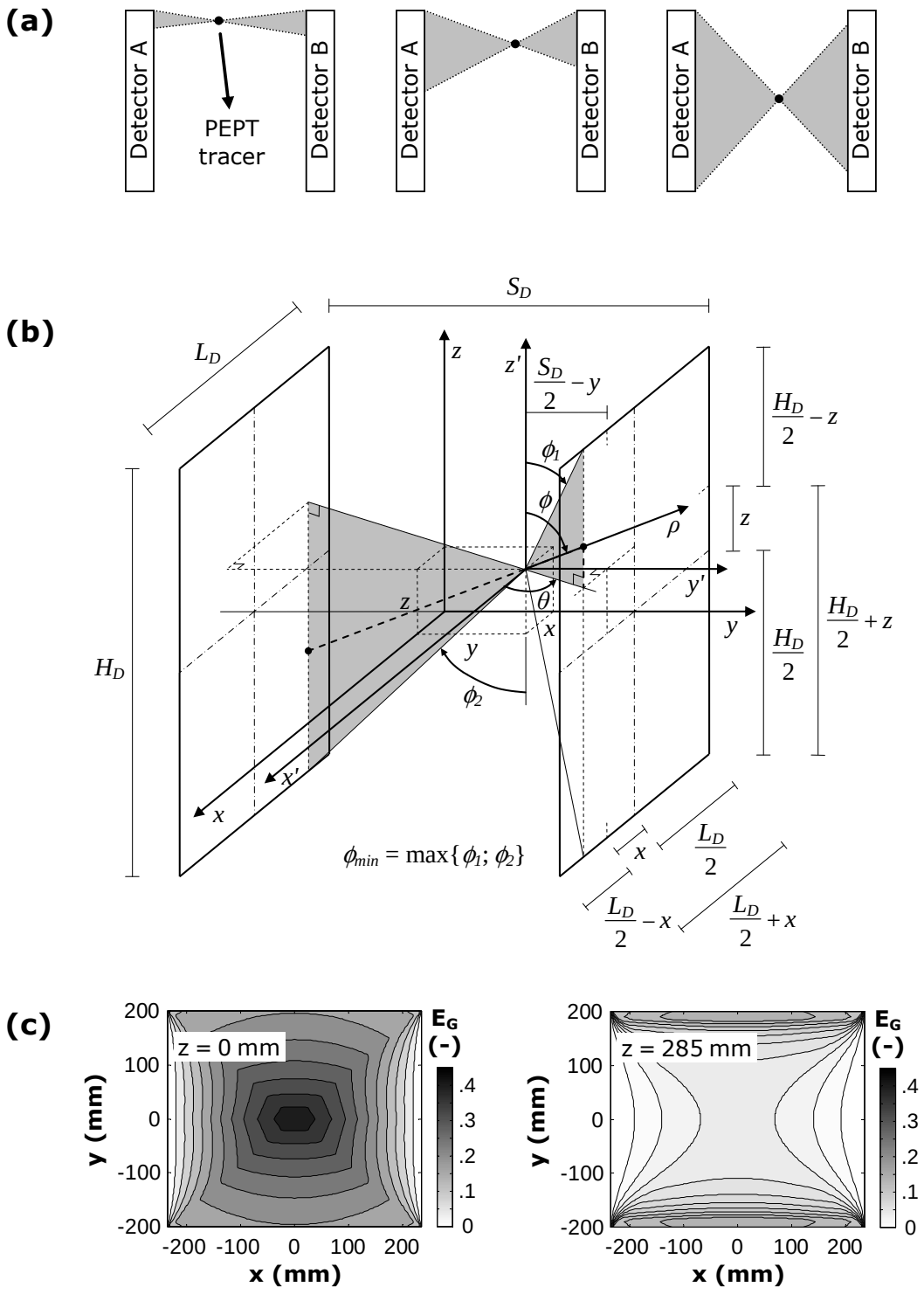

Figure 3.5. PEPT geometric efficiency of detection: (a) two-dimensional representation of its dependency on the angle subtended at the source by both detectors; (b) illustration of the derivation of the E_G function; (c) horizontal *xy* maps of geometric efficiency at two different vertical coordinates for S_D = 400 mm.

the total solid angle (4π). Considering that two γ-rays are emitted, the infinitesimal probability, dE_G, that one of the two photons will travel inside $d\Omega$ can then be written as

$$dE_G = 2\frac{d\Omega}{4\pi} \tag{3.4}$$

Expressing the solid angle $d\Omega$ in spherical coordinates with the origin being located at the instantaneous position of the PEPT tracer (x, y, z) as shown in **Figure 3.5b**, Eq. (3.4) becomes

$$dE_G = \frac{\sin\phi d\theta d\phi}{2\pi} \tag{3.5}$$

The geometric efficiency, E_G, can thus be imagined as the sum of such infinitesimal contributions whose values of θ and ϕ allow the direction of the γ-rays to intersect both detectors; therefore, double integration in θ and ϕ allows the geometric efficiency to be analytically determined. By applying geometric considerations, the zenithal integration limits can be obtained from **Figure 3.5b** as functions of the azimuth θ; thus

$$\phi_{min} = \arctan\left(\max\left\{\frac{S_D - 2y}{H_D - 2z}; \frac{S_D + 2y}{H_D + 2z}\right\}\csc\theta\right) \tag{3.6}$$

and

$$\phi_{max} = \pi - \arctan\left(\max\left\{\frac{S_D - 2y}{H_D + 2z}; \frac{S_D + 2y}{H_D - 2z}\right\}\csc\theta\right) \tag{3.7}$$

The maximum function which is present in both Eqs. (3.6) and (3.7) derives from the condition that both the γ-rays must intersect a detector. In a similar manner, the azimuthal integration limits can be determined using **Figure 3.5b**, thus

$$\theta_{min} = \arctan\left(\max\left\{\frac{S_D - 2y}{L_D - 2x}; \frac{S_D + 2y}{L_D + 2x}\right\}\right) \tag{3.8}$$

and

$$\theta_{max} = \pi - \arctan\left(\max\left\{\frac{S_D - 2y}{L_D + 2x}; \frac{S_D + 2y}{L_D - 2x}\right\}\right) \tag{3.9}$$

A first complete expression of the geometric efficiency, E_G, is established by evaluating the first integral in ϕ and then using basic trigonometric identities, namely

$$E_G = \frac{1}{2\pi}\sum_{q=1}^{2}\int_{\theta_{min}}^{\theta_{max}}\left(\max\left\{\frac{S_D-2y}{H_D+(-1)^q 2z};\frac{S_D+2y}{H_D-(-1)^q 2z}\right\}^2 \csc^2\theta+1\right)^{-\frac{1}{2}} d\theta \tag{3.10}$$

The last integral can also be evaluated analytically leading, however, to a very long expression which, on the other hand, does not exhibit any trigonometric or integral functions. The obtained geometric efficiency $E_G = E_G(x, y, z, L_D, H_D, S_D)$ becomes a 3D-function (only position dependent), for given dimensions L_D and H_D of the rectangular active area of the γ-ray detectors, and a fixed separation S_D between them. Note that whilst L_D and H_D are fixed by the size of the detectors' active area (470×590 mm^2 for the Birmingham Positron Camera), S_D can be varied up to a maximum of 800 mm to suit the size of the flow system under investigation.

Two-dimensional maps of the geometric efficiency are depicted in **Figure 3.5c** at selected heights within the detection space, for a fixed detector separation S_D = 400 mm. E_G is maximum at the origin of coordinates, i.e. at the centre of the detection space, and is zero at the edges. Consequently, the probability and, hence, the number of successfully detected positions of a particle tracer, tends to be highest in the centre between the detectors.

As pointed out above, in high velocity zones the density of tracer detections along the trajectory decreases whilst in regions where the probability of tracer detection is high such a density increases. In a stirred vessel the central region should be affected most by high local velocities, but at the same time the probability of tracer detection there is the highest. On the other hand, near the boundaries of the vessel the velocities are smaller but the probability of detection is lower. Consequently, these two effects tend to approximately cancel each other for an accurately centred tank with dimensions not too close to those of the detectors, and for a separation such that $H_D > S_D > L_D$ so that the detection space is approximately cubical.

Nonetheless, for a better accuracy the filter function operates locally, as pointed out above, and the threshold used to discard occasionally corrupted locations is calculated as a function of the local values of geometric efficiency and the expected magnitude of the local flow velocity.

3-3.3 Location of the vessel axis

An accurate and precise location of the vertical vessel axis (x_o, y_o) and base (z_o) is crucial to correctly define a new system of cylindrical coordinates (ϑ, r, h) which is required for the Eulerian description of a cylindrical mixing vessel. Manual determination of its position without specialised equipment can lead to significant errors. Measuring by PEPT the coordinates of a static tracer placed in specific key-positions, however, enables the three coordinates x_o, y_o and z_o to be accurately located.

This calibration can be avoided when the particle tracer visits every region of the vessel and the vessel boundaries are clearly traced, e.g. in a turbulent system with a sufficiently long runtime. A wrong practice would be to assume that the average position of the particle tracer, obtained as the mean value of the arrays [x_k], [y_k], [z_k], corresponds to the centre of the tank. There is no certainty that the tracer is detected an equal number of times in every region; it could be detected more frequently in some areas than others for various reasons including temporary tracer immobility, for example in a stagnant region or behind a baffle, and non-uniformity of the geometric efficiency for vessels not perfectly placed in the centre of the active area of detection.

This problem is circumvented when each location is projected onto a horizontal plane (xy) and such a plane is 'pixelised'; numerous locations within the same pixel having similar horizontal coordinates x, y are represented by a single pixel regardless of their number and vertical coordinate z (**Figure 3.6a**). Such a pixelised horizontal projection contains 'black' pixels which are positions occupied by the tracer, and 'white' pixels which are positions never visited by the tracer. Assuming a centre and starting from a circumference with radius r_c slightly smaller than $T/2$, the fraction of black pixels q_b intersected by such a circumference is computed. Thus, the fraction q_b is recalculated increasing gradually the radius of the circumference to a value slightly higher than $T/2$. The true centre of the pixel map, corresponding to the vessel axis position, is characterised by the sharpest drop of q_b from ~ 1 to ~ 0 when increasing r_c. Based on the same principles, the position of the vessel base z_o can be obtained using a simpler one-dimensional projection on a vertical straight line.

The accuracy in the above procedure is increased by reducing the pixel size which is usually a fraction of a millimetre; however, the pixel dimensions shown in **Figure 3.6a** have been exaggerated to illustrate the process. In **Figures 3.6b** and **3.6c** the performance of the

subroutine is compared to the result obtained using the average values of the arrays $[x_k]$ and $[y_k]$ to identify the vessel axis location (x_o, y_o). The tracer locations outside the vessel boundary indicate that this last procedure may lead to a wrongly positioned vessel axis. For the particular set of data shown in **Figure 3.6**, the large error obtained using the average position of the particle tracer is engendered by a non-uniform density of locations which is higher within the region delineated by an ellipse in **Figure 3.6c** and, consequently, causes the vessel axis location (x_o, y_o) to be shifted towards this region.

3-3.4 Dummy locations

The code employs a 3D user-defined grid consisting of a large number of equal volume cells, n_c, to obtain an Eulerian description of the flow field inside the vessel based on values of velocity and other quantities determined in each grid cell. Such a cylindrical grid is made up of three kinds of hyperplanes: radial-axial planes (ϑ = const), cylindrical hyperplanes (r = const) and horizontal planes (h = const).

For an accurate data analysis, it is also important to deal with the occasional short interruptions (> 50 ms) in the trajectory caused by very occasional incidents of low frequency of data acquisition occurring, for example, when a particle tracer which, after hours of

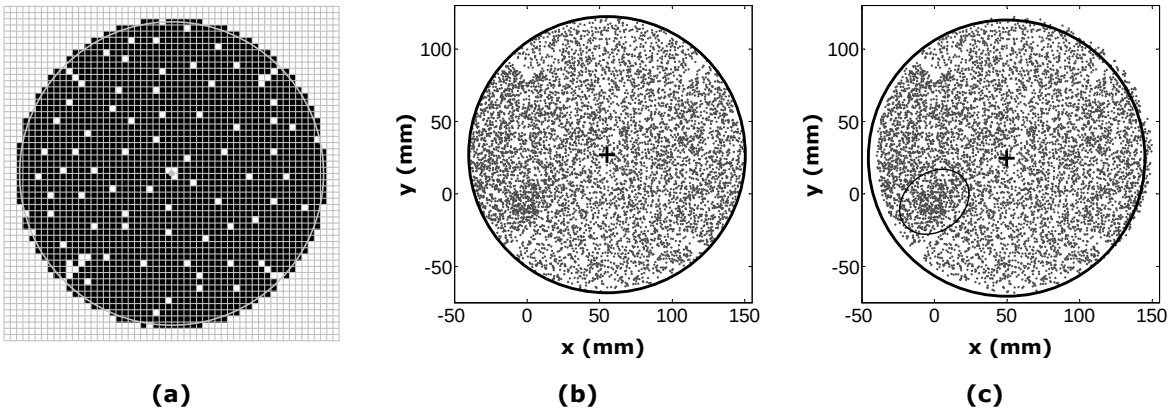

Figure 3.6. Location of the vessel axis: (a) pixelised projection of the tracer locations onto a horizontal plane (note the pixel size has been exaggerated for clarity); (b) axis location by data analysis routine; (c) axis location using the average values of the coordinates x and y (the ellipse delineates a region of high location density causing off-centring of the vessel).

experiments, has lost most of its radioactivity travels across a region characterised by a low geometric efficiency (**Figure 3.5c)** at very high speed. The effect of such short trajectory interruptions is usually negligible but should not be ignored when the tracer is moving at a particularly high velocity. Where there are interruptions in the tracking of the tracer, it is not usually possible to be certain about where the tracer has been during this interruption time, but it is possible as a first approximation to define a linear segment of trajectory between the last and the next detected location assuming that the tracer moves at a constant velocity between the two points. As shown in **Figure 3.7**, the equation of a hyperplane and the two equations of such a 3D linear segment define a system of three equations which in the case of a radial-axial vertical plane (say at $\vartheta = \vartheta^*$) can be expressed by

$$\begin{cases} (y - y_o) = (x - x_o)\tan\vartheta^* \\ y = a_1 x + b_1 \\ z = a_2 x + b_2 \end{cases} \tag{3.11}$$

where Cartesian coordinates are used and the coefficients a_1, a_2, b_1 and b_2 are calculated using the coordinates of the last and the next detected location. In the case of a cylindrical

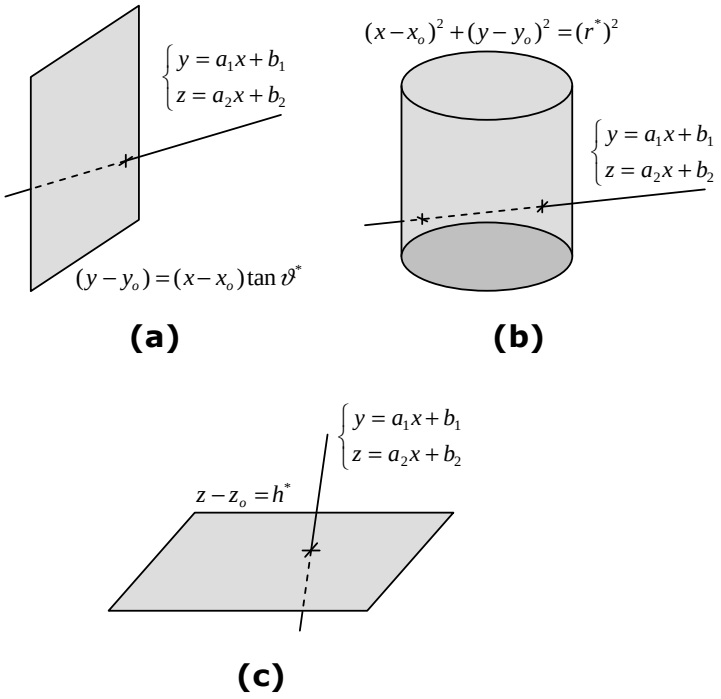

Figure 3.7. Intersection of a 3D straight line with hyperplanes at (a) $\vartheta = \vartheta^*$; (b) $r = r^*$; (c) $h = h^*$.

hyperplane (say at $r = r^*$) or a horizontal plane (say at $h = h^*$) the above system of equations becomes, respectively

$$\begin{cases} (x - x_o)^2 + (y - y_o)^2 = (r^*)^2 \\ y = a_1 x + b_1 \\ z = a_2 x + b_2 \end{cases} \tag{3.12}$$

and

$$\begin{cases} z - z_o = h^* \\ y = a_1 x + b_1 \\ z = a_2 x + b_2 \end{cases} \tag{3.13}$$

Thus, each radial-axial, cylindrical or horizontal hyperplane comprised between these two tracer locations defines a different system of equations, the solutions of which provide the coordinates of the intersections of the 3D linear segment with the whole grid. If the number of such intersections is higher than 1, a dummy location is inserted in the middle between two consecutive intersections with the defined grid, i.e. inside each cell intersected by the fictitious segment of trajectory, as shown in **Figure 3.8**. Note that although the real grid used is based on cylindrical coordinates, for purposes of clarity of the illustration a grid composed of cubical cells is shown.

The entire process can be iterated treating every interval between two consecutive locations as an interruption, so that the particle tracer is characterised by transitions only between adjacent cells. The ratio of the total number of inserted dummy locations to the total number of original detected locations is a useful indication of the degree of fineness of the grid: a high number of dummy locations compared to the original number of detected locations would suggest that the grid is too fine. This operation improves the measurement accuracy of the time the tracer spends in each cell considerably, but the effect on the calculated velocity field is not expected to be significant unless the rate at which tracking is interrupted is particularly high or, equivalently, the grid is too fine.

3-3.5 Lagrangian velocity

A single Lagrangian data point consists of a temporal coordinate *t* and three spatial Cartesian

coordinates x, y, z which are subsequently converted to cylindrical coordinates ϑ, r and h with origin $\mathbf{O} = (x_o, y_o, z_o)$. Using this coordinate system with versors $\hat{\boldsymbol{\theta}}$, $\hat{\mathbf{r}}$ and $\hat{\mathbf{h}}$, the Lagrangian velocity is

$$\mathbf{v} = v_\vartheta \hat{\boldsymbol{\theta}} + v_r \hat{\mathbf{r}} + v_h \hat{\mathbf{h}} = r\frac{d\vartheta}{dt}\hat{\boldsymbol{\theta}} + \frac{dr}{dt}\hat{\mathbf{r}} + \frac{dh}{dt}\hat{\mathbf{h}} \cong r\alpha\hat{\boldsymbol{\theta}} + \beta\hat{\mathbf{r}} + \gamma\hat{\mathbf{h}} \tag{3.14}$$

where α, β, γ are the numerically calculated time derivatives of the three cylindrical tracer coordinates which are contained in the arrays $[\vartheta_k]$, $[r_k]$ and $[h_k]$. The value of α, for instance, could be obtained using differences of ϑ and of t between two consecutive locations, i.e. the ratio between $\vartheta_{k+1} - \vartheta_k$ and $t_{k+1} - t_k$. Although almost negligible, a certain degree of spatial uncertainty characterises each tracer location which may create small fictitious fluctuations in the velocity vector. By using the least squares method, a number of consecutive locations ($n_{LSM} > 2$) could be used to minimise this effect. The values of α, β and γ are then determined as the slopes of the best straight line representing the n_{LSM} points in the Cartesian

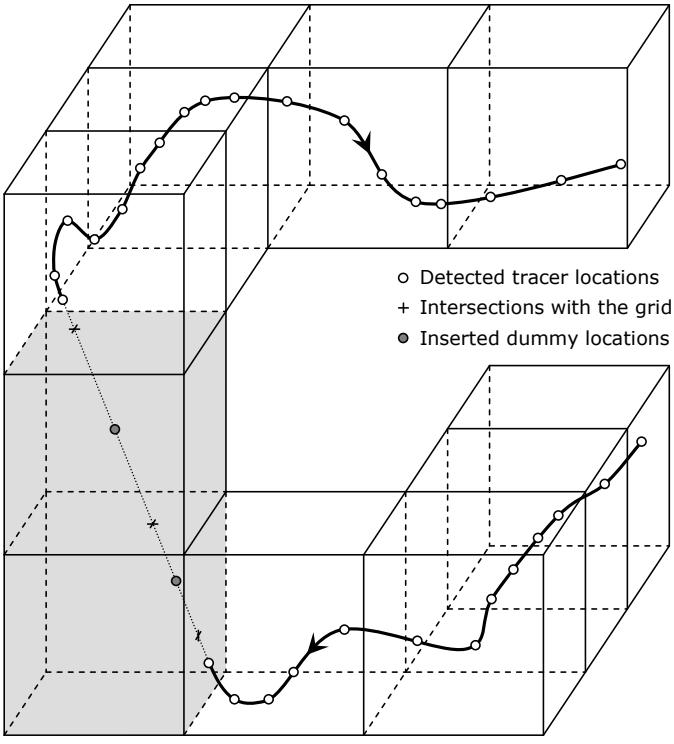

Figure 3.8. Illustration of the computational insertion of dummy locations: note that the real grid used is based on cylindrical coordinates, but cubical cells are shown here for clarity purposes.

planes $t\vartheta$, tr and th, respectively. Thus, the Lagrangian velocity vector (v_ϑ, v_r, v_h) is obtained numerically which is then associated with a new tracer position whose four time-space coordinates are recalculated by averaging the coordinates of the n_{LSM} initial locations. Where overlapping is allowed, the value of n_{LSM} does not significantly affect the length of the newly rewritten arrays [t_k], [ϑ_k], [r_k], [h_k] which are now associated with the arrays [$(v_\vartheta)_k$], [$(v_r)_k$] and [$(v_h)_k$] containing the three cylindrical components of the Lagrangian velocity.

It should be noted that selecting the value of the parameter n_{LSM} is a matter of compromise, as n_{LSM} must be increased for an inaccurate tracer location and decreased for a fast tracer motion to avoid having an excessively smoothed trajectory and, hence, underestimated velocities. The entire sets of PEPT data presented here were analysed using n_{LSM} = 3-5.

3-3.6 Local Eulerian quantities

On the basis of the previously defined 3D cylindrical grid with n_c equal volume cells, the instantaneous 3D position assumed by the particle tracer (ϑ_k, r_k, h_k) can be converted into an integer index, i_k, designating the specific grid cell occupied by the tracer at time t_k. The spatial distribution of the number of detected tracer locations in a cell is then determined simply by counting the number of times each cell index appears in the new array [i_k]. If a sequence of equal indices i^* in [i_k] is compacted into one single element equal to i^* (e.g., the sequence '7 7 7 7 7' is reduced to a single '7') a shorter array [I_k] is created which, by means of the above counting process, leads to the distribution of the number of tracer visits. The two spatial distributions of the number of tracer visits, n_V, and detected locations, n_L, are conceptually different, therefore, the conversion of the Lagrangian velocity components into Eulerian velocities needs to be made taking into account such a distinction.

The time interval between the instants at which the particle tracer enters and leaves a cell may be different each time the tracer visits the same cell. Primarily for this reason, the number of detected locations is not constant at each visit during which a slow tracer is detected a higher number of times than a tracer moving at high speed. Consequently, a simple arithmetic mean of the Lagrangian velocities related to all the tracer locations within the same grid cell, i.e. the arithmetic mean of all the $(v_\vartheta)_k$, $(v_r)_k$ or $(v_h)_k$ corresponding to equal indices in [i_k], would lead to an underestimated mean Eulerian velocity associated with the cell.

This estimation can be improved if, in a given cell, the Eulerian velocity is determined by first

calculating the mean Lagrangian velocities, $\bar{v}_\vartheta$, $\bar{v}_r$, $\bar{v}_h$, along the segment of trajectory intersecting with the cell at each visit, as shown in **Figure 3.9**, before averaging again by the number of visits. This procedure reduces the Lagrangian information to a single velocity vector associated with each tracer visit, regardless of the number of times the tracer is located and the duration of its sojourn in the cell. In computational terms, the arrays $[(v_\vartheta)_k]$, $[(v_r)_k]$ and $[(v_h)_k]$ are reduced to $[(\bar{v}_\vartheta)_k]$, $[(\bar{v}_r)_k]$ and $[(\bar{v}_h)_k]$ of the same length as $[I_k]$, by replacing each sequence which corresponds to equal indices in the parallel array $[i_k]$ with the arithmetic mean of the elements of the sequence itself. The mean Eulerian velocity components, u_ϑ, u_r and u_h, are finally obtained in each cell by averaging all the velocity values in $[(\bar{v}_\vartheta)_k]$, $[(\bar{v}_r)_k]$ and $[(\bar{v}_h)_k]$ corresponding to the same cell index in $[I_k]$. It is worth noting that the same averaging process, performed using the squares of such velocity values, leads to the standard deviations σ_ϑ, σ_r and σ_h of the Eulerian velocity components in each cell.

By employing the previously obtained intersections of the tracer trajectory with the grid and their time coordinate, the time spent by the tracer in a cell during each visit, so-called *residence time*, is noted in a further array $[\delta t_k]$ having also the same length of $[I_k]$. Although intrinsically Lagrangian, this information can be transformed into an Eulerian distribution of the cumulative time, Δt, that the tracer spends within a given grid cell during an experiment,

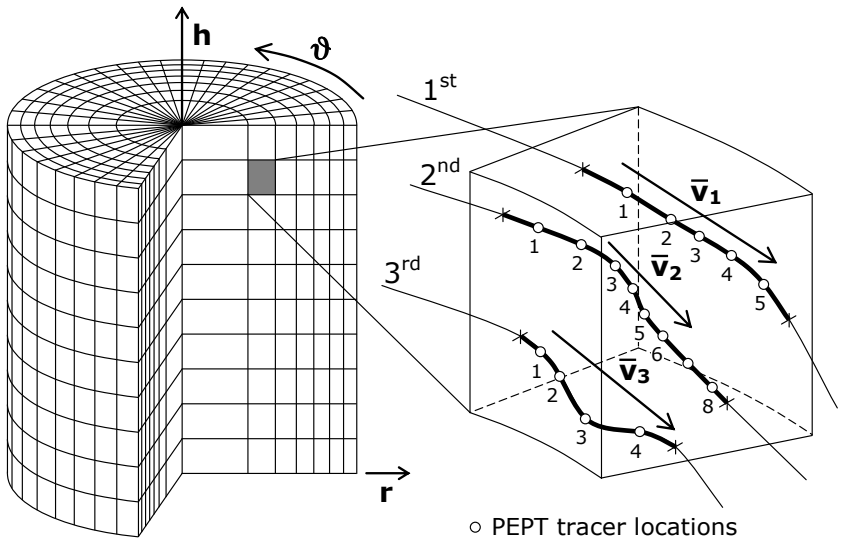

Figure 3.9. Illustration of the cylindrical grid used for the analysis of the Lagrangian data and a grid cell with multiple tracer visits.

also called cumulative residence time or cumulative sojourn time. It is determined by adding together all the time values in $[\delta t_k]$ corresponding to the same cell index in the array $[I_k]$. Furthermore, maps of the mean residence time, $\overline{\delta t}$, can be obtained by dividing the time Δt by the number of tracer visits, n_V, in each cell.

3-3.7 Occupancy

The particle-tracer occupancy distribution within the vessel offers an additional powerful tool for characterising flow behaviour within the mixing tank. Occupancy has traditionally been obtained by calculating the fraction of the total experimental time, t_∞, spent by the tracer in each cell during the experiment. Such a definition establishes a mathematical identity between occupancy and probability of presence of the particle tracer, but undesirably makes occupancy highly dependent on the density of the grid so that as the number of cells increases occupancy tends to zero. If the cells are chosen to have equal volume, however, this problem is circumvented by using the *ergodic time* defined as $t_E = t_\infty / n_c$, instead of the total experimental time t_∞. The ergodic time represents the time that the tracer would spend in any cell if the flow were single-phase and ergodic, an asymptotic status in which the flow tracer has equal probability of presence anywhere within the system. Thus, the local occupancy, O_E, can be defined as

$$O_E = \frac{\Delta t}{t_E} \tag{3.15}$$

where Δt is the time that the tracer spends inside a given cell, i.e. the previously defined cumulative residence time. Thanks to this definition the average value of the vessel occupancy is 1 independently of the chosen number of grid-cells n_c. In addition, as shown below, Eq. (3.15) makes it possible to describe the spatial distribution of each phase component within a multi-phase flow. Note that ergodicity is discussed further in Section 3-5.1.

3-3.8 Eulerian maps

The 3D cylindrical grid used is defined by three initial numerical parameters: the number of cells in the axial direction, n_h, in the radial direction, n_r, and in the azimuthal direction, n_ϑ. When n_ϑ is set to 1, each grid cell assumes the shape of a rectangular cross-section torus and,

therefore, the related Eulerian datum is obtained using those Lagrangian data that can be ascribed to the torus regardless of their azimuthal coordinate ϑ. As a result, Eulerian data are intrinsically ensemble-averaged with respect to the azimuthal position and, although representing the whole mixing volume rather than a single 2D vertical section, such data can be presented in the form of 2D radial-axial maps. Examples of such maps are depicted in **Figure 3.10** which presents a set of quantities obtained within a single-phase turbulent system (aqueous NaCl solution) in a single PEPT experiment.

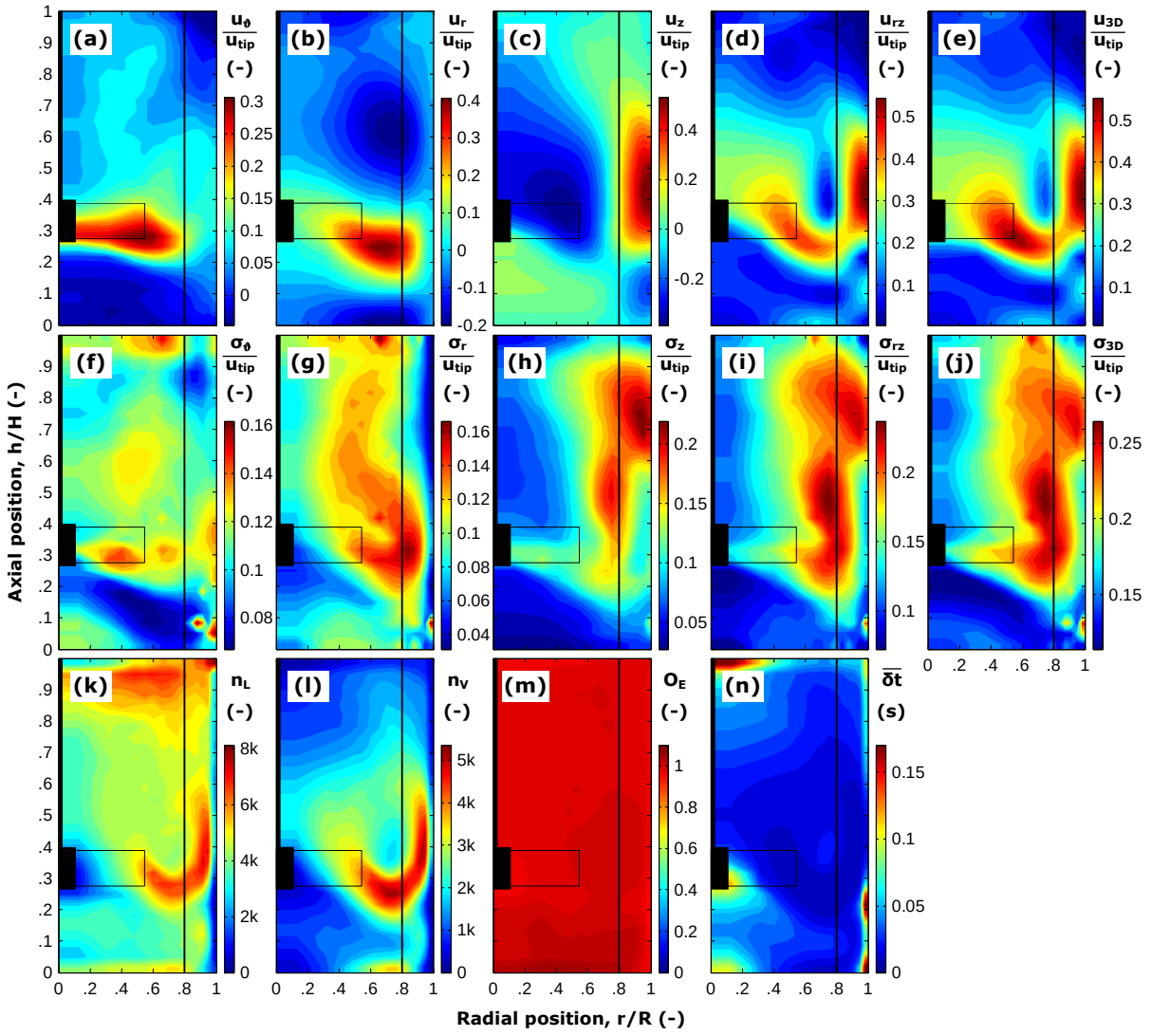

Figure 3.10. Azimuthally-averaged radial-axial maps of Eulerian quantities in a single-phase system: T = 190 mm; aqueous NaCl solution; PBTD; D = 105mm (0.33 T off-bottom clearance); N =220 rpm (Re_{imp} ~ 40000).

Whilst distributions of the three velocity components (u_ϑ, u_r, u_h) normalised by the tip speed of the turbine, u_{tip}, are illustrated in **Figures 3.10a-c**, the normalised magnitudes of the radial-axial 2D velocity vector $\mathbf{u_{rh}}$ and the total 3D velocity vector $\mathbf{u_{3D}}$ are mapped in **Figures 3.10d-e**.

In the case of a solid-liquid system, these velocity maps can be generated for each phase. Furthermore, local time-averaged particle slip velocities can be estimated by locally subtracting the velocity of the solid phase from that of the liquid. This information is of real value to processing applications involving the transfer of heat or mass, such as in chemical reactions or the sterilisation of particulate food mixtures, and cannot currently be obtained using any other technique. A crude assumption often used in practice takes the free terminal settling velocity of the particle as a representative of its mean slip velocity (Atiemo-Obeng *et al.*, 2004). Whilst the values yielded by PEPT are likely to be much more realistic, it is currently difficult to be certain about the accuracy of these estimations given that information on particle rotation and turbulent velocity fluctuations of the two phases is missing, but these features are probably only relevant in very complex turbulent flows.

Furthermore, as pointed out above, the standard deviations σ_ϑ, σ_r and σ_h of the Eulerian velocity components are also determined in each cell and their normalised values together with those of σ_{rh} and σ_{3D} are plotted in **Figures 3.10f-j**; these quantities provide information on the local velocity fluctuations. Using the arrays $[i_k]$ and $[I_k]$, the number of tracer locations n_L and tracer visits n_V are obtained in each cell providing the widely different maps in **Figures 3.10k-l** which confirm, as discussed above, that considering the number of tracer locations instead of visits may lead to a significant underestimation of the Eulerian velocities.

The Lagrangian measurements enable Δt to be computed leading to plots of occupancy, O_E, and average residence time, $\overline{\delta t}$, as shown in **Figures 3.10m-n**. As expected, in a turbulent single-phase flow the occupancy distribution is almost uniform and consequently the average residence time is practically proportional to the inverse of the number of visits.

3-3.9 Phase distribution in multi-phase flow

Considering for example a monodisperse solid-liquid system, the infinitesimal probability, $p(\mathbf{P})dV$, that a specific small solid particle is inside an infinitesimal volume element dV is a function of the particle position $\mathbf{P} = (x, y, z)$ and can be expressed from two different points of

view. From the Lagrangian point of view, it is the ratio of the infinitesimal time *dt* that the tracer spends inside *dV*, to the total time of detection t_∞; in Eulerian terms, however, it is the ratio of the number of solid particles *dn*, contained in *dV*, to the total number of such particles in the vessel *n*. Consequently, it follows that

$$\left\{ p(\mathbf{P})dV = \frac{dt}{t_\infty} \quad \text{and} \quad p(\mathbf{P})dV = \frac{dn}{n} \right\} \Rightarrow \frac{dt}{t_\infty} = \frac{dn}{n} \tag{3.16}$$

Introducing the volume of a single particle V_P, the infinitesimal solid volume dV_S in *dV*, the total solid volume present in the tank V_S, the local solid volume concentration *c*, the mean solid volume concentration in the vessel *C*, and the total volume of the multi-phase suspension V_T, yields

$$\frac{dn}{n} = \frac{V_P dn}{V_P n} = \frac{dV_S}{V_S} = \frac{cdV}{CV_T} \tag{3.17}$$

Combining Eqs. (3.16) and (3.17) leads to a clear correlation between the time that the tracer spends inside *dV* and the local solid volume concentration, that is

$$\frac{dt}{t_\infty} = \frac{cdV}{CV_T} \tag{3.18}$$

If the cell volume, ΔV, in the grid is uniform, the total number of grid cells is then $n_c = V_T / \Delta V$, and rewriting the above equation in discrete terms gives

$$\frac{\Delta t}{t_\infty} = \frac{c\Delta V}{CV_T} \Rightarrow \frac{\Delta t}{t_E} = \frac{c}{C} \tag{3.19}$$

Defining, according to Eq. (3.15), the occupancy O_E as the ratio of time that the tracer spends inside a cell to the ergodic time, Eq. (3.19) then becomes

$$O_E = \frac{c}{C} \tag{3.20}$$

Note that whilst this relationship has been derived for the discrete phase in a monodisperse system, it is equally valid for the fluid component as well as for each component in a suspension containing multiple liquid or solid traceable components. The immediate

important consequence of Eq. (3.20) is that, in addition to phase velocity, it is now possible to fully map by Lagrangian tracking the local concentration of each flow component in an opaque multi-phase system. As shown in **Figure 3.10m**, the occupancy map in a turbulent single-phase system is almost uniform and $O_E \sim 1$ which is in agreement with Eq. (3.20) since in a single-phase system the phase concentration is 100% everywhere. In a single-phase turbulent system the approximation $O_E = 1$, becomes gradually more accurate as the experimental runtime t_∞ is lengthened, strictly tending to infinity (here t_∞ was mostly 30-45 min). Consequently, the uniformity of the occupancy map in a single-phase turbulent system could be used as an index to determine if a long enough runtime t_∞ has been selected.

Considering, for example, a binary solid-liquid suspension where the two solid components are present at the same mean concentration, the local occupancy can be obtained for each of the solid components and the liquid; consequently, the volume concentration of each component can be mapped. In **Figure 3.11**, the distributions of the three components are

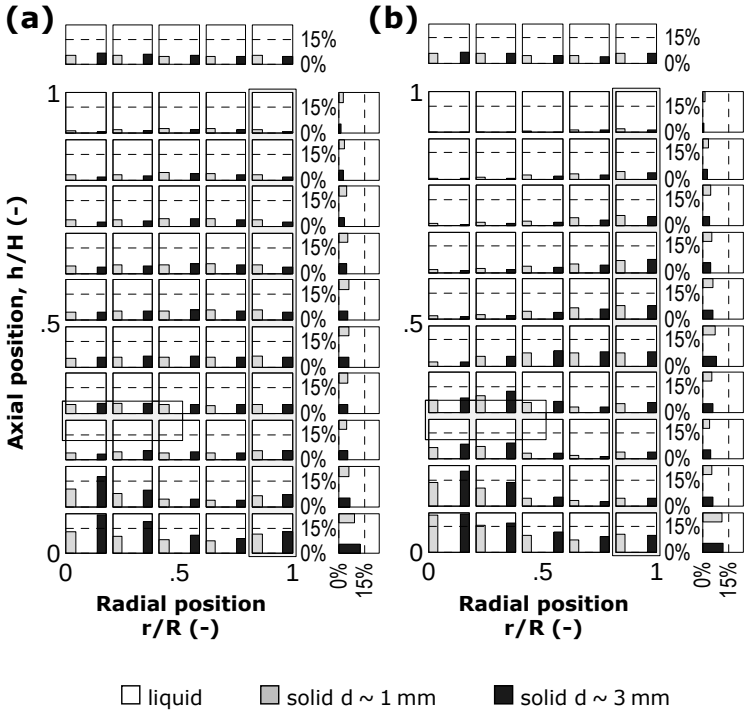

Figure 3.11. Azimuthally-averaged volume concentration maps of a binary suspension in aqueous NaCl solution: X = 20 wt%; T = 288 mm; D = 144 mm (0.25 T off-bottom clearance); $N = N_{js}$ rpm, $\mathrm{Re}_{imp} > 100000$; (a) PBTD; (b) PBTU.

effectively compared using newly developed maps, where the radial-axial plane is divided into square boxes containing information for every solid and liquid component. Each box contains two shaded bars and the fraction of the box area occupied by each bar is equal to the local volume concentration of the corresponding solid component, so that the remaining white area is equal to the local liquid volume concentration. Furthermore, by drawing bars of equal base, their height is also proportional to the local solid volume concentration and, thus, the radial profile of volume solid concentration for each solid component is represented at each horizontal level.

Whilst to the right of each map the vertical profile of the average volume concentration of each horizontal plane is shown, the radial profile of the vertically-averaged volume concentration is shown above the map. In the specific case of **Figure 3.11**, the results show how the pumping direction of the PBT (upwards or downwards) produces significantly different solid distributions in the same suspension which contains 20 wt% of solids consisting of particles of diameters ~ 1 mm and ~ 3 mm. The mixing of these binary systems is studied in more details in Chapter VIII.

3-4 Lagrangian statistical analysis

Lagrangian tracking of the long-term trajectory of a fluid follower provides data which can be exploited to visualise flow structures and obtain statistical information on the mixing performance. The popular concept of residence time distribution (RTD) in a continuous flow system was extended by Villermaux (1996) who introduced the concept of trajectory length distribution (TLD) based on the distance covered by fluid elements or tracer particles carried by the flow from the inlet to the outlet. By using Lagrangian data it is also possible to apply these concepts to a batch system such as a stirred vessel.

3-4.1 Lagrangian frequency distributions

The concept of residence time in a continuous system can be extended to a batch system by considering the time interval related to the multiple trajectories followed by a Lagrangian tracer from the point at which it leaves a given reference plane or volume to the point where it returns back to it. If the selected plane is a horizontal plane close to the impeller discharge,

the concept of residence time is replaced by the circulation time t_c which can be computed by solving systems of equations analogous to the system in Eq. (3.13) with an additional equation including the temporal coordinate. The values of t_c obtained tend to distribute according to the statistical log-normal distribution, as shown in **Figure 3.12a** for a single-phase turbulent system. Such a probability density distribution is called circulation time distribution (CTD).

The trajectory length during each recirculation can also be measured obtaining the path length ℓ_c whose distribution, the trajectory length distribution (TLD), is illustrated in **Figure 3.12b**. Similar to the circulation time distribution, the TLD is also very well represented by a log-

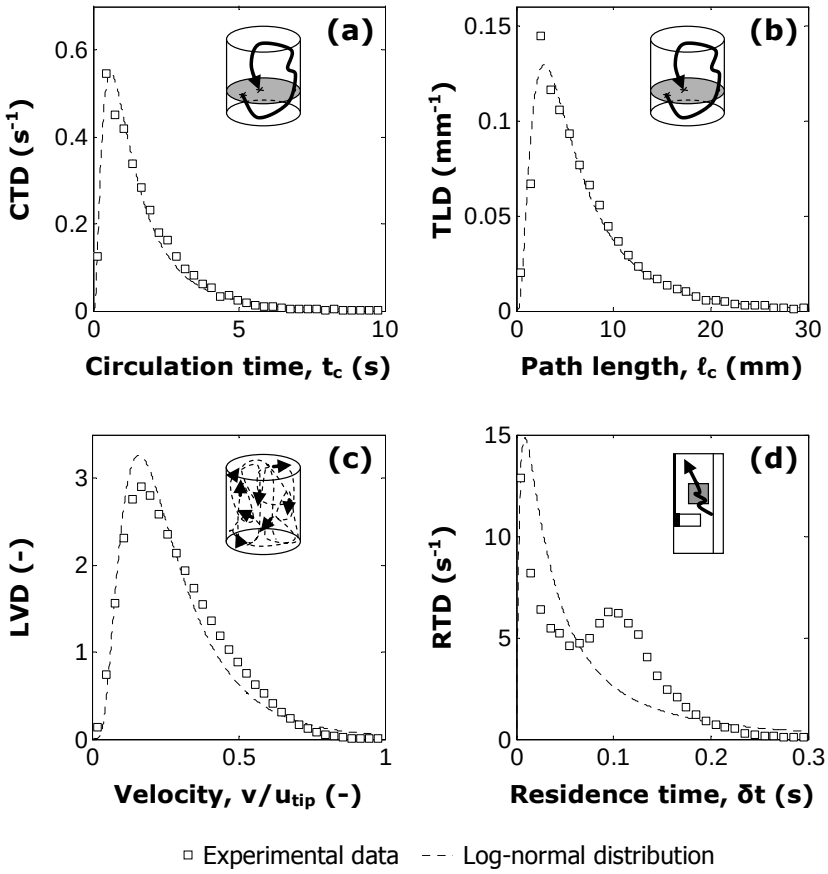

Figure 3.12. Probability density distributions in a single-phase system: T = 190 mm; aqueous NaCl solution; PBTD; D = 105mm (0.33 T off-bottom clearance); N = 220 rpm (Re_{imp} ~ 40000); (a) circulation time distribution for the horizontal plane at 0.25 H; (b) circulation trajectory length distribution for the horizontal plane at 0.25 H; (c) Lagrangian velocity magnitude distribution; (d) residence time distribution within the shaded area.

normal distribution. Additional statistical distributions can be obtained by analysing the Lagrangian velocity components, exploiting the arrays $[(v_\vartheta)_k]$, $[(v_r)_k]$ and $[(v_h)_k]$, or by using the Lagrangian velocity magnitude. The Lagrangian velocity distribution (LVD), i.e. the distribution of the 3D Lagrangian velocity magnitude v, is presented in **Figure 3.12c** which again shows a very good agreement with the log-normal distribution.

The spatial distribution of the mean residence time within a grid cell $\overline{\delta t}$, illustrated above in **Figure 3.10n**, is obtained by averaging the values contained in the array $[\delta t_k]$. Studying this quantity can be done by considering the statistical distribution of the residence time δt related to a selected grid cell or, more generally, to any geometrically defined volume. The residence time distribution (RTD) shown in figure **Figure 3.12d** was obtained for a squared cross-section torus ($0.3\,R < r < 0.5\,R$ and $0.5\,H < h < 0.7\,H$). Contrary to the other distributions, the RTD for the examined volume is not well represented by a log-normal distribution; this effect is probably due to the fact that the closed surface bounding the volume is imaginary and the tracer can penetrate such surface at any point generating, therefore, a high number of short residence times δt which are close to zero.

3-4.2 Decorrelation time

In probability theory and statistics, a correlation between two random variables indicates a mathematical relationship between them, i.e., their departure from reciprocal independence. Where the two variables are vectors, e.g. position vector with three coordinates, the correlation coefficients reveal information about the strength and preferred direction of eventual relationships. If the two variables are functions of time (waveform) and a time-lag is applied to one of them, the correlation coefficient between the two waveforms is also named cross-correlation coefficient; it quantifies their 'similarity' as a function of the time-lag. The cross-correlation between a time function and itself, which is known as autocorrelation is frequently employed in signal processing for finding repeating patterns and represents the similarity between the function and itself shifted by a time τ. The autocorrelation coefficient of a time function, $f(t)$, is given by

$$A_f(\tau) = \frac{\int_{-\infty}^{+\infty} f(t) f(t-\tau) dt}{\int_{-\infty}^{+\infty} f^2(t) dt} \tag{3.21}$$

The three spatial coordinates of the PEPT particle tracer are functions of time and so the autocorrelation coefficients, A_x, A_y and A_z, can be determined. Additionally, a single autocorrelation coefficient of the position vector, **P** = (x, y, z), can be obtained by extending Eq. (3.21) to a vector function, thus

$$A_P(\tau) = \frac{\int_{-\infty}^{+\infty} \mathbf{P}(t) \cdot \mathbf{P}(t-\tau) dt}{\int_{-\infty}^{+\infty} \mathbf{P}(t) \cdot \mathbf{P}(t) dt} = \frac{A_x \langle x^2 \rangle + A_y \langle y^2 \rangle + A_z \langle z^2 \rangle}{\langle x^2 \rangle + \langle y^2 \rangle + \langle z^2 \rangle} \tag{3.22}$$

The above defined autocorrelation coefficients of the Cartesian coordinates and position vector of the PEPT tracer are illustrated in **Figure 3.13** which shows that the position of the PEPT tracer is characterized by a short-term autocorrelation, i.e., the vector **P** influences its own evolution but only for a short time. The autocorrelation function decays rapidly with the time shift and a characteristic timescale can be identified. Wittmer *et al.* (1998) defined the decorrelation time as the time at which the tangent line to the function $A_P(\tau)$ at $\tau = 0$ intersects the time axis. In order to also take into account the negative fluctuations of the

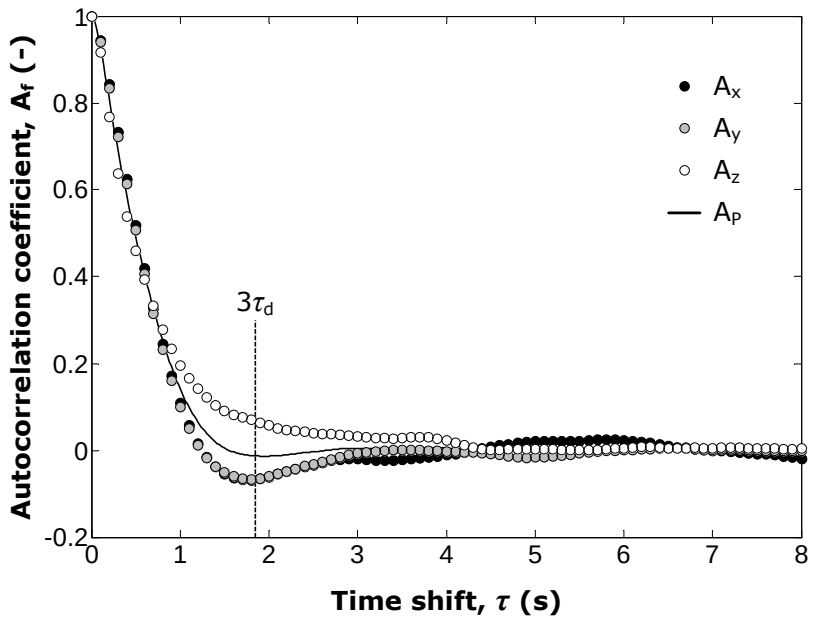

Figure 3.13. Variation of the autocorrelation coefficients of the Cartesian coordinates and position vector of the PEPT tracer with time shift in a single-phase system: T = 288 mm; aqueous NaCl solution; PBTD; D = 144 mm (0.25 T off-bottom clearance); N =300 rpm (Re_{imp} ~ 100000).

autocorrelation coefficient, the decorrelation time τ_d is determined here by the least squares method assuming a one-parametric exponential decay of A_P squared, i.e.,

$$A_P^2(\tau) \cong e^{-2\frac{\tau}{\tau_d}} \tag{3.23}$$

The timescale characterising the decay of the autocorrelation coefficients is representative of how fast the particle tracer loses its memory. The particle tracer can be viewed as a different particle just after a time equal to $3\tau_d$ since the absolute value of the autocorrelation coefficient is lower than 5% of its initial value, $A_P(0) = 1$. The time $3\tau_d$ can be employed as parameter for characterising mixing quality or performance. For the single-phase system represented in **Figure 3.13**, the threshold value $3\tau_d$ was 1.85 s when using a PBTD rotating at N = 300 rpm.

3-4.3 Poincaré maps

Poincaré maps are mathematical entities which are theoretically defined in dynamical system analysis (e.g., Aref and El Naschie, 1995). In this work, they are represented by the intersections of the long Lagrangian trajectory of the tracer with a surface named Poincaré section. Each intersection point is represented by a mark on the surface and, as a result, the number of marks is a function of the mean mass flux through the surface. Therefore, it is possible to visualise flow structures via Poincaré maps. Numerous interesting Poincaré sections may be used to plot Poincaré maps including horizontal plane surfaces, vertical planes and cylindrical surfaces of a smaller radius than the vessel. The number of different intersection points and the spatial dispersion of these points are characteristics of the mixing performance. Once again, the computational process to obtain such maps is based on the solution of numerous systems of equations similar to the systems in Eqs. (3.11), (3.12) and (3.13).

The Poincaré map illustrated in **Figure 3.14a** was obtained using as Poincaré section a horizontal plane at a distance 0.25 H from the vessel base in a tank filled with aqueous NaCl solution and equipped with a PBTD. The cylindrical surface with radius 0.7 R coaxial to the tank is the Poincaré section used to obtain the map in **Figure 3.14b** where the baffles generate four visible structures.

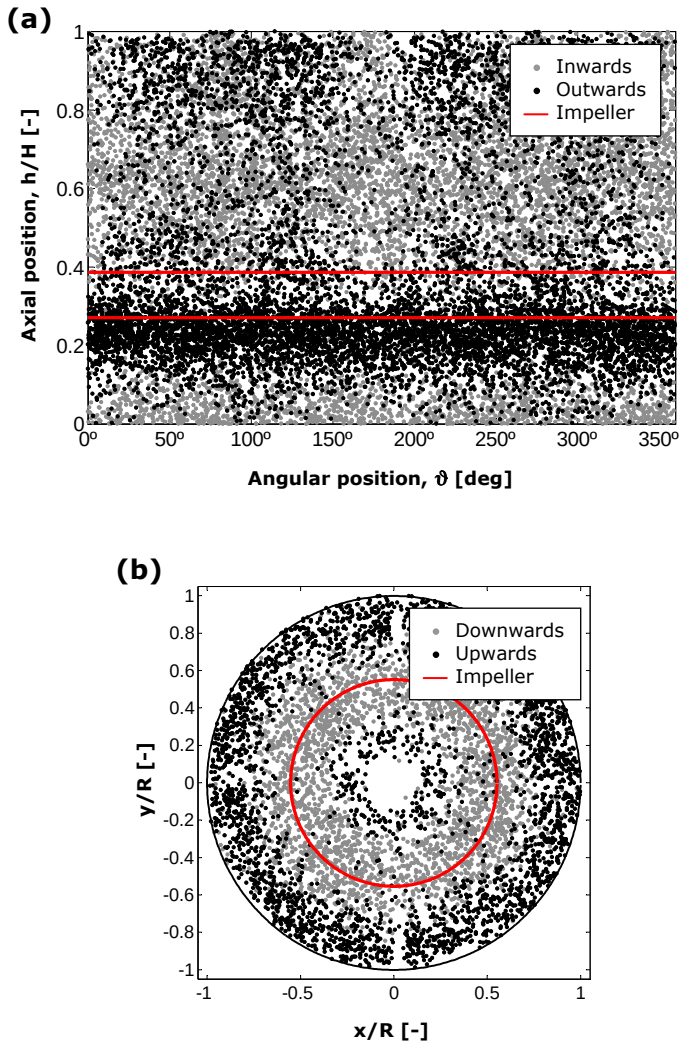

Figure 3.14. Poincaré maps obtained using (a) a cylindrical Poincaré section of radius 0.7 *R*, and (b) a horizontal Poincaré section 0.25 *H* off the vessel base: *T* = 190 mm; aqueous NaCl solution; PBTD; *D* = 105mm (0.33 *T* off-bottom clearance); *N* =220 rpm (Re_{imp} ~ 40000).

3-5 Methods of validating measurements

3-5.1 Ergodicity

The theoretical premise which guarantees that a tracer is representative of all the solid or liquid phase is referred to as ergodicity or iso-probability condition (Wittmer *et al.*, 1998). As already mentioned in Section 3-3.7, for a turbulent single-phase system, such a condition implies an equal probability of tracer presence at every point in the flow. In a multi-phase system, however, the total probability for all phases is required to be uniform, i.e. the sum of

probabilities of presence (weighted by the inverse of the phase volume concentration) of all components of the system must be the same everywhere. Ergodicity is a theoretical state which can be approached only after an infinite tracking time. However, it can be mathematically shown that, if the probability of tracer visit is sufficiently high everywhere, ergodicity can be assumed when the trajectory of the tracer is recorded over a sufficiently long time which achieves adequate data resolution in every region (Wittmer *et al.*, 1998). The PEPT tracking time used was always > 30 min in all the experiments, which was long enough to acquire a sufficient amount of data in all regions of the vessel. Hence, ergodicity could be safely assumed given that in such systems the probability of visit is sufficiently uniform by virtue of the open geometry of the vessel where all regions are more or less equally accessible to the tracer. However, to assess the accuracy of the ergodic condition assumption the probability of tracer presence can be calculated and its uniformity verified. On the basis of Eq. (3.15), when the cells have equal volume the occupancy is proportional to the probability of tracer presence $\Delta t / t_\infty$ and, consequently, **Figure 3.10m** for example shows that the tracer has practically an equal probability of presence everywhere within the vessel.

3-5.2 Mass continuity in a multi-phase system

Mass continuity is an important tool for checking the accuracy and reliability of flow data including Lagrangian PEPT measurements. The net mass flux through a volume bounded by a closed surface *S* should be zero, thus

$$\sum_S \mathbf{u_{3D}} \cdot \Delta \mathbf{S} \cong 0 \tag{3.24}$$

Calculations can be made by considering a closed cylindrical surface *S* with the same vertical axis, base and diameter as the tank but of a shorter height. Because of $\mathbf{u_{3D}}$ being zero over the external surface of the vessel or being parallel to it, the term $\mathbf{u_{3D}} \cdot \Delta \mathbf{S}$ is zero everywhere except in the horizontal plane across the tank, so that *S* can be reduced to such a plane, S_h, and Eq. (3.14) is reduced to a zero average of axial velocities across the horizontal plane considered. A similar situation can be envisaged where *S* is a closed cylindrical envelope with the same vertical axis and height as the tank but with a smaller diameter; Eq. (3.14) then becomes a zero average of radial velocities across the lateral surface, S_r, of the considered cylindrical volume. Testing, for instance, the set of PEPT data collected in binary suspensions of up to 40 wt% glass particles, a very good verification of the mass continuity

was obtained as calculations gave a velocity average close to zero, generally less than $0.03u_{tip}$, as demonstrated in **Figure 3.15**.

3-5.3 Two-dimensional comparison of PEPT with PIV

Comparison between Eulerian velocity maps obtained via Lagrangian tracking and a well established optical technique such as particle image velocimetry (PIV), offers a highly reliable way to validate the Lagrangian data collected, their analysis and the technique of measurement used itself. Unfortunately, the optical nature of the PIV technique tends to restrict comparison to transparent single-phase systems. Even very dilute solid concentrations (~ 1 wt%) make the suspension partially or entirely opaque compromising thus the reliability and applicability of the PIV technique.

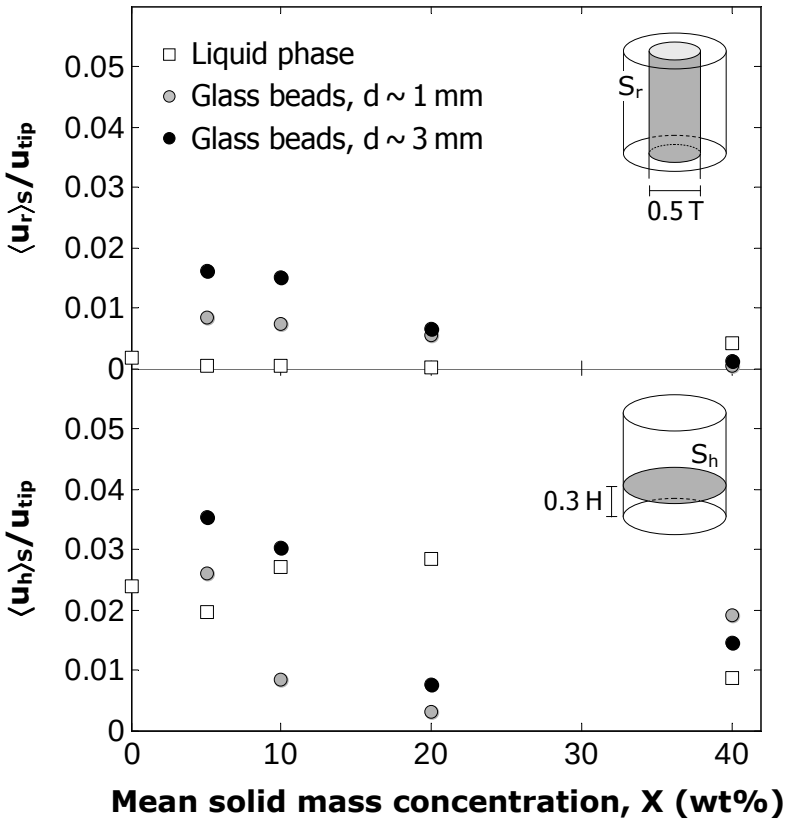

Figure 3.15. Mass continuity verification for PEPT in a binary suspension of glass beads in aqueous NaCl solution: normalised radial and axial velocities averaged on surfaces S_r (of diameter 0.5 T) and S_h (0.3 H off the base), respectively; T = 288 mm; PBTD; D = 144 mm (0.25 T off-bottom clearance); $N = N_{js}$; $Re_{imp} > 100000$.

In **Figure 3.16**, two azimuthally-averaged Eulerian velocity vector plots obtained by PIV and PEPT in an aqueous NaCl solution are compared showing a very good agreement. Both of the two radial-axial maps are representative of the whole mixing vessel since n_ϑ was set to 1 in the analysis of the PEPT data, and the PIV data were collected in planes at 5° intervals over a 90° sector between two adjacent baffles and azimuthally averaged. Such multiplane PIV experiments and data will be thoroughly described and discussed in the next chapter where significant differences in the 2D flow-dynamics between data collected in different planes will be shown.

A more detailed quantitative comparison is shown in **Figure 3.17** where multiple radial and vertical profiles of the radial and axial velocity components u_r and u_h are compared and the agreement appears to be excellent throughout. Due to the importance of such comparison, a

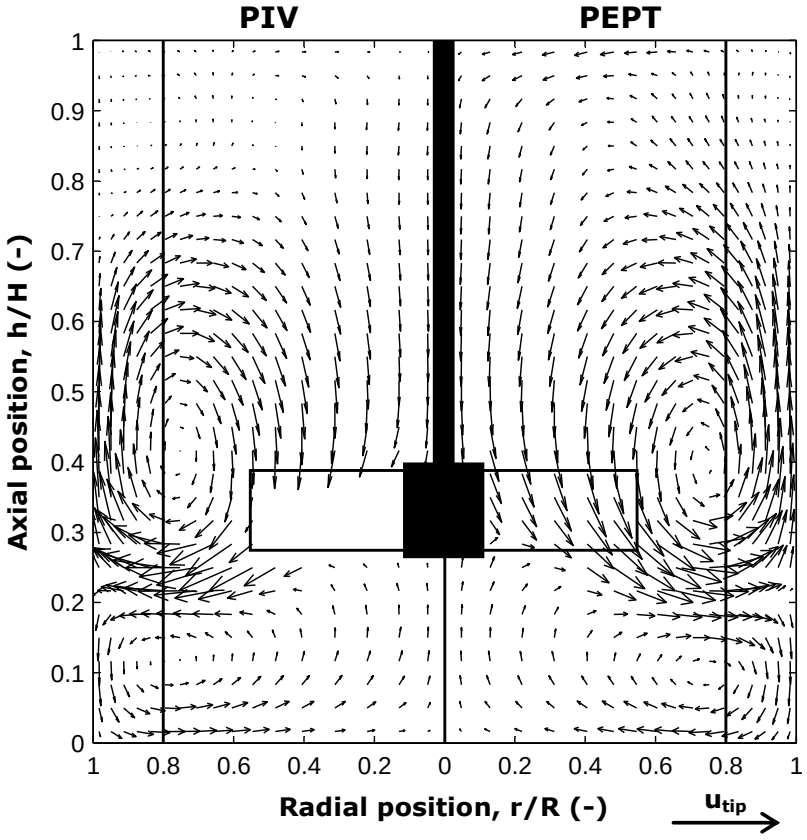

Figure 3.16. Comparison of azimuthally-averaged radial-axial velocity vector plots obtained by PIV and PEPT in a single-phase system: T = 190 mm; aqueous NaCl solution; PBTD; D = 105 mm (0.33 T off-bottom clearance); N =220 rpm (Re_{imp} ~ 40000).

detailed study of the differences in the flow fields obtained with these two techniques is presented in Chapter V.

Finally, the overall accuracy and reliability of both sets of measurements obtained from PEPT and PIV can be examined and compared by verifying the mass continuity throughout the vessel. The radial velocity component averaged over the cylindrical surface S_r is plotted in **Figure 3.18a** as a function of the radius r_s. Outside the impeller region, the average normalised radial velocity is vanishingly small for both techniques, with values below

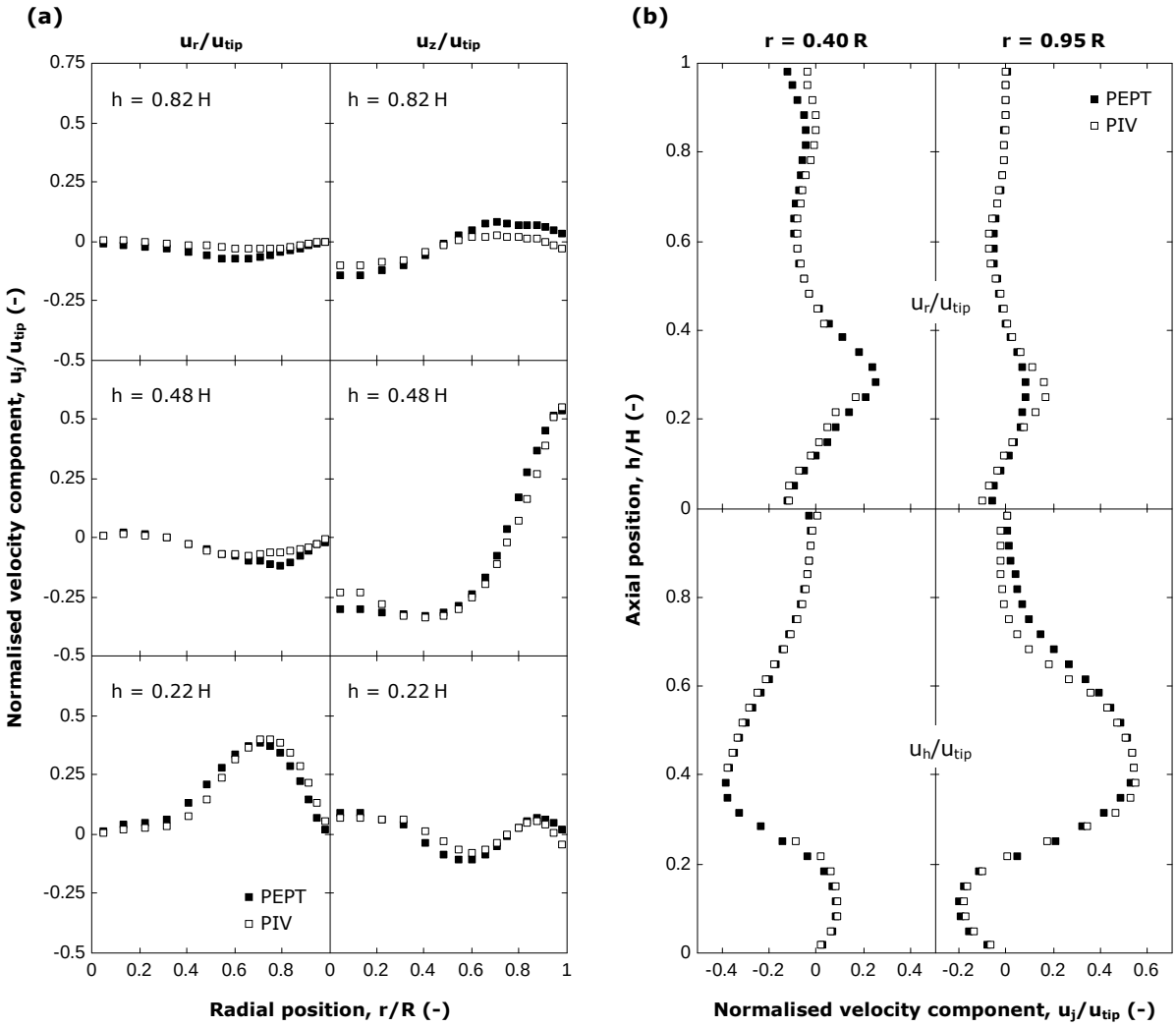

Figure 3.17. Azimuthally-averaged velocity profiles obtained by PIV and PEPT in a single-phase system: T = 190 mm; aqueous NaCl solution; PBTD; D = 105 mm (0.33 T off-bottom clearance); N =220 rpm (Re_{imp} ~ 40000).

0.01 u_{tip}. Where the cylindrical surface S_r intersects with the agitator, PIV data are not available and therefore the error in mass continuity is higher for PIV but remains quite small, mostly below 0.02 u_{tip}. On the other hand, the PEPT tracer continuously tracks the fluid between the opaque impeller blades and the error in mass continuity is still very small for surfaces S_r intersecting with the agitator.

A similar plot is shown in **Figure 3.18b** for the axial velocity component averaged over the vessel cross-section S_h. Again, outside the impeller region such an average velocity is close to zero for both measurement techniques, generally less than 0.02 u_{tip}. In the region affected by

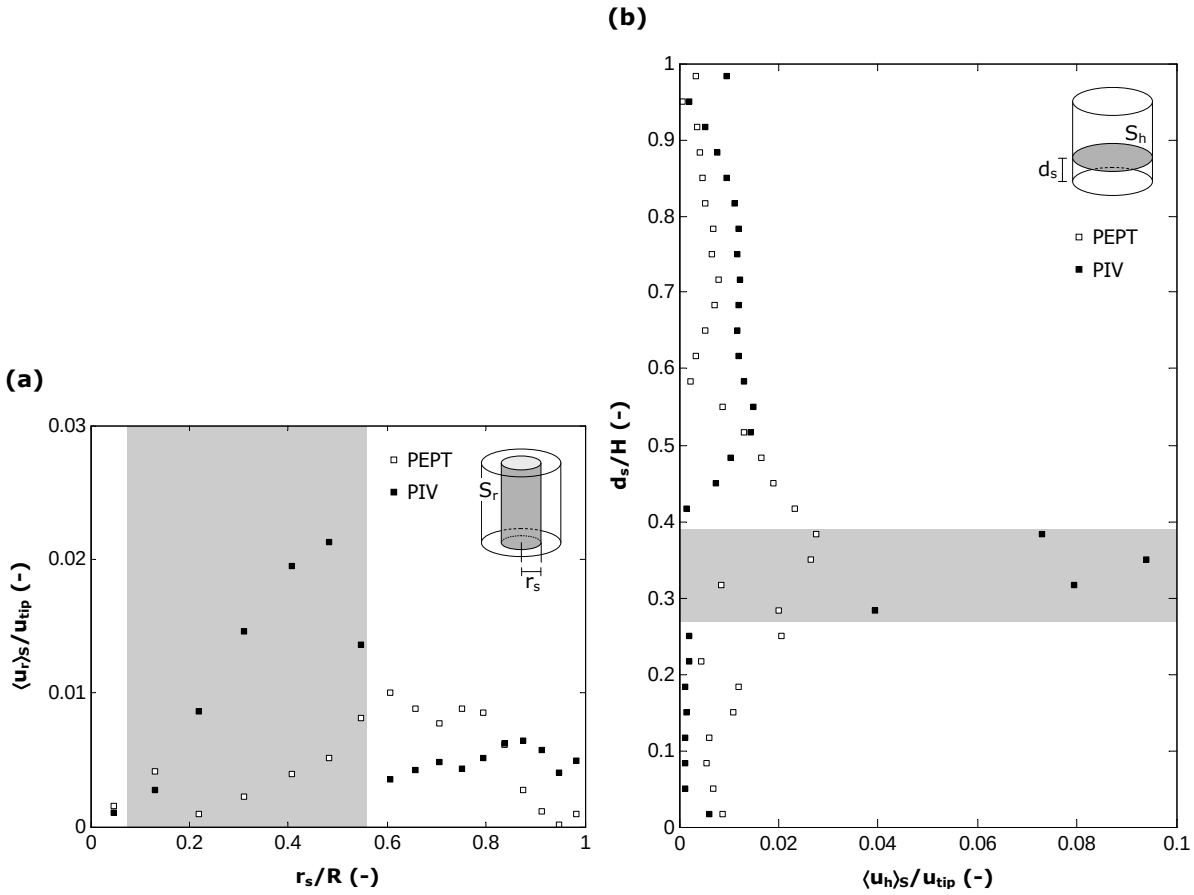

Figure 3.18. Mass continuity verification for PEPT and PIV: T = 190 mm; aqueous NaCl solution; PBTD; D = 105 mm (0.33 T off-bottom clearance); N =220 rpm (Re_{imp} ~ 40000); (a) normalised mean radial velocity averaged over surface S_r as a function of the radius of S_r; (b) normalised mean axial velocity averaged over surface S_h as a function of the position of S_h. The shaded areas are regions of intersection of S_r or S_h with the impeller.

the presence of the impeller the mass continuity error of PEPT is only fractionally higher, whereas for PIV it increases much more almost reaching 0.1 u_{tip}. The impeller swept region which is inaccessible to the laser plane is dominated by axial flow, thus, the deficiency in PIV data in this region causes a much larger error in mass continuity in the axial direction (when averaging over S_h) than in the radial direction (when averaging over S_r).

3-6 Conclusions

The main purpose of this chapter was to present a detailed methodology developed for the analysis and validation of Lagrangian data obtained from tracer trajectories in fluid mixing systems. Such a methodology has been successfully applied to the analysis of data collected in various single-phase and multi-phase solid-liquid systems using position emission particle tracking. More details about the application of the tools developed here are presented in subsequent chapters.

This novel technique is capable of providing unique and accurate Lagrangian flow data within opaque flows. It thus opens up new possibilities for tackling a range of challenging problems in the mixing of opaque single-phase and concentrated multi-phase systems which have remained hitherto unaddressed/unresolved because of a lack of adequate measurement techniques. Thus, it has been possible to visualise the Lagrangian trajectory and the 3D flow structure within the cavern formed around the agitator when mixing a viscoplastic fluid. It has also been possible to analyse Lagrangian multi-phase data to give detailed Eulerian descriptions of various mixing systems including the full 3D velocity field, local occupancy and residence time distributions, and spatial distribution of each phase component. Other features such as the use of hyperplanes and Lagrangian frequency distributions, decorrelation time and Poincaré sections have also been demonstrated.

One of the important tools developed enables the mass continuity of each tracked component within a multi-phase mixture to be accurately tested, which is crucial for the reliability of the measurements. An additional reliability test presented in this chapter consisted of a brief comparison between Eulerian velocity maps obtained in a transparent liquid via Lagrangian tracking by PEPT and the well-established optical technique of PIV, showing an excellent agreement between the two methods.

Notation

Roman letters

a_1 a_2	Slope coefficients of 3D straight line	-
A_f	Autocorrelation coefficient of $f(t)$	-
A_P	Autocorrelation coefficient of $\mathbf{P}(t)$	-
A_x A_y A_z	Autocorrelation coefficients of $x(t)$, $y(t)$, $z(t)$	-
b_1 b_2	Intercept coefficients of 3D straight line	m
c	Local volume concentration of solids	-
C	Mean volume concentration of solids	-
d	Particle diameter	m
d_s	Off-bottom distance	m
D	Impeller diameter	m
E_G	Geometric efficiency	-
f	Time function indicating $x(t)$, $y(t)$ or $z(t)$	m
H	Height of the suspension	m
i I	Cell indices	-
j	Generic cylindrical direction	-
k	Location counter	-
ℓ_c	Circulation trajectory length	m
L_D H_D S_D	Dimensions of detection volume	m
n	Number of particles in the vessel	-
n_c	Number of grid cells	-
n_ϑ n_r n_h	Number of cells in the cylindrical directions	-
n_L	Number of locations per cell	-
n_{LSM}	Number of consecutive locations	-
n_s	Number of particle size fractions	-
n_V	Number of visits per cell	-
N	Impeller rotational speed	s^{-1}
N_{js}	Minimum speed for particle suspension	s^{-1}
$\mathbf{O}$	Origin of cylindrical coordinates vector	|m|
O_E	Occupancy	-
p	Probability density function	m^{-3}

$\mathbf{P}$	Tracer location vector	|m|
q	Index of summation in Eq. (3.10)	-
q_b	Fraction of black pixels	-
$r\ \ h$	Radial-axial cylindrical coordinates	m
r_c	Centring circumference radius	m
r_s	Cylindrical surface radius	m
R	Vessel radius	m
Re_{imp}	Impeller Reynolds number (ND^2/ν)	-
S	Surface area	m^2
t	Time	s
t_∞	PEPT runtime	s
t_c	Circulation time	s
t_E	Ergodic time	s
T	Vessel diameter	m
$u_\vartheta\ \ u_r\ \ u_h$	Cylindrical Eulerian velocity components	m s^{-1}
$\mathbf{u_{3D}}$	Eulerian velocity vector	|m s^{-1}|
$\mathbf{u_{rh}}$	Radial-axial Eulerian velocity vector	|m s^{-1}|
u_{tip}	Impeller tip speed	m s^{-1}
$\mathbf{v}$	Tracer Lagrangian velocity vector	|m s^{-1}|
v	Magnitude of tracer Lagrangian velocity	m s^{-1}
$v_\vartheta\ \ v_r\ \ v_h$	Tracer Lagrangian velocity components	m s^{-1}
$\bar{v}_\vartheta\ \ \bar{v}_r\ \ \bar{v}_h$	Mean velocity components in a visit	m s^{-1}
V	Volume	m^3
V_P	Particle volume	m^3
V_S	Volume of solids in the vessel	m^3
V_T	Total suspension volume	m^3
$x\ \ y\ \ z$	Cartesian coordinates	m
$x_o\ \ y_o\ \ z_o$	Centre of vessel base	m
X	Mean mass concentration of solids	-

Greek letters

α	Numerical time derivative of ϑ	rad s^{-1}

β γ	Numerical time derivatives of r and h	m s^{-1}
δt	Residence time	s
$\overline{\delta t}$	Mean residence time	s
ϑ	Azimuthal coordinate	rad
$\boldsymbol{\theta}$ ϕ	Angular coordinates of spherical system	rad
$\hat{\boldsymbol{\theta}}$ $\hat{\mathbf{r}}$ $\hat{\mathbf{h}}$	Versors of cylindrical coordinate system	-
ν	Kinematic liquid viscosity	m^2 s^{-1}
σ_ϑ σ_r σ_h	Standard deviation of Eulerian velocities	m s^{-1}
σ_{3D}	Standard deviation of $\lvert\mathbf{u_{3D}}\rvert$	m s^{-1}
σ_{rz}	Standard deviation of $\lvert\mathbf{u_{rh}}\rvert$	m s^{-1}
τ	Time shift	s
τ_d	Decorrelation time	s
Ω	Solid angle	sr

Abbreviations

CTD	Circulation time distribution
LVD	Lagrangian velocity distribution
PBT	Pitched blade turbine
PBTD	Down-pumping PBT
PBTU	Up-pumping PBT
PEPT	Positron emission particle tracking
PIV	Particle image velocimetry
RTD	Residence time distribution
TLD	Trajectory length distribution

Chapter IV
Azimuthally Resolved PIV Measurements

Abstract

Two-dimensional particle image velocimetry (PIV) is usually used to determine the complex flow field in mechanically agitated vessels on the basis of measurements taken in a single vertical plane, thus, assuming axial symmetry. In this study, 2D PIV has been used to investigate the effects of the azimuthal position of the measurement plane in a fully baffled vessel agitated by a pitched blade turbine. Seventeen planes located at 5 degree intervals between two adjacent baffles are analysed. To maintain a high spatial resolution of ~ 1 mm when examining each plane, a two-block approach is employed combining data from two fields of view to reconstruct the whole flow field. Time-averaged velocity and turbulent kinetic energy fields are obtained under fully turbulent conditions as a function of the azimuthal position of the laser plane. It is shown that the assumption of axial symmetry for such Eulerian fields is not fully justified within a fully baffled vessel, as there are considerable differences between planes. The results also show for the type and size of impeller used here, the importance of including both the axial and radial discharge contributions for an accurate evaluation of the flow number, otherwise it can be underestimated by up to 60%. The three-dimensional nature of the PIV measurements has also enabled the mass continuity to be accurately verified throughout the vessel.

4-1 Introduction

Among the various flow visualisation techniques, laser Doppler velocimetry (LDV) and particle image velocimetry (PIV) have become the most employed to examine the complex nature of the flow fields in stirred vessels, provided the equipment and fluids used are optically transparent (Kresta and Wood, 1993a; Baldi and Yianneskis, 2004). The flow field in a stirred vessel has been the subject of investigation by LDV for the last 30 years, the use of PIV, however, is much more recent spanning a decade or so.

Most of the works in the literature have reported two-dimensional data which represent time-averaged flow patterns. However, in recent years, some authors have performed so-called angle-resolved measurements, i.e., measurements resolved by the azimuthal angle between the impeller blades to obtain more accurate turbulent quantities, since time-averaged measurements do not take into account the periodicity of the flow due to the passage of the impeller blades (Ducci and Yianneskis, 2006). Angle-resolved LDV measurements have been reported in stirred tanks equipped with a Rushton disc turbine by Lee and Yianneskis (1998), or with a pitched blade turbine (PBT) by Shäfer *et al.* (1998), while, more recently, Chung *et al.* (2009), Gabriele *et al.* (2008) and Khan *et al.* (2006) used angle-resolved PIV to investigate vessels agitated by a PBT. These authors have shown how measurements can be refined by considering the position of the laser sheet relative to the impeller blade, unravelling important characteristics of the turbulent flow which are otherwise masked by time-averaging. It is, however, surprising that seemingly no attention has been given to how the measured 2D flow field is affected by the angular (or azimuthal) position of the laser plane. Measurements have been restricted to a single plane, most commonly the 45° plane between two baffles, assuming that the flow field is axially symmetrical. In consequence, it is quite possible that the use of different planes might be responsible for the occasional discrepancies between different experimental studies reported in the literature. Furthermore, 2D PIV measurements are usually found not to satisfy mass continuity. For this reason, using single plane measurements, Aubin *et al.* (2004) concluded that the flow field may be dependent on the position of the laser plane relative to the baffle, but no detailed study of these effects has been reported.

This chapter reports on the use of 2D PIV to study the influence of the azimuthal position of the measurement plane on the radial-axial flow field in a cylindrical stirred vessel fully

baffled and equipped with a down-pumping pitched blade turbine. Detailed information is obtained on fluid velocities, turbulent kinetic energy and pumping flowrates in 17 planes located at 5° intervals between two adjacent baffles. Mass continuity considerations are used to assess the reliability of the multi-plane measurements.

4-2 Experimental

4-2.1 Apparatus

The stirred vessel used was a flat-base cylindrical glass tank of diameter T = 190 mm, fitted with four equidistant wall baffles of width 0.1 T and agitated by a six-blade 45º pitched-turbine of diameter D = 0.55 T and vertical height 0.12 T, as shown in **Figure 4.1**. The impeller blades were welded onto the hub which had an external diameter equal to 0.14 T, an internal diameter equal to 0.05 T and a height equal to 0.15 T. The off-bottom clearance of the PBT was set at 0.33 T, and the vessel was filled with water to a height $H = T$. The vessel was located inside a square glass tank also filled with water to minimise light distortion. All the experiments were conducted with the impeller operating in the down-pumping mode at a

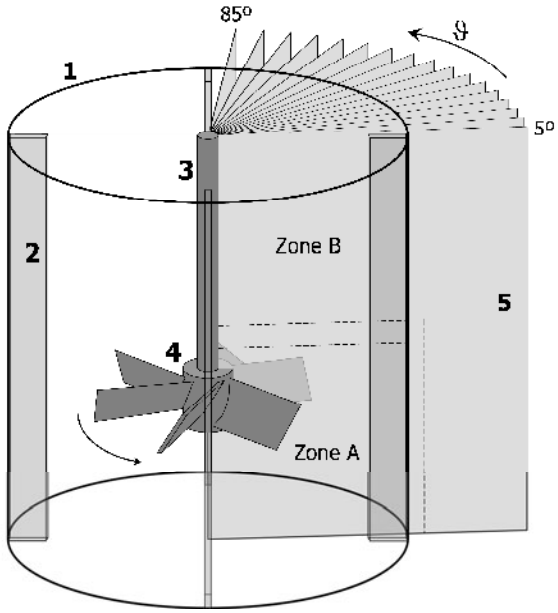

Figure 4.1. Experimental set-up for PIV investigation: 1 cylindrical vessel; 2 baffle; 3 shaft; 4 down-pumping PBT impeller; 5 laser sheet at varying ϑ.

rotational speed of $N = 3.67\ s^{-1}$ corresponding to an impeller tip speed of $1.2\ m\ s^{-1}$. The value of the impeller Reynolds number ($Re = ND^2/\nu$) was 40 000, thus, ensuring fully turbulent conditions which minimise macro-instabilities in the flow field (Roussinova *et al.*, 2000).

4-2.2 PIV experiments

Two-dimensional PIV measurements were conducted using a dual head Nd:YAG 532 nm pulsed laser (New Wave Research Inc., USA) and a single frame-straddling CCD camera (PowerView Plus, TSI Inc., USA) capable of capturing 15 image pairs per second at a resolution of 2048×2048 pixels. Frame and laser sequencing were controlled by a TSI Laserpulse 610035 synchronizer and a workstation running TSI Insight 9.0 software. Fast Fourier Transform (FFT) cross-correlation was used to interrogate each pair of images, which were sectioned into small interrogation areas (IA). For measurement of the liquid velocities, hollow silver coated particles of 10 μm diameter were seeded into the vessel and were illuminated using a 1 mm thick laser sheet.

The flow field in the vessel was analysed in 17 azimuthally equidistant planes comprised between two adjacent baffles. By rotating the cylindrical vessel within the square tank in 5º angular steps, from $\vartheta = 5^o$ to $\vartheta = 85^o$, the laser sheet was used to illuminate the different planes in turn, each plane passing through the vessel axis as illustrated in **Figure 4.1**. Note that the 5º plane is on the leeward side of the baffle, whereas the 85º plane is on the windward side of the baffle. Recently, using a multi-block approach, Khan *et al.* (2004) partitioned the illuminated vertical plane in many blocks which were analysed separately and then assembled together to reconstruct the whole flow field, thus, improving the resolution of PIV measurements significantly. In the present work, a simpler partitioning method was adopted using two blocks (Zone A and Zone B in **Figure 4.1**). Thus, two-dimensional PIV flow data were obtained in both zones at varying ϑ values based on 500 image pairs recorded in each experiment. The frequency of data acquisition was set to 1.01 Hz which, for $N = 3.67\ s^{-1}$, allowed the impeller blades to be captured at 500 fairly evenly distributed angular positions between 0 and 2π. Therefore, the time-averaged results were representative of all the angular positions assumed by the impeller blades with respect to the laser plane.

The images were processed with a recursive Nyquist grid using an IA of 32×32 pixels in the first pass and 16×16 pixels in the second. Since a recursive grid was used to process the

images no further overlapping between adjacent IAs was allowed. Using a resolution of 64.7 μm per pixel, a vector resolution of 1.04 mm was obtained, i.e. a grid was defined where each 16×16 pixel cell represented a region of area 1.04×1.04 mm^2 containing a single vector. The two frames of each image pair were separated by a time interval of 400 μs which ensured a maximum expected displacement (based on $u_{max} \sim 0.5\, u_{tip}$, the maximum fluid velocity expected near the tip of the impeller) within 25% of the length of the IA, as suggested by the 'one-quarter rule' (Adrian, 1986).

The two blocks (Zone A and Zone B in **Figure 4.1**) were joined simply by averaging the velocity values obtained in the cells within the overlapping area. In this area the velocity values obtained from Zone A were generally within 2% of the values obtained from Zone B, thus showing a high degree of measurement reproducibility.

4-3 Theory and data analysis

4-3.1 Mean flow field and flow number

In each of the 17 planes investigated, the mean flow field was determined by ensemble-averaging the 500 instantaneous vector fields obtained in both Zone A and Zone B depicted in **Figure 4.1**. The measurements yielded a large amount of data which required the development of a computer code to manage 51 000 files including images and text files, and extract the required information. Thus, local time-averaged values of the radial and axial fluid velocity components $\bar{u}_r(\vartheta, r, z)$ and $\bar{u}_z(\vartheta, r, z)$ were obtained in terms of cylindrical coordinates. As pointed out above, such time-averaged velocity values are representative of all the angular positions assumed by the impeller blades with respect to the laser plane.

The flow number, *Fl*, is a dimensionless parameter used to measure impeller pumping effectiveness, and is usually defined as the normalised volumetric discharge, i.e.,

$$Fl = \frac{Q}{ND^3} \tag{4.1}$$

For a PBT in a fully baffled configuration, the volumetric discharge, *Q*, has been traditionally estimated by taking into consideration only the vertical flow emerging from the lower horizontal edge of the impeller blades, denoted by Q_2 in **Figure 4.2**. Such an approximation

assumes that Q_2 represents virtually all of the discharge flow, which may not necessarily be true for the type and size of impeller used here. Given the mixed axial-radial nature of the total discharged flow emerging from the PBT, Q should include the radial contribution Q_3 depicted in **Figure 4.2**, so that $Q = Q_2 + Q_3$. In order to assess the importance of each contribution separately, Fl_2 and Fl_3 can be calculated using Eq. (4.1) on the basis of Q_2 and Q_3, respectively, so that $Fl = Fl_2 + Fl_3$. In a similar way, Fl_1 is defined using the volumetric flowrate Q_1 entering at the impeller inlet. Time-averaged velocity data obtained from PIV in the 17 interrogated planes can be used to determine the flowrates Q_1, Q_2 and Q_3 which are defined as

$$Q_1 = \int_{\vartheta=0}^{\vartheta=2\pi} \int_{r=0}^{r=D/2} \overline{u}_z(\vartheta, r, z_1) r \, dr \, d\vartheta \tag{4.2}$$

$$Q_2 = \int_{\vartheta=0}^{\vartheta=2\pi} \int_{r=0}^{r=D/2} \overline{u}_z(\vartheta, r, z_2) r \, dr \, d\vartheta \tag{4.3}$$

$$Q_3 = \frac{D}{2} \int_{\vartheta=0}^{\vartheta=2\pi} \int_{z=z_2}^{z=z_1} \overline{u}_r\left(\vartheta, \frac{D}{2}, z\right) dz \, d\vartheta \tag{4.4}$$

where z_1 and z_2 are, respectively, the axial coordinates of the upper and the lower edge of the impeller blades.

When PIV data are only available in a single vertical plane, as is usually the case, axial symmetry is presumed and the mean velocity components are assumed not to vary with the angular position ϑ of the plane of measurement, hence, the double integrals in Eqs. (4.2), (4.3) and (4.4) are reduced to single integrals or discrete sums multiplied by 2π. While this 2D approximation may be fully justified in an unbaffled system, in a baffled system, however, azimuthal gradients in the mean flow should be expected, but it is not *a priori* clear how significant these are. The experimental data obtained from the 17 planes will allow the calculation of Q_1, Q_2 and Q_3 using the above equations; in addition, using the 2D approximation of the ϑ-invariant mean velocity for each plane, the flowrates $Q_1^{(2D)}(\vartheta)$, $Q_2^{(2D)}(\vartheta)$ and $Q_3^{(2D)}(\vartheta)$ are obtained which are then normalised according to Eq. (4.1) to give $Fl_1^{(2D)}(\vartheta)$, $Fl_2^{(2D)}(\vartheta)$ and $Fl_3^{(2D)}(\vartheta)$, respectively. By analogy with Fl above, the sum of $Fl_2^{(2D)}$ and $Fl_3^{(2D)}$ is equal to $Fl^{(2D)}$ which can be used to verify the validity of the ϑ-

invariance assumption widely used in the literature in experimental investigations of the mean flow in stirred vessels. Note that the flowrates (or flow numbers) obtained using Eqs. (4.2), (4.3) and (4.4), are identically equal to the ϑ-averaged values of the flowrates (or flow numbers) calculated using the 2D approximation and denoted by the superscript '(2D)'.

4-3.2 Turbulent kinetic energy

The turbulent flow regime in a mechanically agitated vessel is characterised by three-dimensional chaotic and unsteady velocity variations in space and time. For flows which are steady on average, it is possible to resolve at any point in the system each of the three instantaneous vector-components of the velocity, u_j, into a time-averaged mean component, $\overline{u}_j$, and a fluctuating component, u'_j, i.e.,

$$u_j = \overline{u}_j + u'_j \tag{4.5}$$

where the subscript j indicates the direction of the vector-component. By definition, the u'_j terms are characterised by a zero average, therefore the root mean square of the fluctuating velocity component, usually called RMS velocity, is used to quantify the degree of 'deviation

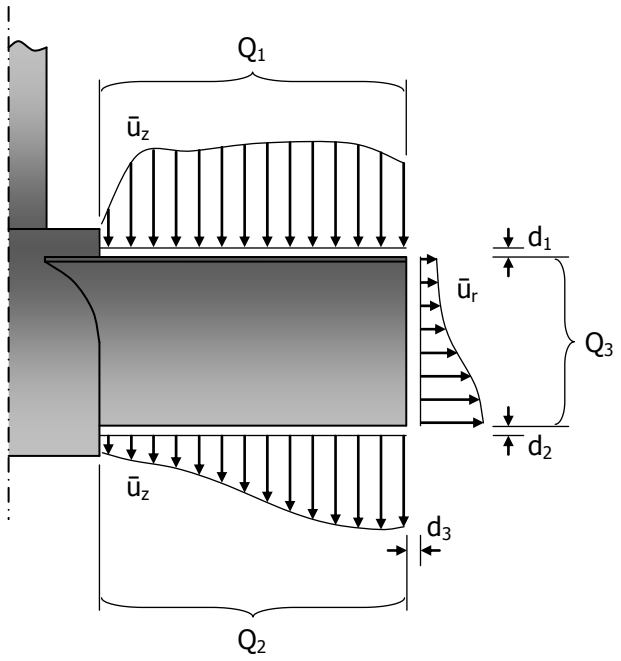

Figure 4.2. Schematic illustration of flowrates Q_1, Q_2, and Q_3 for estimating the flow number of the PBT used.

from the mean', thus

$$\tilde{u}_j = \sqrt{\overline{u_j'^2}} \tag{4.6}$$

RMS velocities provide a local measure of the turbulence level and its direction within the system. For a more detailed analysis, the RMS velocities in a given plane can be further resolved by considering the oscillatory cycle arising from the passage of the rotating impeller blades. Such an analysis would require detailed angle-resolved velocity information between impeller blades, which is beyond the scope of this study.

In a stirred vessel, the impeller imparts kinetic energy to the fluid generating both the mean flow field and the fluctuating velocities associated with it. The turbulent kinetic energy (TKE) is the portion of kinetic energy per unit mass due to the velocity fluctuations and takes the form of the half trace of the Reynolds stress tensor, i.e.,

$$k = \frac{1}{2}\left(\tilde{u}_\vartheta^2 + \tilde{u}_r^2 + \tilde{u}_z^2\right) \tag{4.7}$$

In order to measure the turbulent kinetic energy with sufficient accuracy to reach 95% of the correct value, the spatial resolution should be as small as ~ 20 times the mean Kolmogorov length scale (Saarenrinne *et al.*, 2001), defined as

$$\lambda_K = \left(\frac{\nu^3}{\varepsilon_T}\right)^{\frac{1}{4}} \tag{4.8}$$

where ν is the liquid kinematic viscosity and ε_T is the specific energy dissipation rate. Using the average energy dissipation rate within the tank, the Kolmogorov length scale, λ_K, is estimated as ~ 50 μm which is indeed ~ 20 times smaller than the vector resolution adopted (1.04 mm).

The experimental setup employed in this study yields 2D PIV data in each interrogated plane but there is no measurement of the tangential velocity component and its related RMS. Therefore *k* is estimated using a pseudo-isotropic assumption, i.e.,

$$\tilde{u}_\vartheta^2 \cong \tilde{u}_r^2 \cong \tilde{u}_z^2 \tag{4.9}$$

which postulates that, in the absence of direct measurement, the third RMS velocity component can be estimated by a 2D approximation (Sheng *et al.*, 2000), thus

$$\tilde{u}_{\vartheta}^2 = \frac{1}{2}\left(\tilde{u}_r^2 + \tilde{u}_z^2\right) \tag{4.10}$$

and combining Eqs. (4.7) and (4.10) yields

$$k = \frac{3}{4}\left(\tilde{u}_r^2 + \tilde{u}_z^2\right) \tag{4.11}$$

Although this assumption has no theoretical justification in a stirred tank (Kresta and Wood, 1993b), it has been recently confirmed experimentally by Khan *et al.* (2006) for a PBT using stereoscopic 3D PIV data, and by Chung *et al.* (2007) also for a PBT by reconstructing the 3D flow field from 2D PIV measurements in vertical and horizontal planes inside a miniature fully-baffled stirred vessel. In this work, the analysis of the collected data allowed the radial and axial RMS velocities and TKE to be obtained as a function of the 3D cylindrical coordinates, namely $\tilde{u}_r(\vartheta, r, z)$, $\tilde{u}_z(\vartheta, r, z)$ and $k(\vartheta, r, z)$. The applicability of Eq. (4.9) in this case could be partly assessed by verifying that the measured radial and axial RMS velocities are, in fact, approximately equal.

4-3.3 Mass continuity

As already mentioned in Section 3-5.2, mass continuity is an important means of checking the accuracy and reliability of the PIV measurements. The net mass flux through a volume bounded by a closed surface *S* should be zero, thus

$$\sum_S \bar{\mathbf{u}} \cdot \Delta\mathbf{S} \cong 0 \tag{4.12}$$

Calculations were made by considering a closed cylindrical surface *S* with the same vertical axis, base and diameter as the tank but of a shorter height. Because of $\bar{\mathbf{u}}$ being zero over the external surface of the vessel or being parallel to it, the term $\bar{\mathbf{u}} \cdot \Delta\mathbf{S}$ is zero everywhere except in the horizontal plane across the tank, so that *S* can be reduced to such a plane, S_z, and Eq. (4.12) is reduced to a zero weighted average of axial mean velocities across the horizontal plane considered. PIV results are based on equal interrogation areas and, because of the cylindrical geometry, velocity vectors at different radial position correspond to different IA

volumes. As a consequence, differently than for PEPT, the use of the mass continuity principle involves calculations of weighted velocity averages values instead of simple arithmetical averages. To be properly addressed, mass continuity must be considered from a 3D point of view and, hence, all the measurement planes were taken into account in the verifications conducted.

4-4 Results and discussion

4-4.1 Mean flow field

The statistical reliability of the number of PIV image pairs used in the flow analysis was tested by examining its effect on the mean and RMS values of the measured velocity components. Such an effect is demonstrated in **Figure 4.3** at a typical sample point ($\vartheta = 30^o$, $z = 0.6\ H$, $r = 0.9\ R$) within the vessel, where the velocities and their fluctuating components seem to reach a good degree of convergence already after 200 image pairs. The convergence of the measurement statistics can be tested throughout the vessel by calculating the variation in the mean and RMS velocities when averaging a number of image pairs lower than the one that has been used (Sharp and Adrian, 2001). Calculations conducted at most of the grid

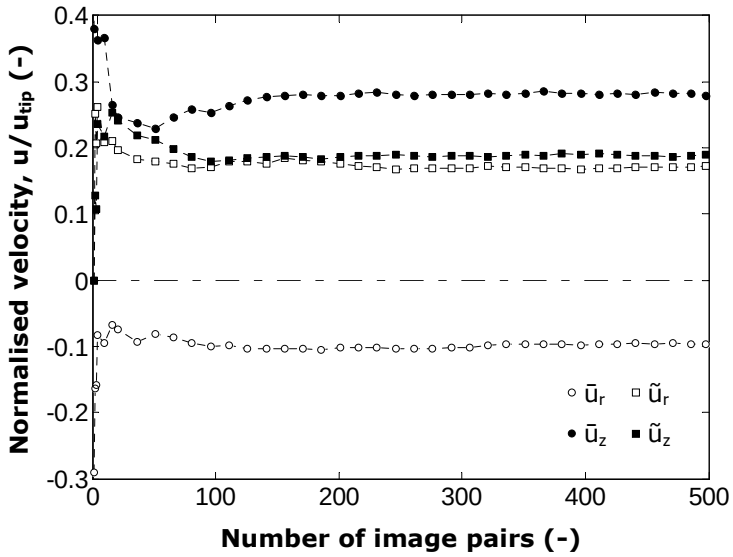

Figure 4.3. Effect of the number of image pairs used on the measured time-averaged and RMS velocity components within a typical sample grid cell: $\vartheta = 30^o$, $z = 0.6\ H$, $r = 0.9\ R$.

points in the flow using 400 image pairs instead of 500 produced variations generally less than 2% in the mean velocities and less than 1% in the RMS velocities.

Using 500 image pairs, two-dimensional maps of the mean radial-axial liquid velocity $\overline{u}_{rz}$ are presented in **Figure 4.4** for all of the 17 planes investigated at different azimuthal positions, where the velocities are normalised by the impeller tip speed $u_{tip} = \pi ND$. As suspected, as ϑ sweeps the sector between the two baffles from 5º to 85º, the planar flow field exhibits

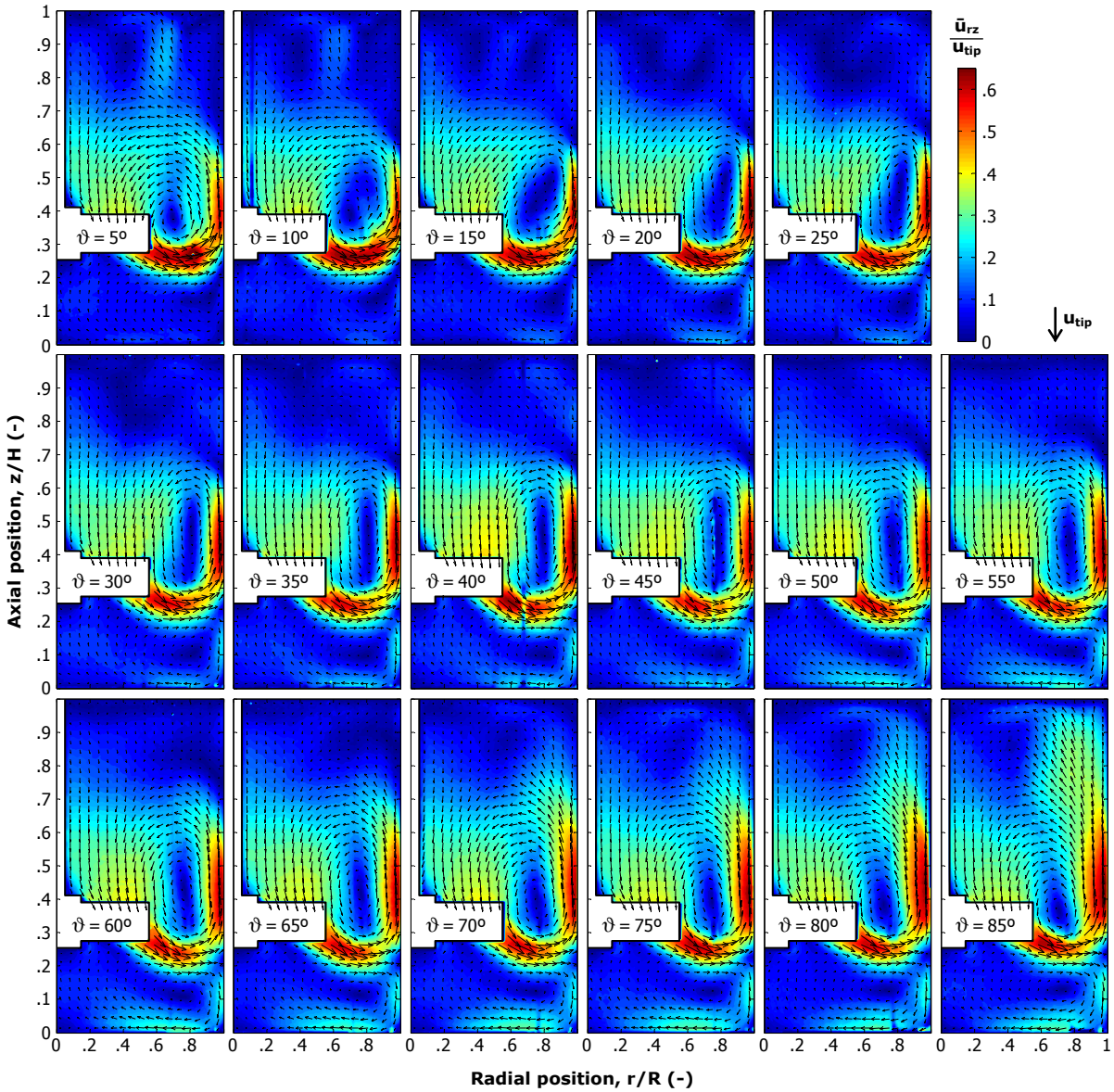

Figure 4.4. Effect of the azimuthal position of the measurement plane on the measured mean radial-axial velocity field.

increasingly significant differences. In each plane, the velocity map shows the usual flow pattern observed in previous studies of a down-pumping PBT using ensemble-averaged data (see for example, Aubin *et al.*, 2001; Jaworski *et al.*, 2001). The observed flow field with a primary anti-clockwise flow loop around the impeller and the bulk region, and a slower less prominent clockwise flow loop underneath the impeller is typical of a down-pumping PBT with a high D/T ratio. Fluid velocities are relatively high above the impeller (> 0.35 u_{tip}) and around the eye of the primary flow loop, where a clearly visible flow region shaped in the form of a 'J' is established which includes the highest velocities (> 0.45 u_{tip}). However, in the upper part of the tank at $z > 0.8\,H$ the flow is relatively quiescent for $\vartheta < 80^o$, with velocities around 0.1 u_{tip}. Underneath the impeller where the flow is reversed, velocities are also around 0.1 u_{tip} creating a region where solid suspension has proved arduous, as shown in Chapters VII-IX.

Rotating the laser plane from $\vartheta = 5^o$ to $\vartheta = 85^o$ reveals gradual transformations in the 2D flow field including changes in the shape and size of the primary loop, the position of its centre, the flow discharge angle, the velocity magnitude in the impeller inlet region, the velocities around

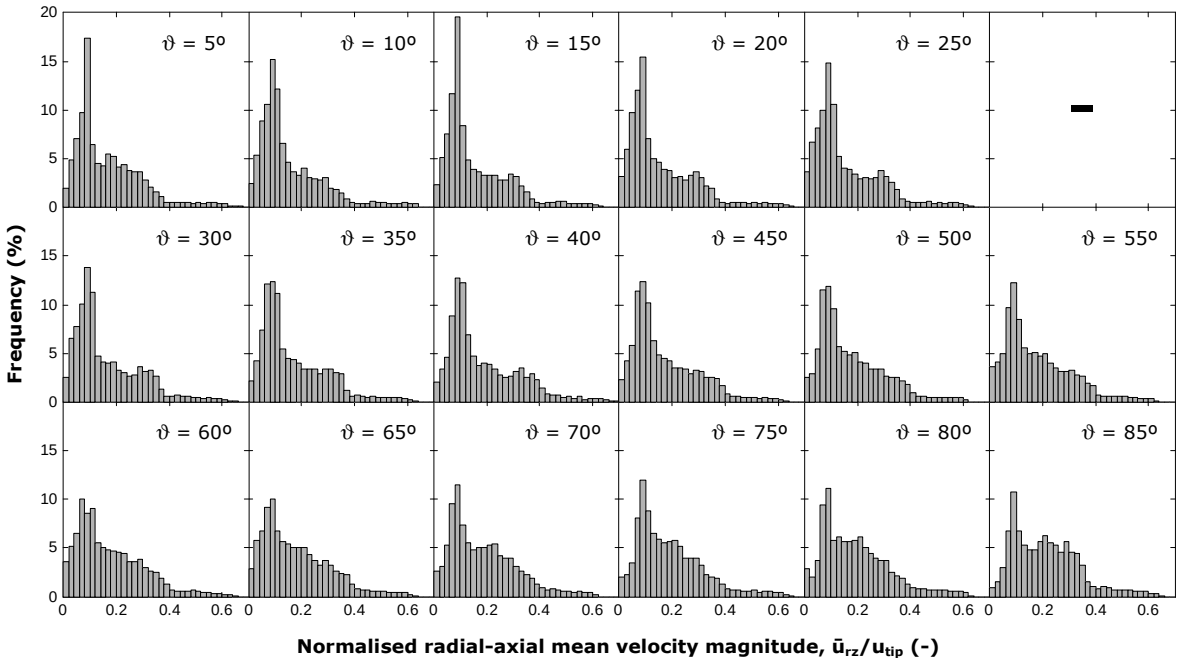

Figure 4.5. Effect of the azimuthal position of the measurement plane on the 2D distribution of the normalised mean radial-axial velocity magnitude.

the lower flow loop and the flow field in the upper part of the tank. **Figure 4.5** shows how the angular position of the measurement plane influences the distribution of the magnitude of the mean 2D velocity in the plane. The distribution gradually changes shape as ϑ varies from 5º to 85º, so that ultimately considerable differences are observed between extremity planes.

An average (weighted by grid cell volume) of all the mean 2D velocity magnitudes measured in each plane, showed that the plane with the lowest average liquid velocity was at $\vartheta = 10º$ (0.16 u_{tip}) while the plane at $\vartheta = 85º$ had a 50% faster average velocity (0.24 u_{tip}). It should be mentioned that this weighted velocity average, normalised by u_{tip}, has been assumed in the literature to be virtually unaffected by the position of the laser plane, so that it has been proposed as an agitation index for characterising global impeller effectiveness (Mavros and Baudou, 1997; Aubin *et al.*, 2001). However, Mavros and Baudou (1997) who originally proposed such an index used it to compare different vessel configurations where all measurements had been made at $\vartheta = 45º$, but they did point out that such an index may be affected by the azimuthal position of the measurement plane. The results presented here show that such an index is indeed a significant function of ϑ and, therefore, 2D comparisons using this criterion should not be made when measurements pertain to different planes.

Quantitative details of the effects observed above are presented in **Figure 4.6** where radial and vertical profiles of the two measured mean velocity components $\overline{u}_r$ and $\overline{u}_z$ are plotted for three different values of ϑ. The radial profiles depicted in **Figure 4.6a** show the effects of the azimuthal position of the measurement plane on both the radial and axial mean velocity components at three different heights in the vessel, i.e., just below the impeller blade at $z = 0.26\ H$, just above the impeller blade at $z = 0.40\ H$, and halfway between the upper edge of the impeller blade and the free surface at $z = 0.70\ H$. In the horizontal plane at $z = 0.26\ H$, away from the wall $\overline{u}_z$ is virtually the same for the two vertical planes on either side of a baffle (i.e., $\vartheta = 5º$ and $\vartheta = 85º$), while for $\vartheta = 45º$, $\overline{u}_z$ is generally higher, up to 40% close to the tip of the impeller. In the same horizontal plane, this effect is reversed in the case of $\overline{u}_r$ which is generally lower for $\vartheta = 45º$. These two observations confirm that the flow discharge angle changes significantly with ϑ, as pointed out earlier in relation to **Figure 4.4**. The maximum angle of discharge detected in the vessel is 40º and is located in the 45º plane close to the tip of the impeller blades. In the planes at $\vartheta = 5º$ and $\vartheta = 85º$ the maximum discharge angle is 29º and 32º, respectively, also occurring near the tip of the impeller. In the horizontal

plane at $z = 0.40\ H$, the radial velocities are close to zero and $\overline{u}_z$ is higher for $\vartheta = 45^o$, except close to the wall. At $z = 0.70\ H$, fluid motion is relatively slow in the 45º plane, significantly faster in the 5º plane and much faster in the 85º plane where $\overline{u}_z$ reaches a positive value of $0.37\ u_{tip}$ at a short distance from the wall. Such dissimilarities indicate that the 2D flow structure in the upper reaches of the tank is strongly dependent on ϑ. However, considering the entire set of radial profiles the effect of ϑ seems to be generally negligible when $r < 0.3\ R$, i.e., sufficiently far from the baffles where probably the assumption of axial symmetry is still reasonable.

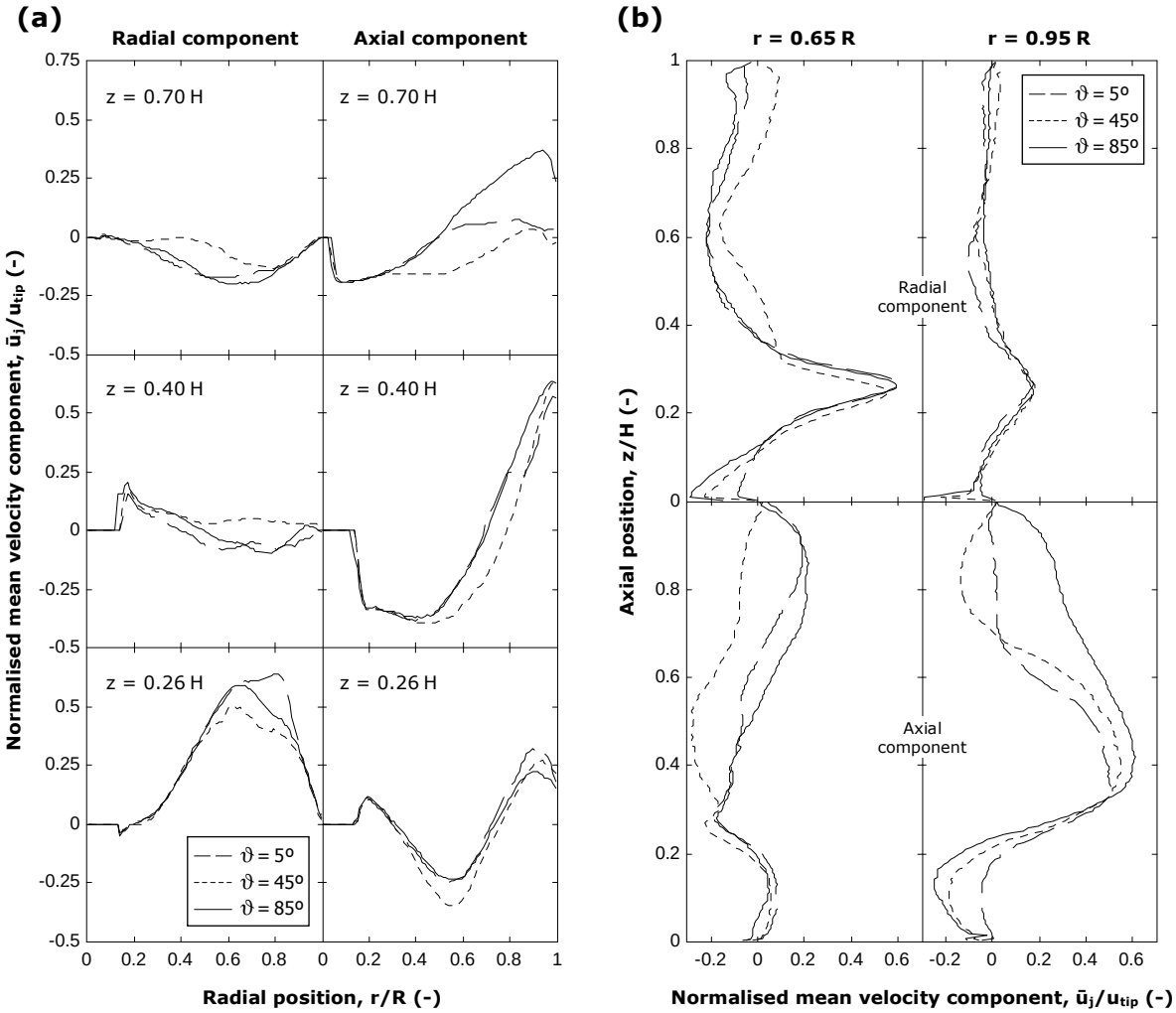

Figure 4.6. Normalised profiles of the radial and axial velocity components $\overline{u}_r$ and $\overline{u}_z$ in the vessel: (a) radial profiles at three different levels; (b) vertical profiles at two different radial positions.

The effects of the measurement plane position on the mean axial velocity profiles, are depicted in **Figure 4.6b** at the radial positions $r = 0.65\,R$ and $r = 0.95\,R$. Whilst there are some significant differences in the axial profiles of $\overline{u}_r$ especially at $r = 0.65\,R$, the axial profiles of $\overline{u}_z$ are strongly affected by ϑ showing large differences between planes; for example, in the vicinity of the wall at $z = 0.8\,H$, the axial velocity $\overline{u}_z$ is negative in the 45º plane ($-0.13\,u_{tip}$), almost zero at $\vartheta = 5º$, and positive in the 85º plane ($0.30\,u_{tip}$).

Whilst the 45º plane has usually been chosen to conduct PIV studies, more recently, the plane 5º in front of a baffle has been preferred to avoid light obstruction by the baffle in front of the camera (Chung *et al.*, 2009; Gabriele *et al.*, 2008). It should be noted that in practice this plane could in fact be situated either on the windward side ($\vartheta = 85º$) or the leeward side ($\vartheta = 5º$) of the baffle, depending on the direction of impeller rotation. Therefore, such a distinction needs to be always clearly made since the results obtained here show important differences in the flow properties between these two planes.

4-4.2 Flow number

Using the 2D approximation of ϑ-invariant mean velocity for each plane, values of $Q_1^{(2D)}$, $Q_2^{(2D)}$ and $Q_3^{(2D)}$ were computed in each measurement plane at a short distance away from the edge of the impeller blade $d_1 = d_2 = 1.14$ mm and $d_3 = 1.86$ mm (see **Figure 4.2**). These flowrates were used to obtain the approximated flow numbers which are plotted as a function of ϑ in **Figure 4.7**, i.e., $Fl_1^{(2D)}$, $Fl_2^{(2D)}$, $Fl_3^{(2D)}$ and $Fl^{(2D)} = Fl_2^{(2D)} + Fl_3^{(2D)}$. Surprisingly, for every interrogated plane, the flow number related to the inlet flow $Fl_1^{(2D)}$ is significantly higher than the flow number related to the discharge flows, $Fl^{(2D)}$. This effect is justified in relation to a single plane as there is no theoretical prerequisite for the 2D mass flow to be balanced in any vertical *rz* plane; i.e., the flow can be predominantly upwards in one plane and predominantly downwards in another. Moreover, the global flow number obtained from the total axial and radial discharge using the data from the 17 measurement planes ($Fl = 0.67$), which is consistent with published values of Fl (Hemrajani and Tatterson, 2004), does not counterbalance the flow number at the inlet ($Fl_1 = 0.81$). This can be attributed to the effect of the finite distances d_1, d_2 and d_3 at which the flow numbers in question were determined; these create gaps in the cylindrical envelope bounding the control volume containing the agitator. In order to examine such an effect, the flowrates Q_1, Q_2 and Q_3, were recalculated extending the three surfaces of integration to close such gaps, as shown in **Figure 4.8**.

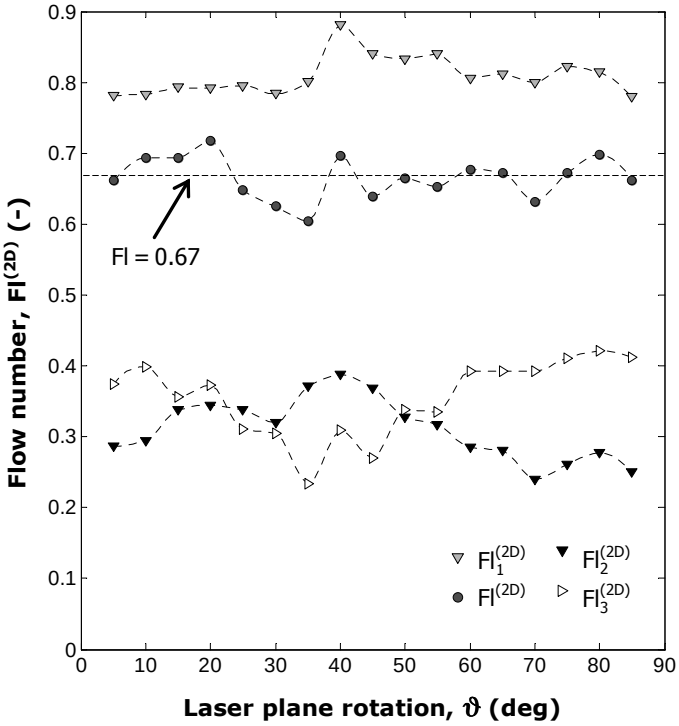

Figure 4.7. Effect of the azimuthal position of the measurement plane on the flow number obtained from the 2D approximation. Note $Fl^{(2D)} = Fl_2^{(2D)} + Fl_3^{(2D)}$.

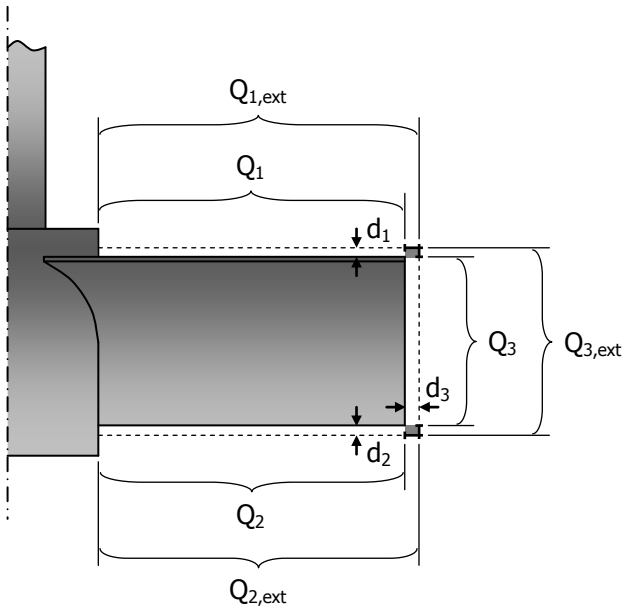

Figure 4.8. Schematic illustration of flowrates $Q_{1,ext}$, $Q_{2,ext}$ and $Q_{3,ext}$ used for correct verification of the mass balance around the agitator.

With this modification, the error in the mass balance between the in-flow ($Q_{1,ext}$ = 0.00405 m^3 s^{-1}) and the out-flows ($Q_{2,ext} + Q_{3,ext}$ = 0.00389 m^3 s^{-1}) was reduced down to only 4%. This highlights the importance of measuring the flow number as close as possible to the impeller tip.

While the radial and axial contributions to the flow number *Fl* are comparable (Fl_2 = 0.31 and Fl_3 = 0.36), **Figure 4.7** shows that the approximated values $Fl_2^{(2D)}$ and $Fl_3^{(2D)}$ fluctuate differently and considerably with ϑ, each making a significant contribution to $Fl^{(2D)}$; in fact, for $\vartheta < 15^o$ and $\vartheta > 55^o$ the radial discharge exceeds the axial discharge by a significant margin, with $Fl_3^{(2D)}$ being up to 67% higher than $Fl_2^{(2D)}$ at $\vartheta = 85^o$ where it exhibits one of its smallest values. If images are collected in planes distant from the baffles ($30^o < \vartheta < 50^o$) $Fl_2^{(2D)}$ is maximum and its value can be up to 64% higher than $Fl_3^{(2D)}$ which is at its minimum. However, the total approximated flow number, $Fl^{(2D)}$, does not appear to be much affected by ϑ, as it fluctuates around its average value of 0.67, with a standard error < 5%. These results show the importance of including both the radial and axial contributions in the estimation of the flow number of an impeller generating mixed flow whether using the ϑ-invariance approximation or 3D data from all the planes. Neglecting the radial contribution here would lead to an underestimation of ~ 40-60%. Such an omission might be at least partly responsible for the significant discrepancies in the *Fl* values reported in the literature.

4-4.3 Turbulent kinetic energy

The 2D contours of Turbulent Kinetic Energy are also affected by the azimuthal position of the measurement plane, as demonstrated in **Figure 4.9**. The energy values were calculated using Eq. (4.11) and normalised by the square of the impeller tip speed. The highest TKE values are generally localised in the radial impeller discharge stream, at the bottom of the primary flow loop and, for a few planes, also at a short distance from the wall. In the regions just above and just below the impeller the energies measured are not significantly affected by the laser plane position; however, the lateral discharge region is characterised by a decrease in the normalised TKE from ~ 0.095 to ~ 0.07 when ϑ varies from 5º to 85º. The zone nearer the wall ($r \sim 0.85\,R$) around the impeller mid-plane presents the highest azimuthal gradients of TKE. The normalised energy values measured there are 0.05-0.06 for $\vartheta > 25^o$ and up to double behind the baffles (ϑ = 5-10º) with a maximum of 0.11 at $\vartheta = 5^o$ which is also the greatest value recorded within the whole vessel. When ϑ increases, the upper half of the tank

shows first a localised rise in TKE at the wall (ϑ = 5-40º), followed by a more uniform redistribution of the energy values (ϑ = 50-85º). The TKE distribution in the planes behind the baffle (i.e., low ϑ) is markedly different from that in the planes in front of the baffle (i.e., high ϑ). Minor variations of TKE are also discernible close to the base of the vessel.

Although the baffles used were transparent, the effect of the edges of the baffle interposed between the laser plane and the camera are visible in **Figure 4.9**, which is hard to avoid. Due

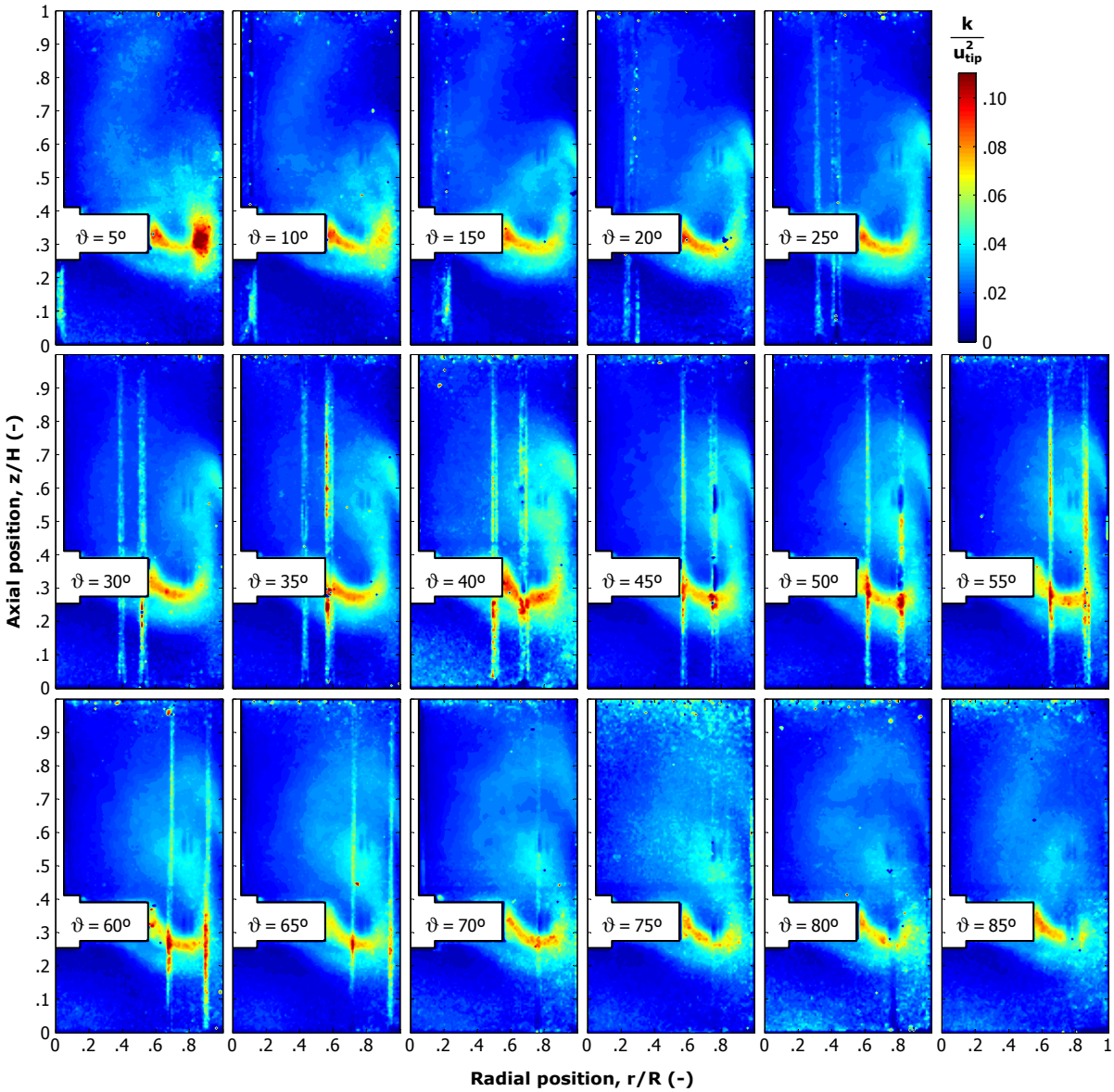

Figure 4.9. Effect of the azimuthal position of the measurement plane on the radial-axial maps of normalised turbulent kinetic energy.

to the statistical nature of the RMS velocities, these optical artefacts are not negligible as in the case of the velocity plots shown in **Figure 4.4**. If desired, it would be possible in principle to filter out such noise by further image processing and data manipulation.

4-4.4 Mass continuity

Finally the overall accuracy and reliability of the measurements was examined by verifying the mass continuity throughout the vessel. The radial velocity component averaged over the cylindrical surface S_r is plotted in **Figure 4.10a**, as a function of the radius r_s. Outside the impeller region, the average normalised radial velocity is vanishingly small, with values well below 0.01 u_{tip}. Where the cylindrical surface S_r intersects with the agitator PIV data are not

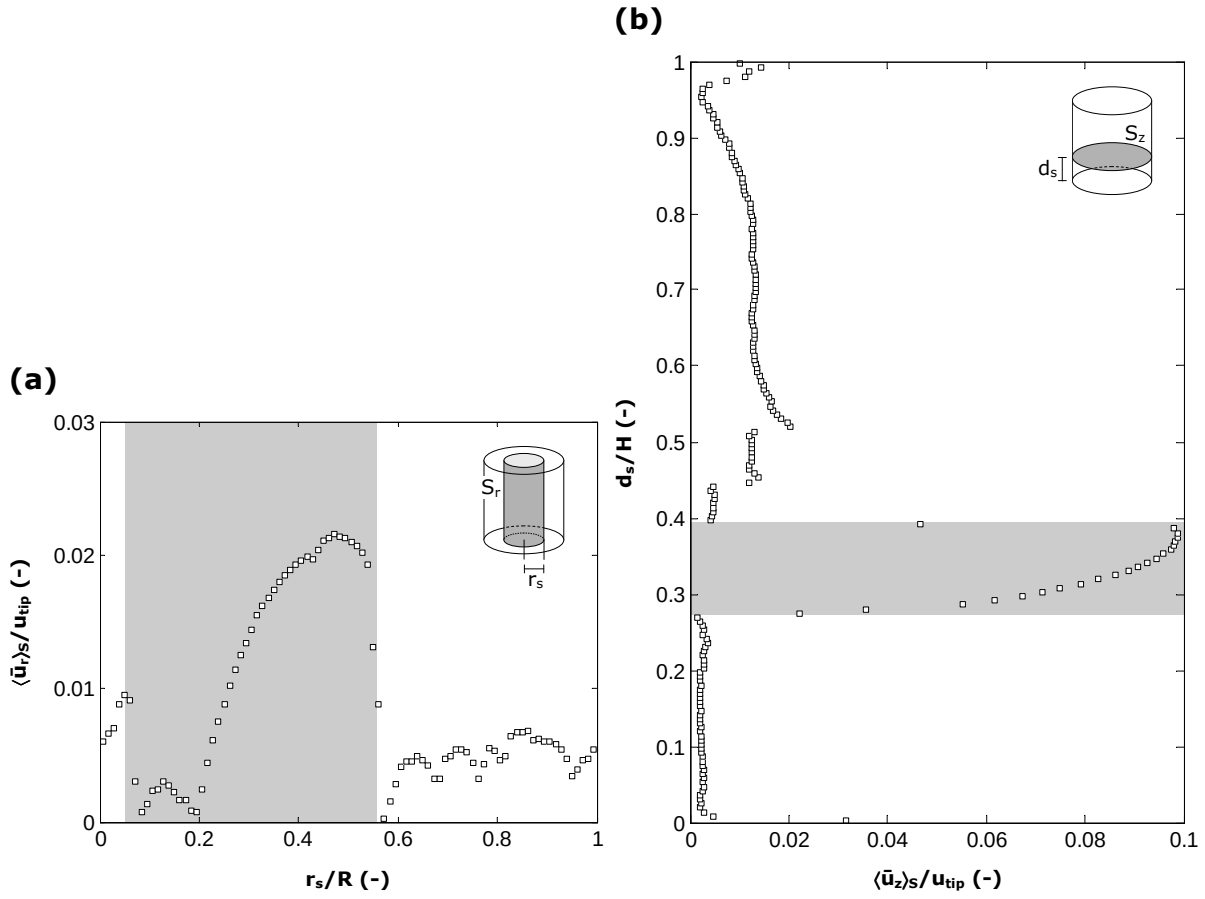

Figure 4.10. Mass continuity validation: (a) normalised mean radial velocity averaged over surface S_r as a function of the radius of S_r; (b) normalised mean axial velocity averaged over surface S_z as a function of the position of S_z. The shaded areas are regions of intersection of S_r or S_z with the impeller.

available, and therefore the error in mass continuity is higher but remains quite small, mostly below 0.02 u_{tip}. A similar plot is shown in **Figure 4.10b** for the axial velocity component averaged over the vessel cross-section S_z. Again, outside the impeller region such an average velocity is close to zero, generally less than 0.02 u_{tip}. In the region affected by the presence of the impeller, however, the mass continuity error increases much more this time almost reaching 0.1 u_{tip}. The impeller swept region which is inaccessible to the laser plane is dominated by axial flow, thus, the deficiency in PIV data in this region causes such a larger error in the mass continuity in the axial direction (when averaging over S_z) than in the radial direction (when averaging over S_r).

4-5 Conclusions

Two-dimensional PIV experiments have been successfully conducted in multiple vertical planes passing through the axis of a fully-baffled vessel agitated by a PBT and operating in the turbulent flow regime. By considering flow through horizontal and cylindrical hyperplanes introduced numerically in the vessel, the overall accuracy and reliability of the PIV measurements has been demonstrated by showing that the mass continuity is verified throughout the vessel.

With the laser sheet set at 17 different azimuthal positions, important details of the 3D Eulerian fields of velocity and turbulent kinetic energy have been obtained. Rotation of the laser plane causes a gradual variation of the measured 2D flow properties ultimately leading to considerable transformations in the velocity distribution in the plane, the shape of the primary flow loop, the position of its centre, the flow discharge angle, the velocity magnitude in the impeller suction, the velocities around the secondary flow loop, the direction of the flow in the upper part of the tank, and the turbulent kinetic energy distribution. The measurement planes at 5° either side of a baffle exhibit the largest differences in flow properties, the plane on the windward side of the baffle (85°) containing the highest velocities. The turbulent kinetic energy appears to be more uniformly distributed in this plane, while the highest TKE values are detected in the 5° plane on the leeward side of the baffle around the impeller discharge region and near the wall.

The agitation index proposed in the literature, based on the average (weighted with the

volume of the grid cells) of the mean 2D velocity magnitude measured in each plane, appears to be unreliable for describing impeller effectiveness as it can vary by up to 50% between measurement planes. On the other hand, using the 2D approximation of the ϑ-invariant mean velocity for each vertical plane, the obtained flow number $Fl^{(2D)}$ is not significantly affected by the rotation of the laser plane, as it fluctuates around its average value (Fl = 0.67) with a standard error < 5%. The results have shown for the type and size of impeller used here, the importance of including both the axial and radial discharge contributions for an accurate evaluation of the flow number.

The findings of this study suggest, overall, that the ϑ-invariance of the flow field cannot be assumed in a baffled configuration without a considerable loss of information. As a result, instead of using a single vertical plane, most of the results obtained by PEPT and shown in Chapters VI-IX will be presented as azimuthally averaged Eulerian maps or profiles, which contain the whole 3D information.

Notation

Roman letters

D	Impeller diameter	m
d	Distance from the edge of impeller blade	m
d_s	Axial position of surface S_z	m
Fl	Flow number	-
$Fl^{(2D)}$	Approximated flow number	-
H	Vessel fill height	m
k	Turbulent kinetic energy	$m^2\ s^{-2}$
N	Impeller rotational speed	s^{-1}
Q	Impeller pumping rate	$m^3\ s^{-1}$
$Q^{(2D)}$	Approximated impeller pumping rate	$m^3\ s^{-1}$
r	Radial distance	m
R	Vessel radius	m
Re	Impeller Reynolds number (ND^2/ν)	-
r_s	Radius of surface S_r	m
S	Surface area	m^2
S_r	Vertical cylindrical surface area	m^2
S_z	Horizontal planar surface area	m^2
T	Vessel diameter	m
$\overline{\mathbf{u}}$	3D mean velocity vector	$\lvert m\ s^{-1} \rvert$
u_j	Instantaneous velocity component	$m\ s^{-1}$
$\overline{u}_j$	Mean velocity component	$m\ s^{-1}$
u'_j	Fluctuating velocity component	$m\ s^{-1}$
$\widetilde{u}_j$	RMS velocity component	$m\ s^{-1}$
$\overline{u}_r \quad \overline{u}_z$	Mean radial and axial velocity components	$m\ s^{-1}$
$\overline{u}_{rz}$	Mean radial-axial velocity magnitude	$m\ s^{-1}$
u_{tip}	Impeller tip speed	$m\ s^{-1}$
$\widetilde{u}_\vartheta \quad \widetilde{u}_r \quad \widetilde{u}_z$	Cylindrical components of RMS velocity	$m\ s^{-1}$
z	Axial distance	m

Greek letters

ε_T	Specific energy dissipation rate	$m^2\ s^{-3}$
λ_K	Kolmogorov length scale	m
ν	Kinematic liquid viscosity	$m^2\ s^{-1}$
ϑ	Azimuthal position of measurement plane	deg

Abbreviations

2D	Two-dimensional
3D	Three-dimensional
CCD	Charge-coupled device
IA	Interrogation area
PBT	Pitched blade turbine
PEPT	Positron emission particle tracking
PIV	Particle image velocimetry
RMS	Root mean square
TKE	Turbulent kinetic energy

Chapter V
PEPT compared to PIV and PLIF

Abstract

Three-dimensional Eulerian velocity measurements made by positron emission particle tracking (PEPT) in a mechanically agitated cylindrical vessel are compared directly with those performed in multiple planes via particle image velocimetry (PIV) using the same mixing equipment and fluid. Additionally, cavern boundaries in a viscoplastic fluid with an apparent yield stress, which were visually detected using a planar laser induced fluorescence (PLIF) technique, are compared with PEPT data collected on the same non-Newtonian system. This study aims to investigate possible minor local discrepancies obtained by two different measurement techniques and develop an understanding of the reasons behind their existence. Such a detailed and pointwise comparison between techniques will allow PEPT to be reliably used to obtain accurate data throughout the entire complex three-dimensional flow field in a range of mechanically agitated, laminar or turbulent, single- or multi-phase systems previously not amenable to quantitative analysis.

5-1 Introduction

Previously performed comparisons between the PEPT and PIV techniques using water involved optical measurements collected in one single plane and azimuthally-averaged maps obtained from tracking the whole 3D system (Pianko-Oprych *et al.*, 2009). The minor discrepancies in the profiles of axial velocity, close to the trailing vortex system of the impeller, were attributed to the different type of data collected and the different way of ensemble-averaging of the two techniques. In a baffled configuration, as demonstrated in Chapter IV, rotation of the laser plane causes a significant variation of the optically measured 2D flow properties ultimately leading to considerable transformations in the planar flow field. If axial symmetry of the flow field cannot be assumed, intrinsic differences are to be expected when comparing optical data collected in one single 2D vertical plane and azimuthally averaged data related to the whole 3D system.

In Section 3-5.3 the comparison between Lagrangian tracking by PEPT and the well-established optical technique of PIV was refined by using azimuthally-averaged 3D data for both methods. Results showed an excellent agreement between the two methods; however, due to the importance of such comparison, a detailed study of the differences in the flow fields obtained with these two techniques in multiple vertical planes is still needed.

In the mixing of viscoplastic fluids, which exhibit an apparent yield stress, the agitator creates a cavern within which fluid is in flow, but in the bulk where the shear stresses are below the yield stress the fluid is stagnant (Adams and Barigou, 2007; Adams *et al.*, 2008; Adams, 2009; Elson, 1990; Nienow and Elson, 1988). In this case, the PEPT particle tracer visits only a portion of the vessel volume delineating the boundaries of the cavern formed as already shown in **Figure 3.4b**. Such boundaries can also be detected in a transparent fluid by using the now well established optical PLIF technique.

In this chapter, the reliability of the PEPT technique is tested firstly in a non-Newtonian environment by comparing cavern boundaries optically visualised via PLIF with those detected by PEPT Lagrangian tracking. Secondly, Eulerian flow fields obtained by PEPT in a Newtonian turbulent fluid are directly compared with 2D PIV measurements performed in the same system. For each method, radial-axial velocities were determined in 17 vertical planes located at 5° intervals between two adjacent baffles.

5-2 Experimental procedures

5-2.1 Cavern boundary visualisation

An aqueous solution of 0.1 wt% carbopol 940 was used for both the experimental PLIF visualization of caverns as well as PEPT Lagrangian tracking. The pH of this solution was adjusted to 4.6 to give a viscous fluid whose rheology was described by a Herschel-Bulkley model; i.e., the shear stress, τ, as a function of the shear rate, $\dot{\gamma}$, is given by

$$\tau = \tau_y + k\dot{\gamma}^n \tag{5.1}$$

where τ_y is the yield stress, k is fluid consistency coefficient and n is the flow behaviour index.

The mixing vessel used was a flat-bottom cylindrical glass tank of diameter T = 150 mm, was equipped with four baffles of width 0.1 T and thickness 0.01 T, and was stirred by a six-bladed 45º down-pumping pitched-blade turbine of diameter D = 0.33 T and height 0.08 T. The off-bottom clearance of the PBT was set at 0.33 T, and the fluid height was set at $H = T$. The vessel was located inside a square glass tank which, during the PLIF experiments, was filled with water to minimise light distortion. Both PLIF and PEPT experiments were conducted with an impeller rotational speed of N = 3.33 s^{-1} corresponding to an impeller tip speed of 0.52 m s^{-1}.

PLIF measurements were conducted using a Nd:YAG 532 nm pulsed laser (New Wave Research Inc., USA) and a CCD camera (PowerView Plus, TSI Inc., USA) capable of capturing 30 images per second at a resolution of 2048×2048 pixels. Frame and laser sequencing were controlled by a TSI Laserpulse 610035 synchronizer and a workstation running TSI Insight 9.0 software. A small volume (5 ml) made up of a 5 mg of fluorescent Rhodamine 6G tracer in 1 l of test fluid, was injected at a point just above the impeller blades. By firing a laser sheet onto the vessel, the process of cavern formation and fluid mixing within was captured by the CCD camera at a rate of 1 frame per second. The final vertical cross-sectional area of the caverns was stored electronically.

PEPT experiments were performed by using a neutrally-buoyant resin tracer of 400 μm diameter labelled with ^{18}F. The PEPT runtime was 6 h, long enough to allow the Lagrangian tracer to reach all regions of the cavern including those close to the cavern boundary where, due to the poor mixing, the probability of visit can be very low.

In order to avoid entrapment of air bubbles which can affect the fluid rheology, a fresh aliquot taken from a large batch of carbopol solution was transferred to the mixing vessel for each experimental run before adjusting the pH. For both measurements by PEPT and PLIF, the pH was adjusted with particular caution, since the rheology of such a solution is highly sensitive to pH. Nevertheless, in order to verify that the fluids examined by PLIF and PEPT had effectively the same characteristics, fluid samples were extracted from the cavern region at the end of each experiment, and their rheology measured via parallel plate viscometry using a stress controlled rheometer (AR-1000, TA Instruments). The obtained rheograms showing the Herschel-Bulkley behaviour of Eq. (5.1) are presented in **Figure 5.1**. The discrepancy between the two curves obtained probing the fluids examined by PLIF and PEPT is practically negligible, so that the fluid used for PEPT measurements can be safely considered the same of that used during the PLIF experiments.

5-2.2 Multiplane Eulerian flow fields

The PEPT experiments were carried out in the same mixing vessel described in Chapter IV where the 17 vertical planes had already been investigated by 2D PIV. The glass tank used

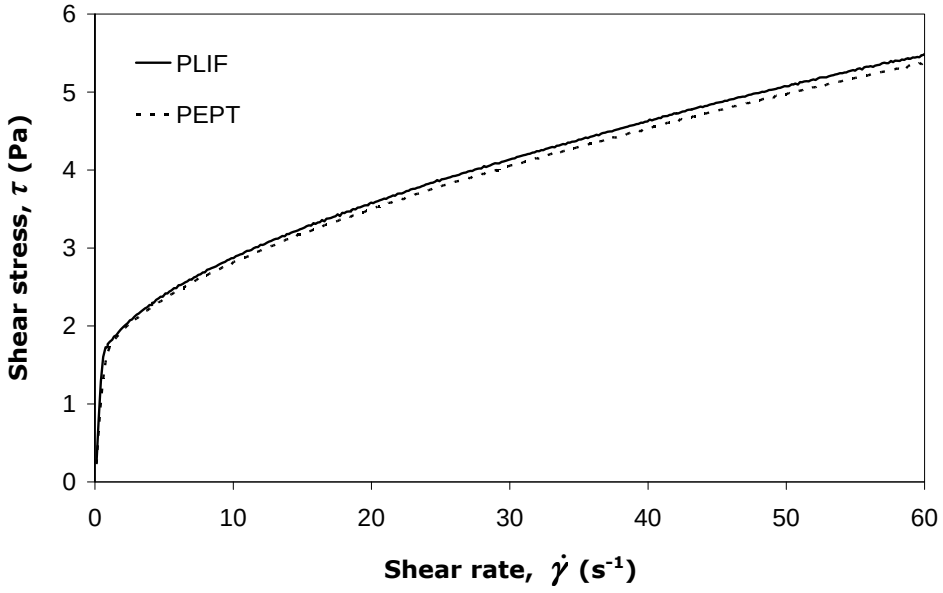

Figure 5.1. Measured variation of the shear stress with the shear rate for samples of aqueous solutions used for the PLIF and PEPT experiments; 0.1 wt% carbopol 940; pH = 4.6.

was flat-bottomed of diameter T = 190 mm, fitted with four equidistant wall baffles of width 0.1 T and thickness 0.01 T and agitated by a six-blade 45º down-pumping pitched-turbine of diameter D = 0.55 T and height 0.12 T. The impeller blades were welded onto the hub which had an external diameter equal to 0.14 T, an internal diameter equal to 0.05 T and a height equal to 0.15 T. The off-bottom clearance of the PBT was set at 0.33 T, and the vessel was filled with water to a height $H = T$.

Both PEPT and PIV experiments were conducted with the impeller rotating at a constant rotational speed of N = 3.67 s^{-1} corresponding to an impeller tip speed of 1.2 m s^{-1}. The value of the impeller Reynolds number ($Re_{imp} = ND^2/\nu$) was 40 000, thus, ensuring fully turbulent conditions. A neutrally-buoyant resin tracer of 400 μm diameter labelled with ^{18}F by Ion Exchange was used to track the water. The PEPT runtime was 6 h, long enough to obtain numerous tracer locations in every region of the vessel. This enabled the full Eulerian description of each thin vertical 5º cylindrical sector of the tank. It should be noted that shorter PEPT experiments allow accurate azimuthally-averaged data to be obtained, as shown in Chapter III, but for accurate plane-by-plane analysis a long experiment is required. The multi-plane PIV measurements conducted using the same fully baffled cylindrical stirred vessel are described in details in Section 4-2.2.

5-3 Comparison PEPT-PLIF

For viscoplastic materials, the boundary of the cavern is normally defined as the locus of points at which the shear stress in the fluid is equal to the apparent yield stress of the material. In such conditions, fluid motion outside the boundaries of the cavern is unexpected. Whereas the injection of the fluorescent Rhodamine tracer is made within the cavern, the only mass transfer phenomenon that allows the dye to reach the static fluid is molecular diffusion.

After injection, the fluorescent dye mixes within the cavern and the volume of dyed fluid slowly expands to colour the whole cavern volume. After this point, additional stirring has no effect on the size and shape of the illuminated vertical cross-section; thus, it can be safely assumed to be equal to the cavern cross-section. The original captured image (**Figure 5.2a**) was processed using digital image elaboration software to give an enhanced image of the cavern (**Figure 5.2b**) where boundaries are clearly identifiable (**Figure 5.2c**).

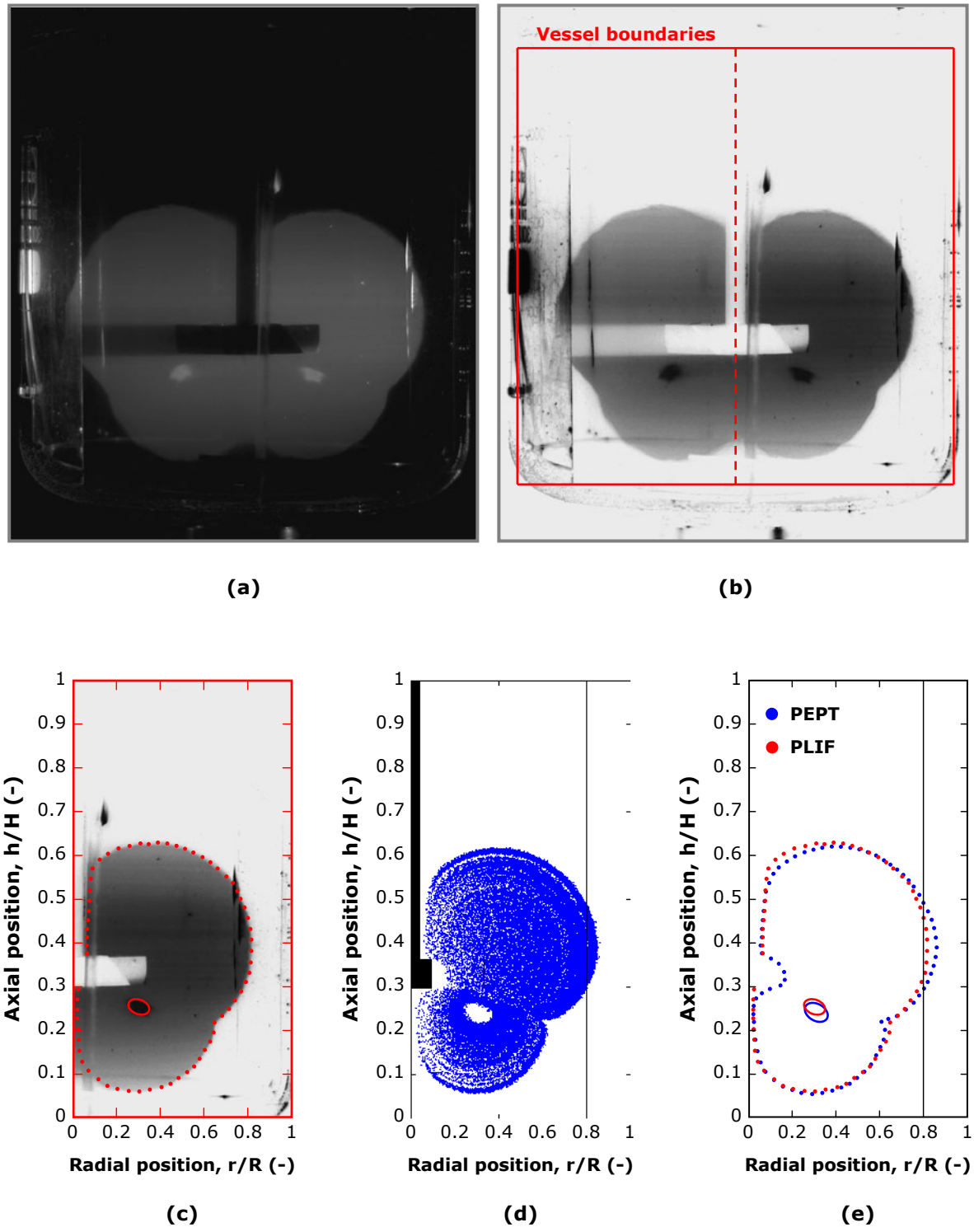

Figure 5.2. Caverns in a Herschel-Bulkley fluid: (a) PLIF original image; (b) processed PLIF image indicating vessel boundaries; (c) cavern boundaries detected by PLIF; (d) locus of PEPT particle tracer locations within cavern; (e) comparison of cavern boundaries detected by PEPT and PLIF.

As discussed in Section 3-3.1 and shown in Appendix A, a PEPT data file is a text file containing four main columns representing the four time-space coordinates of consecutive particle tracer locations. Converting these four columns of numbers to four numerical arrays is the first step of the code written for the Lagrangian -Eulerian analysis. The Lagrangian space information is then converted from Cartesian to Cylindrical coordinates with the origin at the intersection between the axis and the base of the vessel.

As shown in **Figure 5.2a-b**, the cylindrical symmetry in such system is a safe assumption, as the boundaries of the formed cavern are barely affected by the presence of the baffles. It could be said that, with reference to the area of interest, the vessel is virtually unbaffled. Therefore, plotting in a 2D plane the whole array containing the axial tracer coordinate, *h*, against the array containing the radial coordinate, *r*, will result in a radial-axial projection (and hence a section) of the cavern formed around the agitator, as shown in **Figure 5.2d**.

The direct comparison between cavern boundaries obtained by both PEPT and PLIF is finally completed by superimposing the two results in **Figure 5.2e** which shows an excellent agreement between these two methods.

Since the viscosity of the fluid is not known *a priori*, the impeller Reynolds number can not be determined immediately. However, the rheological measurements shown in **Figure 5.1** can be used to estimate the effective viscosity of the fluid, μ_e, defined as the ratio between the effective shear stress, τ_e, and the effective shear rate, $\dot{\gamma}_e$. This allows the Reynolds number to be evaluated as

$$\mathrm{Re}_{imp} = \rho \frac{ND^2}{\mu_e} \tag{5.2}$$

The broadly accepted Metzner-Otto (1957) hypothesis assumes that, in the impeller region, the effective shear rate is proportional to the impeller rotational speed, that is

$$\dot{\gamma}_e = k_s N \tag{5.3}$$

The constant k_s has a value in the range 10-13, slightly dependent on impeller type and size; but for most practical purposes the value of 11 is generally recommended and was used here (Adams and Barigou, 2007). Based on the value of $\dot{\gamma}_e$ calculated via Eq. (5.3), the value of τ_e (and hence μ_e) was determined using the rheogram in **Figure 5.1**, leading to $\mathrm{Re}_{imp} \sim 70$.

5-4 Comparison PEPT-PIV

The information contained in the long Lagrangian trajectory of the neutrally-buoyant PEPT tracer was extracted using the code for the Lagrangian-Eulerian data analysis, as described in Chapter III. Using the cylindrical symmetry of the four sectors generated by the four vertical baffles the whole vessel domain can be reduced to one quarter, namely the volume of fluid comprised within one of the four quadrant defined by two orthogonal vertical planes containing the vessel axis. Therefore, the four fields of Lagrangian velocities contained in the four cylindrical sectors are superimposed to obtain, as an added bonus, a 300 % higher resolution in one quadrant.

In order to obtain Eulerian flow fields in planes spaced at 5º, the 3D cylindrical grid used for the data analysis was defined with 18 cells in the azimuthal direction. The 18th plane ($\vartheta = 0^o$ or $\vartheta = 90^o$), which is not presented here, corresponds to the plane containing the baffle and thus is not accessible by the laser sheet during the PIV data collection (Guida *et al.*, 2010b).

The set of PEPT results are directly compared to the time-averaged PIV velocity components presented in Chapter IV. Both sets of Eulerian velocity data are normalised by the impeller tip speed $u_{tip} = \pi ND$.

The plane by plane comparisons are performed on the basis of four aspects: the modular error in the 2D velocity magnitudes, radial axial velocity vector plots, axial velocity profiles and radial velocity profiles. The modular error of the 2D velocity magnitudes u_{rh} is defined as

$$\varepsilon_m = \frac{\left| u_{rh}^{(PIV)} - u_{rh}^{(PEPT)} \right|}{u_{tip}} = \frac{\left| \sqrt{\left(u_r^{(PIV)}\right)^2 + \left(u_h^{(PIV)}\right)^2} - \sqrt{\left(u_r^{(PEPT)}\right)^2 + \left(u_h^{(PEPT)}\right)^2} \right|}{u_{tip}} \tag{5.4}$$

where the superscripts (PIV) and (PEPT) indicate the technique used to obtained the velocity value. The details of such comparisons are presented in **Figures 5.3-5.19**

Apart from the high turbulence regions, where ε_m reaches values of 0.1, the modular error is generally < 0.02. Whilst excellent visual agreement is obtained between vector plots at each plane, a quantitative assessment can be done on the basis of the axial and radial velocity comparisons. Small discrepancies in both velocity components are discernible throughout the whole vessel but no particular trend can be identified, i.e., neither techniques consistently underestimates or overestimates fluid velocity (radial or axial) at any specific position.

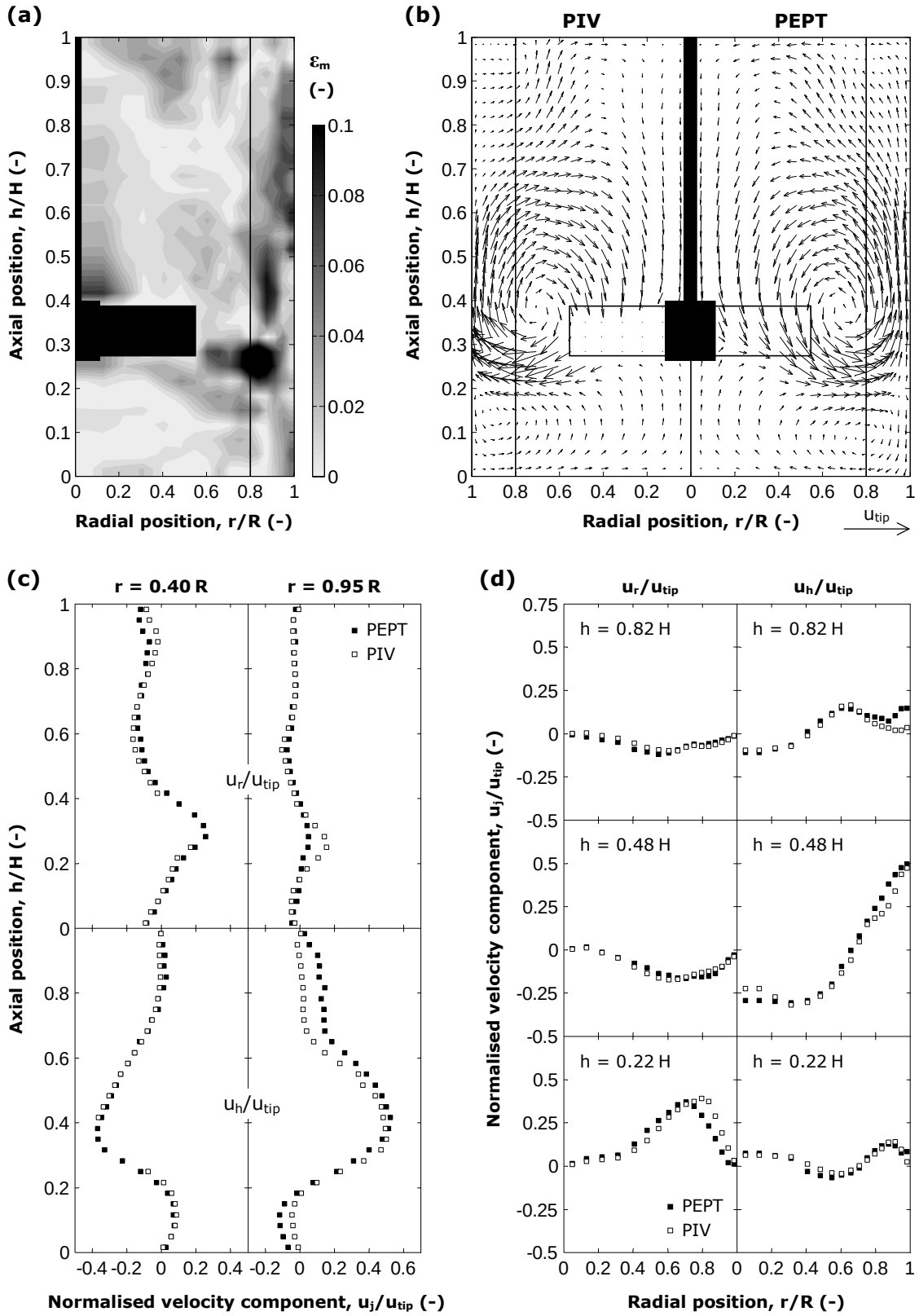

Figure 5.3. Comparison of radial-axial velocity obtained by PEPT and PIV at $\vartheta = 5^{o}$: (a) normalised modular difference; (b) vector plot; (c) normalised vertical and (d) radial profiles.

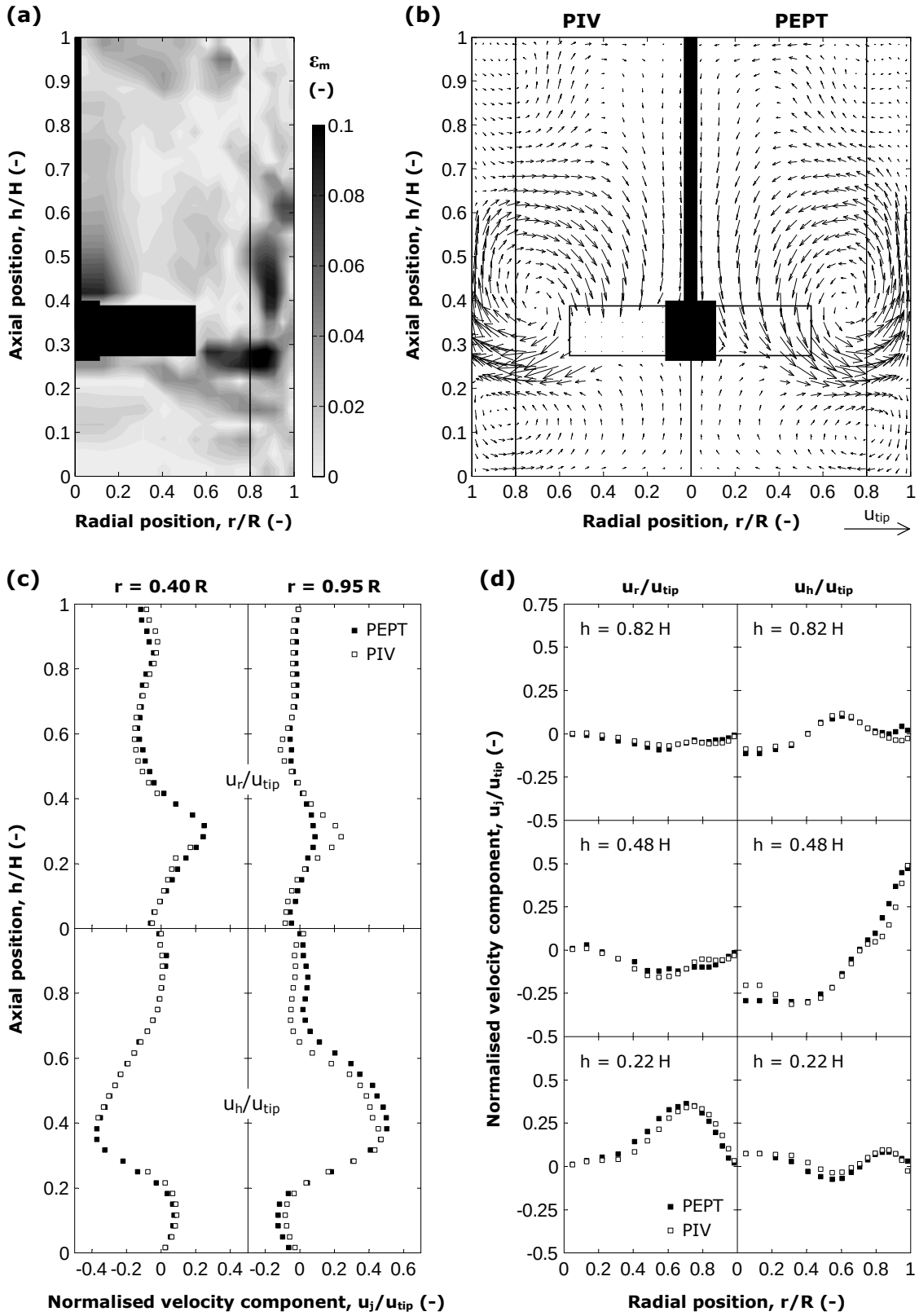

Figure 5.4. Comparison of radial-axial velocity obtained by PEPT and PIV at $\vartheta = 10^{o}$: (a) normalised modular difference; (b) vector plot; (c) normalised vertical and (d) radial profiles.

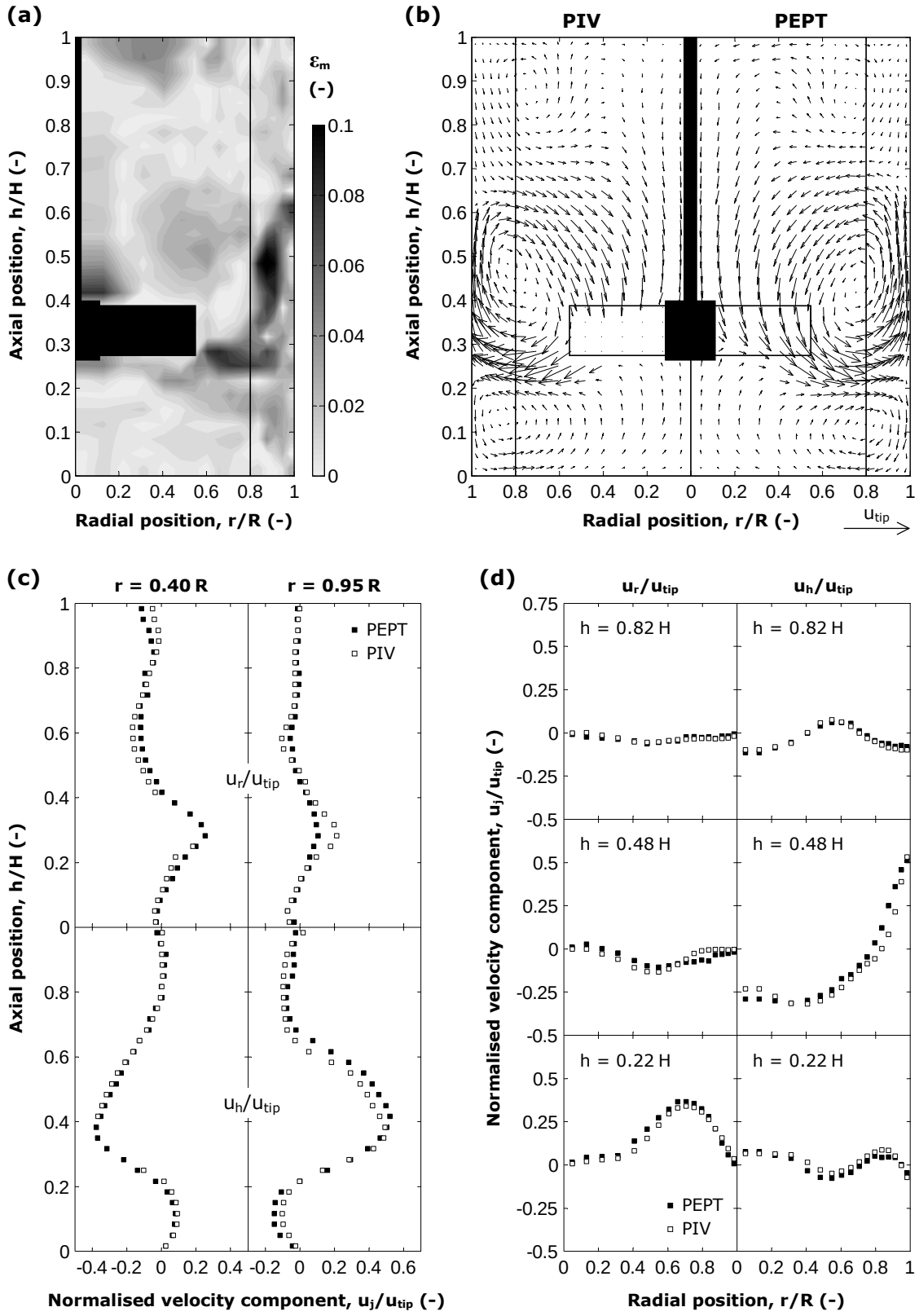

Figure 5.5. Comparison of radial-axial velocity obtained by PEPT and PIV at $\vartheta = 15^{o}$: (a) normalised modular difference; (b) vector plot; (c) normalised vertical and (d) radial profiles.

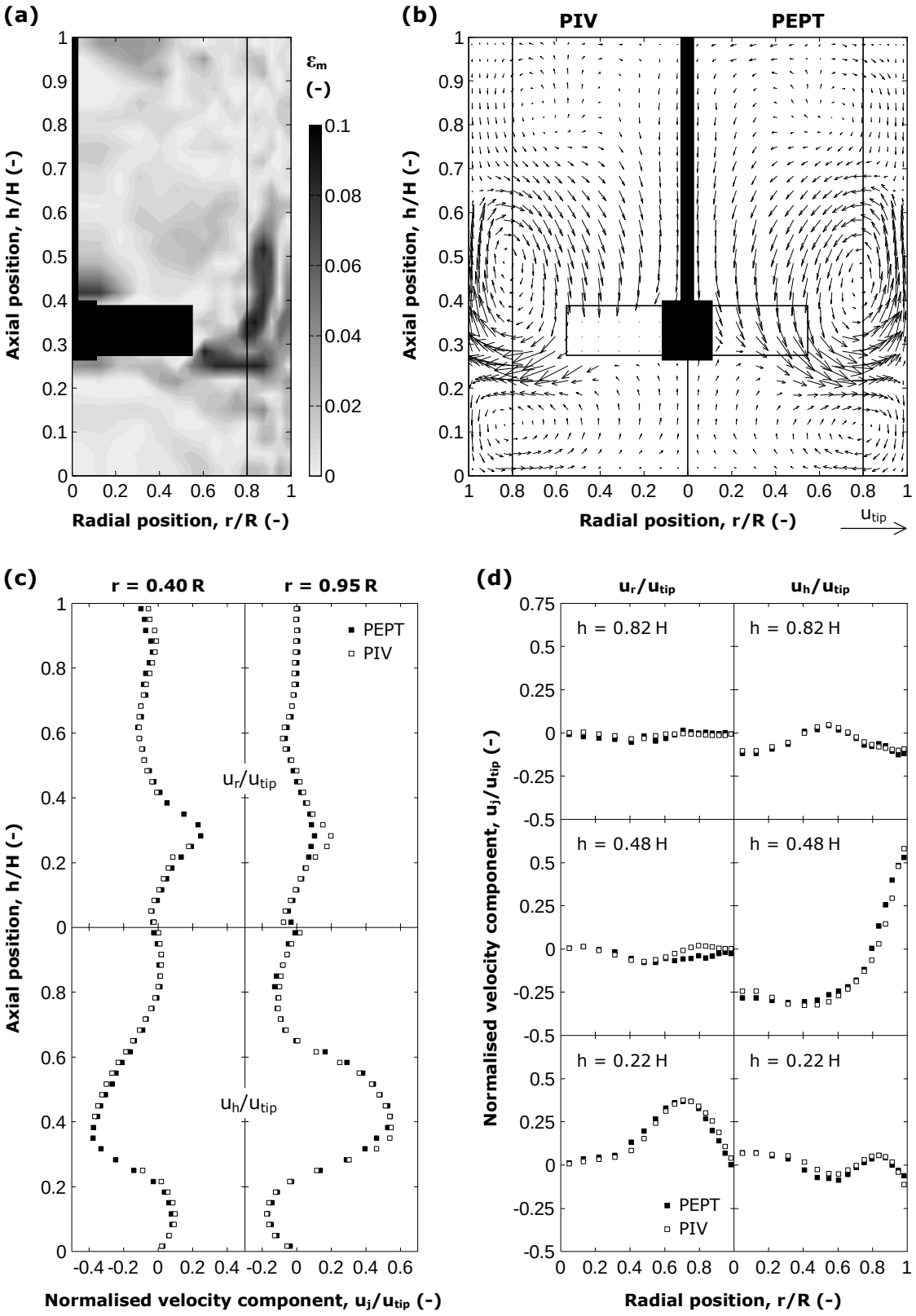

Figure 5.6. Comparison of radial-axial velocity obtained by PEPT and PIV at $\vartheta = 20^{o}$: (a) normalised modular difference; (b) vector plot; (c) normalised vertical and (d) radial profiles.

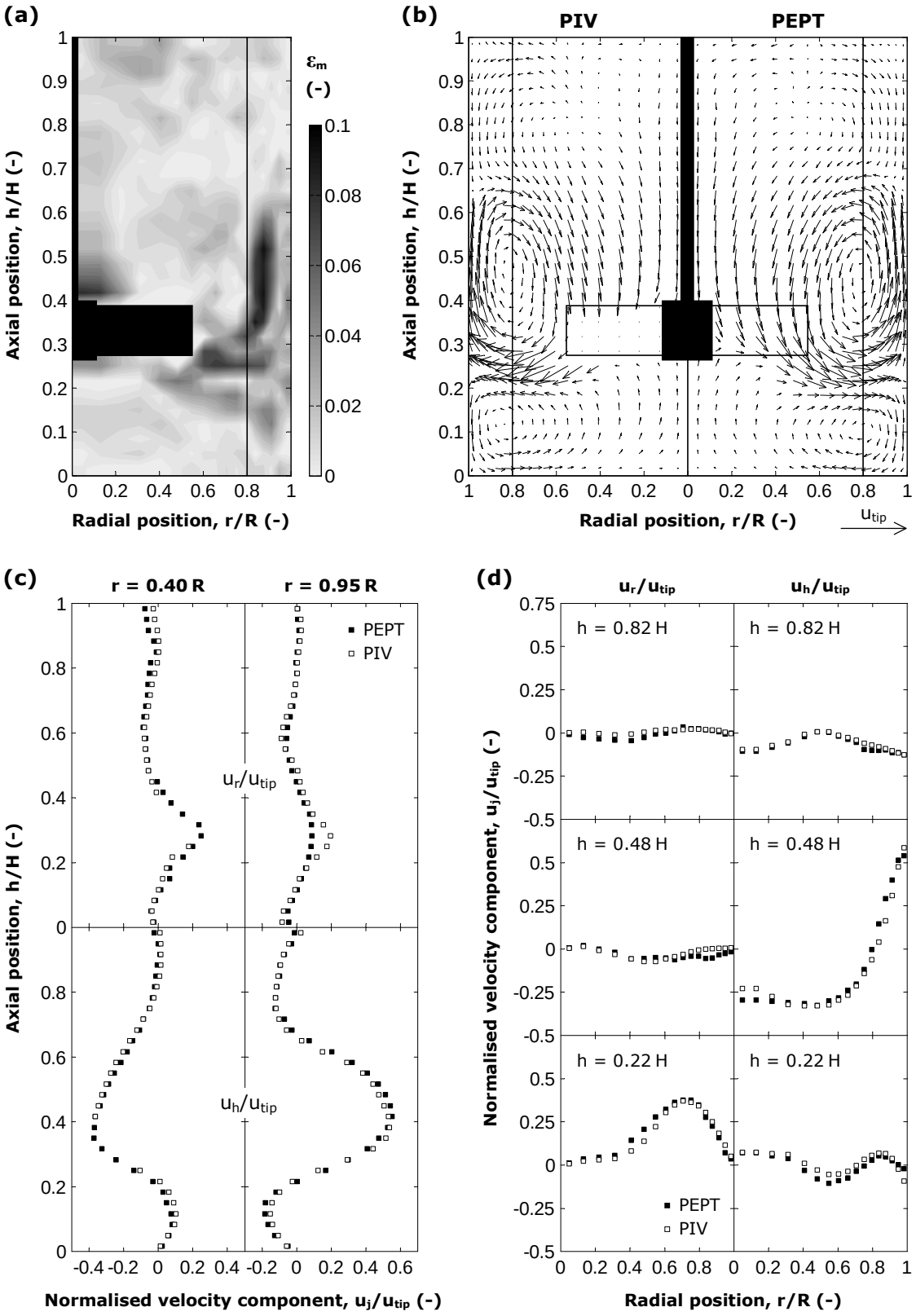

Figure 5.7. Comparison of radial-axial velocity obtained by PEPT and PIV at $\vartheta = 25^{o}$: (a) normalised modular difference; (b) vector plot; (c) normalised vertical and (d) radial profiles.

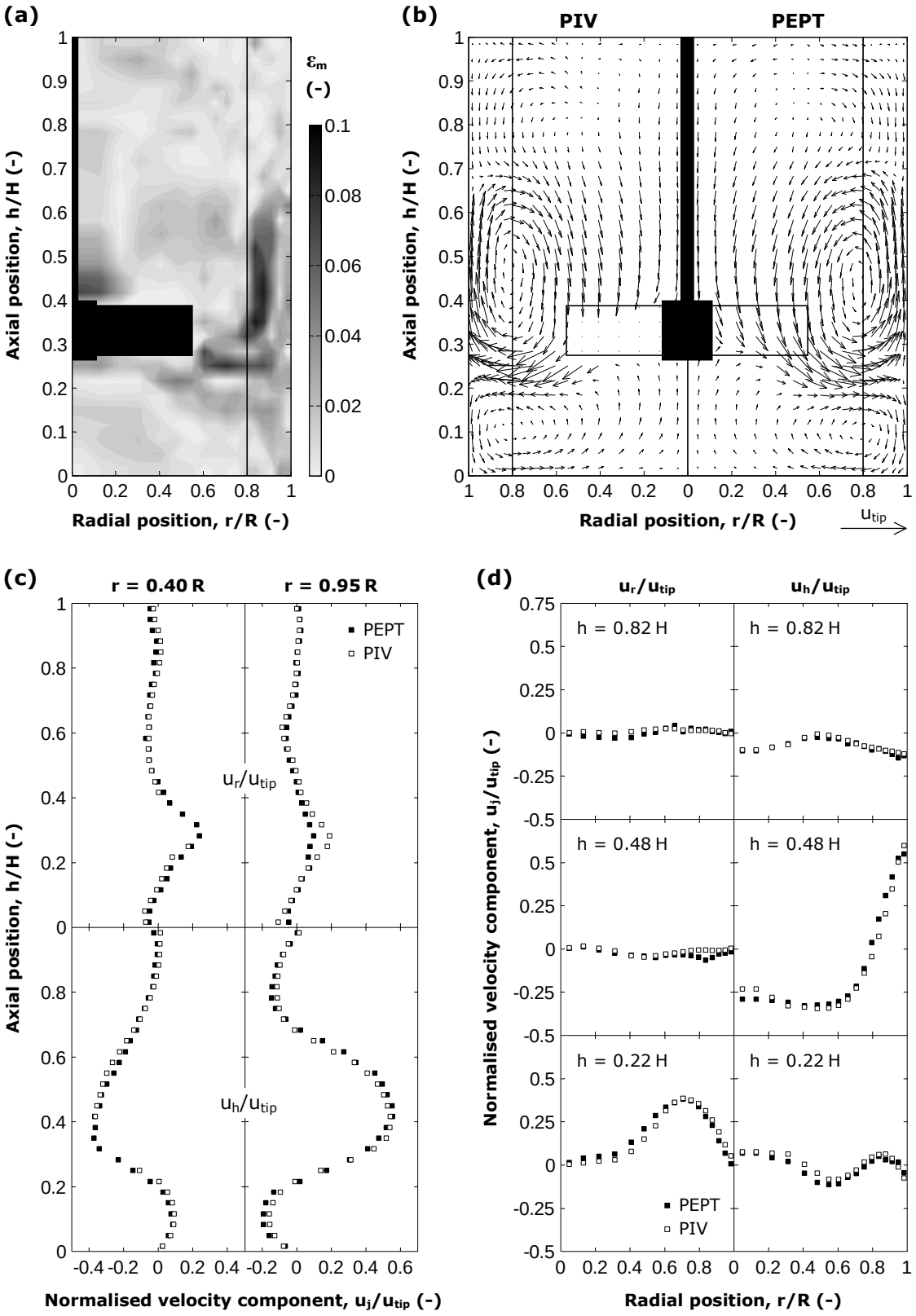

Figure 5.8. Comparison of radial-axial velocity obtained by PEPT and PIV at $\vartheta = 30^{o}$: (a) normalised modular difference; (b) vector plot; (c) normalised vertical and (d) radial profiles.

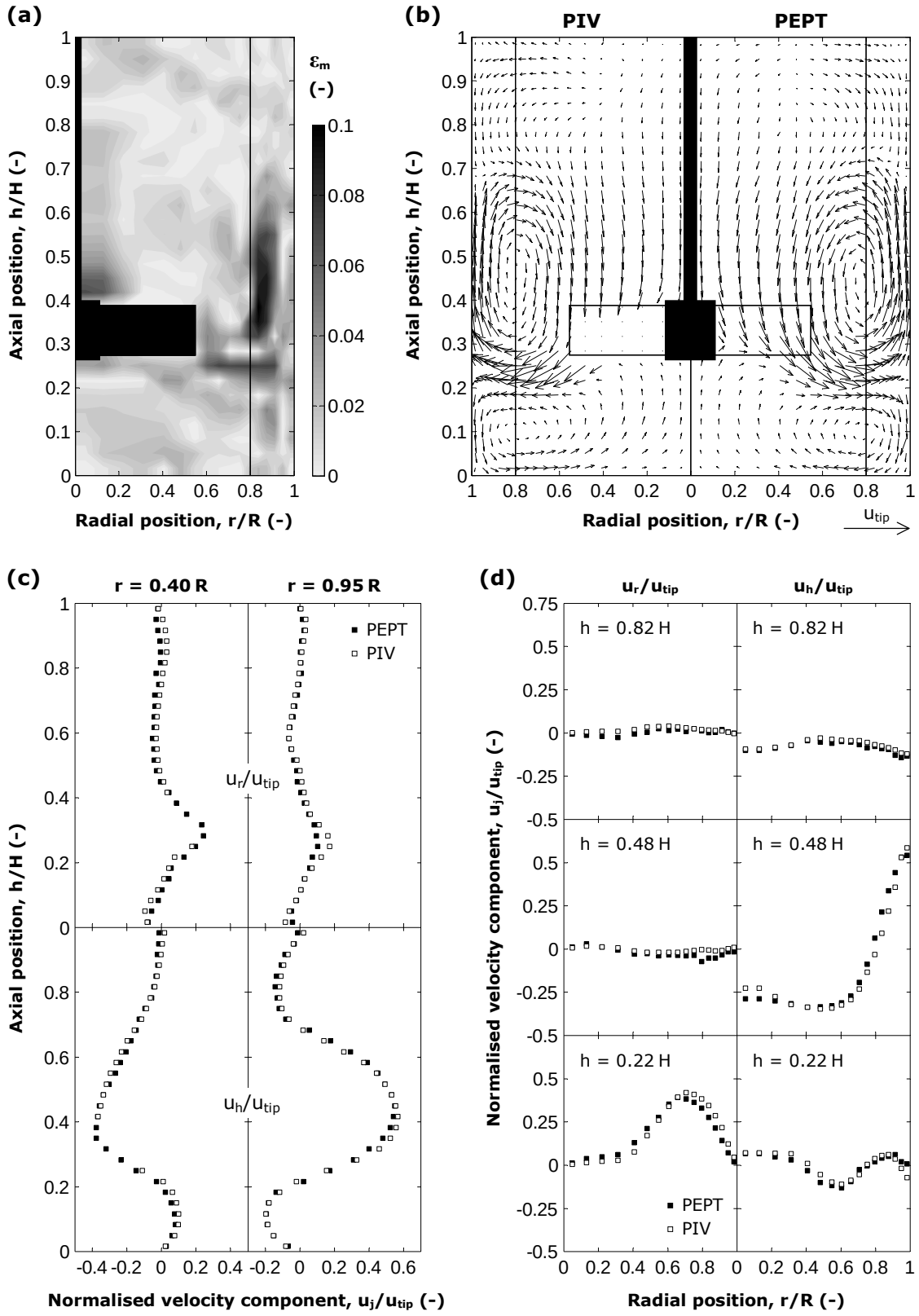

Figure 5.9. Comparison of radial-axial velocity obtained by PEPT and PIV at $\vartheta = 35^{o}$: (a) normalised modular difference; (b) vector plot; (c) normalised vertical and (d) radial profiles.

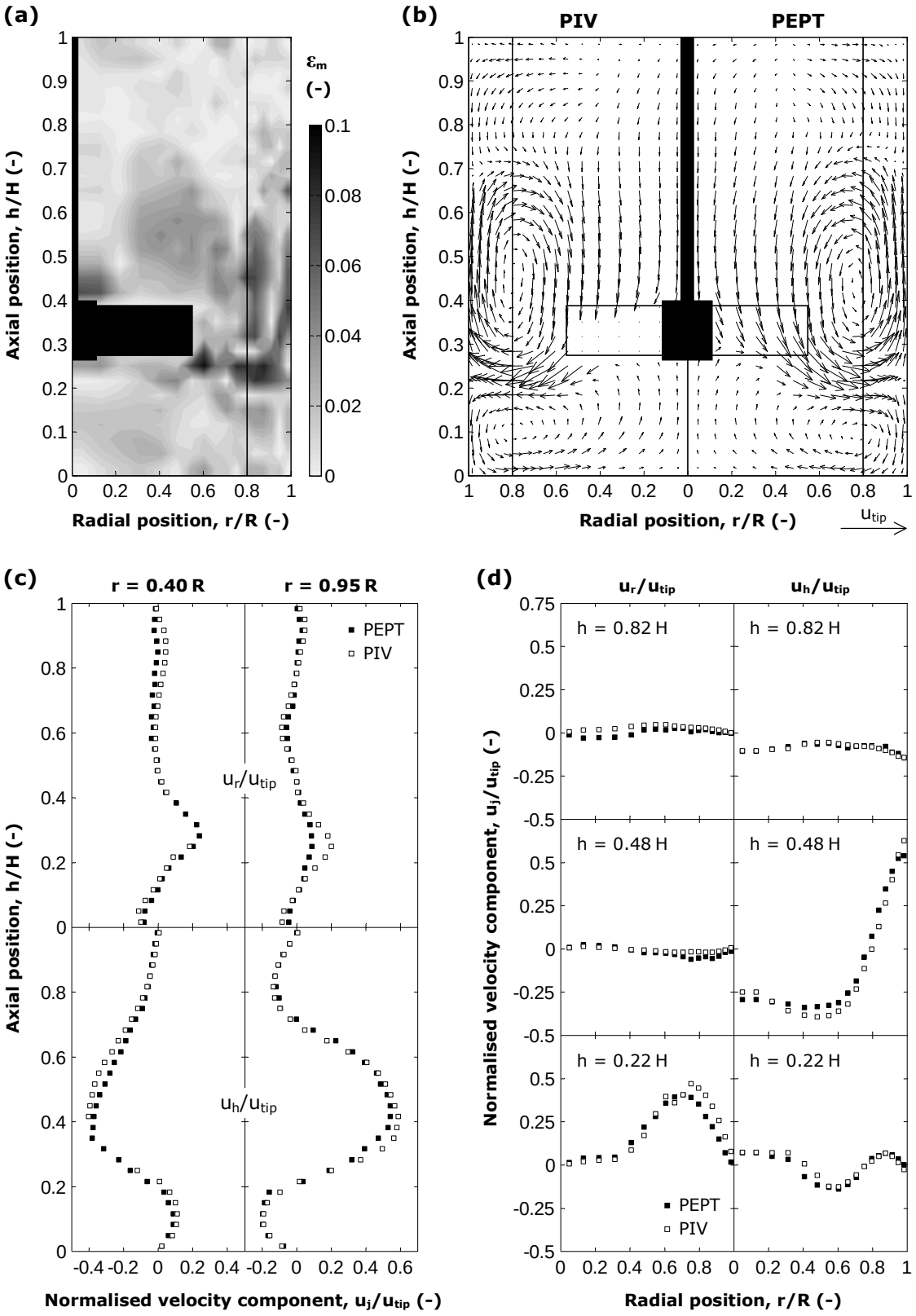

Figure 5.10. Comparison of radial-axial velocity obtained by PEPT and PIV at $\vartheta = 40^{o}$: (a) normalised modular difference; (b) vector plot; (c) normalised vertical and (d) radial profiles.

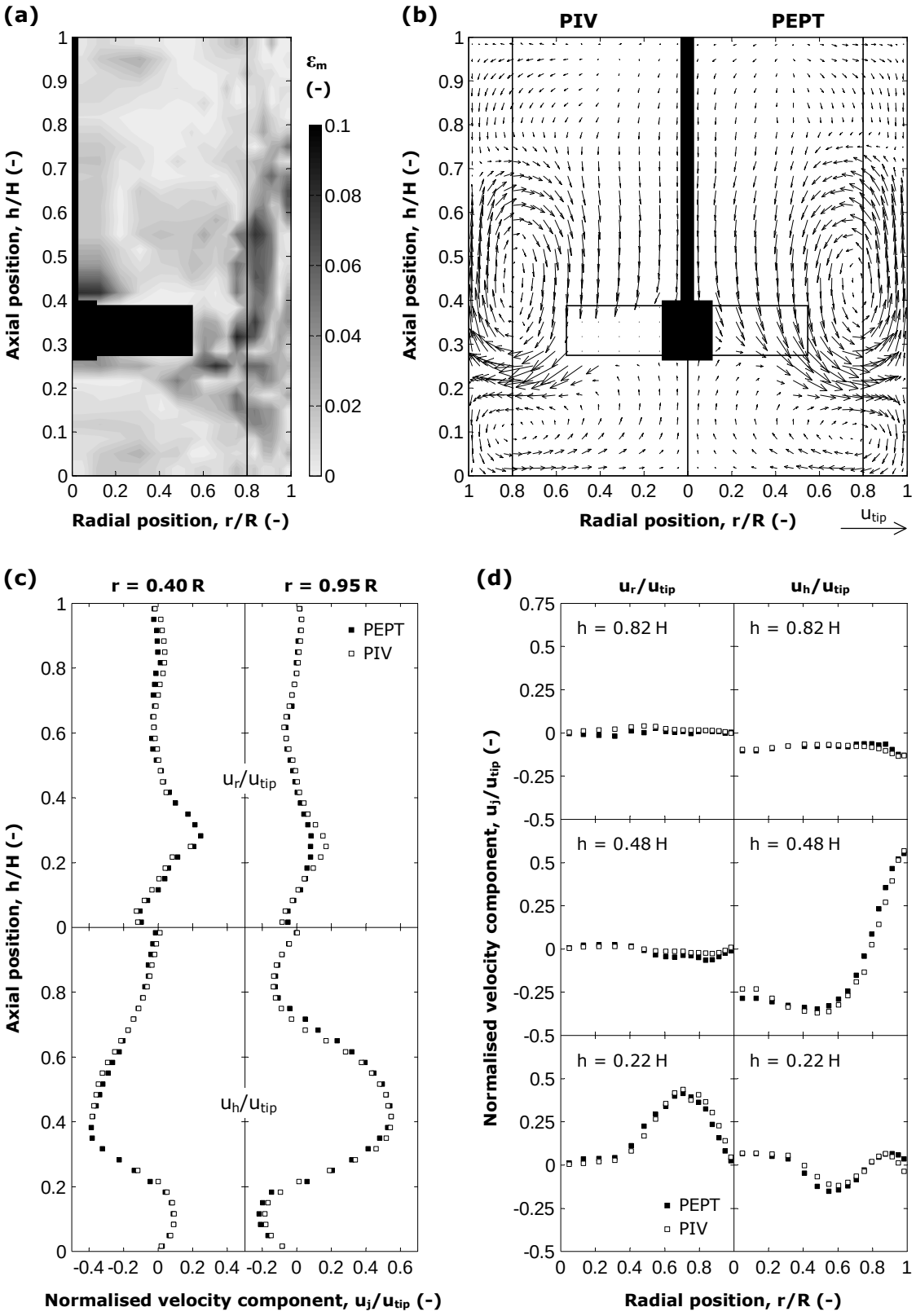

Figure 5.11. Comparison of radial-axial velocity obtained by PEPT and PIV at $\vartheta = 45^{o}$: (a) normalised modular difference; (b) vector plot; (c) normalised vertical and (d) radial profiles.

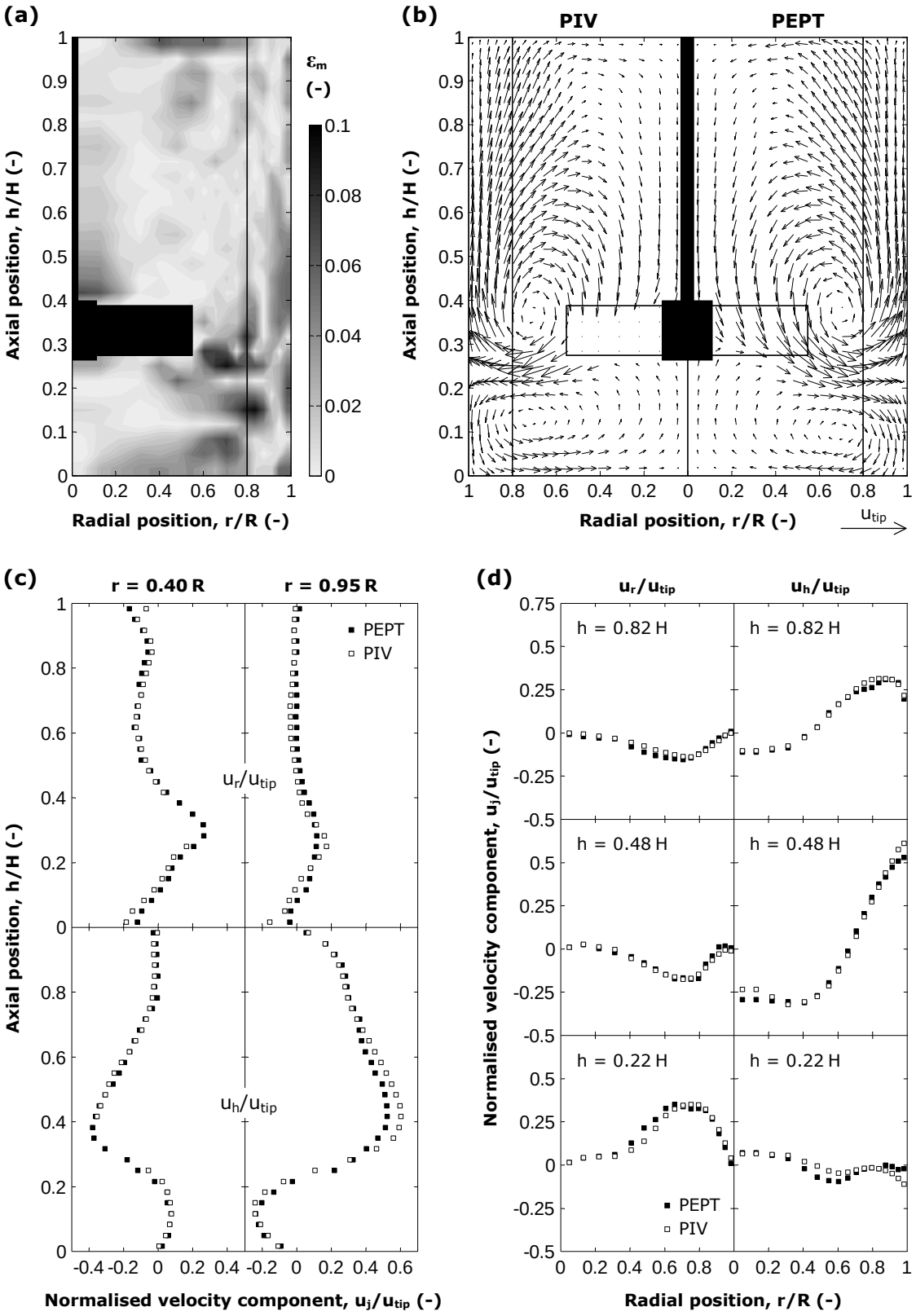

Figure 5.12. Comparison of radial-axial velocity obtained by PEPT and PIV at $\vartheta = 50^{o}$: (a) normalised modular difference; (b) vector plot; (c) normalised vertical and (d) radial profiles.

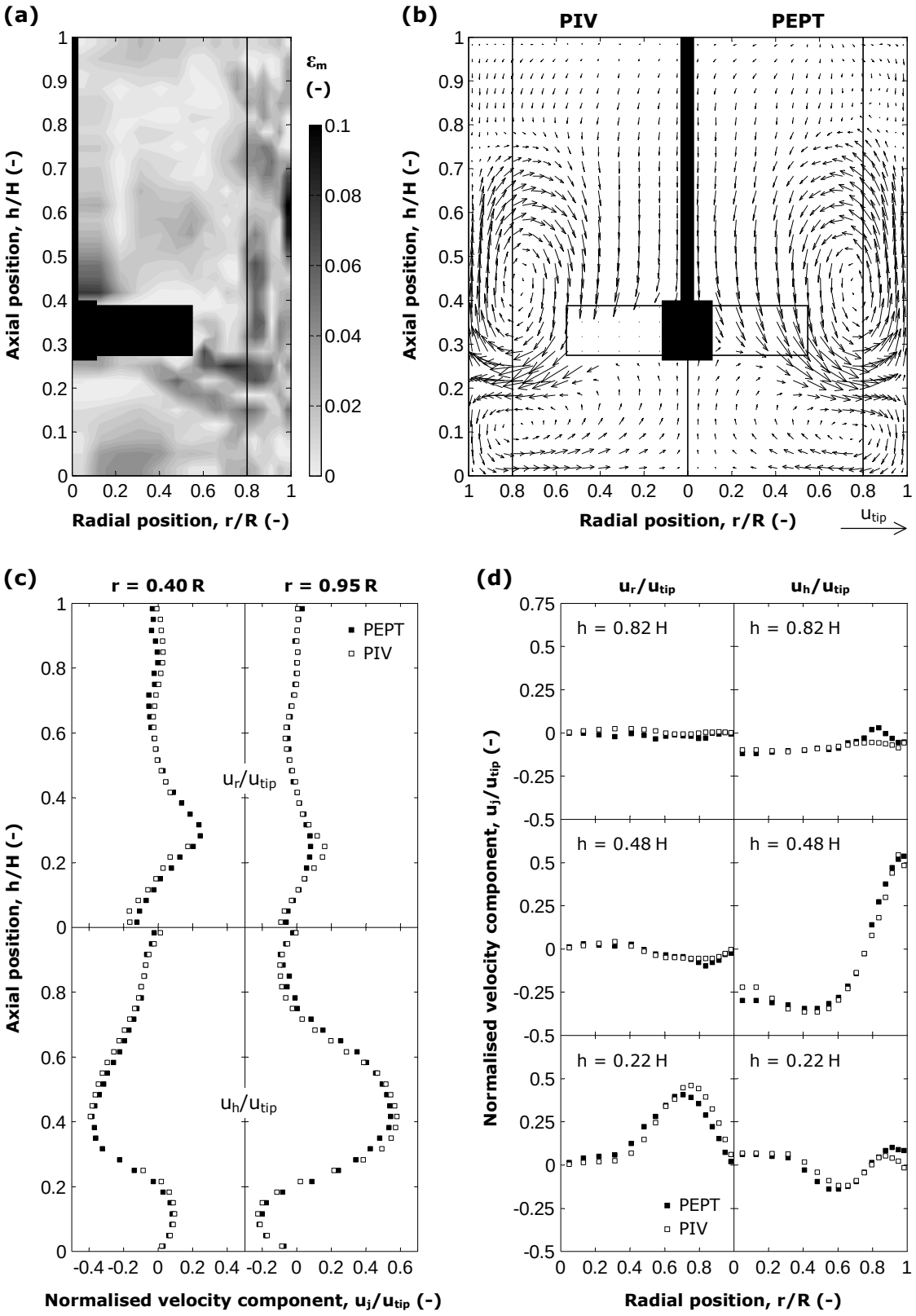

Figure 5.13. Comparison of radial-axial velocity obtained by PEPT and PIV at $\vartheta = 55^{o}$: (a) normalised modular difference; (b) vector plot; (c) normalised vertical and (d) radial profiles.

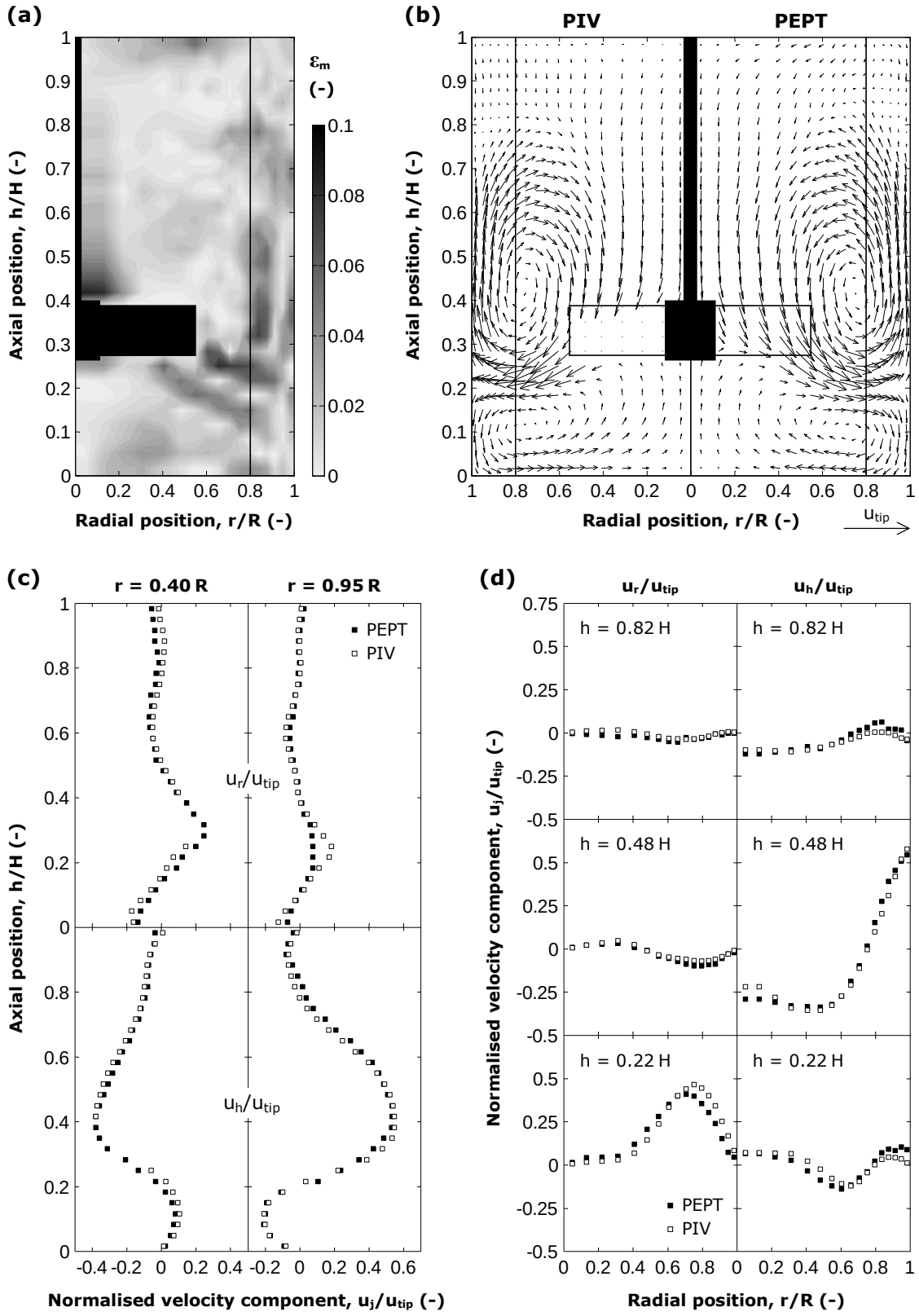

Figure 5.14. Comparison of radial-axial velocity obtained by PEPT and PIV at $\vartheta = 60^{o}$: (a) normalised modular difference; (b) vector plot; (c) normalised vertical and (d) radial profiles.

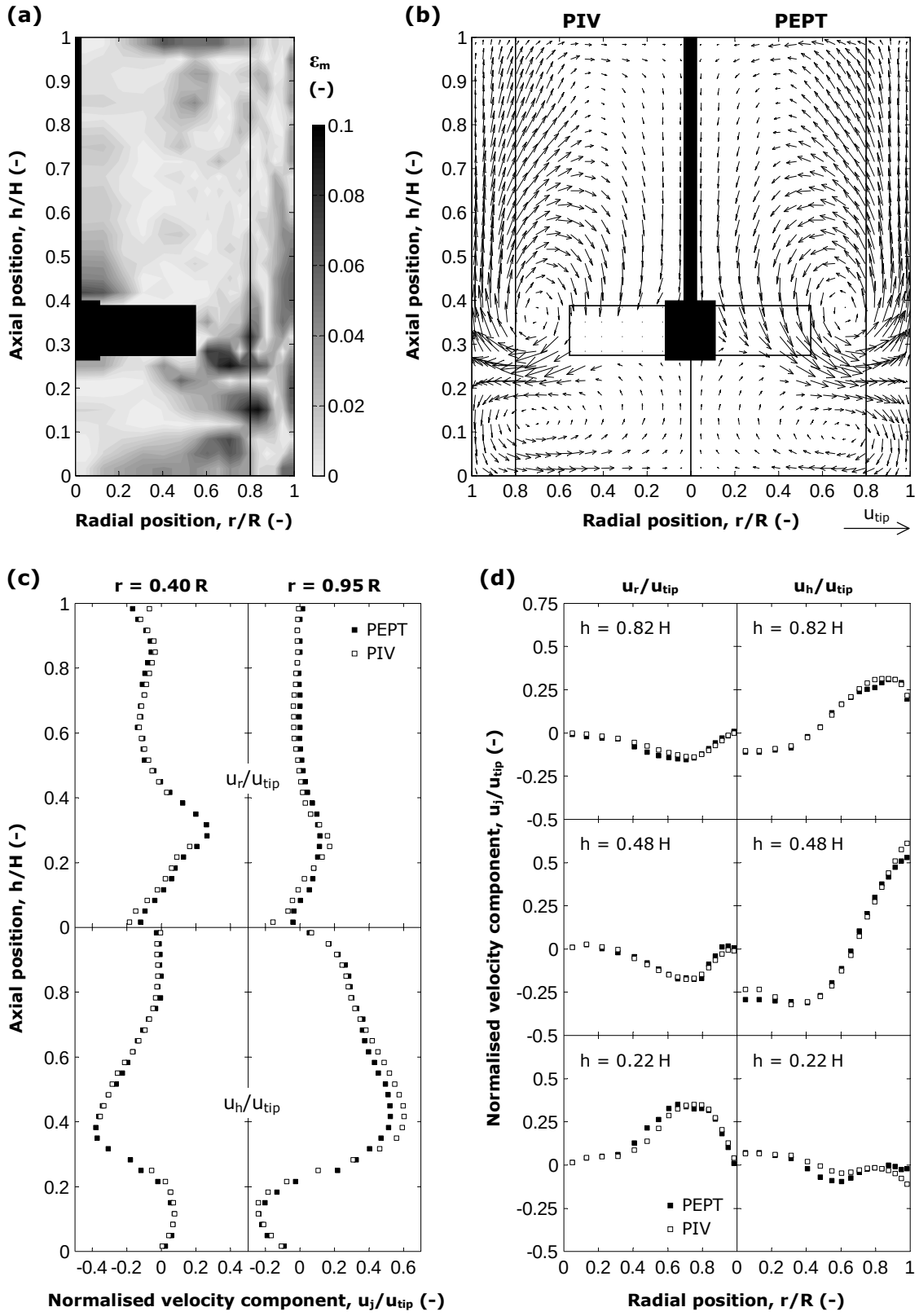

Figure 5.15. Comparison of radial-axial velocity obtained by PEPT and PIV at $\vartheta = 65^{o}$: (a) normalised modular difference; (b) vector plot; (c) normalised vertical and (d) radial profiles.

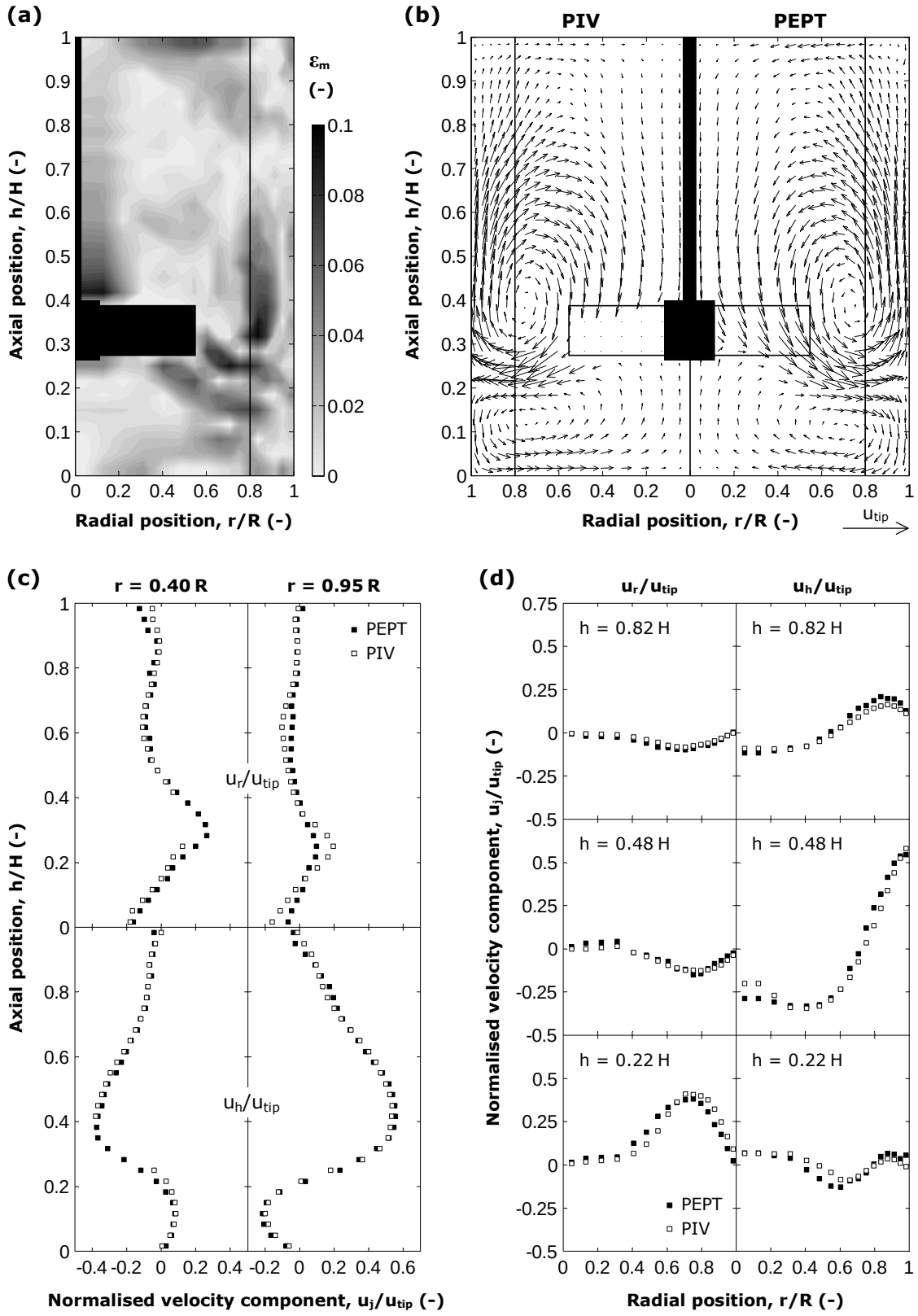

Figure 5.16. Comparison of radial-axial velocity obtained by PEPT and PIV at $\vartheta = 70^{o}$: (a) normalised modular difference; (b) vector plot; (c) normalised vertical and (d) radial profiles.

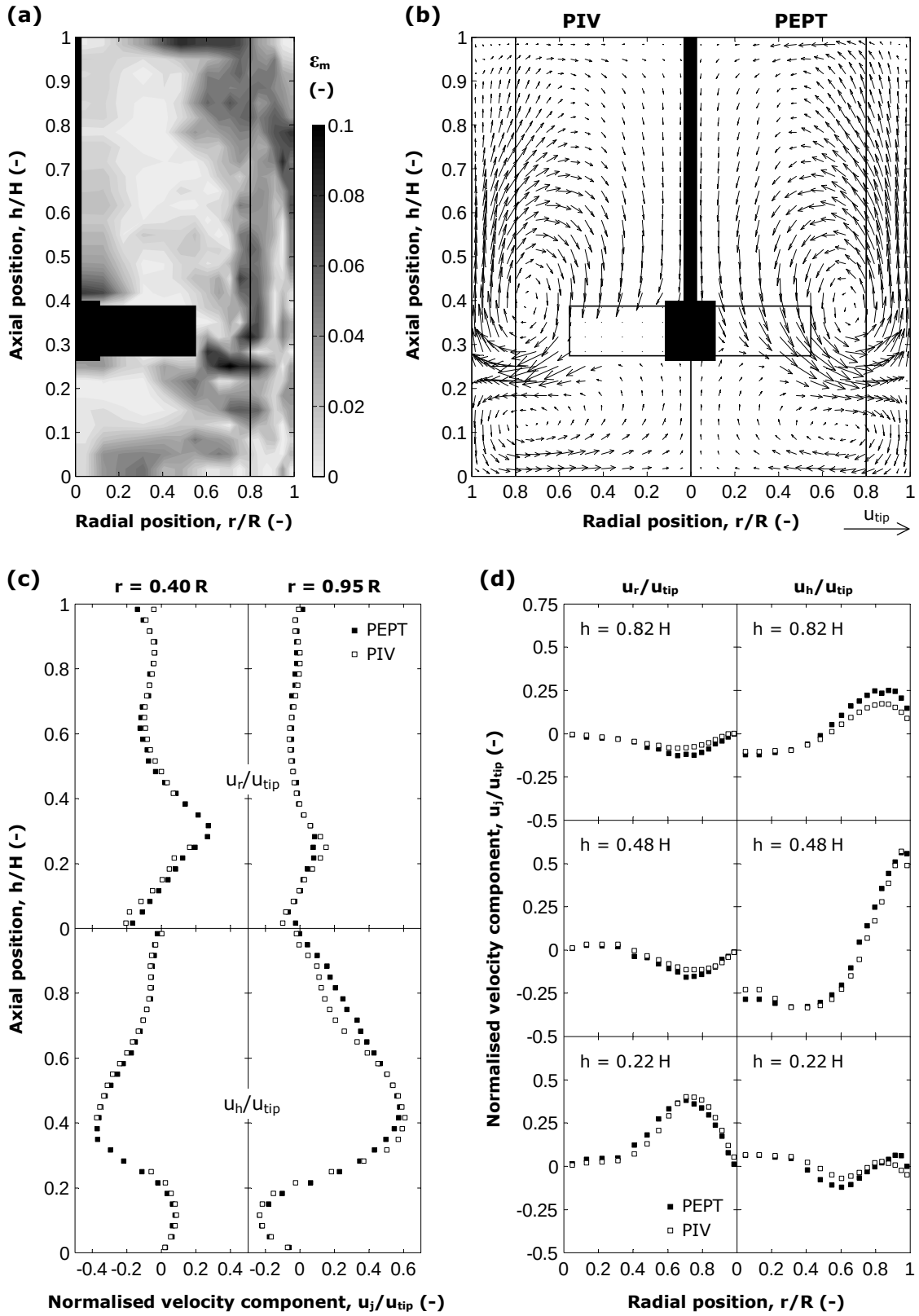

Figure 5.17. Comparison of radial-axial velocity obtained by PEPT and PIV at $\vartheta = 75^{o}$: (a) normalised modular difference; (b) vector plot; (c) normalised vertical and (d) radial profiles.

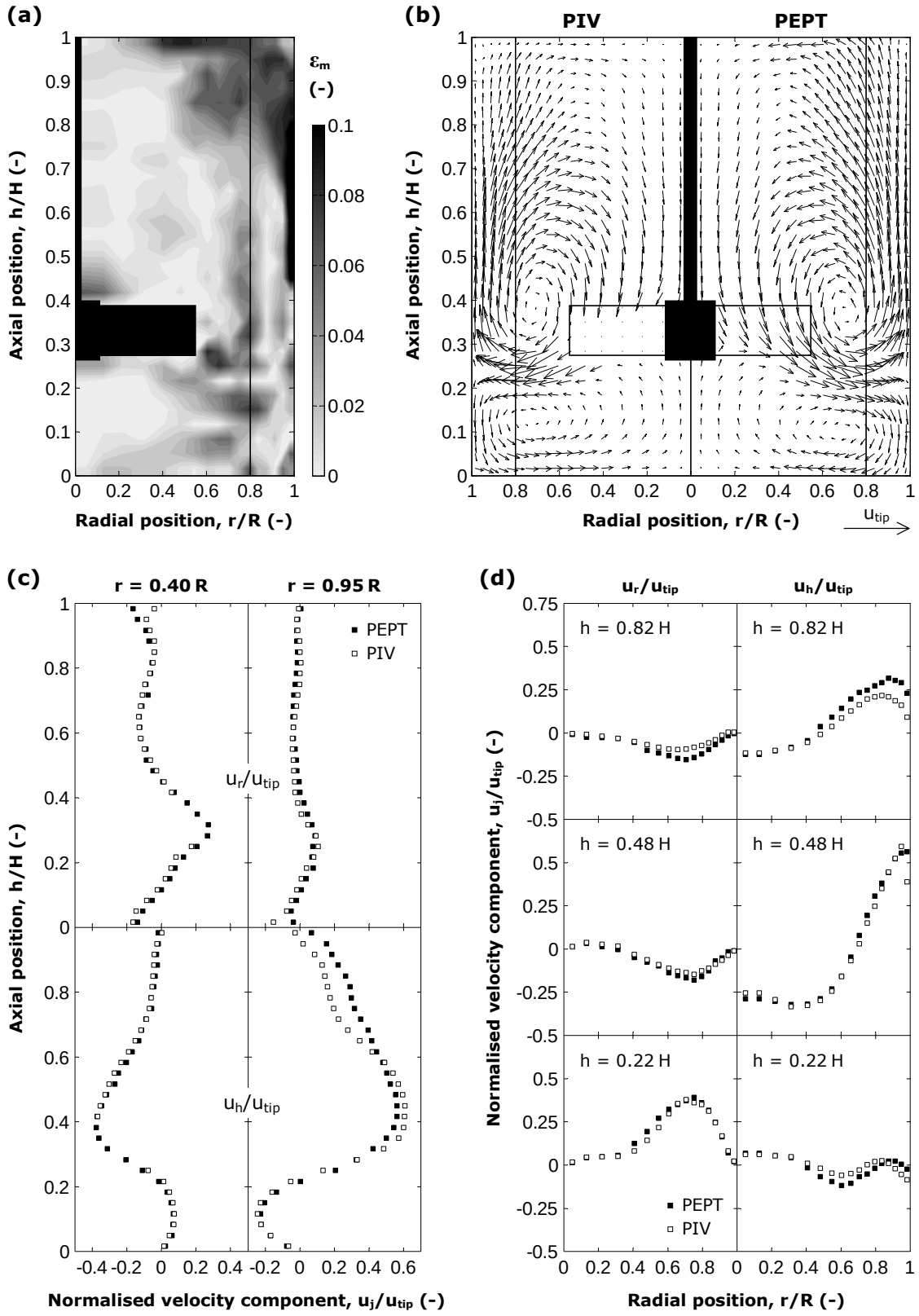

Figure 5.18. Comparison of radial-axial velocity obtained by PEPT and PIV at $\vartheta = 80^{o}$: (a) normalised modular difference; (b) vector plot; (c) normalised vertical and (d) radial profiles.

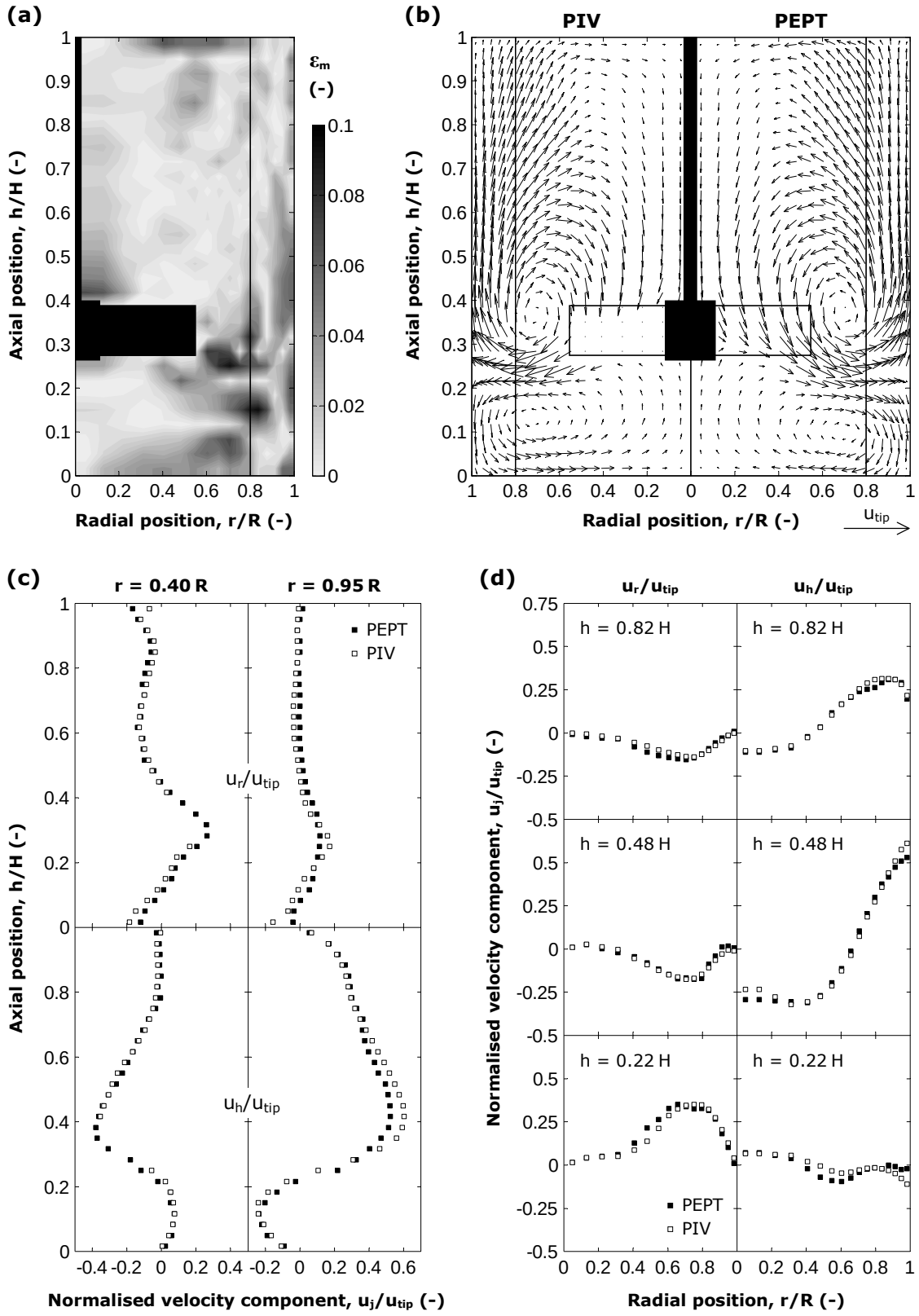

Figure 5.19. Comparison of radial-axial velocity obtained by PEPT and PIV at $\vartheta = 85^{o}$: (a) normalised modular difference; (b) vector plot; (c) normalised vertical and (d) radial profiles.

In order to probe the impeller discharge and suction regions, which are the parts of the vessel where the difference between PIV and PEPT axial velocities is usually maximum (Pianko-Oprych *et al.*, 2009), horizontal colour contours of axial velocity at these two levels (at h =0.25 H and at h =0.41 H) are shown in **Figure 5.20**.

Similar flow structures can be identified between maps; however, PIV detected higher axial velocities in the discharge plane close to the impeller tip for $\vartheta \sim 45^{o}$ while PEPT detected

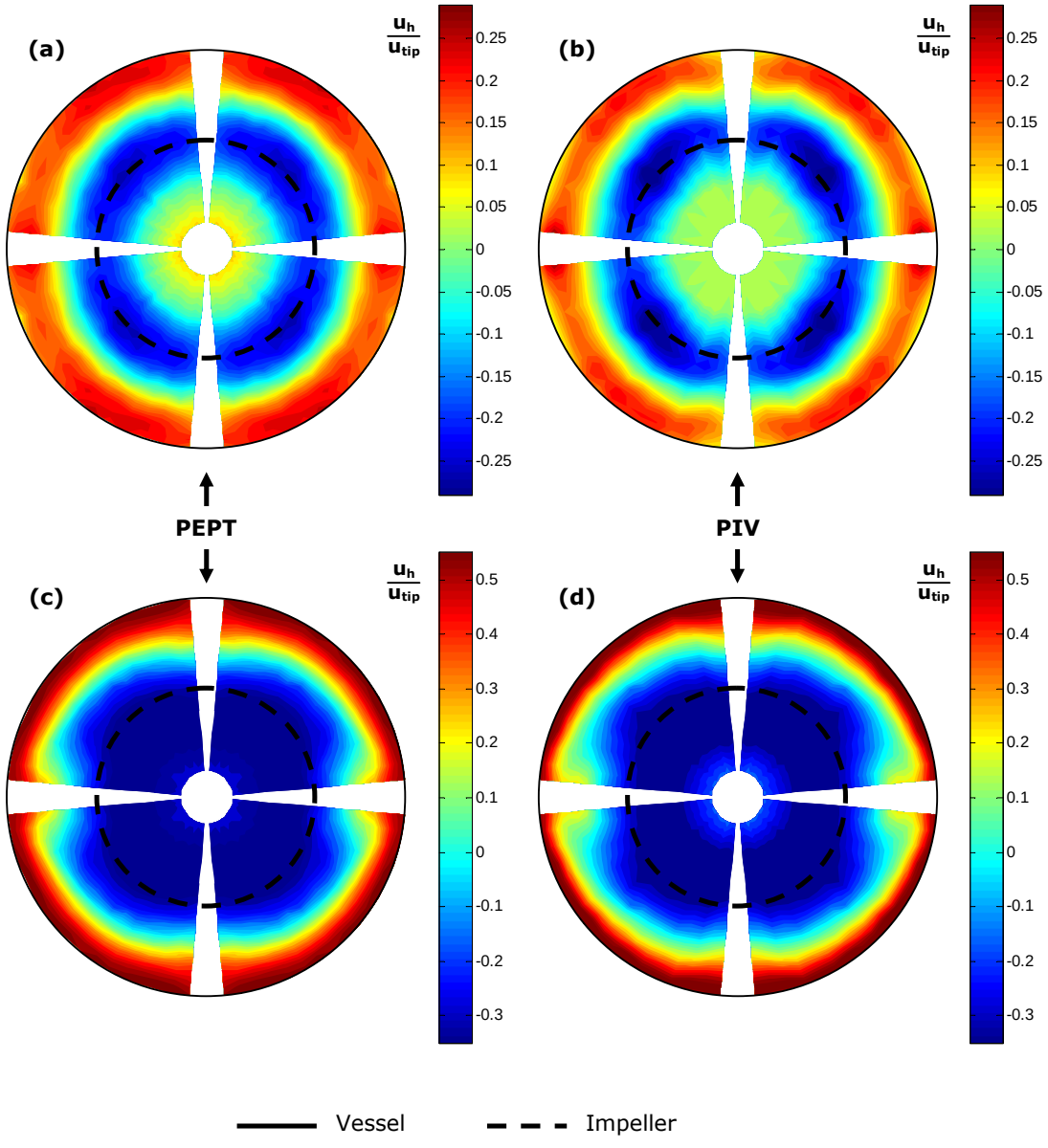

Figure 5.20. Normalised axial velocity maps in a horizontal plane: (a) PEPT, discharge plane at h =0.25 H; (b) PIV, discharge plane at h =0.25 H; (c) PEPT, suction plane at h =0.25 H; (d) PIV suction, plane at h =0.25 H.

higher velocities close to the wall at $\vartheta \sim 20^{o}$ and $\vartheta \sim 80^{o}$. Conversely, PEPT detected higher axial velocity in the suction plane in correspondence to the agitator, and PIV close to the wall. Both methods gave equally valid measurements, and considering that these are the areas where the worst agreement between the two measurement techniques was found by Pianko-Oprych *et al.*, 2009, probably because of the trailing vortex system of the impeller, the comparisons showed in **Figure 5.20** are, overall, satisfactory.

5-5 Conclusions

A previously performed comparison between 2D-PIV and PEPT involving, respectively, measurements conducted in one single plane and azimuthally-averaged maps obtained from tracking the whole 3D system, showed an overall satisfactory agreement between the two techniques (Pianko-Oprych *et al.*, 2009). However, the two-dimensional PIV measurements presented in Chapter IV show that cylindrical symmetry of the flow field cannot be assumed in a baffled configuration without a considerable loss of information. The comparison was then refined, as presented in Chapter III, by using azimuthally-averaged Eulerian velocity fields obtained in a transparent liquid both via Lagrangian tracking by PEPT and by Eulerian PIV measurements.

Nevertheless, due to the importance of such comparison, a detailed 3D study of the differences in the flow fields obtained with these two techniques in multiple vertical planes is presented in this chapter. Eulerian velocity fields in 17 vertical planes obtained by three-dimensional PEPT measurements are compared directly with those performed in each of these planes via PIV using the same equipment and fluid.

A part from some restricted high turbulence regions, where differences in velocity between the two techniques reached values of $0.1\ u_{tip}$, the discrepancy between the local modules of the PEPT and PIV radial-axial velocity vector is generally $< 0.02\ u_{tip}$. Excellent overall agreement is obtained between vector plots at each of the 17 planes, and a quantitative assessment based on axial and radial velocity component profiles confirms that.

Small discrepancies in both velocity components are discernible throughout the whole vessel but no particular trend can be identified, i.e., neither techniques consistently underestimates or overestimates fluid velocity (radial or axial) at any specific radial or axial position. The

discharge plane of the impeller is the area where the worst agreement between the two measurement techniques is found. Such a minor discrepancy can be attributed to velocity fluctuations generated by the trailing vortex system of the impeller.

Additionally, cavern boundaries in the same viscoplastic fluid with an apparent yield stress, were visualised via a planar laser induced fluorescence (PLIF) technique and radioactively detected using PEPT. The superimposition of the cavern profiles measured by these two different methods show no significant discrepancy between these two methods.

PEPT has now been successfully tested in detail in two different fluids and different flow regimes through detailed comparisons with well-established optical techniques. PEPT can now be reliably used to obtain accurate data throughout the entire complex three-dimensional flow field in a range of mechanically agitated, laminar or turbulent, single- or multi-phase opaque systems previously not amenable to quantitative analysis.

Notation

Roman letters

D	Impeller diameter	m
h	Axial distance	m
H	Vessel fill height	m
j	Cylindrical direction index (ϑ, r or h)	-
k	Fluid consistency coefficient	Pa s^n
k_s	Proportionality constant in Eq. (5.3)	-
n	Flow behaviour index	-
N	Impeller rotational speed	s^{-1}
r	Radial distance	m
R	Vessel radius	m
Re_{imp}	Impeller Reynolds number	-
T	Vessel diameter	m
u_r u_h	Radia and axial velocity components	m s^{-1}
u_{rh}	2D radial-axial velocity magnitude	m s^{-1}
u_{tip}	Impeller tip speed	m s^{-1}

Greek letters

$\dot{\gamma}$	Shear rate	s^{-1}
$\dot{\gamma}_e$	Effective shear rate	s^{-1}
ϑ	Azimuthal coordinate	rad
ε_m	Velocity modular error	-
μ_e	Effective viscosity of the fluid	Pa s
ν	Kinematic liquid viscosity	m^2 s^{-1}
ρ	Density of the fluid	kg m^3
τ	Shear stress	Pa
τ_e	Effective shear stress	Pa
τ_y	Yield stress	Pa

Abbreviations

CCD	Charge-coupled device

PBT	Pitched blade turbine
PBTD	Down-pumping PBT
PBTU	Up-pumping PBT
PEPT	Positron emission particle tracking
PIV	Particle image velocimetry
PLIF	Planar laser induced fluorescence

Chapter VI
Shannon Entropy Analysis by PEPT

Abstract

If 100 dice cannot be cast simultaneously, one single die can be cast 100 times. On the basis of this simple principle, the experimental technique of positron emission particle tracking has been used to develop and implement a new methodology for quantifying the local and global mixing characteristics within a mechanically-agitated fluid batch system. Using a high data acquisition rate, the PEPT tracer was continuously tracked in 3D space and time to accurately determine its trajectory over a considerable period of time. By partitioning its long trajectory, the single particle tracer can be regarded as thousands of simultaneously tracked particles which are instantaneously, locally and non-invasively injected in the mixing system at varying feed positions. A large amount of PEPT data were collected for impeller rotational speeds ranging from 100 to 500 rpm which allowed new statistical tools derived from Information Theory, such as Shannon entropy and uncertainty, to be implemented in the data analysis. Thus, measurements of newly defined entropy mixing indices were obtained as a function of position, time and impeller speed. The method also allowed the determination of characteristic time parameters including the macroscale mixing time which agreed very well with correlations of the dimensionless mixing time available in the mixing literature. Detailed local information is provided on minimum mixing time positions for feed and withdrawal of material, which can be used to optimise the design or operation of stirred batch mixing systems.

6-1 Introduction

Mixing can be defined as the increase in homogeneity through input of mechanical energy in a single or multiphase system to achieve a desired process result. This is an important industrial operation which is often conducted in a mechanically agitated vessel and is critical to the successful manufacturing of numerous products. Blending of fluids is a common mixing operation whose objective is to mix fluids to a desired level of homogeneity, and the length of time required to achieve it is referred to as the blend time, macroscale mixing time or simply mixing time.

Mixing time is often used as an important indicator of mixing quality and chemical reactor performance, and a number of techniques are available for its measurement. Two that are widely used are dye injection and acid-base colorization-decolorization (Cronin *et al.*, 1994). Both techniques provide similar results for blend time and have the advantage of allowing visual observation of the mixing patterns and the location of any dead zones in the vessel. However, they are subjective and they are also restricted to clear vessels, which makes them useless in industrial tanks. Image processing can potentially circumvent the problem of subjectivity using planar laser induced fluorescence (PLIF) (Chung *et al.*, 2007; 2009) or the colorimetric method itself (Cabaret *et al.*, 2007); nevertheless, the transparency constraint still presents a serious limitation to these applications. Other techniques are the fluorimetric method (Pineault and Cloutier, 1970), the dual indicator method (Melton *et al.*, 2002), the thermographic technique (Lee and Yianneskis, 1997), and electrical resistance tomography (e.g., Holden *et al.*, 1998).

The use of temperature sensors positioned at various locations in the vessel to measure temperature uniformity provides a technique which is applicable in opaque vessels (Brown *et al.*, 2004). The method is fairly simple and reliable provided the material added to alter the temperature in the vessel can generate a strong enough disturbance that a response can be measured, and provided also that the rate of bulk mixing is significantly faster than the rate of thermal diffusion. Another technique which is also suitable in non-transparent systems is conductivity measurement, which consists of injecting a small amount of a conductive (salt) tracer and using one or more conductivity probes to monitor changes in conductivity at selected locations in the vessel (Ruszkowski, 1994). The mixing time is measured as the time taken to reach a certain fraction (usually 95%) of the equilibrium conductivity in the vessel.

This technique has become more or less a standard method for measuring mixing time for aqueous systems, while other techniques such as dielectric response have been proposed for use in organic-phase solutions (Shervin *et al.*, 1992).

Most mixing studies have focused on global measurements of mixing time including occasionally a visualisation of flow patterns. These studies have been experimental in the main and correlations have been proposed which match experimental data to give tractable engineering solutions (Grenville and Nienow, 2004). However, theoretical mixing models are rare and the lack of fundamental understanding, such as it exists, lies as much in weaknesses in the theory as in the need for improved experimental techniques. A more detailed localised description of the internal mixing performance of a stirred vessel in terms of dispersion, homogenisation, microscale and macroscale mixing times and flow structures is increasingly becoming necessary to provide a better basis for design. For example, several authors (Ducci and Yianneskis, 2007a-b; LaRoche, 2005; Guillard and Trägårdh, 2003) reported a dependence of the mixing time on the feed position in a mixing vessel, indicating the existence of 'preferred' positions for feed insertion. Usually, more by-product is formed at feed points where local mixing is slow which has important product quality implications for many processes such as precipitation for catalysts manufacture (Edwards *et al.*, 2009). Consequently, careful selection of the feed location is required. However, only a small number of investigations have attempted to quantitatively describe the influence of feed position on mixing performance (Ducci and Yianneskis, 2007a). This has been mainly due to the lack of suitable techniques that can be used to measure detailed local flow properties in such systems, especially when these are opaque.

Shannon entropy is used in Information Theory to measure the uncertainty about the outcome of a random event and describe statistical phenomena in terms of information content and uncertainty about the outcome. Where a set of possible events has a flat probability distribution, intuitively, an observer cannot be more uncertain about the outcome. A quantitative approach centred on this uncertainty enables evaluation of the degree of uniformity of the probability distribution, allowing mixing capacity/quality indices to be specifically defined for the systems in which the physical phenomena are studied. Mixing can be viewed as a process by which a complex exchange network between regions of the system is generated. Thus, Shannon entropy, as used in Information Theory, appears to be a useful

parameter for describing mixing efficiency in a system in terms of uncertainty about the possible transitions or exchanges between zones. Ogawa *et al.* (1980) discussed the possibility of using Information Theory to describe mixing processes, but hitherto this idea has not been fully developed and validated so that it can be exploited in mixing studies.

The idea behind this application of Shannon entropy is that the related probability spectra in a mixing system can be accurately measured by tracking a single particle in 3D space and time; thus, by judiciously partitioning its long trajectory into appropriate segments, a single particle tracer can be regarded as thousands of simultaneously tracked particles which are instantaneously, locally and non-invasively injected in the tank at varying feed positions. This chapter reports on the development of a new methodology based on the concept of Shannon entropy for the study of the local and global mixing characteristics in a batch mixing vessel using PEPT.

6-2 Experimental

The PEPT experiments were conducted in a flat-bottom cylindrical vessel of diameter T = 288 mm equipped with four baffles of width $B = 0.1\,T$. The agitator used was a 6-blade 45º pitched-turbine (PBT) of diameter $D = 0.5\,T$ and height $w = 0.1\,T$. The height of the fluid in the vessel was set at $H = T$ and the impeller off-bottom clearance was $C = 0.25\,T$. A resin particle of 250 μm diameter, activated with ^{18}F by an ion-exchange technique, was used as the PEPT tracer. The working fluid was water whose density was adjusted to 1100 kg m^{-3} by adding sodium chloride to make the particle tracer neutrally buoyant. Measurements were performed at a rotational speed, N, varying from 100 rpm to 500 rpm, in the fully turbulent regime such that the impeller Reynolds number was $\mathrm{Re}_{imp} = ND^2/\nu > 30\,000$, where ν is the liquid kinematic viscosity. The PBT agitator was studied in both down-pumping (PBTD) and up-pumping (PBTU) modes.

In each experiment, the trajectory of the particle tracer was recorded over a period of ~ 45 min. Such a PEPT runtime was long enough to achieve an adequate resolution in terms of tracer locations. However, a brief study of the probability of tracer presence, P_{tr}, was conducted to assess the accuracy of the ergodic condition assumption (see Section 3-5.1). Dividing the vessel volume in 10 horizontal sections, P_{tr} was estimated by the fraction of time

spent by the particle tracer in each section during the experiment. The plots in **Figure 6.1** show that P_{tr} was approximately equal to its theoretical value ($P_{tr,\infty}$ = 1/10) in all the sections; consequently, supported by theory and experimental evidence, ergodicity of flow could be safely assumed.

6-3 Theory and Data Analysis

6-3.1 Information and uncertainty

The foundation of Information Theory is a quantification of information. The class of objects to which the quantity information is related are occurrences of events associated with a probabilistic interpretation. In 1948, Shannon the main pioneer of the mathematical formulation of the Information Theory, defined information qualitatively as that which reduces uncertainty (Shannon, 1948). Information is something that regardless of its form (stories, description, rumour, etc.) and value to an individual (likes and dislikes, good and bad, merits and demerits, etc.) replaces uncertain knowledge with more certain knowledge (Ogawa, 2007).

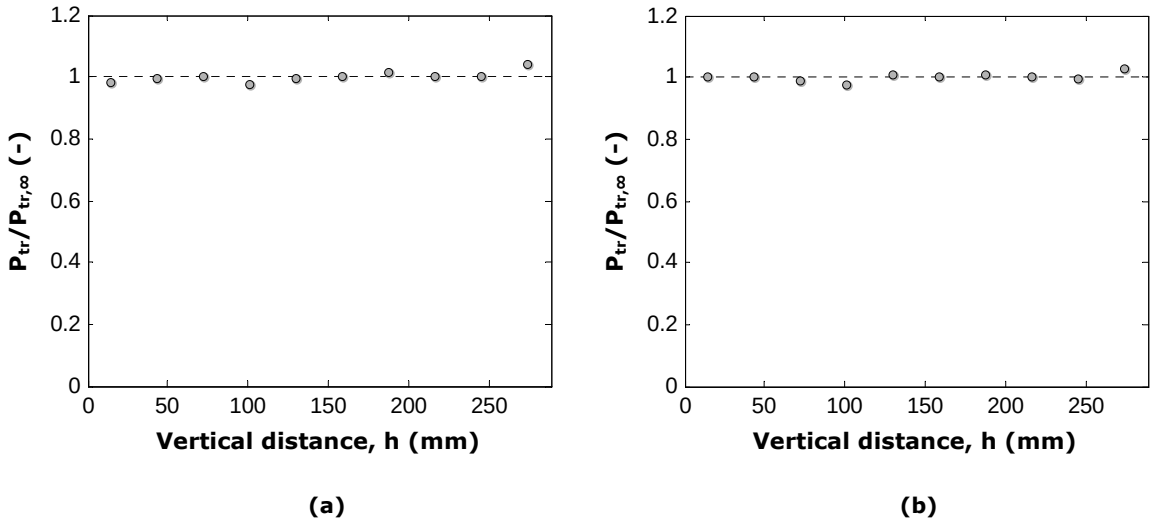

Figure 6.1. Probability of tracer presence normalised by the theoretical value ($P_{tr,\infty}$ = 1/10) at different vertical positions in the vessel for N = 300 rpm, for both (a) PBTD and (b) PBTU.

From a probabilistic perspective, uncertainty of knowledge exists as different possible results can be considered for an occurring phenomenon. The actual event is the one selected from a set of possible events and can be interpreted as the result or outcome of the examined process. An occurring event can be considered a container of information quantified by a certain amount of uncertainty related to the unknown outcome. Such an uncertainty vanishes when the information contained in the occurring event is produced and the outcome is known.

If the number of equally likely possible events in a set is finite, then this number or any monotonically increasing function of this number can be regarded as a measure of the amount of information produced when the outcome is known. Similarly, such a function is an expression of the uncertainty about the outcome. However, there are other requirements related to the functional form of the uncertainty about the outcome.

In **Figure 6.2** an experiment X whose outcome is to be revealed is schematically illustrated. An example of X can simply be a quantity (e.g. velocity) expressed by a random variable. For the moment, particular attention will be paid to the case in which the n possible events of experiment X are all equally likely. In this special case, the uncertainty about the outcome will be a monotonically increasing function of n, say $f(n)$.

If, as illustrated in **Figure 6.3**, X is a compound experiment consisting of two independent experiments Y and Z with n_1 and n_2 equally likely events, respectively, the total number of events, n, of the compound experiment is the product of n_1 and n_2. Revealing the outcome of X is, therefore, equivalent to revealing the outcomes of Y and Z separately. Thus the information produced when the outcome of X is known must be the sum of the informations produced when the outcomes of Y and Z are known. Likewise, the uncertainty about the

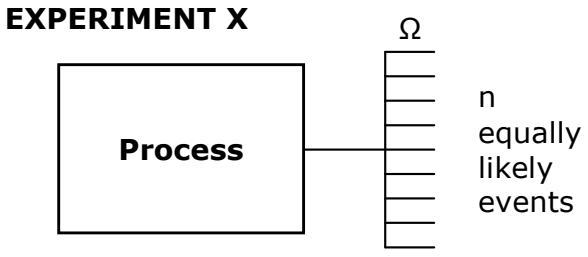

Figure 6.2. Schematic representation of a hypothetical experiment from a probabilistic point of view.

outcome of *X* must be the sum of the uncertainties about the outcomes of *Y* and *Z*, i.e.,

$$f(n) = f(n_1) + f(n_2) \tag{6.1}$$

where

$$n = n_1 n_2 \tag{6.2}$$

It can be shown that the only monotonically increasing functions of *n* which are solutions of the functional equation represented by Eqs. (6.1) and (6.2) are multiples of the natural logarithm of *n*, here denoted by log (see for example, Hankerson *et al.*, 2003); thus

$$f(n) = c \log n \tag{6.3}$$

where *c* is a positive constant. The probability, *p*, that one of the *n* equally likely events will occur is uniform and equal to 1/*n*. Consequently, the information produced when the outcome of *X* is known or, equivalently, the uncertainty about the outcome of *X* can be defined as

$$I(X) = -c \log p \tag{6.4}$$

If the possible events of the experiment are not all equally likely, intuitively the amount of information contained in the occurring event cannot be the same for each possible event. However, the definition of information can be extended to cover such a general case. A possible event, ω_i, of experiment *X* is an element of the set of all the possible events, Ω, and its probability of occurrence, p_i, characterises the event itself. Where p_i is not uniform, the

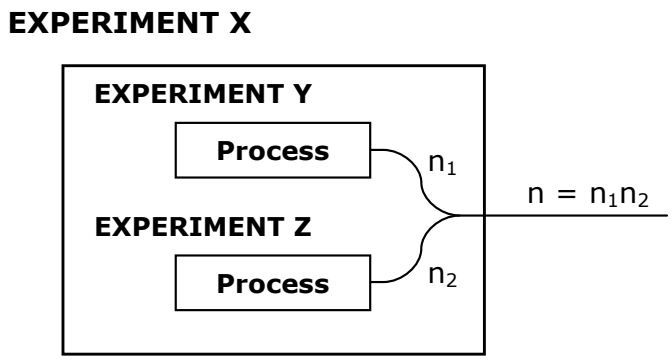

Figure 6.3. Combination of two independent experiments into one.

term used to define the information that a specific event indeed occurred is self-information. The self-information contained in an event, ω_i, depends only on the probability of the event itself and it is defined as

$$I(\omega_i) = -c \log p_i \tag{6.5}$$

Tribus (1961) later named the term $I(\omega_i)$ surprisal. Surprisal is the degree to which an observer is surprised to see a result. When p_i is maximum (equal to 1), $I(\omega_i) = 0$ and there is zero surprise at observing the result. As the probability of the specific event decreases below 1, its surprisal value increases tending to $+\infty$.

Where the events are pairwise mutually exclusive, the uncertainty about the outcome is given by the average of the respective values of self-information. The average self-information is obtained as the sum of the self-information of each possible event weighted by the probability of occurrence of the event itself, i.e.,

$$H(X) = \sum_{i=1}^{n} p_i I(\omega_i) = -c \sum_{i=1}^{n} p_i \log p_i \tag{6.6}$$

where

$$\sum_{i=1}^{n} p_i = 1 \tag{6.7}$$

If one (or more) of the probabilities is zero, its related term in Eq. (6.6) is indeterminate ($0 \times \infty$) and consequently $H(X)$ should also be indeterminate. However, any such term is conventionally set to zero, which effectively excludes it from the calculation of $H(X)$. The convention $0 \times \log 0 = 0$ extends Eq. (6.6) to cases in which zero probability events are involved, and its use is justified by the limit

$$\lim_{p \to 0} (-p \log p) = 0 \tag{6.8}$$

An indication that supports the postulation that $H(X)$ represents the uncertainty about the outcome when the n events are not necessarily equally likely, is the limiting case of equally likely events in which $p_i = 1/n$, and hence $I(X) = H(X)$. Another indication can be obtained by considering experiment Y depicted in **Figure 6.4**; it has m equally likely possible events

assembled into two groups, containing m_1 and m_2 possible events, such that

$$m_1 + m_2 = m \tag{6.9}$$

Where an observer is not really interested in the particular outcome of the experiment *Y*, but only in whether the outcome is a possible event of the first or the second group, the significant outcome is one of two events ω_1 and ω_2, having probabilities

$$p_1 = \frac{m_1}{m_1 + m_2} \quad \text{and} \quad p_2 = \frac{m_2}{m_1 + m_2} \tag{6.10}$$

Consequently, it is possible to define experiment *X* as having only two not equally likely possible events, ω_1 and ω_2, with probabilities p_1 and p_2, respectively. To determine the uncertainty about the outcome of *X*, it is possible to start with the amount of information provided (or uncertainty about the outcome that vanishes), when one of the *m* equally probable events of the experiment *Y* is known, thus

$$I(Y) = c \log m \tag{6.11}$$

which contains a surplus of information. It is possible to subtract the excess information provided (or uncertainty about the outcome that vanishes) when one of the m_1 equally probable events is known, i.e., $c \log m_1$. However, this occurs not all the time but only for a proportion of the time equal to m_1/m. Similarly, the amount of information contained in an occurring event among the m_2 equally likely events of the second subgroup is $c \log m_2$, and it occurs for a proportion of time equal to m_2/m. The calculation then gives

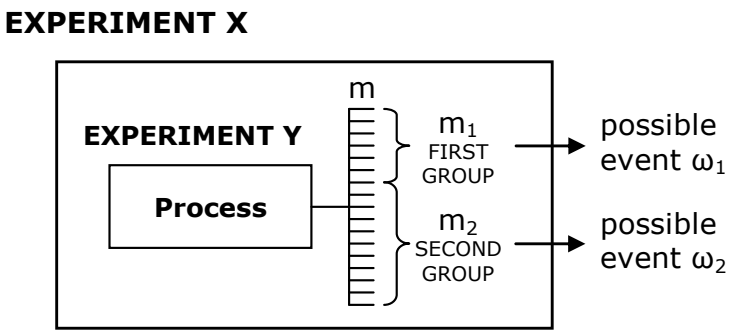

Figure 6.4. An experiment with two outputs of unequal probability.

$$I(X) = I(Y) - \frac{m_1}{m} c \log m_1 - \frac{m_2}{m} c \log m_2 = -c\left(p_1 \log p_1 + p_2 \log p_2\right) \tag{6.12}$$

In the case of n subgroups, $I(X)$ will assume the form of $H(X)$ in Eq. (6.6) justifying the postulate that $H(X)$ represents the uncertainty about the outcome for a set of n possible events not necessarily equally likely.

6-3.2 Shannon entropy

The sum in Eq. (6.6) bears a formal resemblance to thermodynamic entropy as defined in Statistical Mechanics introduced by Boltzmann in the 19th century and further discussed by Gibbs and Von Neumann (see for example, Tsallis, 1988). For this reason $H(X)$ is also called the entropy function of $p_1, p_2, \ldots, p_n$ and is sometimes written as $H(p_1, p_2, \ldots, p_n)$. Other names such as 'information entropy' or 'Shannon entropy' have also been used in the literature.

Shannon (1948) showed, in a more rigorous way than used here to arrive at Eq. (6.12), that the only function $H(X)$ able to represent the uncertainty about the outcome of an experiment X is of the form indicated by Eq. (6.6). The proof was based on three properties pertaining to the function $H(X)$ which quantifies the uncertainty about the outcome of an experiment X with a set of possible events, Ω, whose individual probabilities of occurrence are $p_1, p_2, \ldots, p_n$: (i) $H(X)$ must be continuous in p_i; (ii) $H(X)$ must be a monotonically increasing function of n, when all the p_i's are equal; and (iii) if an event is broken down into two successive events, the original $H(X)$ should be the weighted sum of the individual values of $H(Y)$, $H(Z)$, etc; this property is illustrated in **Figure 6.5** for a case with three possible events.

The unit of Shannon entropy depends on the logarithmic base used, as changing the value of the constant c is equivalent to imposing $c = 1$ and varying the base of the logarithm. In this work, the logarithm used is the natural logarithm to the base e, thus

$$H(X) = -\sum_{i=1}^{n} p_i \log p_i \tag{6.13}$$

and the unit is called *nat* (natural units). However, the unit used is immaterial and should not be a cause for concern since Shannon entropy is usually discussed in terms of relative values.

The concept of information entropy can be extended to events with conditional probabilities or redefined for continuous random variables with a probability density function. However,

the entropy expression given by Eq. (6.13) bears enough significance and is sufficiently powerful for the purposes of this study.

6-3.3 Maximum entropy

The entropy function given by Eq. (6.13) satisfies many interesting properties including additivity, symmetry, concavity, sub-additivity and recursivity. One of the most important characteristics of the entropy function concerns its maximum. It can be shown that

$$-\sum_{i=1}^{n} p_i \log p_i \le \log n \tag{6.14}$$

with equality holding if and only if $p_i = 1/n$ regardless of i (see for example, Hankerson *et al.*, 2003). In other words, the uncertainty about the outcome of an experiment X (quantified by the entropy function) is maximum when the discrete distribution of probabilities of the possible events is uniform. For example, in the case of only two possible events ($i = 1, 2$) with probabilities p and $1 - p$, the entropy function in Eq. (6.13) can be represented as a function of p, thus

$$H(X) = -p \log p - (1-p)\log(1-p) \tag{6.15}$$

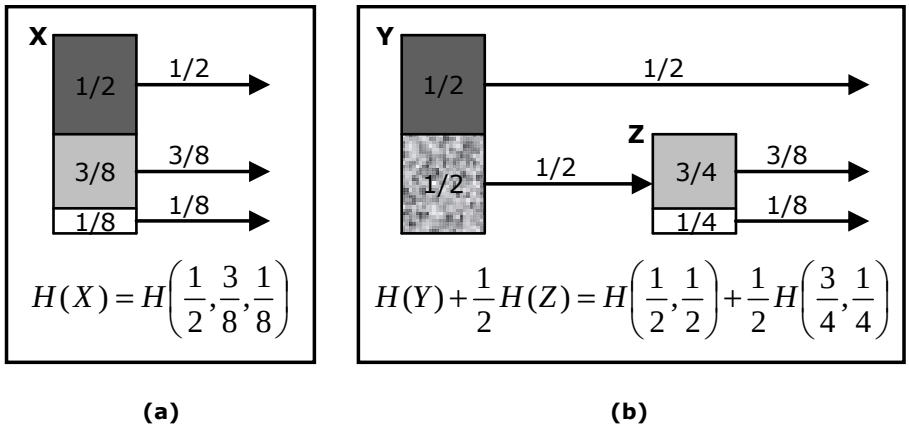

Figure 6.5. Decomposition of (a) an experiment X with three possible events into (b) two consecutive experiments, Y and Z, both with two possible events. The values of entropy before and after the decomposition must agree.

which is plotted in **Figure 6.6**. The graph depicts the property expressed by Eq. (6.14): the entropy is maximum when $p = 1 - p = 0.5$ and its value is $H_{max} = 0.693$ nat (i.e., log 2). The figure shows that the entropy function increases if the two probabilities are replaced with another two that better approximate a uniform probability distribution.

6-3.4 Entropy and mixing

The entropy concept offers a very good means of describing probabilistic phenomena in terms of uncertainty. Thus, local or global quality indices can be defined on the basis of the uncertainty about the outcome of a random variable, which makes entropy ideally suited to the study of mixing phenomena. In this work, the objective is to describe local and global mixing in a batch stirred vessel, and the spectrum of *transition probabilities* of an injected substance (e.g. a dye) and the estimation of the related uncertainty about the occurred transition will, therefore, form the first basis for the application of the above concepts. Given a three-dimensional grid with equal volume cells which defines the system, the transition from the *i*-th cell (the injection cell) to the *j*-th cell occurs when an element of the injected substance is located in the *j*-th cell after a fixed time interval, Δt, during which knowledge of the location of the element is irrelevant.

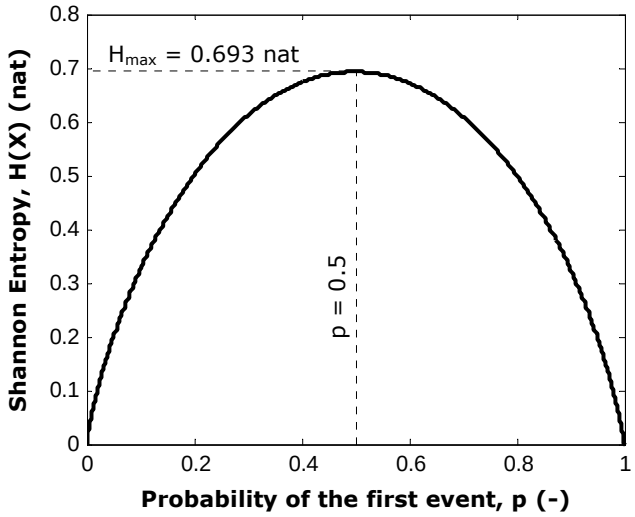

Figure 6.6. Entropy function, $H(X)$, as given by Eq. (6.15) for the case of two possible events with probabilities p and $1 - p$.

In the hypothetical condition of zero-mixing, the substance will never exit the injection cell. On the other hand, in the case of perfect mixing the injected substance is able to reach any cell, distributing itself uniformly throughout the whole vessel. In the case of zero-mixing, the sole non-zero transition probability is related to the transition from the *i*-th cell to the *i*-th itself (the injection cell), while the transition from the *i*-th cell to a different cell *j* has a zero probability of occurrence, thus

$$p_{ii}^{\uparrow} = 1,\ p_{ij}^{\uparrow} = 0 \quad \text{where} \quad j \neq i \tag{6.16}$$

The superscript ↑ indicates that the transition from cell *i* is outward. In this case, the transition *ii* is a certain outcome and, consequently, the uncertainty about the outcome must be zero. The case of plug flow, where the substance moves but without dispersing, can be considered as another extreme example of the zero-mixing condition where the transition *ii* has zero probability and another specific transition *ij* is certain. However, by judiciously renaming the destination cells, Eq. (6.16) maintains its validity; i.e., one single p_{ij} is non-zero and could be renamed as p_{ii}.

In the case of perfect mixing any transition *ij* has the same probability of occurrence, thus

$$p_{ij}^{\uparrow} = \frac{1}{n_C} \quad \text{where} \quad j = 1,2,...,n_C \tag{6.17}$$

where n_C is the total number of grid cells. Intuitively, in this case, an observer cannot be more uncertain about the occurring transition and, consequently, the uncertainty about the outcome must be maximum.

In order to prove the above conjectures concerning the uncertainty about the outcome in the cases of zero-mixing and perfect mixing, Shannon entropy can be employed to estimate such an uncertainty in both cases. Using the probability distribution defined by Eq. (6.16), estimation of the entropy via Eq. (6.13) gives $H_i^{\uparrow} = 0$ nats, where *i* denotes the injection cell and the convention $0 \times \log 0 = 0$ is used. If the probability distribution is uniform as defined by Eq. (6.17), the value of entropy obtained via Eq. (6.13) is $H_i^{\uparrow} = \log n_C$ and, by virtue of Eq. (6.14), such a value is the maximum obtainable with a set of n_C possible events. In consequence, $H_i^{\uparrow}$ is a non-negative continuous function which gradually increases from 0 to its maximum value at $H_{i,\max}^{\uparrow} = \log n_C$, when the transition probability distribution tends to the

uniform distribution defined by Eq. (6.17).

The more uncertain an observer is about the occurred transition, the less predictable the transition itself is, the more uniform the transition probability spectrum is, and the better the fluid is mixed. Since mixedness increases with the uncertainty about the occurred transition up to the condition of perfect mixing, the evaluation of such an uncertainty can be used to define an index quantifying the mixing capacity, i.e., the ability to mix, thus

$$M_i^{\uparrow} = \frac{H_i^{\uparrow}}{H_{i,\max}^{\uparrow}} = -\frac{1}{\log n_C} \sum_{j=1}^{n_C} p_{ij}^{\uparrow} \log p_{ij}^{\uparrow} \tag{6.18}$$

where $M_i^{\uparrow}$ is the *first entropy mixing index* and its value lies between 0 and 1. It is important to note that the entropy mixing index is related to the injection cell *i* and its value, therefore, will vary with the location of the injection point.

Nevertheless, the definition of the first entropy mixing index is not entirely satisfactory. It uses transition probabilities to estimate the dispersion capacity of a substance following a localised injection, however, the quality of mixing is not only governed by the ability of an injected substance to disperse but also by the degree of diversification of the flow. In other words, for good mixing it is also important that elements of a pre-dispersed substance flowing into a cell, would emanate from a large number of different cells (Guida *et al.*, 2010c).

Where the tracer substance is already fully dispersed in the vessel, the movement of the tracer, with reference to the *i*-th cell, can be classified into two types according to its direction: outflow, from cell *i* to a cell *j* and inflow, from a cell *j* to cell *i*. If the flow regime can be assumed to be unaffected by the introduction of the tracer substance, taking as reference the *i*-th cell, the presence of other amounts of tracer in the rest of the vessel is inconsequential to the evaluation of the outflow. Therefore, the *i*-th cell can be considered as the 'injection' cell and the elements of the tracer substance located in the cell can be marked and followed as the only elements of the inner substance. Consequently, the estimations of the outflow, the related transition probability distribution as well as the consequent uncertainty lead again to Eq. (6.18). In order to expand the definition of the entropy mixing index, therefore, it is necessary to analyse the inflow of the tracer substance in the *i*-th cell.

We refer to the probability, $p_{ij}^{\downarrow}$, that an element of the tracer substance was located in cell *j*

some time Δt before flowing in the *i*-th cell, as *provenance* probability which provides a probability spectrum useful to estimating a new parameter $M_i^{\downarrow}$, the entropy mixing index associated with the diversification of the inflow to the *i*-th cell. Using intuitive considerations and theoretical verifications analogous to those presented for the transition probability spectrum above, the entropy function of a set of provenance probabilities, $H_i^{\downarrow}$, assumes the value 0 for a zero-mixing condition and $H_{i,\max}^{\downarrow} = \log n_C$ for a perfect mixing state.

In a similar way to Eq. (6.18), the entropy function of a set of provenance probabilities, normalised by its maximum value, provides the *second entropy mixing index* which is associated with the inflow to the *i*-th cell, thus

$$M_i^{\downarrow} = \frac{H_i^{\downarrow}}{H_{i,\max}^{\downarrow}} = -\frac{1}{\log n_C} \sum_{j=1}^{n_C} p_{ij}^{\downarrow} \log p_{ij}^{\downarrow} \tag{6.19}$$

Mixing performance can hence be imagined as being the combination of two factors related to dispersion of the local outflow and diversification of the local inflow. Finally, supposing that these two phenomena contribute equally to the total mixing performance, the arithmetic average of the two local entropy mixing indices described above yields the *third entropy mixing index*; that is

$$M_i = \frac{M_i^{\uparrow} + M_i^{\downarrow}}{2} \tag{6.20}$$

This more complete mixing index gives a description of mixing performance based on both the local outflow and the local inflow. It takes into consideration how well the fluid elements disperse after flowing out of a cell as well as how diverse is the fluid flowing into the cell, i.e., it considers both the past and future history of the local flow. It should be noted that the three mixing indices defined above are all highly dependent on Δt which is set initially for estimating the two probability spectra; i.e., $p_{ij}^{\downarrow} = p_{ij}^{\downarrow}(\Delta t)$ and $p_{ij}^{\uparrow} = p_{ij}^{\uparrow}(\Delta t)$.

6-3.5 Multiple tracking

Quantification of the two probability spectra, $p_{ij}^{\uparrow}$ and $p_{ij}^{\downarrow}$, is the first experimental challenge. Where the position of multiple elements of the tracer substance (e.g. small particles) can be readily detected, the number of elements contained in each grid cell, n_i, is known at any time. Furthermore, if the Lagrangian trajectory of each individual particle can be depicted, the

number of transitions from the *i*-th to the *j*-th cell occurring during a fixed time interval, Δt, is expressed by the number of particles, $n_{ij}^{\uparrow}$, which at $t = t_o$ are inside cell *i* and at $t = t_o + \Delta t$ will be inside cell *j*. A sufficiently large number of such tracked particles allows statistical considerations, so that the frequency of transition occurrence is a good approximation of probability and

$$p_{ij}^{\uparrow} = n_{ij}^{\uparrow} / n_i \tag{6.21}$$

Similarly, considering the provenance of the particles flowing into the *i*-th cell, the number of particles, $n_{ij}^{\downarrow}$, which at $t = t_o$ are inside cell *i* and at $t = t_o - \Delta t$ were inside cell *j*, can be determined, thus

$$p_{ij}^{\downarrow} = n_{ij}^{\downarrow} / n_i \tag{6.22}$$

The process for computing the numerical values of n_i and $n_{ij}^{\uparrow}$ is schematically illustrated in **Figure 6.7**; a similar procedure is used to obtain $n_{ij}^{\downarrow}$. These numbers of particles are of the same order of magnitude as the ratio between the number of tracked particles and n_C^2, as n_i is of the order of the ratio between the number of tracked particles and n_C.

In principle, an experiment could be conceived using a large number of particles. If this is not possible, because of the nature of the process, a single experiment can be repeated a large number of times considered sufficient to obtain a good accuracy of measurement, e.g. one die can be cast 100 times if 100 dice cannot be cast simultaneously. In order to avoid erroneous results, however, the experiment must be repeated under identical conditions. Such an approach can be used to measure the above probability spectra. Thus, by accurate Lagrangian tracking of a single particle, the technique of positron emission particle tracking provides a unique and powerful tool for measuring transition and provenance probabilities.

The single radioactive neutrally-buoyant particle tracer visits a grid cell many times during an experiment. The tracer could be viewed as a different particle every time it leaves a cell and returns to it, thus, a multiple tracking procedure could be emulated by partitioning the tracer trajectory in as many segments as the number of times the particle tracer visits the cell. In order to evaluate whether the particle tracer can be treated as a different particle when revisiting the same grid cell, it is necessary to estimate the minimum segment of the past particle tracer trajectory which will affect the rest of its trajectory, i.e., the minimum time

necessary for the tracer to lose its memory.

6-3.6 Decorrelation time

As already discussed in Section 3-4.2, the autocorrelation coefficient, A_P, of the position vector **P**(x,y,z) offers an effective tool to quantitatively determine a time range during which the instantaneous location of the tracer is influenced by its initial position. The autocorrelation coefficient of a single Cartesian coordinate, for example $x(t)$, is computed via the numerical approximation of the equation

$$A_x(\tau) = \frac{\int_{-\infty}^{+\infty} x(t)x(t-\tau)dt}{\int_{-\infty}^{+\infty} x^2(t)dt} \tag{6.23}$$

where τ is the time shift. As demonstrated by Eq. (3.22), a combination of the three

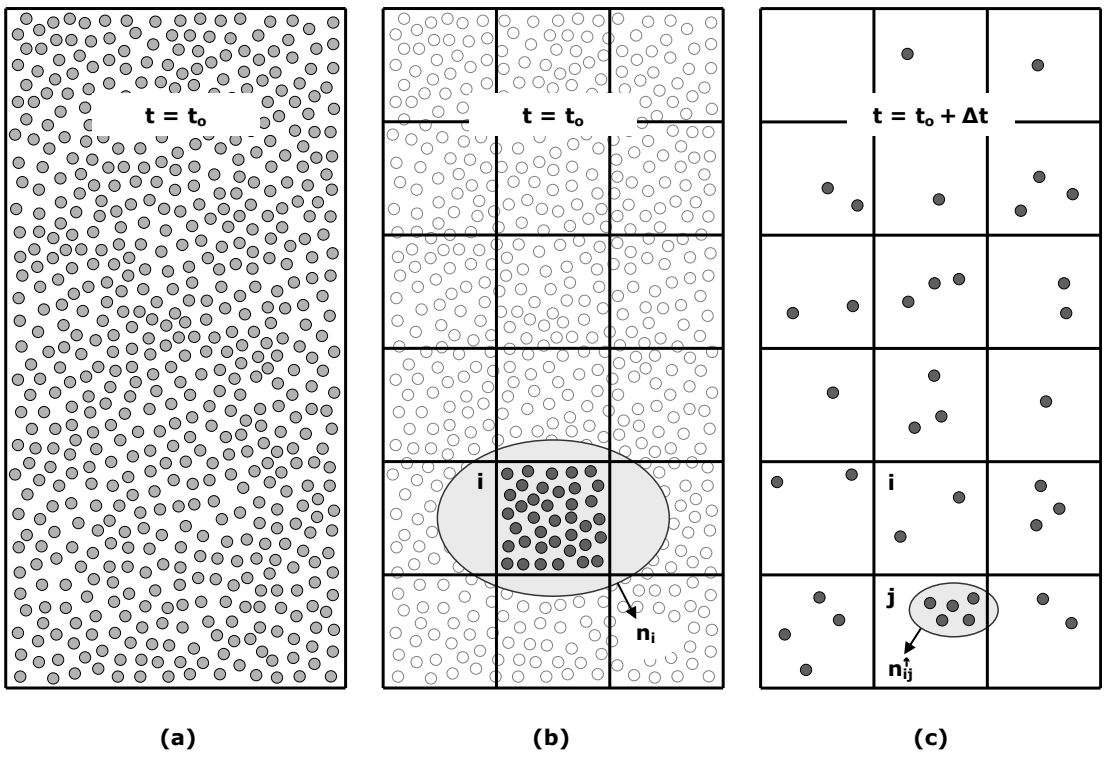

Figure 6.7. Two-dimensional illustration of the computational process to estimate n_i and $n_{ij}^{\uparrow}$: (a) the particles are dispersed within the vessel at time t_o; (b) a grid is defined, n_i particles are inside cell i at time t_o and the remaining particles are disregarded; (c) after a time interval Δt, $n_{ij}^{\uparrow}$ of n_i particles are within cell j.

coefficients A_x, A_y and A_z, provides the autocorrelation coefficient of the position vector **P**, that is

$$A_P(\tau) = \frac{\langle x^2 \rangle A_x(\tau) + \langle y^2 \rangle A_y(\tau) + \langle z^2 \rangle A_z(\tau)}{\langle x^2 \rangle + \langle y^2 \rangle + \langle z^2 \rangle} \tag{6.24}$$

The decorrelation time, which is identified by the timescale characterising the decay with the time shift of the autocorrelation coefficient A_P, is representative of how fast the particle tracer loses its memory. The numerical value of the decorrelation time, τ_d, is determined here by the least squares method assuming a one-parametric exponential decay of A_P squared as given by

$$A_P^2(\tau) \cong e^{-2\frac{\tau}{\tau_d}} \tag{6.25}$$

For correct data analysis, the particle tracer can be viewed as a different particle only after a time $3\tau_d$ since the absolute value of the autocorrelation coefficient is lower than 5% of its initial value, $A_P(0) = 1$. In the instance of N = 300 rpm, the threshold value $3\tau_d$ was 1.85 s, as shown in **Figure 3.13**.

6-3.7 PEPT runtime

A PEPT runtime of 45 min provides 250-300 thousands of tracer locations (n_L) under the present turbulent conditions; consequently, the average number of locations contained in a cell is 2500-3000 where a grid of ~ 100 cells is used. Some of the detected locations in a cell cannot be used to simulate a different particle as they are separated by time intervals which are too short. An iterative filter function discards locations (generally < 20%) in order to ensure $\Delta t > 3\tau_d$ between two locations within the same cell. The remaining average number of locations per cell is nonetheless sufficiently large to enable an accurate estimation of transition and provenance probabilities.

Since in the stirred vessel, as established above, the ergodicity condition is fulfilled and the grid cells have the same volume, the actual number of PEPT locations contained in each grid cell is approximately the same and, thus, will be a good approximation to the mean number of locations per cell. The tracer trajectory partitioned in as many segments as the number of times the tracer visits the *i*-th cell, will emulate the tracking of usually more than 2000 particles. Although a longer PEPT runtime would enhance resolution, 2000 ‘tracked’

particles and ~ 100 toroidal grid cells are sufficient to give a very detailed 2D description (radial-axial) of mixing efficiency hitherto unreported in mixing studies.

6-4 Results and discussion

6-4.1 Mixing indices

A computational code was developed for the analysis of PEPT data based on the theory described above. Using cylindrical coordinates, maps of the different entropy mixing indices are obtained by defining a grid consisting of n_C equal volume cells ($i, j = 1, 2,\ldots, n_C$), estimating the decorrelation time τ_d so that the correct n_i are obtained, and calculating the probability spectra $p_{ij}^{\uparrow}$ and $p_{ij}^{\downarrow}$ with reference to a pre-fixed Δt ranging from 0 to 2 min. Two-dimensional maps of entropy mixing indices are shown in **Figure 6.8**, for both the PBTD and PBTU where $n_C = 98$. The plots highlight the differences between the two agitation modes: the use of an up-pumping instead of a down-pumping impeller clearly impairs the local mixing efficiency especially in the upper part of the vessel, and increases non-uniformity between different regions of the vessel.

In **Figure 6.8a** and **d** the first entropy mixing index, $M_i^{\uparrow}$, is very dependent on position confirming that the feed position has a strong effect on the measured local dispersion capacity. On the other hand, in **Figure 6.8b** and **e** the maps of $M_i^{\downarrow}$ demonstrate that the outlet position strongly influences the local degree of flow diversification in a system where there are multiple injections (of several different substances) distributed in the vessel. As a result, the third mixing index, M_i, shown in **Figure 6.8c** and **f** which describes both the local ability to disperse flow and the local state of flow diversification, varies significantly with position and it is maximum at $r = 0.85\ R$ and $h = 0.55\ H$ for the PBTD, and at $r = 0.85\ R$ and $h = 0.47\ H$ for the PBTU. It is important to point out here that a system presenting similar maps of the mixing indices but obtained with a shorter time interval, Δt, is to be preferred (i.e., it achieves similar mixing results but in less time).

6-4.2 Global mixing index

Where a quick comparison between two systems is needed or multiple inlets and outlets are present, a global entropy mixing index can be very useful. As the grid cells are of equal

volume, such a global index can be defined as the arithmetic mean of the local indices M_i, i.e.,

$$G = \frac{1}{n_C} \sum_{i=1}^{n_C} M_i \tag{6.26}$$

Similarly, global values can be obtained for $G^{\uparrow}$ and $G^{\downarrow}$. However, **Figure 6.9** which represents the variation of the mixing indices as a function of Δt, reveals that $G \cong G^{\uparrow} \cong G^{\downarrow}$ for any given rotational speed and agitation mode of the PBT. The global mixing index, G, is

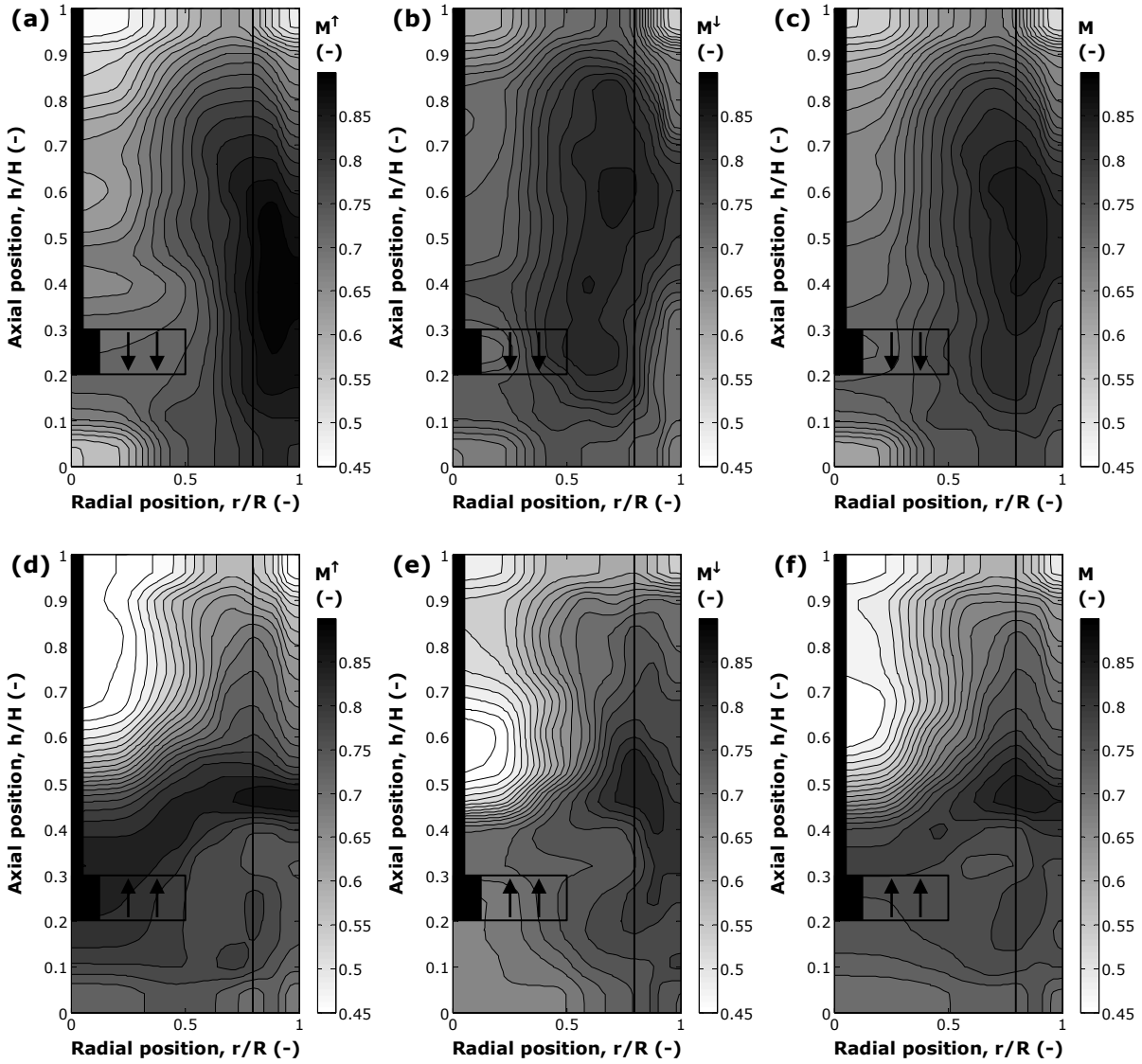

Figure 6.8. Radial-axial maps of the three entropy mixing indices $M^{\uparrow}$, $M^{\downarrow}$ and M at N = 300 rpm, n_C = 98, Δt = 200 ms: (a-c) PBTD; (d-f) PBTU.

a saturation curve with an asymptotic value of 1, i.e., $G \to 1$ as $\Delta t \to \infty$. Increasing the agitation speed increases the slope of the curve which, as expected, improves mixing; however, at the same speed, the PBTD always achieves better mixing than the PBTU.

In order to obtain information on the functional expression $G(\Delta t)$, the logarithm of the residual $(1 - G)$ and its square have been examined as shown in **Figure 6.10**; note that the final part of the curves is flat because of the experimental error due to the non-infinite number of particles used to estimate the transition and provenance probabilities. Ignoring the flat part of the curves, $\log(1 - G)$ in **Figure 6.10a** show a parabolic trend while $(\log(1 - G))^2$ in **Figure 6.10b** can be well fitted by a straight line, thus

$$G \cong 1 - \exp\left(-(\lambda \Delta t)^{0.5}\right) \tag{6.27}$$

where the decay parameter λ is obtained by the least squares method. A convergence time can then be determined as a function of λ using Eq. (6.27); for example t_{99} is the time necessary to have $G = 0.99$ and its value is $\sim 21/\lambda$. In **Figure 6.11** values of t_{99} are plotted depicting an approximately linear relationship with $1/N$. Consequently, $N\,t_{99}$ is approximately constant

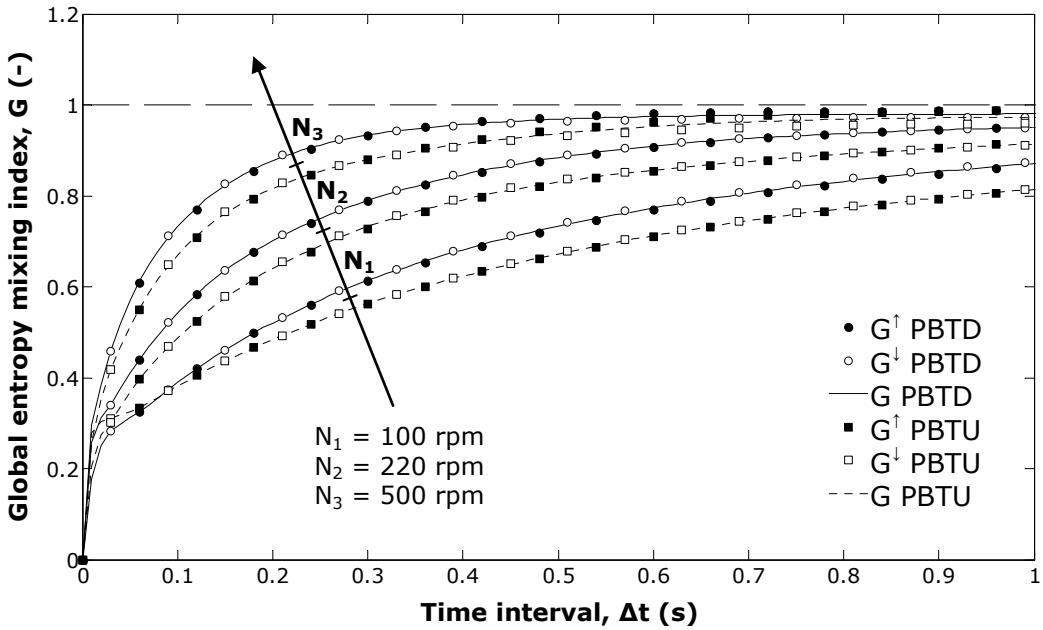

Figure 6.9. Variation of the global entropy mixing indices, $G^{\uparrow}$, $G^{\downarrow}$ and G, with Δt for different rotational speeds and PBT agitation modes.

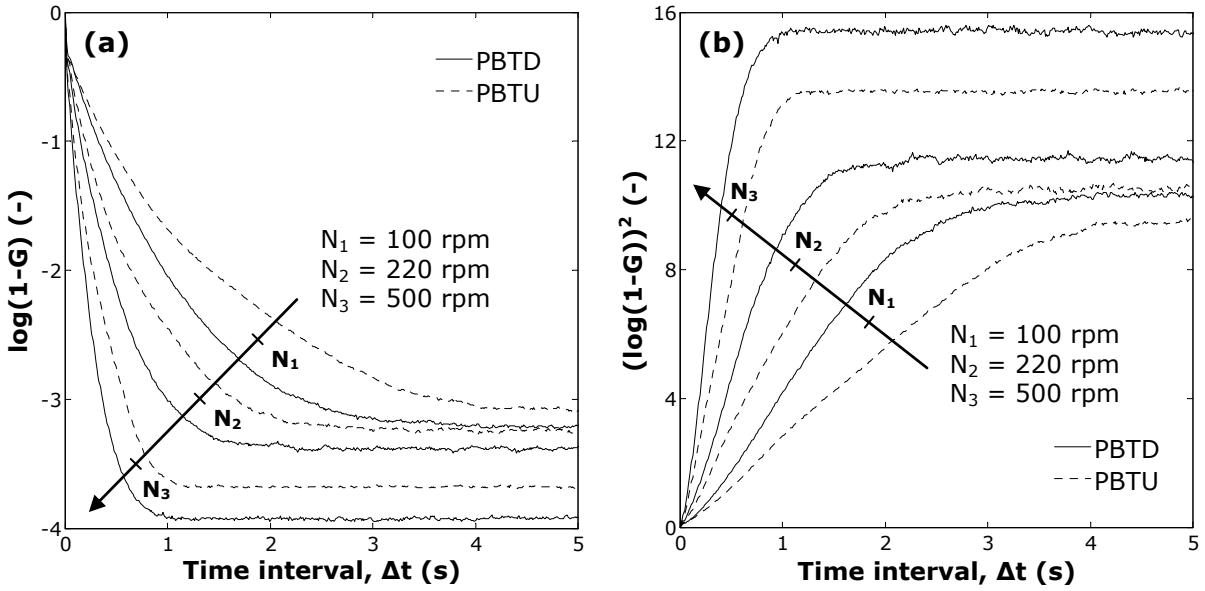

Figure 6.10. Two functions of G versus Δt at different rotational speeds and PBT agitation modes.

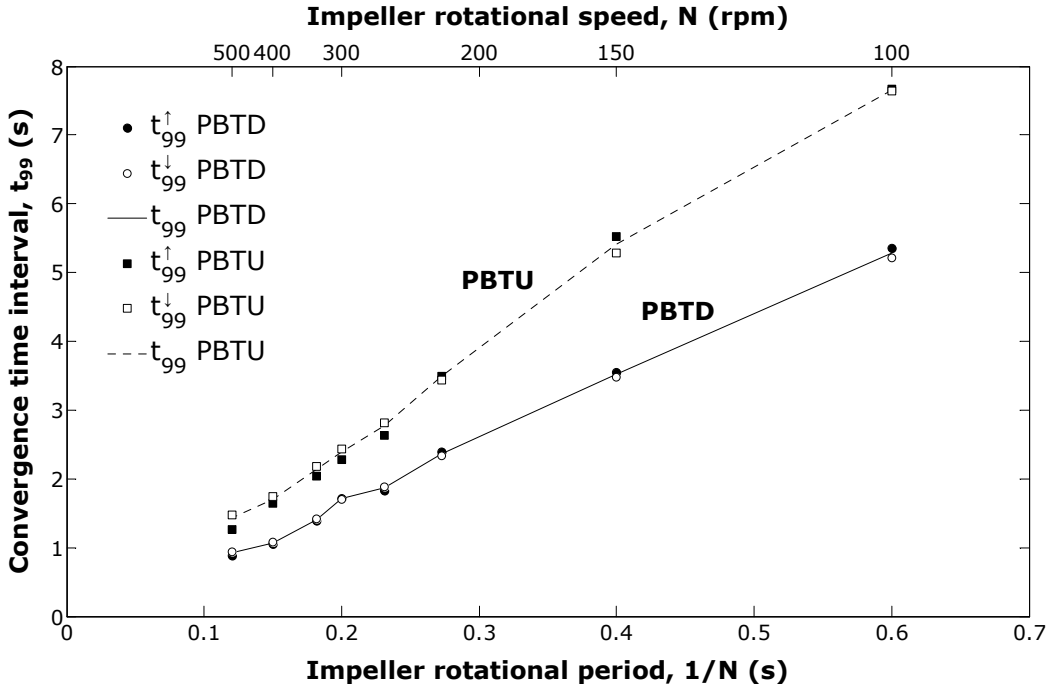

Figure 6.11. Convergence time intervals $t_{99}^{\uparrow}$, $t_{99}^{\downarrow}$ and t_{99} of the three global entropy mixing indices, $G^{\uparrow}$, $G^{\downarrow}$ and G, as a function of $1/N$ for both PBT agitation modes.

showing a clear resemblance to the macroscale mixing time, or simply mixing time, typically used for characterising stirred vessels (Nienow, 1997a).

Note that the above approximation $G \cong G^{\uparrow} \cong G^{\downarrow}$ applicable for the global indices may not be admissible in the case of a local analysis, so that $M_i \cong M_i^{\uparrow} \cong M_i^{\downarrow}$ may not necessarily be valid. However, a dependence of the local entropy mixing indices, $M_i^{\uparrow}$ and $M_i^{\downarrow}$, on Δt similar to the one illustrated in **Figure 6.9** for the global mixing indices will be shown below, and Eq. (6.27) can therefore be used to fit the experimental data related to the local mixing indices $M_i^{\uparrow}$ and $M_i^{\downarrow}$.

6-4.3 Macroscale mixing time

The basis of the technique used to quantify the spectrum of transition probabilities can be employed to simulate a localised injection of a tracer substance and obtain information about its local volume concentration after a time interval Δt. Knowledge of the initial number of particles n_i in cell i and the number of particles which move from cell i to cell j can lead to knowledge of the local concentration of particles in cell j. If V_P is the volume of a single particle tracer and ΔV is the volume of a grid cell, the initial volume concentration in the injection cell is

$$c_{io} = \frac{n_i V_P}{\Delta V} \tag{6.28}$$

For cells of equal volume, $\Delta V = V_T/n_C$ where V_T is the volume of the tank. After a theoretically infinite time, the concentration in the tank is uniform and its value is $c_i = c_{io}/n_C$. When $\Delta t \neq 0$, a number of particles subjected to the ij transition, $n_{ij}^{\uparrow}$, generate a non-zero volume concentration in cell j, that is

$$c_{ij} = \frac{n_{ij}^{\uparrow} V_P}{\Delta V} \tag{6.29}$$

The variance (for varying j and fixed i) of the local volume concentration normalised by its final value, c_i, is an index of the homogeneity achieved in the vessel and is given by

$$\sigma_i^2 = \frac{1}{n_C} \sum_{j=1}^{n_C} \left(\frac{c_{ij}}{c_i} - 1 \right)^2 \tag{6.30}$$

Combining Eqs. (6.21) and (6.28)-(6.30), σ_i^2 can be expressed as a function of the transition probabilities, thus

$$\sigma_i^2 = n_C \sum_{j=1}^{n_C} \left(p_{ij}^{\uparrow}\right)^2 - 1 \tag{6.31}$$

While in previous experimental works such a variance was, for example, determined as the variance of the output of usually 1-3 conductivity probes following the localised injection of a salt tracer, in this case Eq. (6.31) provides the variance of the output from the equivalent of a set of 98 non-intrusive local concentration probes uniformly distributed in the vessel. Moreover, the calculation can be repeated by changing the index *i*, which is experimentally equivalent to changing the feed point of the tracer. Thus, 98 different injection points can be investigated in the tank. The two quantities σ_i^2 and $M_i^{\uparrow}$ are both dependent only on the set of transition probabilities $p_{ij}^{\uparrow}$ whose distribution changes with Δt. While σ_i^2 is a measure of the quality of mixing achieved after a time Δt, the entropy mixing index $M_i^{\uparrow}$ is a measure of the level of dispersion obtainable in Δt. Their physical significance as well as their mathematical definitions given by Eqs. (6.18) and (6.31), suggest that it should be possible to find some relationship between these two parameters.

The experimental measurement of σ_i^2 as a decreasing function of time allowed the definition of the (macroscale) mixing time as the time necessary to reach a pre-determined degree of homogeneity (Ruszkowski, 1994). Conventionally, the mixing time θ_m is the time necessary to obtain a degree of homogeneity of 95%, that is $\sigma_i = 0.05$, corresponding to a local concentration mainly between 95% and 105% of the average concentration in the vessel; thus $\sigma_i^2 = 0.0025$ for $\Delta t = \theta_m$. When such a degree of homogeneity is reached, the measured quantities tend towards their limiting values; i.e., $p_{ij}^{\uparrow} \to 1/n_C$, $\sigma_i^2 \to 0$ and $M_i^{\uparrow} \to 1$. Consequently, some approximations can be used.

A real function $f(\eta)$ that is infinitely differentiable in a neighbourhood of a real number *a*, can be approximated by its Taylor series:

$$f(\eta) = \sum_{q=0}^{\infty} \frac{f^{(q)}(a)}{q!} (\eta - a)^q \tag{6.32}$$

where $f^{(q)}(a)$ denotes the *q*-th derivative of *f* evaluated at point *a*; the zero-th derivative of *f*

is defined as *f* itself. If the range of interest of η is 'sufficiently' close to *a*, the series can be even truncated at the first-order term, so that

$$f(\eta) \cong f(a) + \left.\frac{df}{d\eta}\right|_a (\eta - a) \tag{6.33}$$

Consequently, the above approximation can be applied to the natural logarithm function $\log p_{ij}^{\uparrow}$ when $p_{ij}^{\uparrow} \to 1/n_C$, so that

$$\log p_{ij}^{\uparrow} \cong \log\left(\frac{1}{n_C}\right) + n_C\left(p_{ij}^{\uparrow} - \frac{1}{n_C}\right) = n_C p_{ij}^{\uparrow} - (1 + \log n_C) \tag{6.34}$$

and as a result, Eq. (6.18) can be modified to give another expression of the first entropy mixing index valid only when $p_{ij}^{\uparrow} \to 1/n_C$, thus

$$M_i^{\uparrow} \cong -\frac{n_C}{\log n_C}\sum_{j=1}^{n_C}\left(p_{ij}^{\uparrow}\right)^2 + \frac{1+\log n_C}{\log n_C} \tag{6.35}$$

Combining Eqs. (6.31) and (6.35) yields the sought relationship between the variance of the normalised local volume concentration σ_i^2 and the entropy mixing index $M_i^{\uparrow}$, thus

$$M_i^{\uparrow} \cong 1 - \frac{\sigma_i^2}{\log n_C} \tag{6.36}$$

However, the validity of this correlation is limited to the values of Δt for which a high degree of homogeneity has already been reached. If the mixing time θ_m is the time necessary to achieve $\sigma_i = 0.05$, according to Eq. (6.36), θ_m is also the time necessary to achieve $M_i^{\uparrow}(\theta_m) = 0.9994$ where $n_C = 98$. In a similar way to the case of the global entropy mixing index *G*, a convergence time $t_{99x}^{\uparrow}$ can be defined as the time required to reach $M_i^{\uparrow} = 0.9994$, so that

$$t_{99x}^{\uparrow} \cong \theta_m \tag{6.37}$$

This important result allows the mixing time to be directly calculated via an entropy study of the system and it paves the way for an extended investigation of such a fundamental parameter. The subscript *i* in $M_i^{\uparrow}$ indicates the injection point of the tracer, therefore, the mixing time in this case can be measured for 98 feed positions. An extension of the concept

of mixing time can be found in the meaning of $t_{99x}^{\downarrow}$, the time necessary to achieve $M_i^{\downarrow} = 0.9994$. By similar considerations, it can be shown that $t_{99x}^{\downarrow}$ is the time necessary to find a similar ($\sigma = 0.05$) concentration of n_C different tracer substances in cell *i* (outlet) starting from an initial state in which each equal volume cell contains the same amount of a different tracer (i.e., totally segregated system). Alternatively, $t_{99x}^{\downarrow}$ could be perceived as the imaginary mixing time if the temporal evolution of the flow were inverted.

The definition in Eq. (6.20) indicates that values of the third entropy mixing index M_i are constantly between $M_i^{\uparrow}$ and $M_i^{\downarrow}$ which are modelled using the expression of Eq. (6.27). The convergence time, t_{99x}, necessary to achieve $M_i = 0.9994$, could therefore be approximated by the arithmetic mean of $t_{99x}^{\uparrow}$ and $t_{99x}^{\downarrow}$. However, in this work such a convergence time, t_{99x}, which contains in its definition the concepts of flow dispersion and diversification, was calculated in a more accurate way numerically solving in each grid cell the transcendental equation

$$\exp\left(-\left(\lambda^{\uparrow} t_{99x}\right)^{0.5}\right) + \exp\left(-\left(\lambda^{\downarrow} t_{99x}\right)^{0.5}\right) = 2(1 - 0.9994) \tag{6.38}$$

which is obtained by combining Eq. (6.20) and Eq. (6.27) used for both $M_i^{\uparrow}$ and $M_i^{\downarrow}$. The decay parameters $\lambda^{\uparrow}$ and $\lambda^{\downarrow}$ are obtained locally using the least squares method based on the monoparametric expression of Eq. (6.27).

6-4.4 Local analysis

As discussed above, the maps depicted in **Figure 6.8** were obtained using Δt = 200 ms. For Δt = 0 s the mixing indices are zero (maps uniformly white) while for Δt = 10 s the indices will converge to 1 (maps uniformly black). A similar variation of the local mixing indices with the time interval shown in **Figure 6.9** for the global mixing index is expected and **Figure 6.12** confirms such a supposition, the expression in Eq. (6.27) can therefore be safely used to fit the experimental data related to the local mixing indices. The figure shows how in different positions of the tank the convergence of the mixing indices could require very different time intervals and so, as anticipated above, the approximation $M_i \cong M_i^{\uparrow} \cong M_i^{\downarrow}$ is indeed not strictly valid in the case of a local analysis. Moreover, the curves in **Figure 6.12c** and **d** show that, although a PBTD mode generally offers a faster convergence, for certain feed or outlet positions the PBTU may in fact perform better.

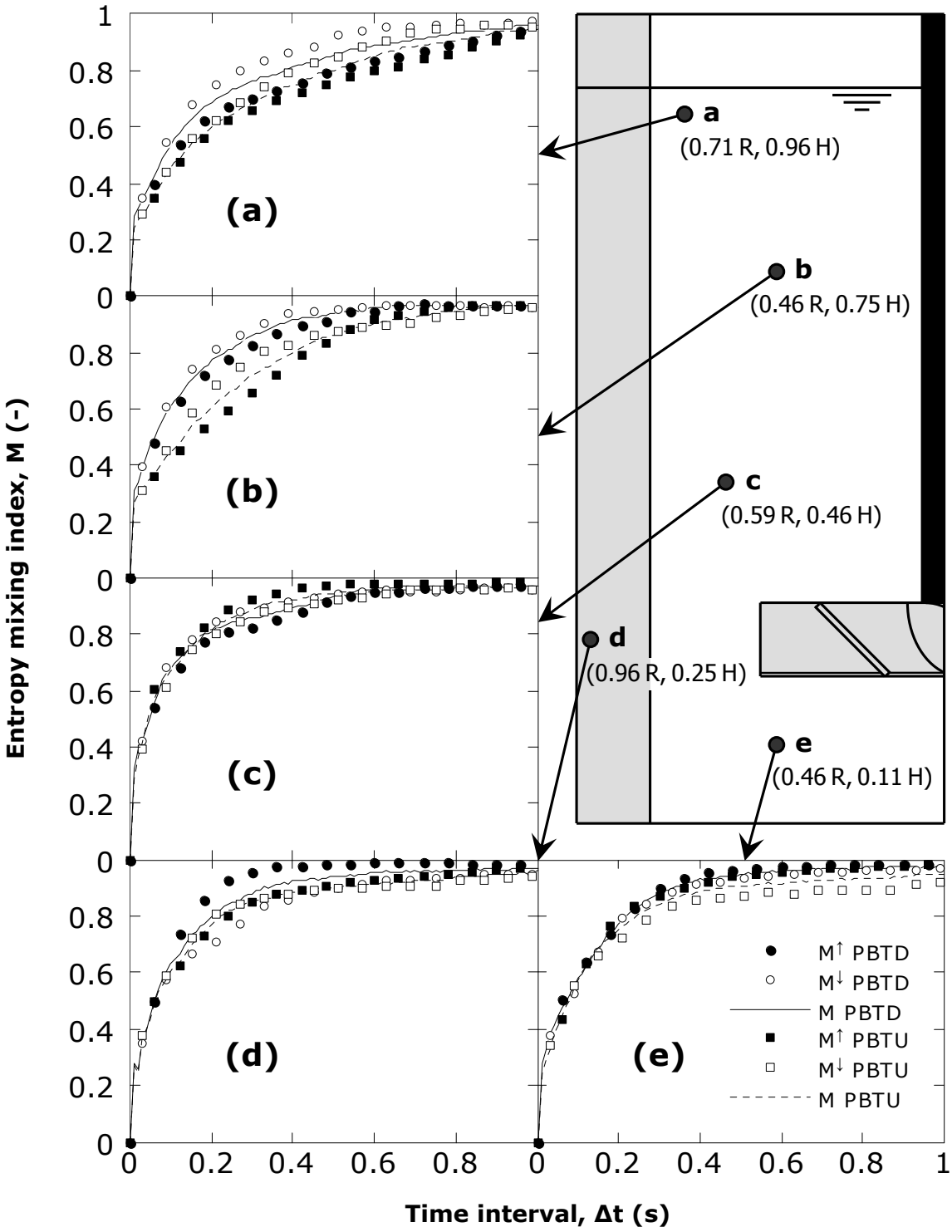

Figure 6.12. Local variation of the three entropy mixing indices $M_i^{\uparrow}$, $M_i^{\downarrow}$ and M_i with the time interval Δt at N = 300 rpm, n_C = 98.

The maps in **Figures 6.13-6.15** offer an interesting means of estimating the local mixing capacity at various inlet/outlet positions for different agitation speeds. The qualitative resemblance between the convergence time maps at different rotational speeds is evident due to the linear dependence of the local convergence times on 1/*N*. However, the maps are quantitatively different as increasing *N* proportionally reduces the convergence times. Plots similar to **Figure 6.11** can be obtained for each one of the 98 grid cells, and an example is

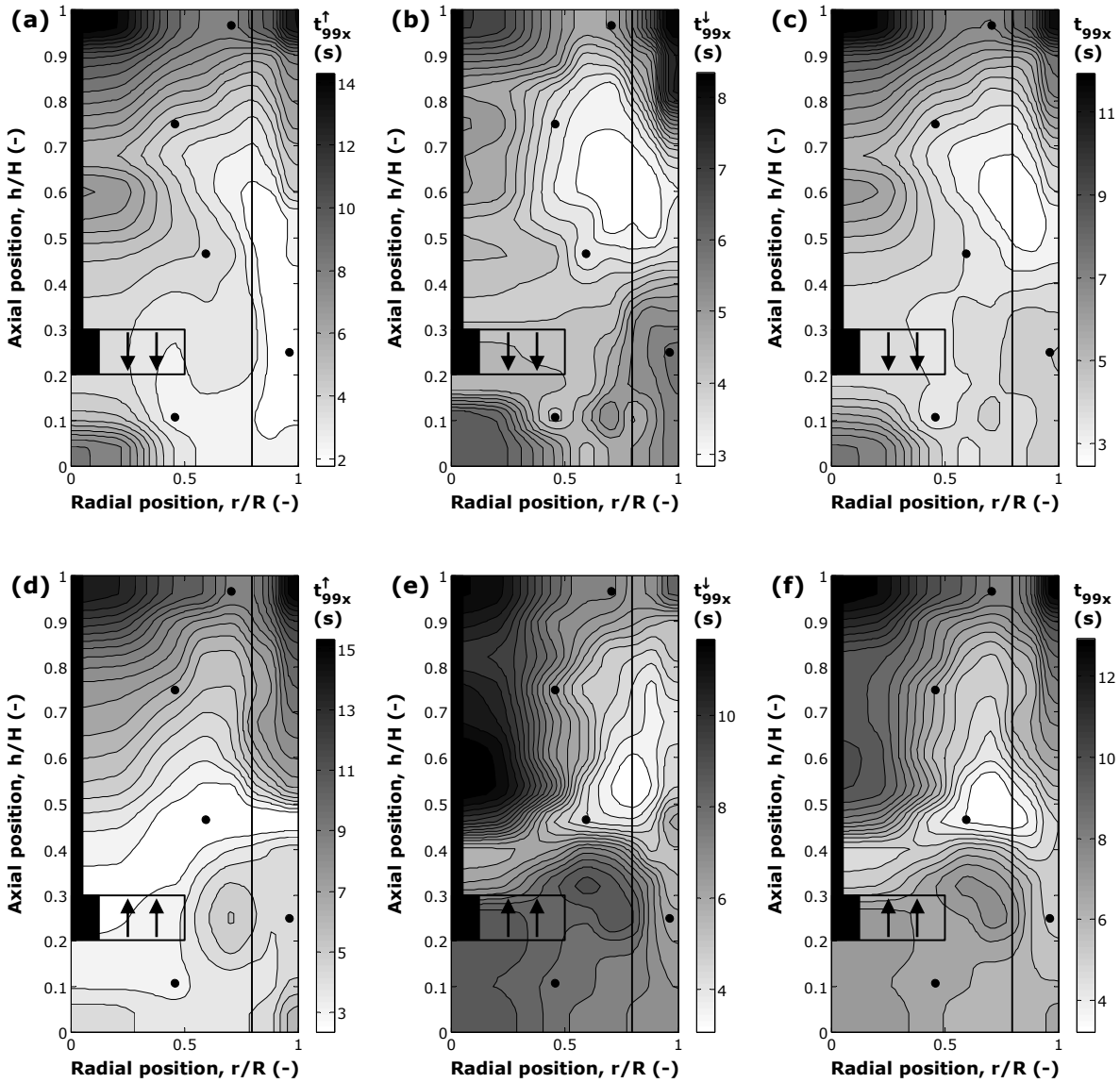

Figure 6.13. Radial-axial maps of the three convergence time intervals $t_{99x}^{\uparrow}$, $t_{99x}^{\downarrow}$ and t_{99x} of the three entropy mixing indices $M_i^{\uparrow}$, $M_i^{\downarrow}$ and M_i at N = 300 rpm, n_C = 98: (a-c) PBTD; (d-f) PBTU. The black dots represent the positions examined in **Figure 6.12**.

shown in **Figure 6.16** for $r = 0.5\,R$ and $h = 0.75\,H$. The figure confirms the above proportionality so that local values of the dimensionless convergence times, $Nt_{99x}^{\uparrow}$, $Nt_{99x}^{\downarrow}$ and Nt_{99x}, are practically constant at different impeller rotational speeds.

Previous experimental studies which measured mixing time in single phase turbulent flow report that the tracer is usually injected at the surface, and where a PBT type impeller is employed it is used in the down-pumping mode (PBTD) and its off-bottom clearance is

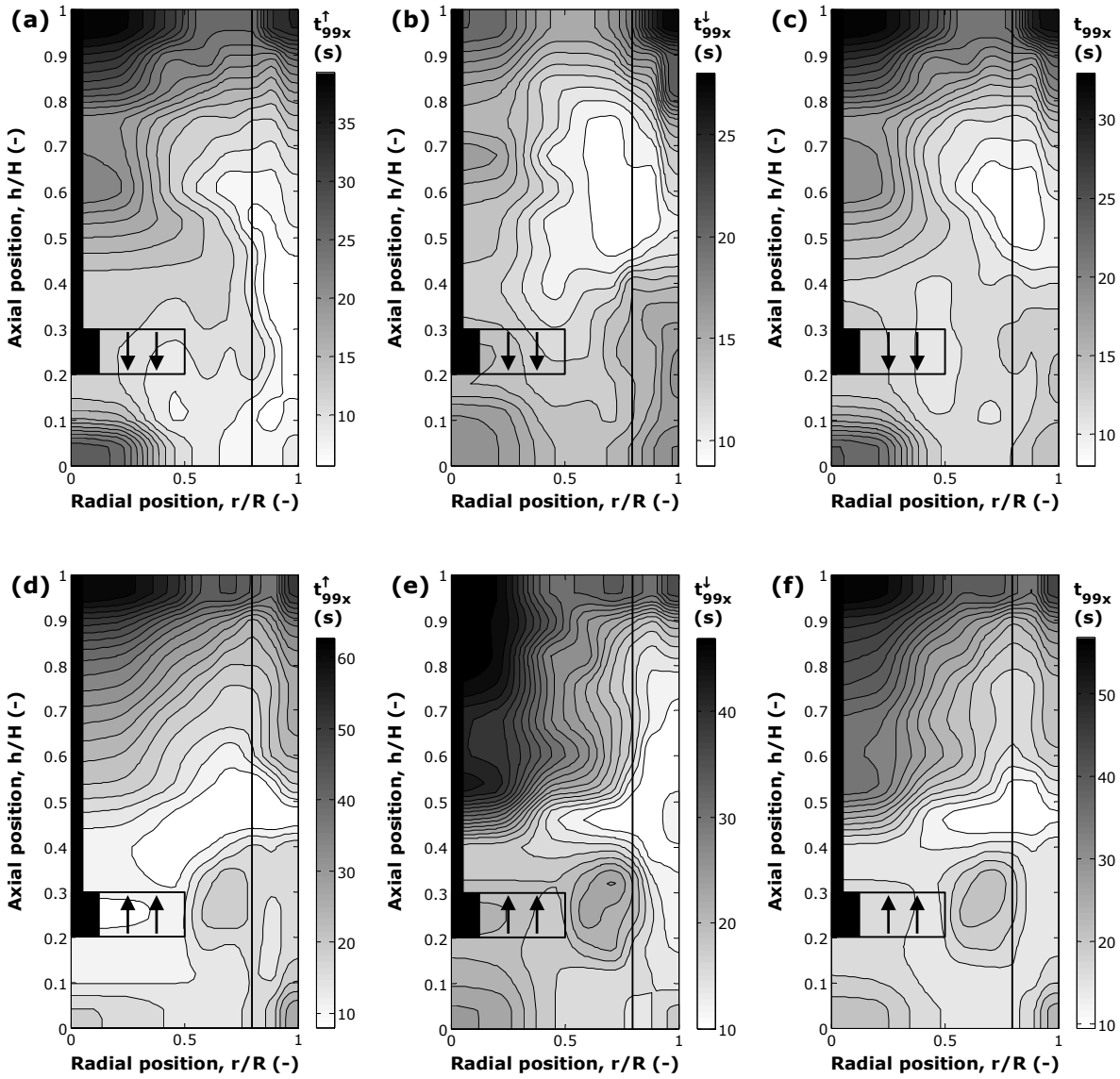

Figure 6.14. Radial-axial maps of the three convergence time intervals $t_{99x}^{\uparrow}$, $t_{99x}^{\downarrow}$ and t_{99x} of the three entropy mixing indices $M_i^{\uparrow}$, $M_i^{\downarrow}$ and M_i at N = 100 rpm, n_C = 98: (a-c) PBTD; (d-f) PBTU.

0.33 *T*. Since the clearance used here was $C = 0.25\ T$, the injection point was selected at 2 *C* above the impeller mid-plane ($h = 0.75\ H$) and halfway between the vessel axis and the wall ($r = 0.5\ R$), so that the values of $t_{99x}^{\uparrow}$ for the PBTD presented in **Figure 6.16** can be compared to experimental results from the literature.

The majority of the mixing literature has reported on the basis of single surface feed-point measurements that in the turbulent regime the dimensionless mixing time, i.e., the product of

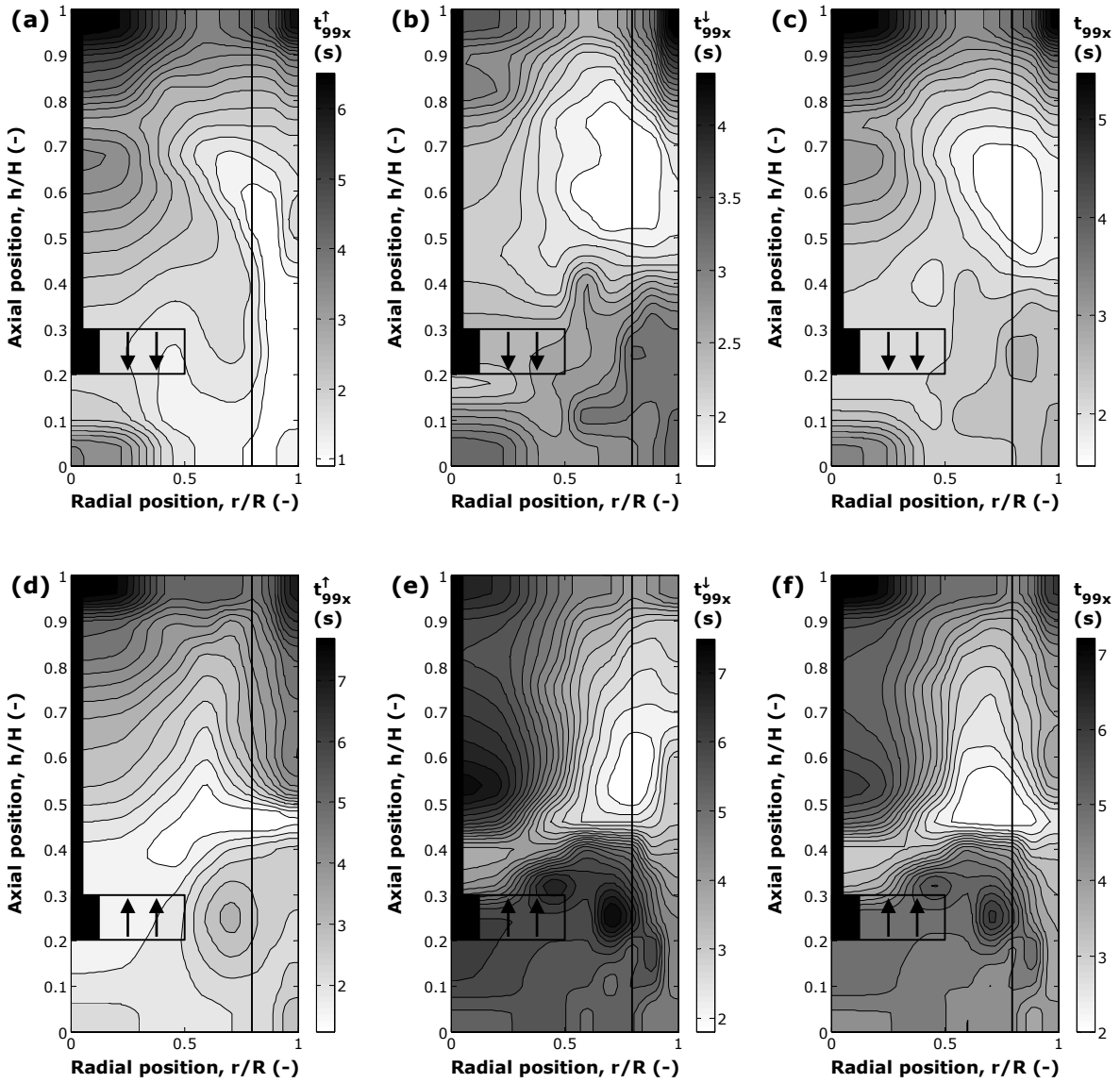

Figure 6.15. Radial-axial maps of the three convergence time intervals $t_{99x}^{\uparrow}$, $t_{99x}^{\downarrow}$ and t_{99x} of the three entropy mixing indices $M_i^{\uparrow}$, $M_i^{\downarrow}$ and M_i at $N = 500$ rpm, $n_C = 98$: (a-c) PBTD; (d-f) PBTU.

the measured mixing time and the impeller speed, is a constant independent of the impeller Reynolds number. The value of this constant, however, is dependent on the impeller type and also on the impeller-to-tank diameter ratio D/T when $H = T$. The design correlations given by Ruszkowski (1994), Grenville and Nienow (2004) and Nienow (1997b) are all of the form

$$N\theta_m = A\,Po^{-1/3}\left(\frac{T}{D}\right)^2 \tag{6.39}$$

where Po is the dimensionless power number of the impeller (~1.33 for a down-pumping pitched blade turbine under turbulent conditions with $C = 0.25\,T$) and the constant A varies slightly in the literature from 5.2 to 6. The average value of $Nt_{99x}^{\uparrow}$ at the above selected position for the PBTD, was 21.5 which agrees very well with the value of the dimensionless mixing time ($N\theta_m$ = 19-22) predicted by Eq. (6.39).

Such a comparison between the mixing times obtained by the Lagrangian PEPT data and the empirical correlation expressed in Eq. (6.39) is a further confirmation of the validity of

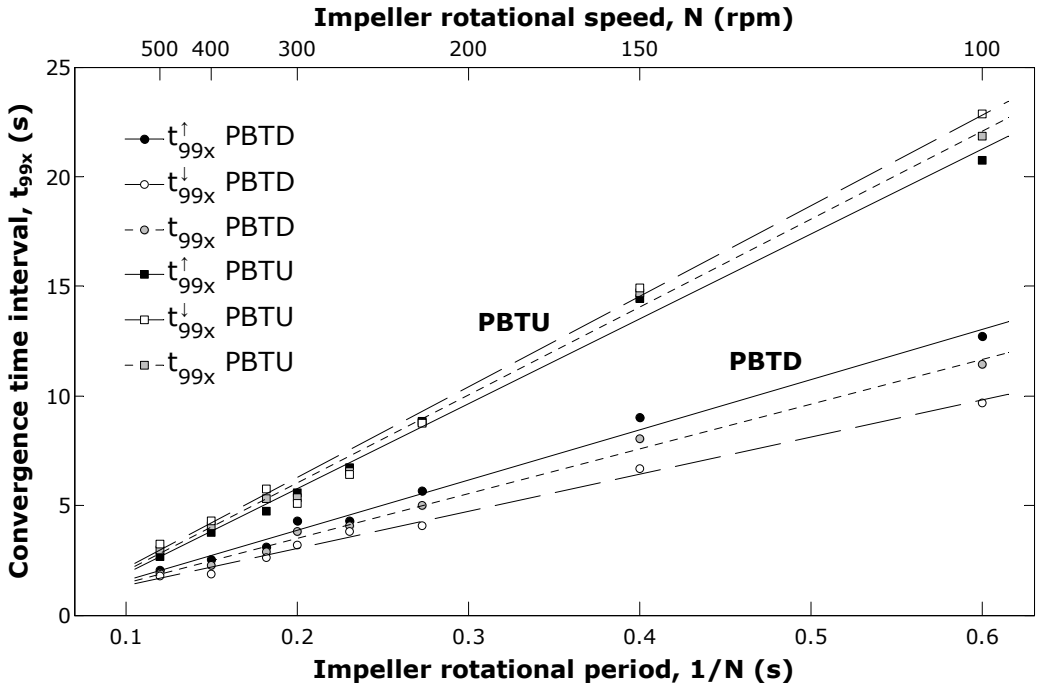

Figure 6.16. Convergence time intervals $t_{99x}^{\uparrow}$, $t_{99x}^{\downarrow}$ and t_{99x} of the three entropy mixing indices $M_i^{\uparrow}$, $M_i^{\downarrow}$ and M_i at ($r = 0.5\,R$, $h = 0.75\,H$) as a function of $1/N$ for both PBT agitation modes.

Eq. (6.37). As a result, the convergence times, $t_{99x}^{\uparrow}$, $t_{99x}^{\downarrow}$ and t_{99x}, can now be called respectively, *first*, *second* and *third entropy mixing time*, i.e., $t_m^{\uparrow}$, $t_m^{\downarrow}$ and t_m. The first entropy mixing time is identical to the (macroscale) mixing time used in the mixing literature. In **Figure 6.17** maps of the dimensionless entropy mixing times, $Nt_m^{\uparrow}$, $Nt_m^{\downarrow}$ and Nt_m, are plotted for each agitation mode. Given that the dimensionless entropy mixing times are practically independent of *N*, the average of the 8 data sets corresponding to different agitation speeds is

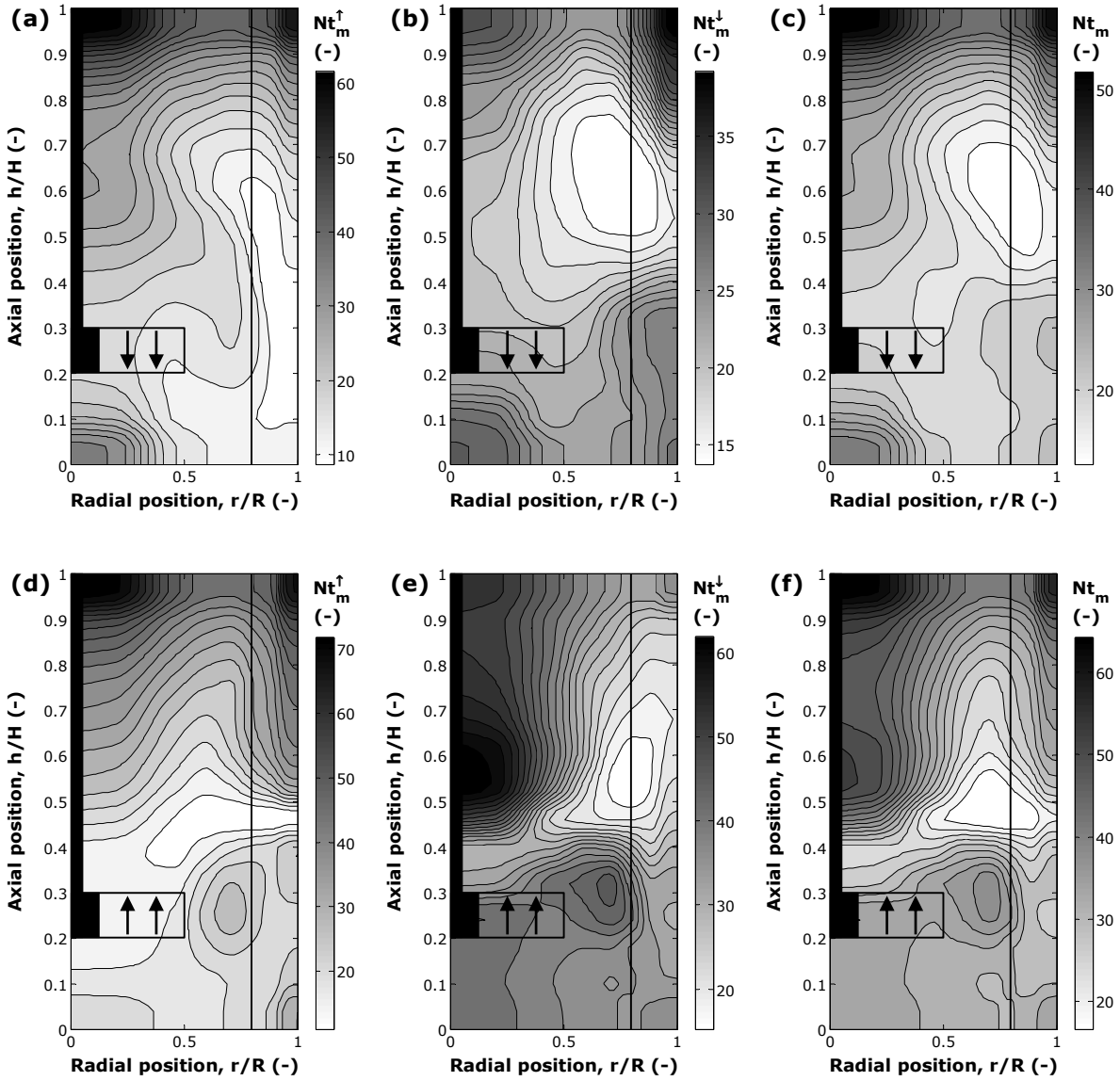

Figure 6.17. Radial-axial maps of the first, second and third dimensionless entropy mixing times $Nt_m^{\uparrow}$, $Nt_m^{\downarrow}$ and Nt_m : n_C = 98; (a-c) PBTD; (d-f) PBTU.

presented for better accuracy. The plots demonstrate that the first dimensionless entropy mixing time, equivalent to $N\theta_m$, varies considerably with the feed position.

6-4.5 Design of mixing processes

Little attention has been devoted in the mixing literature to the effect of the feed position on mixing efficiency and, as mentioned above, previous studies have focused on the effects on the mixing time of the impeller type and size, vessel dimensions and agitation speed with the tracer typically injected at the surface. Nevertheless, a ~ 30% reduction in mixing time was reported by Ducci and Yianneskis (2007a-b) when the tracer was carefully inserted inside the core of the detected macro-instability vortex generated by a radial flow impeller rather than outside it. Through PIV measurements, Doulgerakis *et al.* (2009) concluded that even more substantial mixing enhancements can be achieved by using feed pipes located within the flow where the macro-instability energy maxima are found. Similarly, Guillard and Trägårdh (2003), by measuring instantaneous pH values in 3, 12 and 30 m^3 stirred vessels, demonstrated that both under unaerated and aerated conditions the location at which the tracer is added substantially affects the dimensionless mixing time $N\theta_m$.

In addition, by numerically simulating the paths followed by 100 000 particles released at three different points in the flow (just below the free surface, at the impeller mid-plane and halfway between the PBT and the surface), LaRoche (2005) showed that the location of the feed pipe can have a huge effect on the mixing efficiency. Finally, by positioning a static feed pipe at a point close to the impeller where energy dissipation is considerable, Assirelli *et al.* (2005) showed that the micromixing efficiency (although conceptually different from the macromixing efficiency being considered here) is enhanced by several folds.

The final results presented in **Figure 6.17** show a very wide variation in local entropy mixing times throughout the vessel. In addition to the numerical quantification of the entropy mixing times, these results enable rapid identification of the regions within the vessel producing the fastest flow dispersion or reaching the fastest flow diversification, and the regions where both effects are considerably fast. Such detailed maps could be used to inform equipment and/or process design so as to maximise the overall mixing efficiency of the system.

For the stirred vessel geometry considered here, the best positions for feeding or withdrawing material are shown in **Figure 6.18**. The location and orientation of the inlet stream were

chosen on the basis of the position and shape of the white zones in **Figure 6.17a** and **d** for the PBTD and PBTU, respectively, where $Nt_m^{\uparrow}$ is lowest. In this case, it is apparent from the local values of $Nt_m^{\uparrow}$ that a PBTD generally allows a better mixing efficiency. However, for processes where there is a requirement to position the feed (or withdrawal) point at a pre-determined location it might be advantageous to use a PBTU; for example, **Figure 6.17a** and **d** show that when feeding in the vicinity of the upper edge of the impeller, $Nt_m^{\uparrow}$ for a PBTU is smaller than for a PBTD. Note that the best withdrawal positions for both PBT configurations, which are located in the regions where $Nt_m^{\downarrow}$ is minimum and the diversification of the flow is fastest, are essentially the same. Moreover, the maps of Nt_m in **Figure 6.17c** and **f** could be used to design a stirred tank where the feed and withdrawal streams alternate using the same line since t_m is the convergence time of the third entropy mixing index M_i which by definition includes both concepts of flow dispersion and local diversification. The above findings suggest that the usual practice of injecting at the surface and withdrawing at the base should be reconsidered to maximise mixing in stirred vessels. Finally, the entire computational process is summarised in the form of a block diagram in **Figure 6.19**.

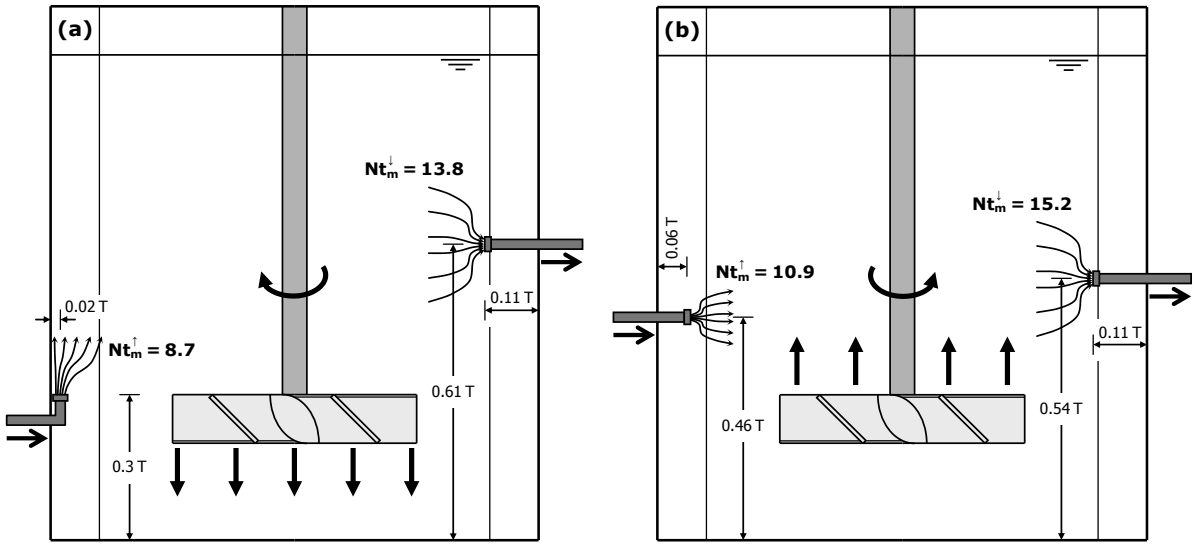

Figure 6.18. Best feed and withdrawal positions in the vessel: (a) PBTD; (b) PBTU.

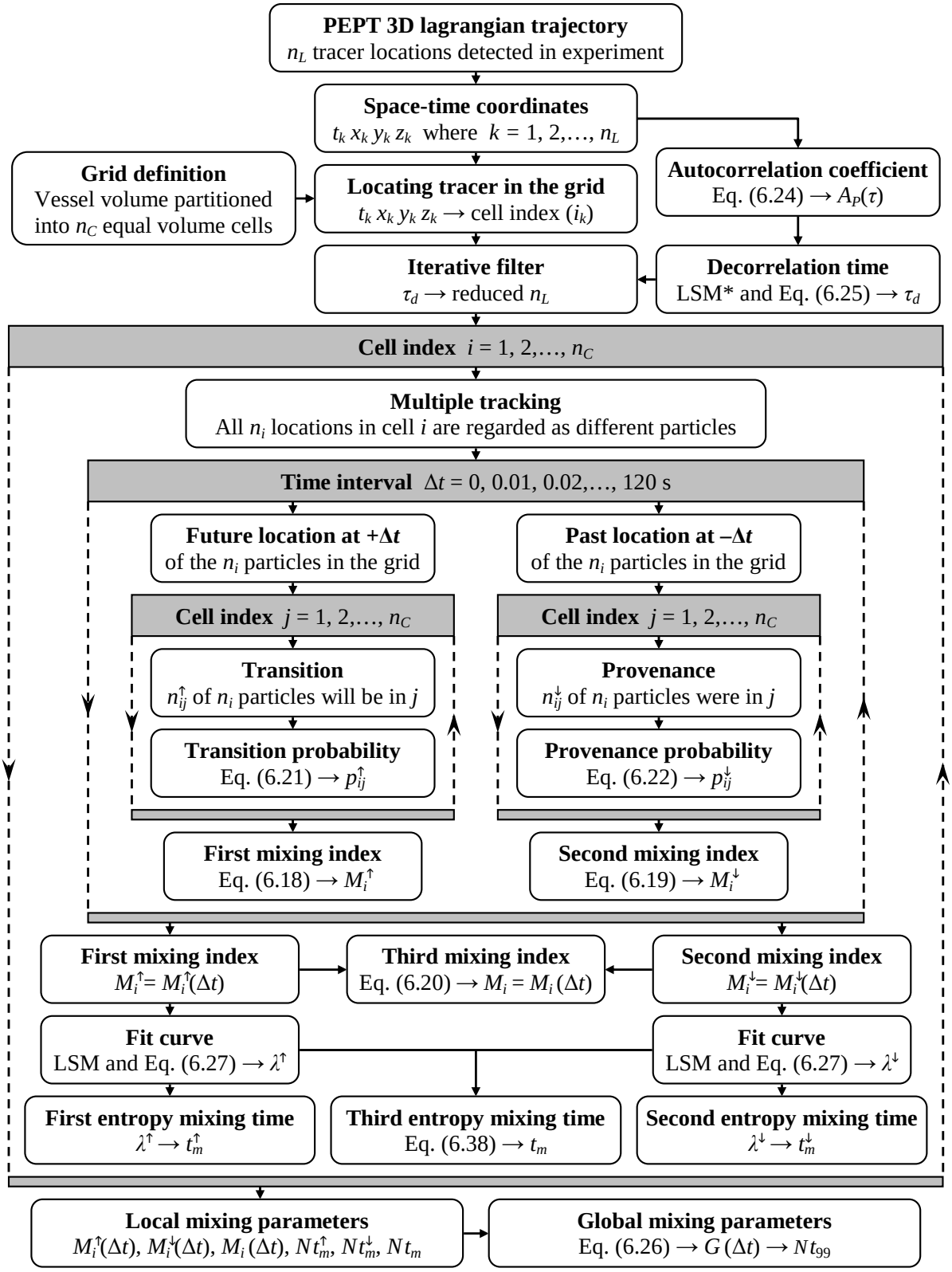

Figure 6.19. Block diagram of the entire computational process: the process is repeated for various N values. *Least squares method.

6-5 Conclusions

A new methodology based on the concept of Shannon entropy has been developed for studying the local and global mixing performance in a batch stirred vessel. The Lagrangian technique of positron emission particle tracking has been used to conduct experiments in the fully turbulent regime.

Three newly defined local entropy mixing times have been proposed which enable rapid identification of the regions within the vessel producing the fastest flow dispersion or reaching the fastest flow diversification, and the regions where both effects are considerably fast. Such detailed results could be used to inform the design of experiments to study mixing phenomena or equipment design to maximise the global or local mixing efficiency of the system.

For the stirred vessel configuration and pitched blade turbine considered here, the best positions for feeding have been located relatively close to the wall in line with the upper edge of the impeller for a PBTD or slightly above it for a PBTU, whilst the best withdrawal positions are found approximately a baffle-width away from the wall slightly above the central horizontal plane of the vessel regardless of the orientation of the PBT. A better global and local mixing performance is generally obtainable using a PBTD rather than a PBTU; however, for processes where there is a requirement to use a specific feed or withdrawal position, both impeller configurations should be considered as a PBTU might be preferred to a PBTD.

Despite the additional complexity generated when a pipe is placed deep inside the flow (e.g. vortex shedding around the pipe or influence of the feed rate), the common industrial practice of injecting at the surface and extracting at the base should be reconsidered to achieve better mixing efficiency in these systems.

Notation

Roman letters

a	Constant in Eq. (6.32)	-
A	Constant in Eq. (6.39)	-
A_P	Autocorrelation coefficients of $\mathbf{P}(t)$	-
A_x A_y A_z	Autocorrelation coefficients of $x(t)$, $y(t)$, $z(t)$	-
B	Baffle width	m
c	Arbitrary constant in Eq. (6.3)	-
C	Impeller off-bottom clearance	m
c_i	Mean tracer volume concentration	-
c_{ij}	Tracer volume concentration in cell j	-
c_{io}	Initial tracer volume concentration in cell i	-
D	Impeller diameter	m
f	Generic function	-
G $G^{\uparrow}$ $G^{\downarrow}$	First, second and third global mixing indices	-
h	Axial distance	m
H	Vessel fill height	m
$H_{ij}^{\uparrow}$	Shannon entropy of transition probabilities	nat
$H_{ij}^{\downarrow}$	Shannon entropy of provenance probabilities	nat
$H(X)$	Shannon entropy function	nat
i j	Cell indices	-
$I(X)$	Uncertainty about the outcome of X	-
$I(\omega_i)$	Self-information contained in ω_i	-
k	Location counter in **Figure 6.19**	-
M_i $M_i^{\uparrow}$ $M_i^{\downarrow}$	First, second and third entropy mixing indices	-
n m	Number of possible events	-
N	Impeller rotational speed	s^{-1}
n_C	Number of grid cells	-
n_i	Number of particles within cell i	-
$n_{ij}^{\uparrow}$	Number of particles flowing from i into j	-
$n_{ij}^{\downarrow}$	Number of particles emanating from j	-

n_L	Number of PEPT locations	-
p	Probability	-
p_i	Probability of the event ω_i	-
$p_{ij}^{\uparrow}$	Transitional probability	-
$p_{ij}^{\downarrow}$	Provenance probability	-
Po	Impeller power number	-
P_{tr}	Probability of tracer presence	-
$P_{tr,\infty}$	Theoretical limit value of P_{tr}	-
q	Summation index in Eq. (6.32)	-
$r \quad h$	Radial-axial cylindrical coordinates	m
R	Tank radius	m
Re_{imp}	Impeller Reynolds number (ND^2/ν)	-
T	Tank diameter	m
t	Time	s
$t_{99} \quad t_{99}^{\uparrow} \quad t_{99}^{\downarrow}$	Convergence time intervals of $G^{\uparrow}$, $G^{\uparrow}$, $G^{\downarrow}$	s
$t_{99x} \quad t_{99x}^{\uparrow} \quad t_{99x}^{\downarrow}$	Convergence time intervals of M_i, $M_i^{\uparrow}$, $M_i^{\downarrow}$	s
$t_m \quad t_m^{\uparrow} \quad t_m^{\downarrow}$	First, second and third entropy mixing times	s
V_P	Particle volume	m^3
V_T	Total volume of the working fluid	m^3
w	Impeller height	m
$x \quad y \quad z$	Cartesian coordinates	m
X, Y, Z	Experiments	-

Greek letters

ΔV	Grid cell volume	m^3
η	Variable in Eq. (6.32)	-
θ_m	Macroscale mixing time	s
$\lambda \quad \lambda^{\uparrow} \quad \lambda^{\downarrow}$	Decay parameters of $G^{\uparrow}$, $M_i^{\uparrow}$, $M_i^{\downarrow}$	s^{-1}
ν	Kinematic liquid viscosity	$m^2\ s^{-1}$
σ_i	Standard deviation of normalised c	-
τ	Time shift	s

τ_d	Decorrelation time	s
ω_i	Possible event	-
Ω	Set of possible events	-

Abbreviations

LSM	Least squares method
PBT	Pitched blade turbine
PBTD	Down-pumping PBT
PBTU	Up-pumping PBT
PEPT	Positron emission particle tracking
PIV	Particle image velocimetry
PLIF	Planar laser induced fluorescence

Chapter VII
Mixing of Monodisperse Solid-Liquid Suspensions

Abstract

The technique of Positron emission particle tracking (PEPT) has been used to determine the two-phase flow field and spatial phase distribution in a stirred vessel containing coarse glass particles suspended in water. The Lagrangian flow data provided by PEPT have been converted to give a detailed Eulerian description of the two-phase flow generated by a pitched blade turbine (PBT) operating in up-pumping or down-pumping mode. For the first time, it has been possible to determine the full 3D velocity and concentration fields of both the liquid and the solid phase within an opaque dense slurry of this type containing up to 40 wt% solids. The detailed PEPT measurements have also enabled the solids mass balance and the mass continuity of the two phases to be accurately verified throughout the vessel. The data show that the pumping effectiveness of the PBT is unaffected at moderate solid fractions, but is considerably reduced at high fractions and even more so in the up-pumping mode. A uniformity index based on the variance of the local solids concentration in the vessel shows that, overall, a down-pumping PBT achieves a significantly better homogeneity than an up-pumping PBT.

7-1 Introduction

Solid-liquid mixtures are widely encountered in a variety of industrial processes including the manufacture of fine chemicals, pharmaceuticals, personal/home care products, polymers, food, paper and pulp. Numerous difficult mixing problems are found with solid-liquid processing, some 80 % of products in the chemical industry, for example, being of this type (Shamlou, 1993). Operations involving the suspension of solids in a continuous phase such as bio-slurries, crystallisation and catalytic processes frequently employ mechanically agitated vessels. Design, control and performance are dependent on a thorough understanding of the flow dynamics. The choice of design parameters to ensure an adequate solid distribution is still an open problem for design engineers. In such systems one crucial aspect is the achievement of good mixing which allows for an efficient interaction between the two phases. The methods generally used for designing stirred vessels for solid-liquid mixing tend to be based on a global 'black-box' approach, and a more detailed description of the internal flow structure is needed to aid the development of rational design rules. Recently, with the advent of powerful measurement and modelling techniques, more effort is increasingly being devoted to this field of research to try and fully understand the mechanisms behind particle suspension and distribution (Unadkat *et al.*, 2009; Tamburini *et al.*, 2009; Guha *et al.*, 2007; Kagoshima and Mann, 2006).

A localized hydrodynamic approach provides a better basis for design since it enables a detailed description of the multi-phase flow structure to be obtained. Whereas for translucent systems Eulerian data have been available through the use of well established techniques such as laser Doppler velocimetry (LDV) and particle image velocimetry (PIV), these optical instruments, however, have only been applied to very dilute suspensions and cannot be applied to dense slurries which are opaque. So far, other attempts at local measurements have been mainly limited to the investigation of mean axial solid-concentration profiles at relatively low concentrations using a single vertical conductivity or capacitance probe traverse or a withdrawal technique (Brunazzi *et al.*, 2004; Barresi and Baldi, 1987). However, these methods give limited information and cannot be used to probe concentrated suspensions in detail or to measure the 3D distribution of both liquid and solid.

In this chapter, the technique of positron emission particle tracking (PEPT) is used to study the mixing of dense suspensions of monodisperse coarse glass particles in water. Extensive

data for suspensions containing up to 40 wt% solids are presented here. Detailed information is obtained on particle and fluid trajectories which is converted to give a pointwise Eulerian description of the two-phase flow field as well as the spatial distribution of both the liquid and solid phases.

7-2 Experimental

PEPT experiments were conducted in a flat-base cylindrical vessel of diameter T = 288 mm made of Perspex, as shown in **Figure 7.1**. The vessel was fitted with four wall baffles of width 0.1T and was agitated by a 6-blade 45º pitched-turbine (PBT) of diameter D = 0.5T and height 0.1T as depicted in **Figure 7.2**. The off-bottom clearance of the PBT was 0.25T, and the height of the suspension in the vessel was set at $H = T$. The suspending liquid used was water whose density was adjusted to 1150 kg m^{-3} by adding NaCl to make the PEPT particle tracer used to track the liquid phase neutrally buoyant. Nearly monomodal and nearly spherical glass beads (d = 2.85-3.30 mm) having a density of 2485 kg m^{-3} were used to make a two-phase suspension with a mean solid mass concentration, X, varying in the range 0 to 40 wt% (or, equivalently, with the mean solid volume concentration, C, varying in the range 0-23.6 vol%). Experiments were conducted at the minimum rotational speed for particle suspension, N_{js}, visually determined experimentally according to the well-known Zwietering criterion, i.e. no particle should remain stationary on the base of the vessel for longer than 1-2 s (Zwietering, 1958).

Mixing of the suspension was investigated with the impeller operating in the down-pumping mode (PBTD) and in the up-pumping mode (PBTU). The experimental conditions are summarised in **Table 7.1**. At a given solid fraction, the measured N_{js} values for the PBTD and PBTU in this case are the same within experimental error. It should be noted, however, that while the concept of N_{js} is simple, its accurate measurement is not especially under conditions of high solids concentration. Determination of N_{js} tends to be somewhat subjective and even more so under such turbid conditions, so that accurate measurement of N_{js} using the Zwietering criterion can be difficult.

For a given solid-liquid suspension, PEPT experiments consisted of independently resolving the full three-dimensional trajectories of the fluid phase and of the solid phase in two

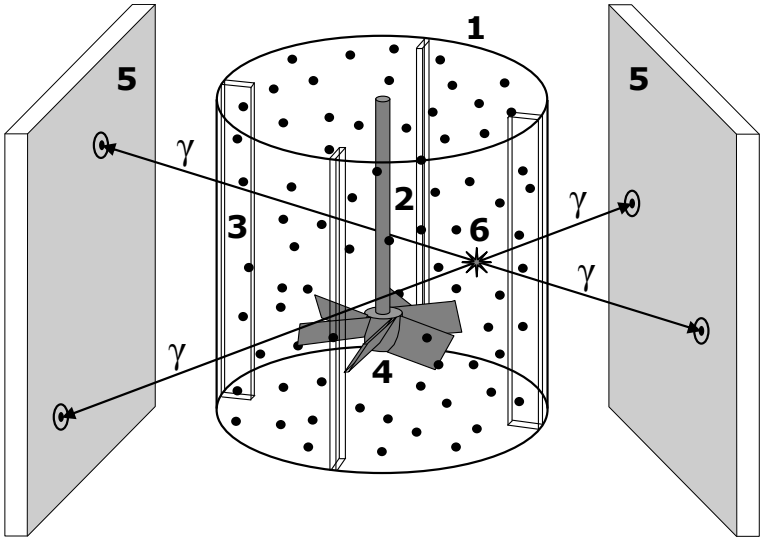

Figure 7.1. Experimental PEPT set-up: 1 cylindrical tank; 2 shaft; 3 baffle; 4 PBT impeller; 5 γ-ray detectors; 6 PEPT particle tracer.

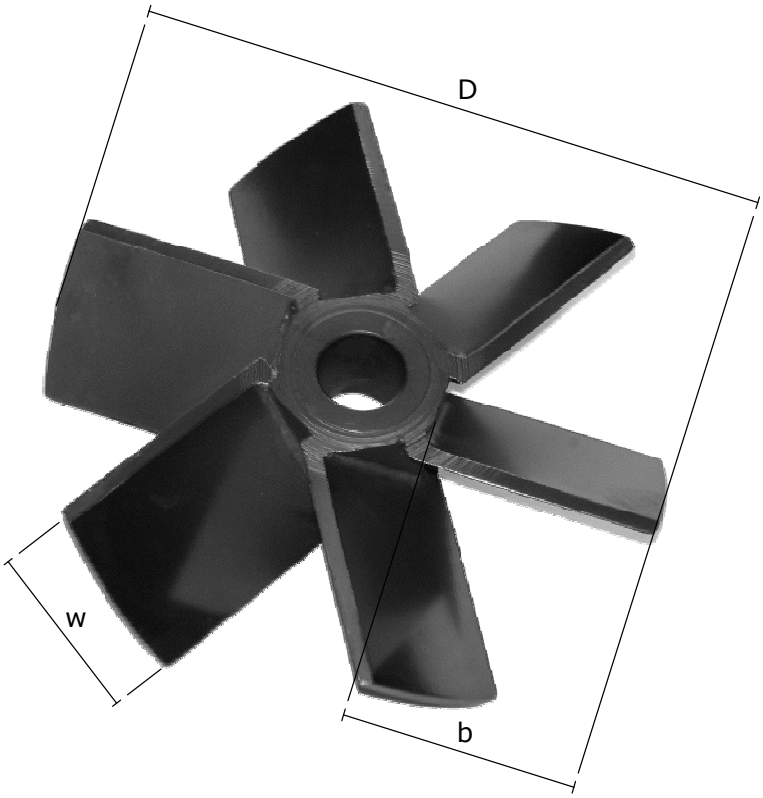

Figure 7.2. Mixed flow impeller used: 45º pitched-blade turbine, D = 144 mm, w = 41 mm, b = 55 mm.

successive and distinct experiments. A representative glass particle radioactively labelled with ^{18}F, by direct irradiation, was used to track the solid phase, whilst a neutrally-buoyant resin tracer of 600 μm diameter also labelled with ^{18}F was used to track the liquid phase.

Fore each experiment, the PEPT tracking time, t_∞, in this study was set at 30 min for each phase, which was long enough to acquire a sufficient amount of data in all regions of the vessel, so that ergodicity could be safely assumed given that in such a system the probability of visit is sufficiently uniform by virtue of the highly turbulent state of the suspension ($\mathrm{Re}_{imp} = N_{js}D^2/\nu > 10^5$), and the open geometry of the vessel where all regions are more or less equally accessible by the tracer. Ergodicity is discussed in more details in Section 3-5.1.

7-3 Results and discussion

7-3.1 Liquid and solid velocity fields

For each experimental investigation, PEPT provides the Cartesian (x, y, z) coordinates of a single particle tracer moving within the system being studied as a function of time, as illustrated in **Figure 7.3**. These sets of raw data were analysed using the code described in Chapter III with a number of grid cells $n_c = 512$. The vector velocity maps of the agitated liquid obtained with no solid particles present in the vessel are shown in **Figure 7.4** for both the PBTD and PBTU at $N = 5.5\ \mathrm{s}^{-1}$. Using cylindrical coordinates, the radial-axial 2D velocity maps were obtained by azimuthally averaging the 3D velocity data and projecting them onto the 2D radial-axial plane (rh), as described in Section 3-3.8. Whilst being two

Table 7.1. Experimental conditions for the study of monodisperse solid-liquid suspensions.

X (wt%)	C (vol%)	N *or* N_{js} (s^{-1})		Re_{imp} (-)	
		PBTD	PBTU	PBTD	PBTU
0	0	5.50	5.50	1.31×10^5	1.31×10^5
5.2	2.5	6.00	6.25	1.43×10^5	1.49×10^5
10.6	5.2	6.75	6.83	1.61×10^5	1.63×10^5
20.0	10.4	8.00	7.83	1.91×10^5	1.87×10^5
40.0	23.6	9.83	9.67	2.34×10^5	2.31×10^5

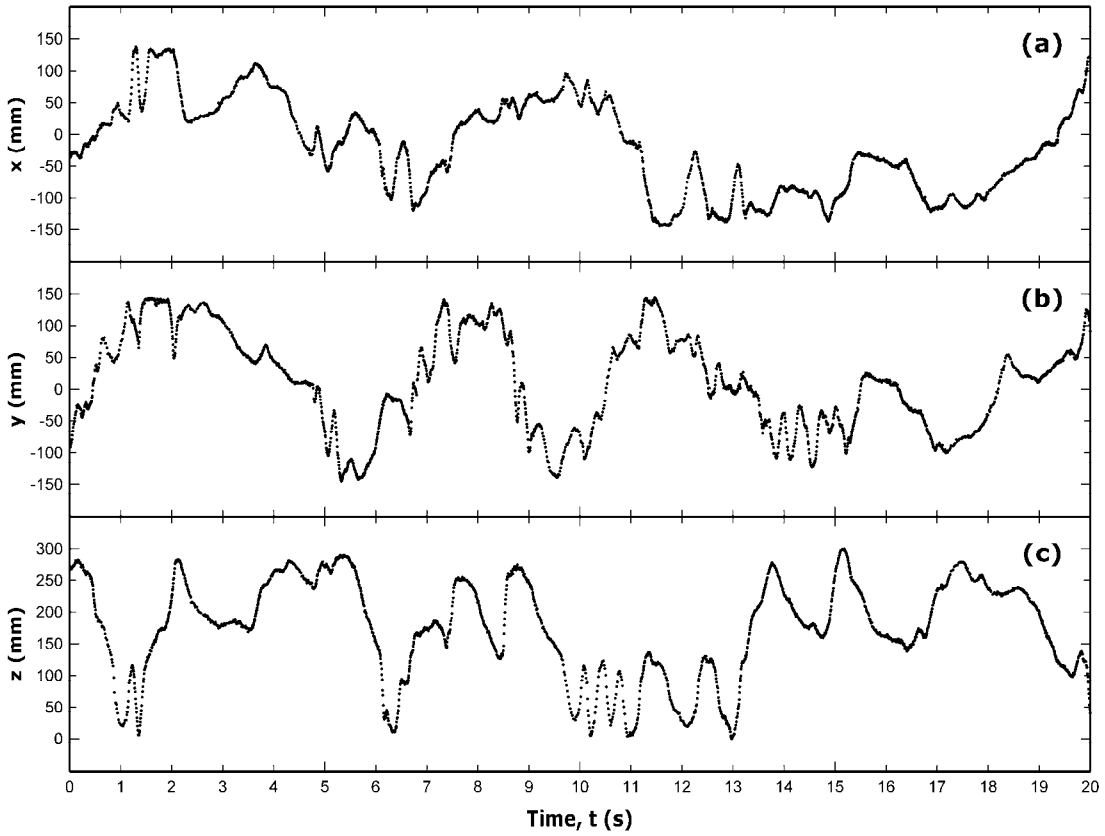

Figure 7.3. Segment of liquid tracer trajectory in a stirred suspension: (a) horizontal Cartesian coordinate $x(t)$; (b) horizontal Cartesian coordinate $y(t)$; (c) vertical Cartesian coordinate $z(t)$.

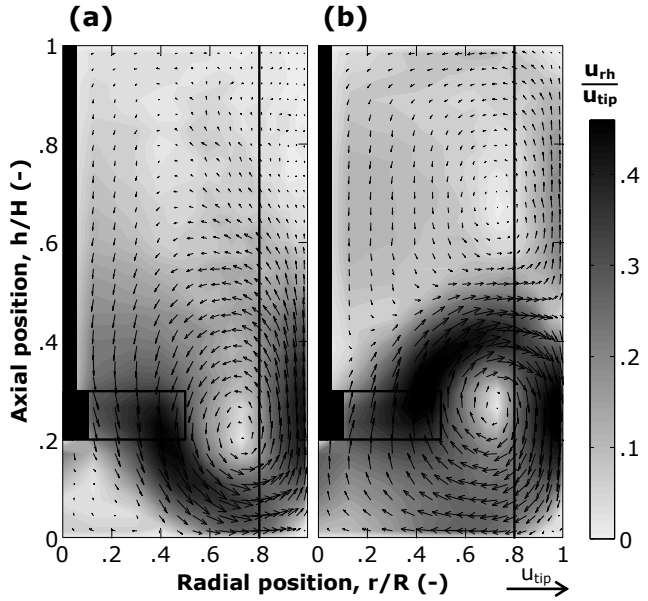

Figure 7.4. Azimuthally-averaged radial-axial velocity maps of the liquid phase in the absence of solid particles at $N = 5.5\ s^{-1}$: (a) PBTD; (b) PBTU.

dimensional, these flow maps are representative of the whole 3D velocity field. The observed flow field with a single flow loop is typical of a down-pumping PBT with a low impeller off-bottom clearance, whilst an up-pumping PBT usually gives rise to a double flow loop. As expected, fluid velocities are relatively high in the impeller region and around the centre of the flow loops but low in the upper parts of the tank and in the centre of the loops. For ease of comparison, all the velocity plots presented have been normalised by the impeller tip speed, u_{tip}.

The effects of the mean solid concentration, X, on the fluid and solid phase velocity fields generated by the PBTD are depicted in **Figures 7.5 and 7.6**. A comparison of the liquid flow maps under single-phase flow conditions (**Figure 7.4a**) and in the presence of the solid phase (**Figure 7.5**) shows global qualitative similarities in the flow pattern even at X = 40 wt%. A more detailed scrutiny of the images reveals no significant quantitative changes in the velocity field up to 10.6 wt% of solids, followed by a significant diminution of the normalised velocity in the impeller discharge region above 10.6 wt%, accompanied by a slight variation in the shape and position of the flow loop; the centre of the loop slowly changes position axially upwards from $h = 0.2H$ (X = 0 wt%) to $h = 0.25H$ (X = 40 wt%) and radially inwards from $r = 0.73R$ to $r = 0.63R$. The ability to detect such fine details in these opaque systems is testimony to the power of the PEPT technique. Similarly, increasing the solid concentration up to 10.6 wt% does not produce any significant effects on the solid phase velocities, but at higher concentrations there is a clear damping effect on the solid flow field around the impeller, as depicted in **Figure 7.6**. Such a damping effect appears to be more pronounced at 20 wt% than at 40 wt%. These results, however, should be considered in conjunction with the solid phase distributions presented later in **Figure 7.9** which show a much higher relative solid presence around the impeller at 20 wt%, and thus explain the lower local Eulerian velocities.

The liquid and solid flow patterns generated by the PBTU are shown in **Figures 7.7** and **7.8**, and similar to the PBTD, a first qualitative analysis suggests that the flow maps on the whole are not extensively affected by the increase in mean solid concentration, while a more detailed analysis reveals the presence of secondary effects. There is a significant reduction in the magnitude of the normalised fluid velocity in the impeller discharge region at concentrations above 10.6 wt% solids, but there are no noticeable effects below that (**Figure 7.4b** and

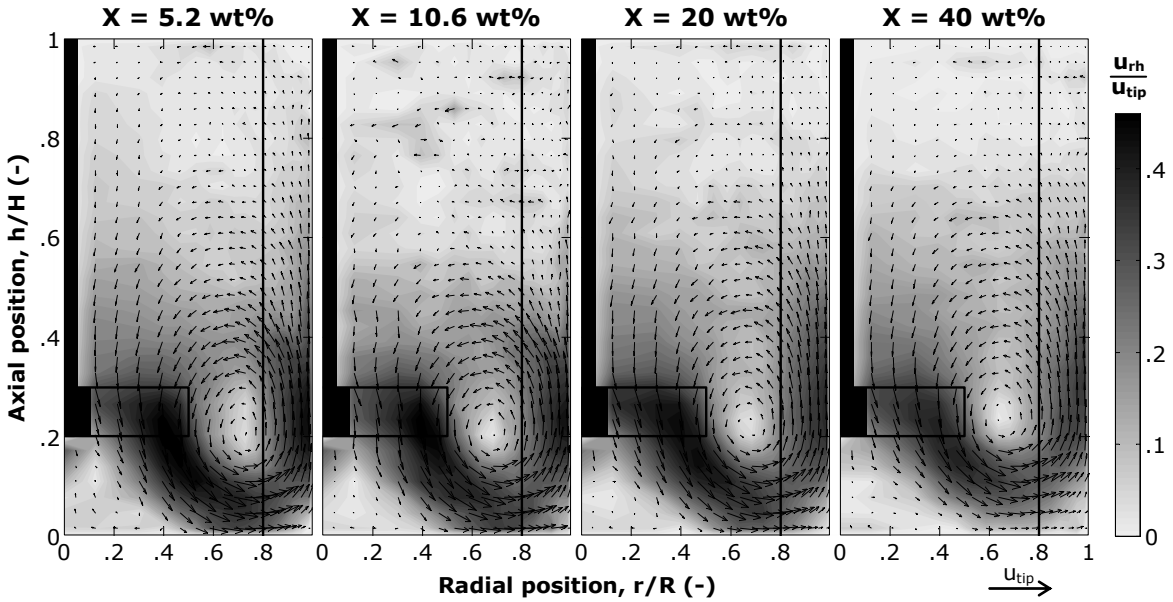

Figure 7.5. Azimuthally-averaged radial-axial velocity maps of the liquid phase for the PBTD at varying X and $N = N_{js}$.

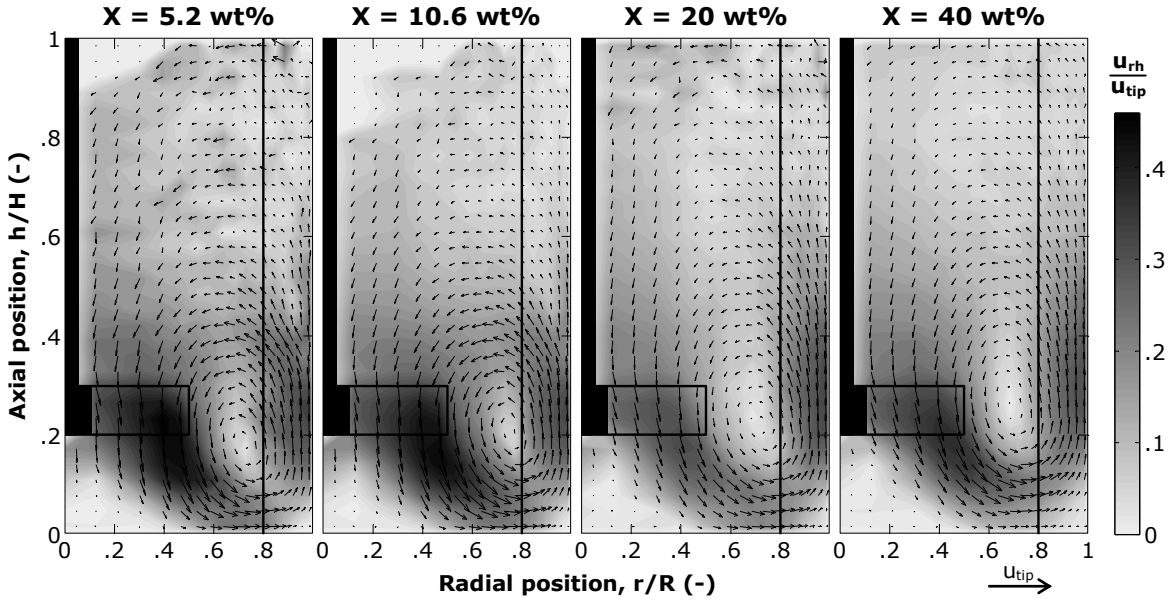

Figure 7.6. Azimuthally-averaged radial-axial velocity maps of the solid phase for the PBTD at varying X and $N = N_{js}$.

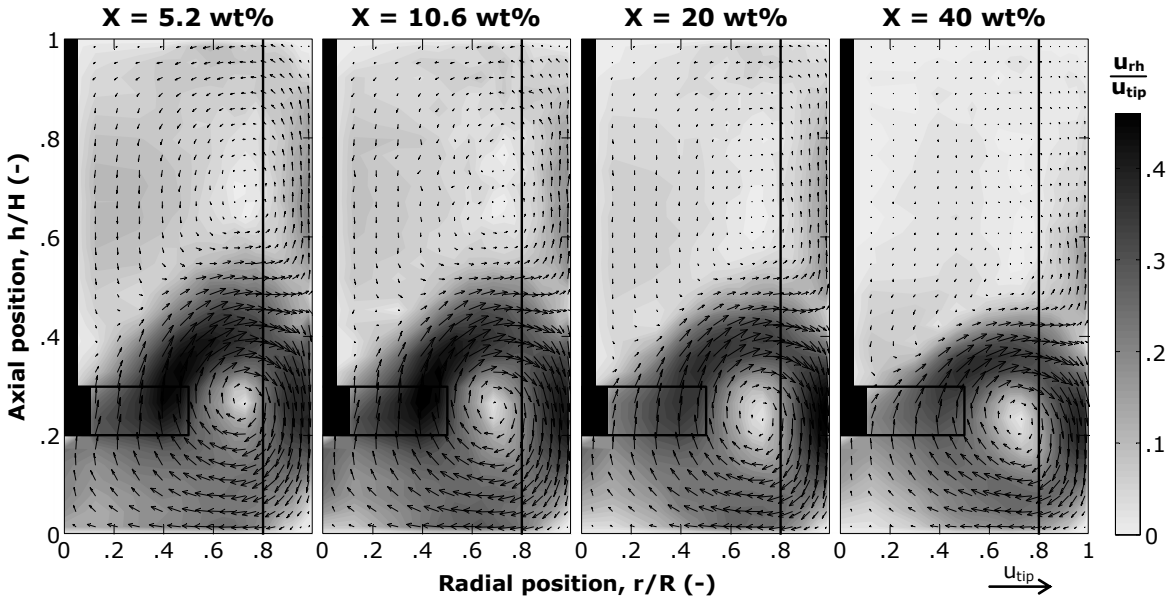

Figure 7.7. Azimuthally-averaged radial-axial velocity maps of the liquid phase for the PBTU at varying X and $N = N_{js}$.

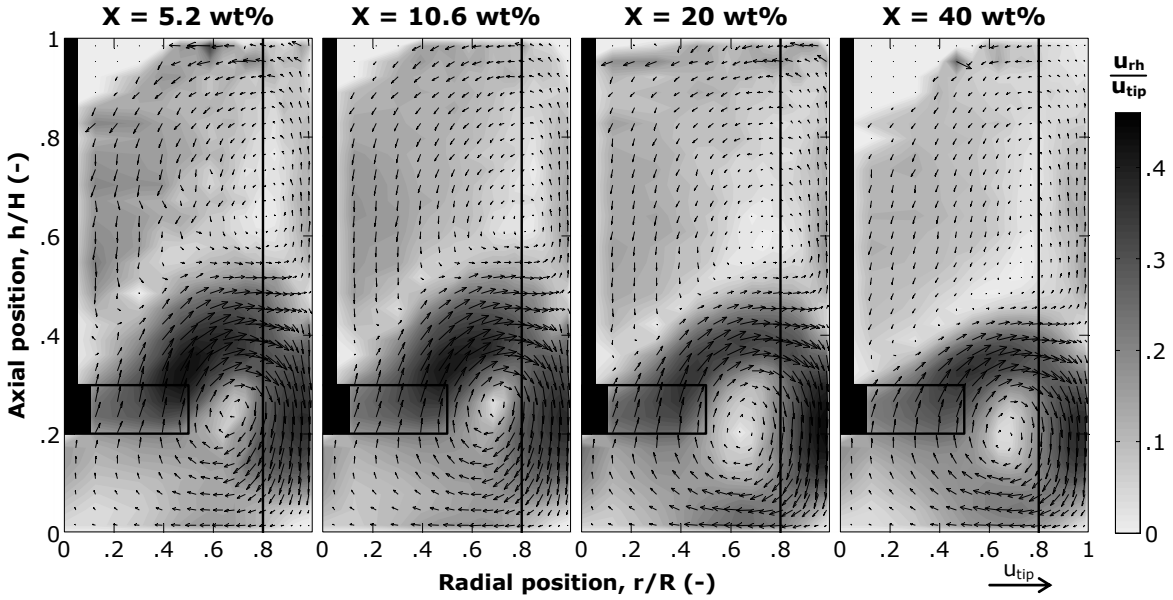

Figure 7.8. Azimuthally-averaged radial-axial velocity maps of the solid phase for the PBTU at varying X and $N = N_{js}$.

Figure 7.7). At the highest concentration of 40 wt%, the lower flow loop appears to have contracted significantly with the centre shifting downwards by half the impeller height (0.05*H*), while the upper flow loop has virtually disappeared. Similar observations can be made concerning the effects of solid concentration on the magnitude of the normalised particle velocity in the impeller discharge region, as shown in **Figure 7.8**. Again, the contraction of the lower flow loop at 40 wt% solids is noteworthy.

The above observations are quantitatively confirmed in **Figure 7.9** which shows details of the effects of the mean solid concentration on the three velocity components of both the liquid and solid phases. The plots exhibit radial distributions of the three velocity components (u_ϑ, u_r, u_h) for both liquid and solid in the horizontal impeller discharge plane, i.e. along the

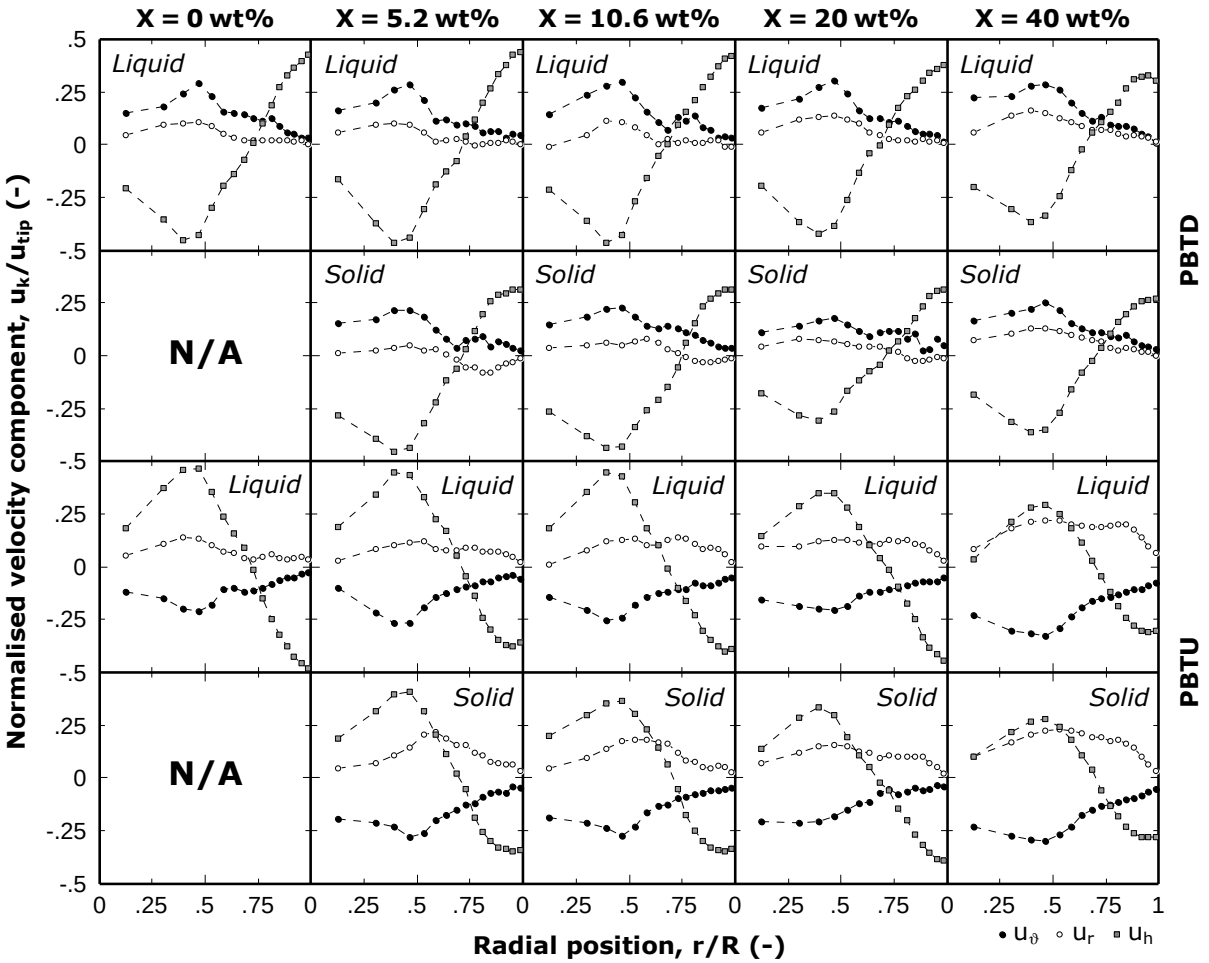

Figure 7.9. Azimuthally-averaged radial profiles of the three velocity components in the horizontal impeller discharge plane at $h = 0.2H$ for the PBTD and $h = 0.3H$ for the PBTU; $N = N_{js}$.

lower edge of the impeller blade at $h = 0.2H$ for the PBTD, and along the upper edge of the impeller blade at $h = 0.3H$ for the PBTU. As done for the flow maps, all the velocity plots have been normalised by the impeller tip speed, u_{tip}, for ease of comparison. As expected, the dominant component in this plane is the axial velocity. The tangential velocity component is only significant close to the impeller and declines to almost zero away from it. The radial component is generally relatively small except at 40 wt% solids in the case of the PBTU where for both liquid and solid it is comparable to the axial component. This indicates a change in the impeller pumping direction down to approximately 45° which confirms the observed contraction of the lower flow loop in **Figures 7.7** and **7.8.**

7-3.2 Spatial phase distribution

As demonstrated in Chapter III, in addition to location and velocity information, PEPT allows the occupancy distribution of the particle tracer to be determined via measurements of the time that the particle spends within each cell. As shown by Eq. (3.20), the occupancy O_E is directly proportional to the local volume concentration c, so that, in the examined two-phase system, phase distributions can be mapped using PEPT. Therefore, the azimuthally-averaged radial solid concentration profiles were estimated and are shown in **Figure 7.10** for both the PBTD and PBTU. All the solid volume concentration profiles have been normalised by the mean solid volume concentration, C. A high solid accumulation underneath the impeller is visible for every value of the mean solid concentration. This effect is more pronounced in the case of the PBTU at 5.2 wt% and 10.6 wt%. Everywhere else in the vessel, both pumping modes generate more or less similar radial concentration profiles. The vertical profiles of the normalised volume concentration of the solid phase averaged azimuthally and radially, c_h, are displayed in **Figure 7.11** for both pumping modes. The plots highlight the high degree of vertical non-uniformity of the solid distribution, with a local minimum at the impeller level and a local maximum above it, near the central plane; these salient points are much more prominent in the case of the PBTU. The shape of these profiles bears a good resemblance to the so-called 'belly-plots' available in the literature obtained by a number of other studies using either a single vertical probe traverse or a withdrawal technique (e.g., Barresi and Baldi, 1987). The results presented here, however, are much more detailed as solid concentration values are accurately determined on a pointwise 3D grid covering the whole vessel, which has not been possible before with any technique including sampling and probe methods.

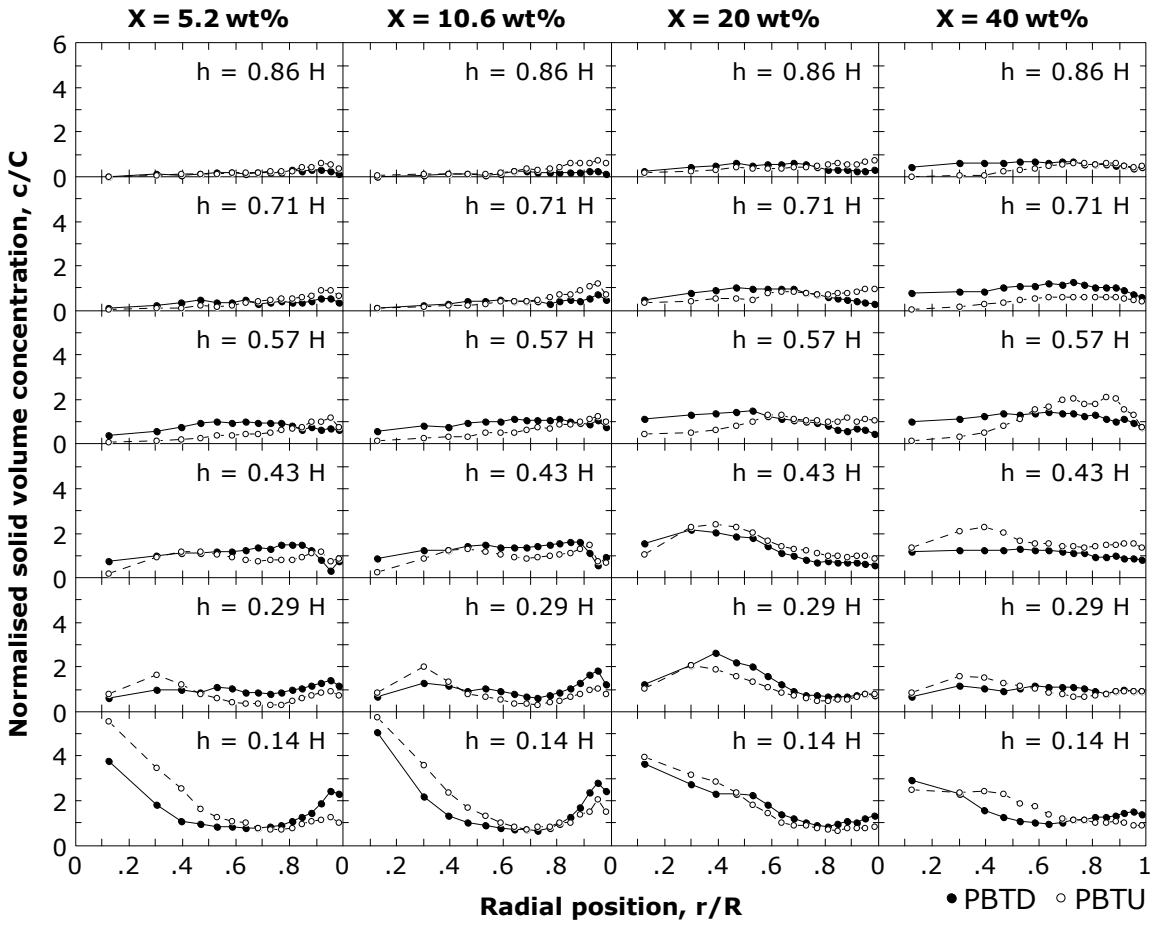

Figure 7.10. Azimuthally-averaged radial solid volume-concentration profiles at different heights in the vessel; $N = N_{js}$.

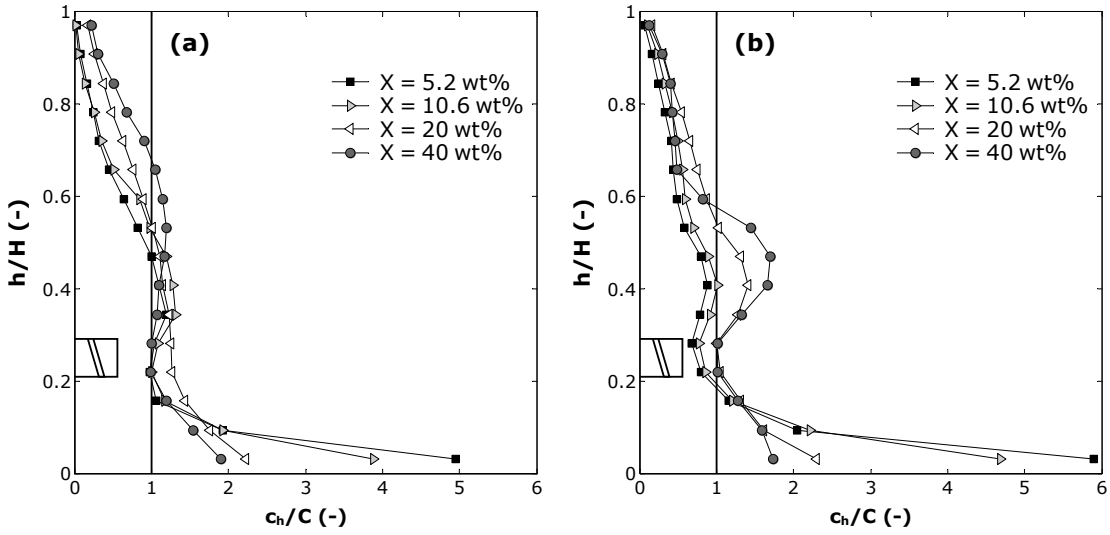

Figure 7.11. Vertical normalised profiles of azimuthally and radially-averaged solid volume concentration at $N = N_{js}$: (a) PBTD; (b) PBTU.

7-3.3 Flow number

In order to further assess the magnitude of the effect of the presence of particles on the flow field inside the stirred vessel, the dimensionless flow number was estimated. Because of the significant quantity of solids used, the volumetric flow rate, $Q^{(j)}$, discharged by the agitator needs to be determined separately for each phase j taking into account its local volume concentration. For each phase, $Q^{(j)}$ was calculated along the horizontal edge of the impeller blade corresponding to the impeller discharge plane, by integrating the axial velocity profile weighted by the local phase volume concentration, i.e. by (1–c) for the liquid phase and by c for the solid phase. Thus, the usual definition of the flow number used to estimate the pumping effectiveness of impellers in single-phase systems was extended to this two-phase problem. The flow number was computed for each phase using the following expressions:

$$Fl^{(L)} = \frac{Q^{(L)}}{ND^3} = \frac{1}{ND^3} \int_{PBT} (1-c) u_h^{(L)} dS \tag{7.1}$$

and

$$Fl^{(S)} = \frac{Q^{(S)}}{ND^3} = \frac{1}{ND^3} \int_{PBT} c u_h^{(S)} dS \tag{7.2}$$

where the superscripts L and S refer to the liquid and solid, respectively, and the integral in each case is evaluated over the horizontal discharge edge of the impeller blade (upper for PBTU and lower for PBTD). The sum of $Q^{(L)}$ and $Q^{(S)}$ represents the total volumetric discharge, Q, and introducing the two-phase flow number, Fl, it follows that

$$Fl = \frac{Q}{ND^3} = \frac{Q^{(L)} + Q^{(S)}}{ND^3} = Fl^{(L)} + Fl^{(S)} \tag{7.3}$$

As shown in **Figure 7.12**, low to moderate solid concentrations up to ~ 10 wt% seem to cause only a small reduction in $Fl^{(L)}$ which is compensated for by the increase in $Fl^{(S)}$ (due to the local rise in c); accordingly, the two-phase flow number, Fl, remains approximately constant. At higher solid concentrations above ~ 10 wt%, the increase in $Fl^{(S)}$ fails to counterbalance the steep reduction in $Fl^{(L)}$ caused by the presence of solid particles, consequently leading to a substantial reduction in Fl. This effect is much more significant when the impeller operates in the up-pumping mode; as such Fl diminishes by 18% when X rises from 10.6 to 40 wt% with

a PBTD, whilst incurring a massive reduction of 40% with a PBTU.

7-3.4 Uniformity of suspension

The substantial variation of the local solid concentration throughout the vessel, as demonstrated by the radial distributions in **Figure 7.10** and the axial profiles in **Figure 7.11**, justifies the introduction of a global uniformity index, ξ, to enable a quantitative description of the degree of uniformity of the distribution, thus:

$$\xi = \frac{1}{\sigma^2 + 1} = \frac{1}{\frac{1}{N_C}\sum_{i=1}^{N_C}\left(\frac{c_i - C}{C}\right)^2 + 1} = \frac{C^2}{\langle c^2 \rangle} \tag{7.4}$$

where i is the cell number within the measurement grid. The index is conveniently defined so that as $\xi \rightarrow 0$ the uniformity of the suspension is at its minimum (condition achieved for a theoretically infinite variance, σ^2, of the normalised local concentration); and when $\xi = 1$ the

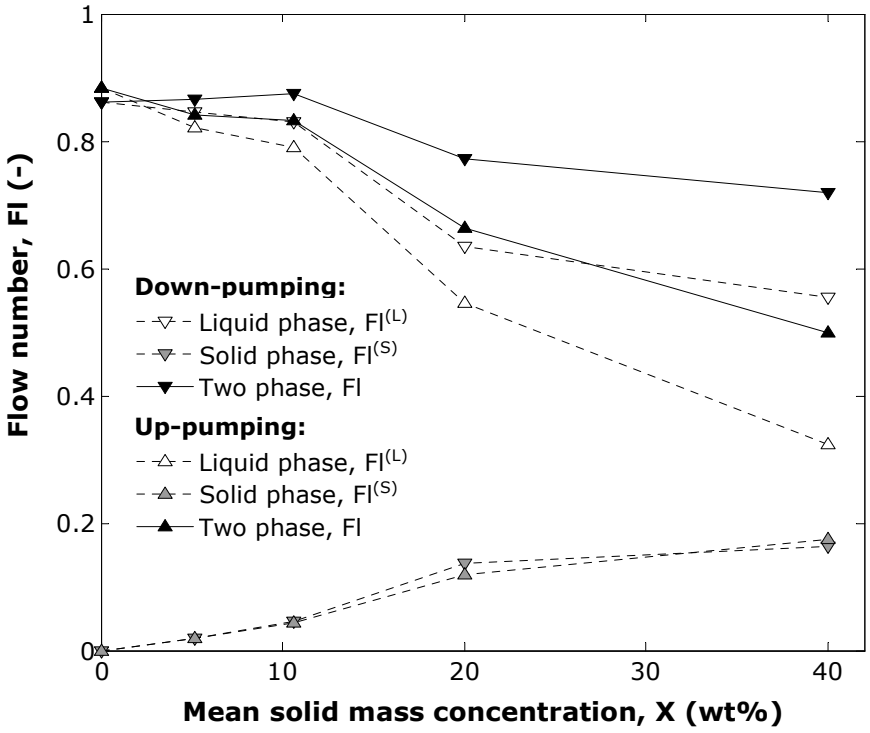

Figure 7.12. Effect of the mean mass concentration of the solid phase on the flow number.

solids are uniformly distributed within the vessel volume, i.e. there are no solid concentration gradients present and the local solid concentration everywhere is equal to the average concentration in the vessel (i.e. $\sigma^2 = 0$). Values of the index ξ for different average mass concentrations are reported in **Figure 7.13**, for both the up-pumping and down-pumping PBT. The results show that ξ increases with X for both modes of impeller operation. This seems to suggest, perhaps counter-intuitively, that as long as the particles are in suspension mode more concentrated suspensions will tend towards a homogeneous state by virtue of their increased solids loading. However, the results in **Figure 7.13** show that above ~ 20 wt% the rate of increase in ξ reduces dramatically for the PBTU, seemingly suggesting an inability to cope with the distribution of particles in suspensions of high solid fractions as demonstrated by the formation of a prominent 'belly' in **Figure 7.11b**. The data clearly demonstrate how a PBTD generally achieves a significantly more homogeneous suspension than a PBTU.

7-3.5 Verification of mass balance and mass continuity

The pointwise measurements obtained with PEPT have now enabled the solids mass balance throughout the vessel to be accurately verified, i.e. the measured local values of the solid volume concentration balance the experimental parameter C, so that

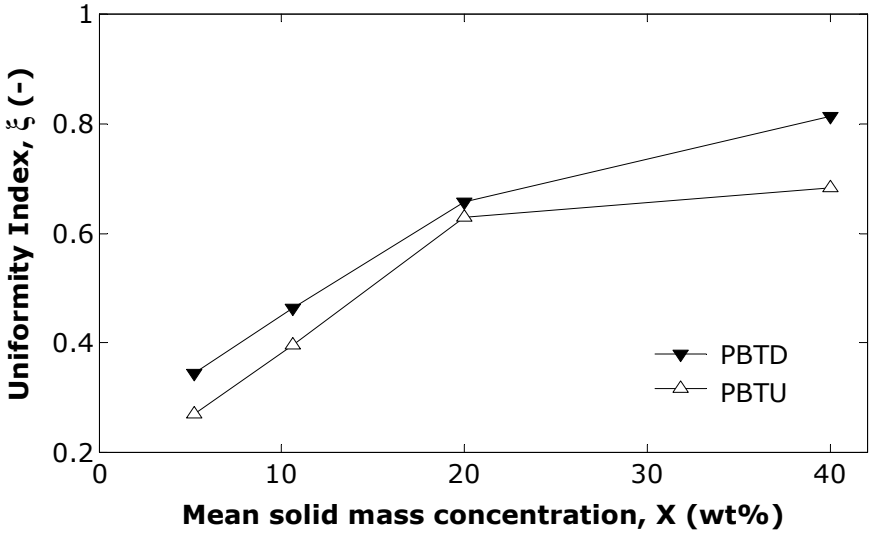

Figure 7.13. Variation of the uniformity index ξ as a function of mean solid mass concentration.

$$\frac{1}{n_c}\sum_{i=1}^{n_c} c_i \equiv C \tag{7.5}$$

The identity symbol '≡' appears in Eq. (7.5) because the local concentration is obtained from Eq. (3.20) through the measurement of local values of the occupancy O_E whose average value is by definition identically equal to 1.

An additional confirmation of the accuracy and reliability of the PEPT measurements can be obtained by verifying the mass continuity of the two phases. The net mass flux through a volume bounded by a closed surface S should be zero, thus

$$\sum_S \mathbf{u}\cdot\Delta\mathbf{S} \cong 0 \tag{7.6}$$

Calculations were made considering a cylindrical closed surface S with the same vertical axis, base and diameter as the tank but with a shorter height. Because of **u** being zero over the external surface of the vessel or being parallel to it the term $\mathbf{u}\cdot\Delta\mathbf{S}$ is zero everywhere except in

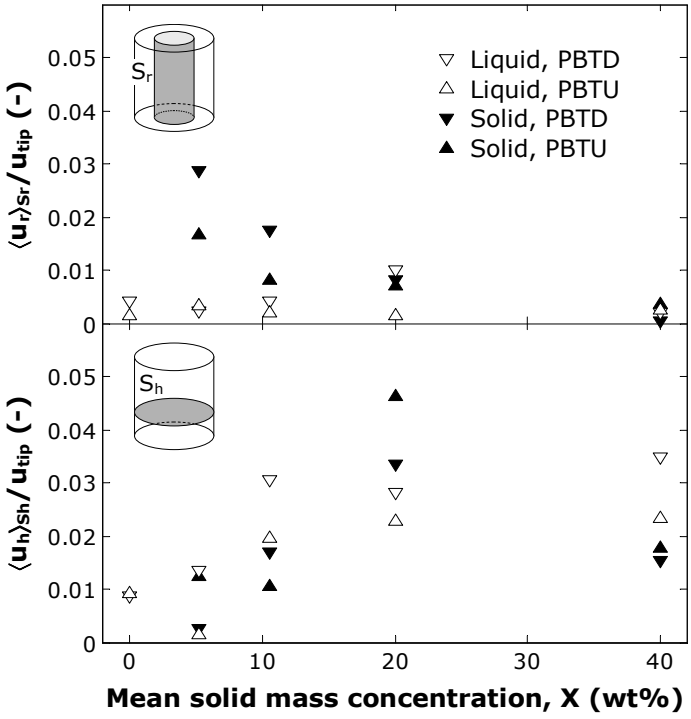

Figure 7.14. Normalised radial and axial velocities averaged on surfaces S_r (of diameter 0.5T) and S_h (0.3H off the base), respectively.

the horizontal plane across the tank, so that S can be reduced to such a plane (S_h). Dividing the vessel into equal volume cells makes $|\Delta\mathbf{S}|$ a constant, which reduces Eq. (7.6) to a zero sum (or average) of axial velocities across the horizontal plane considered. A similar situation can be obtained when considering a cylindrical closed surface with the same vertical axis and height as the tank but with a smaller diameter; Eq. (7.6) then becomes a zero sum (or average) of radial velocities across the lateral surface, S_r, of the considered cylinder. For the PEPT velocity fields presented above, calculations gave a velocity average close to zero, generally less than $0.03u_{tip}$, as demonstrated in **Figure 7.14**.

7-4 Conclusions

PEPT has been successfully applied to the study of turbulent solid-liquid suspensions in a stirred vessel. For the first time, the flow field in dense suspensions of up to 40 wt% solids has been probed in detail, which serves to demonstrate the exceptional power of PEPT as a non-invasive technique for the analysis of opaque multi-phase systems. It has been possible to obtain the trajectory, the full 3D velocity field and spatial distribution of both the liquid and solid phases, thus, yielding a substantial amount of unique experimental data.

Values of the two-phase flow number indicate that the pumping effectiveness of the PBT agitator is preserved for low to moderate concentrations. At high solid concentrations, however, the flow number is significantly reduced for a PBTD and even much more so for a PBTU.

The azimuthally and radially-averaged vertical solids distributions show qualitative resemblance with the very limited literature data obtained in a number of other studies using either a single vertical probe traverse or a withdrawal technique. A criterion based on the variance of the local solids concentration in the vessel has been used to quantitatively describe the uniformity of the suspension and a PBTD has been shown to achieve in general a significantly more homogeneous suspension than a PBTU.

Furthermore, the detailed pointwise measurements obtained with PEPT have enabled the solids mass balance throughout the vessel and the mass continuity of the two phases to be accurately verified; a unique result which has not been achieved by any other technique.

The technique will now be extended to study a number of unaddressed/unresolved problems in the area of solid-liquid mixing including complex polydisperse systems where particles of different size fractions can be selectively labelled and tracked.

Notation

Roman letters

b	Blade length	m
c	Local volume concentration of solids	-
C	Mean volume concentration of solids	-
c_h	Mean volume concentration at level h	-
d	Particle diameter	m
D	Impeller diameter	m
Fl	Two-phase flow number	-
$Fl^{(L)}$	Flow number of the liquid phase	-
$Fl^{(S)}$	Flow number of the solid phase	-
h	Axial distance	m
H	Height of the suspension	m
i	Cell number	-
j	Phase index	-
k	Cylindrical direction index (ϑ, r or h)	-
n_c	Number of grid cells	-
N	Impeller rotational speed	s^{-1}
N_{js}	Minimum speed for particle suspension	s^{-1}
O_E	Occupancy	-
$\mathbf{P}$	Tracer location vector	|m|
Q	Total impeller pumping rate	$m^3\ s^{-1}$
$Q^{(L)}$	Impeller liquid pumping rate	$m^3\ s^{-1}$
$Q^{(S)}$	Impeller solid pumping rate	$m^3\ s^{-1}$
r	Radial distance	m
R	Vessel radius	m
Re_{imp}	Impeller Reynolds number ($N_{js}D^2/\nu$)	-
S	Surface area	m^2
S_h	Horizontal planar surface area	m^2
S_r	Vertical cylindrical surface area	m^2
t	Time	s
T	Vessel diameter	m

t_∞	PEPT runtime	s
u	3D velocity vector	$\lvert m\ s^{-1} \rvert$
u_{rh}	2D radial-axial velocity magnitude	$m\ s^{-1}$
u_{tip}	Impeller tip speed	$m\ s^{-1}$
$u_\vartheta\ u_r\ u_h$	Cylindrical velocity components	$m\ s^{-1}$
w	Blade width	m
X	Mean mass concentration of solids	-
$x\ y\ z$	Cartesian coordinates	m

Greek letters

ν	Kinematic liquid viscosity	$m^2\ s^{-1}$
ξ	Uniformity index	-
σ	Standard deviation of normalised c	-

Abbreviations

PBT	Pitched blade turbine
PBTD	Down-pumping PBT
PBTU	Up-pumping PBT
PEPT	Positron emission particle tracking
PIV	Particle image velocimetry

Chapter VIII
Mixing of Binary Solid-Liquid Suspensions

Abstract

In this study, the three-component flow field and spatial phase distribution of binary mixtures of glass particles suspended in water in a stirred vessel have been resolved using positron emission particle tracking (PEPT). The Lagrangian flow data provided by the technique have been converted to give a detailed Eulerian description of each of the three phase components of the flow generated by a down-pumping pitched blade turbine (PBTD). It has been possible to determine the full 3D velocity and concentration fields of the liquid phase and both the solid components within opaque dense slurries of this type containing up to 40 wt% solids. Spatial distributions of local time-averaged slip velocity have also been obtained for each solid component showing wide variations. The detailed measurements have enabled the solids mass balance and the mass continuity of the three components to be accurately verified throughout the vessel. Using a pitched blade turbine pumping upwards (PBTU) rather than downwards, the experimental campaign and data analysis procedure were repeated to obtain similar results for this agitation mode and compare the different mixing performances of the two agitation modes.

8-1 Introduction

The processing of solid-liquid suspensions such as bio-slurries, crystallisation and catalytic mixtures is frequently conducted in mechanically agitated vessels. In such systems one crucial aspect is the achievement of good mixing which allows for an efficient interaction between the different flow components.

Among the various flow visualisation techniques, laser Doppler velocimetry (LDV) and particle image velocimetry (PIV) have become the most reliable to examine the complex nature of the flow fields in optically transparent single-phase systems (e.g., Ducci and Yianneskis, 2006; Chung *et al.*, 2007; 2009). Application to multi-phase studies, however, has been restricted to extremely dilute suspensions as these techniques fail completely in dense systems which are opaque (e.g. Unadkat *et al.*, 2009). One of the important aspects in the local description of multi-phase or multi-component mixtures is the measurement of phase distribution which has remained a challenge. Attempts at local measurements in these systems have been mainly limited to the measurement of mean axial solid-concentration profiles at relatively low concentrations, using a single vertical conductivity or capacitance probe traverse or a withdrawal technique (Brunazzi *et al.*, 2004; Barresi and Baldi, 1987). More recent experimental studies using electrical resistance tomography (ERT) demonstrated, albeit mainly qualitatively, how visualisation of gas, solid or liquid distribution can help improve understanding of mixing processes (e.g., Wang *et al.*, 2000). However, none of these methods is suitable to probe concentrated suspensions in detail to acquire quantitative information on the local flow dynamics of the different phase components or their individual 3D distribution.

A number of mixing studies have reported that in stirred solid-liquid systems variation in the particle size produces significant effects on the fluid dynamics and phase distribution. For example, Virdung and Rasmuson (2007) showed that the fluid velocity fluctuation, detected via LDV measurements, due to the turbulence levels in the liquid phase were higher in solid-liquid suspensions than in a single phase flow, an effect that increased with particles size. Although their simulations involved particle sizes less than 0.1 mm, Altway *et al.* (2001) showed that the pattern of solid concentration contours for different particle sizes was qualitatively similar; however, smaller particles showed a more uniform distribution. Using larger particles with 0.1 mm < d < 0.5 mm, Špidla *et al.* (2005) experimentally confirmed by

means of a conductivity probe that smaller solid particles generate a more homogeneous suspension. The results also showed that the homogeneity of the solid-liquid suspension improved with increasing average solid concentration. The same effect has been observed using coarse monosized particles ($d \sim 3$ mm) in Chapter VII, as more homogeneous suspensions were obtained when the solids content was increased.

This chapter reports on the use of the PEPT technique to study the mixing of dense binary mixtures consisting of glass beads of two different size classes suspended in water. Extensive data for these binary systems containing up to 40 wt% solids are presented here. Detailed information is obtained on particle and fluid trajectories which is converted to give a pointwise Eulerian description of the flow field as well as the spatial distribution of each of the liquid and two solid components of the mixture.

8-2 Experimental

8-2.1 Multi-component positron emission particle tracking

As discussed in details in Chapter III, the Lagrangian technique of positron emission particle tracking primarily involves the use of a labelled particle tracer, a positron camera and a location algorithm for computing the tracer location.

In the case of a multi-component system, the full three-dimensional trajectory of each component must be resolved separately using different particle tracers. Currently, PEPT can most accurately track one particle at a time. For this reason, PEPT multi-component investigations consist of multiple successive and distinct experiments, i.e. one for a single-phase system, two for a monodisperse suspension, and three for a binary suspension. The Lagrangian evolution of the flow components for the binary systems discussed in this chapter is presented in Appendix B as sequence of images. These images were obtained via emulated multiple particle tracking as discussed in Section 6-3.5).

8-2.2 Experimental apparatus and procedure

Using a similar experimental set-up to that used for the analysis of monodisperse systems in Chapter VII, the PEPT experiments were conducted in a fully-baffled flat-base vessel of

diameter T = 288 mm, agitated by a 6-blade 45º pitched-turbine (PBT) of diameter D = 0.5 T, as shown in **Figure 8.1**. The height of the suspension was set at $H = T$ and the impeller off-bottom clearance was 0.25 T. The suspending liquid was an aqueous solution of NaCl of density 1150 kg m^{-3} - NaCl was added to enable the water density to be matched to that of the resin PEPT tracer used to track the liquid - and the solid particles used were spherical glass beads of density 2485 kg m^{-3}. Two nearly-monomodal particle size fractions, (d_1 = 1.00-1.25 mm, d_2 = 2.85-3.30 mm) were used to make a binary solid-liquid suspension. The two size fractions were mixed in equal proportions with a total solid mass concentration, X, varying from 0 to 40 wt%, i.e. $X_1 = X_2 = 0.5\ X$.

During the first experimental campaign, suspension of the solids was investigated with the PBT impeller pumping downwards (PBTD). Experiments were conducted at the minimum rotational speed for particle suspension in the binary mixture, N_{js}, visually determined through the transparent walls of the vessel according to the well-known Zwietering criterion, i.e. no particle should remain stationary on the base of the vessel for longer than 1-2 s (Zwietering, 1958). The experimental campaign was repeated using a pitched blade turbine pumping upwards (PBTU) rather than downwards. The experimental conditions are summarised in **Table 8.1**

Each component of the suspension was tracked and its full trajectory separately determined in three successive experiments. A neutrally-buoyant radioactive resin tracer of 600 μm diameter was used to track the liquid phase, and from each particle size fraction a

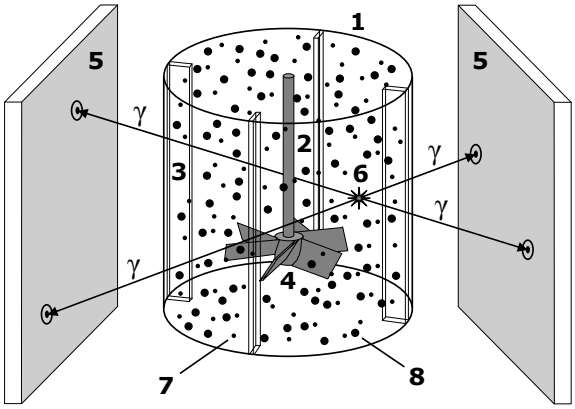

Figure 8.1. Experimental PEPT set-up for studying the mixing of a binary suspension: 1 tank; 2 shaft; 3 baffle; 4 PBT; 5 γ-ray detectors; 6 PEPT tracer; 7 glass beads (d ~1 mm); 8 glass beads (d ~3 mm).

representative glass particle was taken, was directly irradiated via a cyclotron and its motion tracked within the agitated slurry. The PEPT tracking time was 30 min in each case, long enough so that adequate data resolution was obtained in every region of the vessel and ergodicity of flow, given that the probability of visit is well-distributed by virtue of the open geometry of the vessel where all regions are more or less equally accessible by the tracer, and the highly turbulent state of the suspension where $\mathrm{Re}_{imp} = N_{js}D^2/\nu > 10^5$. Ergodicity is discussed in details in Section 3-5.1.

8-2.3 Data analysis

PEPT only provides the Cartesian (x, y, z) coordinates of a single particle tracer moving within the system being studied as a function of time. The newly developed code, whose computational procedures are presented in Chapter III, has been used to analyse PEPT flow data. Using cylindrical coordinates to calculate Lagrangian velocities along the trajectory of the tracer, the Lagrangian velocities are converted to Eulerian velocities using a 3D user-defined grid consisting $n_c = 512$ equal volume cells.

In addition to location and velocity information, PEPT allows the particle-tracer occupancy distribution within the vessel volume to be computed and, on the basis to Eq. (3.15) applied to the flow systems studied here, the local occupancy of each of the three component of the mixture, O_j, can be defined as

Table 8.1. Experimental conditions for the study of binary solid-liquid suspensions.

X (wt%)	C (vol%)	N *or* N_{js} (s^{-1})		Re_{imp} (-)	
		PBTD	PBTU	PBTD	PBTU
0	0	5.00	5.00	1.19×10^5	1.19×10^5
5.2	2.5	6.33	6.00	1.51×10^5	1.43×10^5
10.6	5.2	7.50	7.00	1.79×10^5	1.67×10^5
20.0	10.4	8.50	8.00	2.03×10^5	1.91×10^5
40.0	23.6	10.17	10.00	2.43×10^5	2.38×10^5

$$O_j = \frac{\Delta t_j}{t_E} \tag{8.1}$$

where Δt_j is the time that the tracer of the j-th component (solid or liquid) of the mixture spends inside a given cell and the ergodic time, $t_E = t_\infty / n_c$, is used instead of the total experimental time t_∞. For the binary systems examined in this work, the index j assumes values 1, 2 or 3 where $j = 1, 2$ denotes the solid components, and $j = 3$ denotes the liquid phase also sometimes designated by the symbol L.

Given the above definition, the average value of the occupancy is 1 independently of the chosen number of grid-cells n_c. Considering the system at hand, a specific small solid particle having diameter d_j selected from the solid component j has an infinitesimal probability, $f(\mathbf{P})dV$, to be inside an infinitesimal volume element dV, which is a function of the particle position $\mathbf{P}$ and can be expressed from two different points of view. From the Lagrangian point of view, it is the ratio of the infinitesimal time dt_j that the solid particle spends inside dV to the total time of detection t_∞. In Eulerian terms, however, it is the ratio of the number of solid particles dn_j, contained in dV, to the total number of such particles in the vessel n_j. Consequently, it follows that

$$\left\{ f(\mathbf{P})dV = \frac{dt_j}{t_\infty} \quad \text{and} \quad f(\mathbf{P})dV = \frac{dn_j}{n_j} \right\} \quad \Rightarrow \quad \frac{dt_j}{t_\infty} = \frac{dn_j}{n_j} \tag{8.2}$$

Considering the j-th solid component, and introducing the volume of a single particle V_{Pj}, the infinitesimal solid volume dV_j in dV, the solid volume present in the tank V_j, the local solid volume concentration c_j, the mean solid volume concentration in the vessel C_j, and the total volume of the multi-phase suspension in the vessel V_T, yields

$$\frac{dn_j}{n_j} = \frac{V_{Pj} dn_j}{V_{Pj} n_j} = \frac{dV_j}{V_j} = \frac{c_j dV}{C_j V_T} \tag{8.3}$$

Combining Eq. (8.2) and Eq. (8.3) leads to a clear correlation between the time that the tracer spends inside dV and the local solid volume concentration, i.e.

$$\frac{dt_j}{t_\infty} = \frac{c_j dV}{C_j V_T} \tag{8.4}$$

If the cell volume, ΔV, in the grid is uniform, the total number of grid cells is then $n_c = V_T / \Delta V$, and rewriting the above equation in discrete terms gives

$$\frac{\Delta t_j}{t_\infty} = \frac{c_j \Delta V}{C_j V_T} \quad \Rightarrow \quad \frac{\Delta t_j}{t_E} = \frac{c_j}{C_j} \tag{8.5}$$

Now, using the definition given by Eq. (8.1) for the occupancy O_j as the ratio of time that the tracer spends inside a cell to the ergodic time, Eq. (8.5) then finally becomes

$$O_j = \frac{c_j}{C_j} \tag{8.6}$$

In the same way of Eq. (3.20), although Eq. (8.6) has been derived for a discrete phase component, such an expression of the occupancy is equally valid for the continuous fluid component ($j = 3$). The consequential implication which readily follows from Eq. (8.6) is that, even in a complex multi-component solid-liquid suspension, it is possible to fully resolve the local concentration distribution of each flow component (solid and liquid).

8-3 PBTD: results and discussion

Extensive data were obtained through Lagrangian tracking of the solid and liquid components of the binary suspensions described above. Results are presented as azimuthally-averaged Eulerian maps or profiles which represent the whole flow field including the effect of the baffles. This is an effective way of presenting 3D data in a reduced form. Furthermore, in order to enable efficient consultation and comparison of data, results are presented in a concise format using sets of images judiciously produced by grouping together multiple graphs, greyscale contours, or vector plots. Results include for each component of the mixture, flow fields, spatial distributions, slip velocities, flow numbers and uniformity indices. Finally, evidence of the reliability of the PEPT technique and the related data analysis is provided via three-component mass continuity calculations conducted throughout the vessel.

8-3.1 Flow fields

As mentioned above, raw data were analysed by defining a cylindrical grid consisting of

n_c = 512 equal volume cells. The vector velocity map of the agitated liquid obtained with no solid particles present in the vessel (X = 0 wt%) is shown in **Figure 8.2** for an impeller rotational speed N = 5 s^{-1} = 300 rpm. Using cylindrical coordinates, the radial-axial 2D velocity map was obtained by azimuthally averaging the 3D velocity data and projecting them onto the 2D radial-axial plane (*rh*). As pointed out above, whilst two-dimensional these flow maps are representative of the whole 3D velocity field. The observed flow field with a single flow loop is typical of a down-pumping PBT with a low impeller off-bottom clearance. As expected, fluid velocities are relatively high in the impeller region and around the flow loop, but low in the upper parts of the tank and in the centre of the loop. For ease of comparison, all the velocity plots presented are normalised by the impeller tip speed, u_{tip}.

The effects of the mean solid concentration, X, on the velocity fields of the liquid phase and the two solid components are depicted in **Figure 8.3**. A comparison of the liquid flow maps

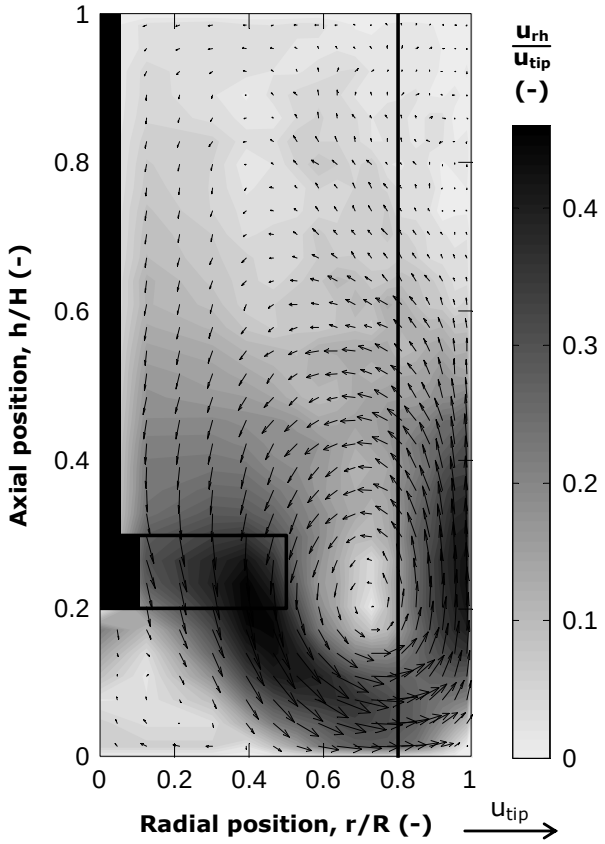

Figure 8.2. Azimuthally-averaged radial-axial velocity map of the liquid phase in the absence of solid particles (X = 0 wt%) at N = 5.0 s^{-1}; PBTD.

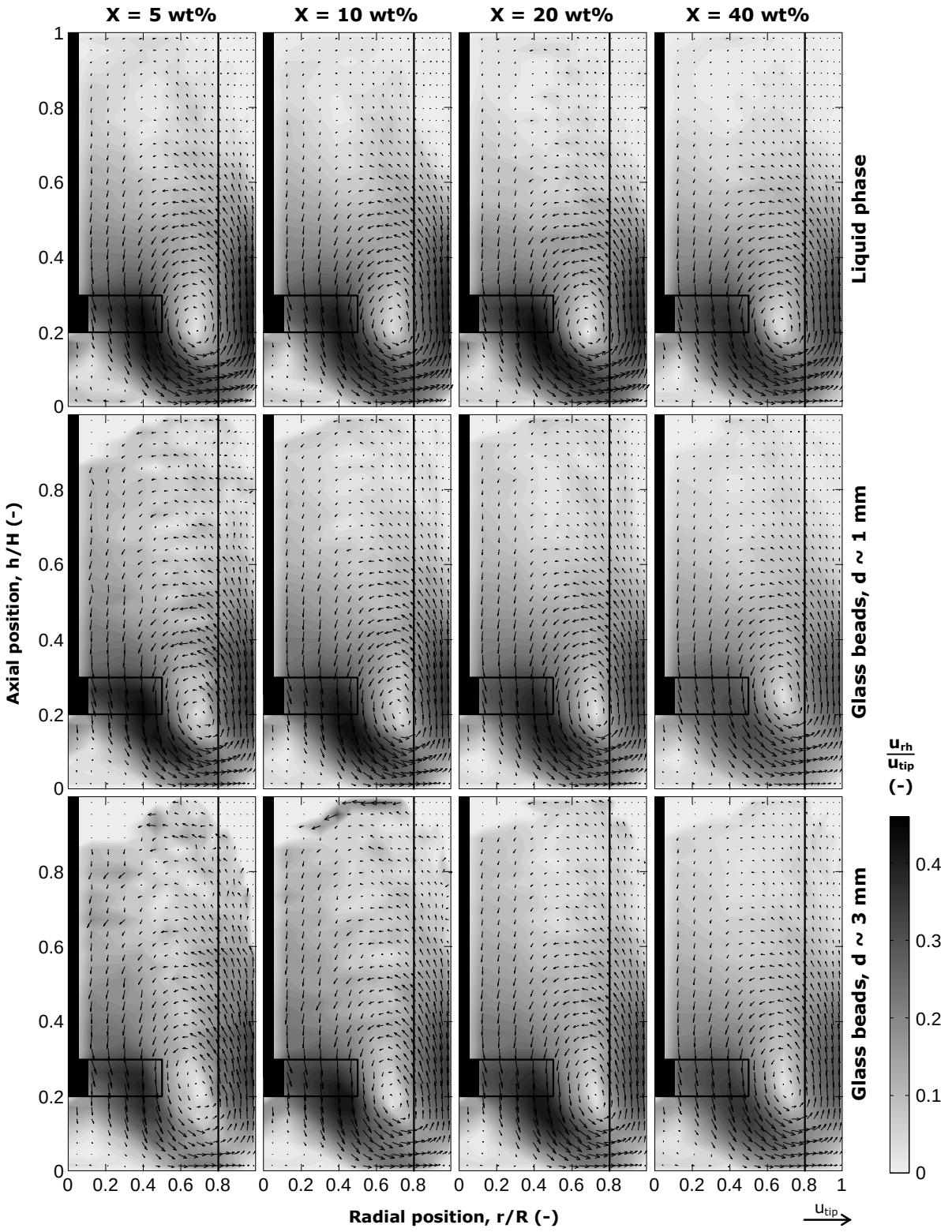

Figure 8.3. Azimuthally-averaged radial-axial velocity maps of the three components of the suspension at varying X; $N = N_{js}$; PBTD.

under single-phase flow conditions (**Figure 8.2**) and in the presence of the solid phase (first row in **Figure 8.3**) shows global qualitative similarities in the flow pattern even at X = 40 wt%. A more detailed scrutiny of the images reveals that, excluding the impeller discharge region, no significant quantitative changes occur in the velocity field up to 20 wt% solids, but a distributed small diminution of the normalised velocity is observed at X = 40 wt%. In addition, the contours suggest that the normalised velocity in the discharge region diminishes as X increases up to 10 wt%, but slightly recovers at 20 wt% before further declining at 40 wt%.

Unlike the liquid phase, more significant qualitative and quantitative variations in the flow field can be observed for the smaller solid particles having d ~ 1 mm, as shown in the second row of **Figure 8.3**. At X = 5 wt%, the flow field is affected by large fluctuations which make the vector plot appear slightly irregular. This is caused by the scarce presence of solids in the upper part of the vessel which drops to almost zero close to the surface; such an effect was visually confirmed during the experiments and will be highlighted again below when analysing the phase distributions. Whilst the normalised velocity in the discharge region decreases monotonically as X increases from 5 wt% to 40 wt%, the centre of the loop slowly shifts upwards from $h = 0.2H$ (X = 5 wt%) to $h = 0.25H$ (X = 40 wt%).

Similarly, the flow fields of the second solid component consisting of glass beads with d ~ 3 mm (third row in **Figure 8.3**), are affected by the low particle occupancy of the upper part of the tank. In this case, however, the irregularities are more pronounced and extend to the suspension with X = 10 wt%. In a similar way to the smaller particles, there is a clear damping of the solid flow field in the impeller region at X = 40 wt%.

The above considerations are complemented by **Figure 8.4**, which shows the contours of the azimuthally-averaged tangential velocity component for the three components of the suspension. As expected, all the greyscale maps exhibit their maxima ($0.2\text{-}0.25u_{tip}$) near the lower tip of the impeller blades. The liquid phase is characterised by the highest tangential velocities whose magnitude and spatial distribution are not significantly affected by X. In a similar way to the radial-axial velocities, at 5 wt% the contours of the two solid components are affected by small irregularities which generate a uniformity effect in the velocity map for the larger particles. Both solid components show significantly reduced tangential velocities for X = 40 wt%.

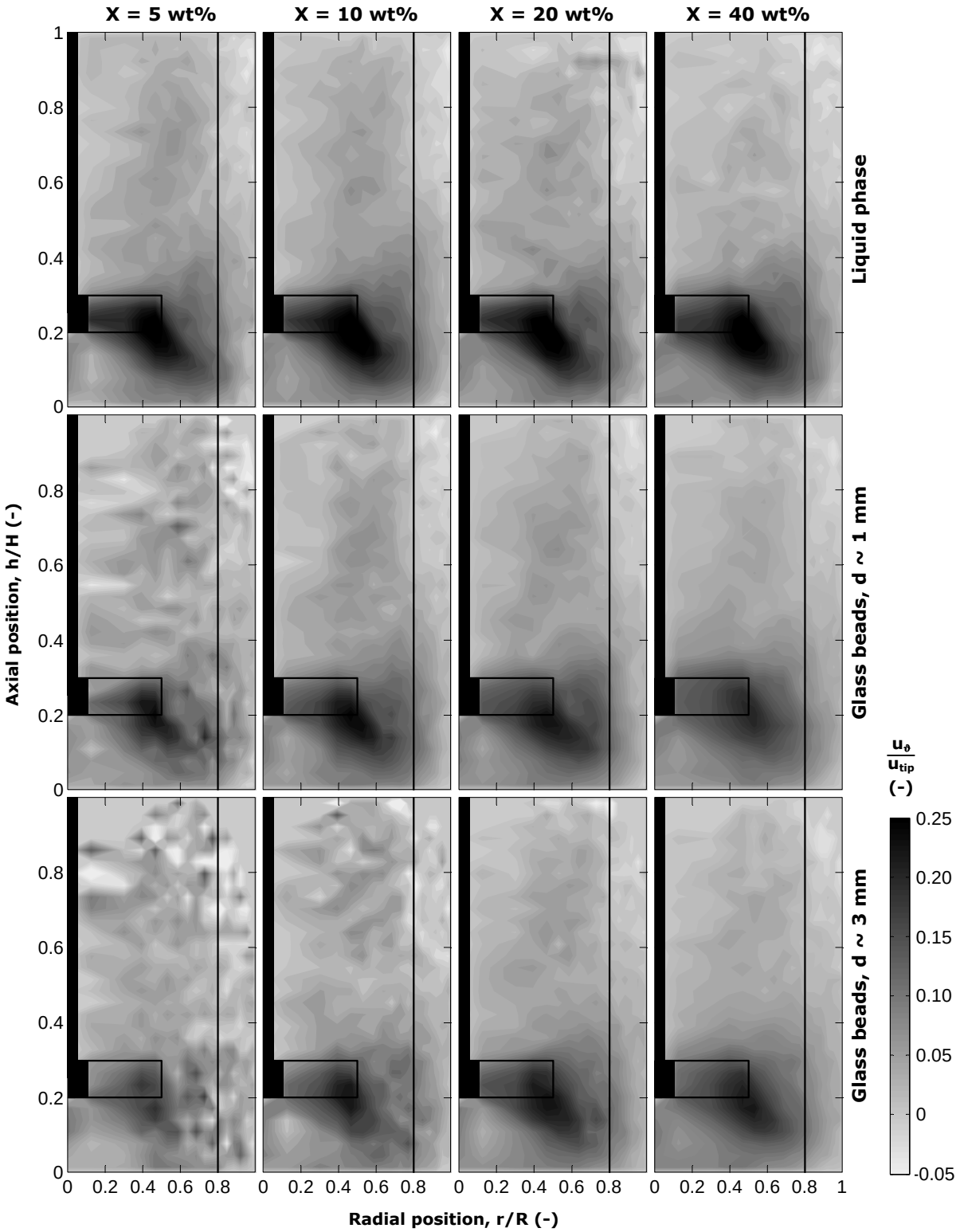

Figure 8.4. Azimuthally-averaged tangential velocity maps of the three components of the suspension at varying X; $N = N_{js}$; PBTD.

The observations made above are quantitatively confirmed in **Figure 8.5** which shows details of the effects of the mean solid concentration on the three velocity components for each component of the mixture. The plots exhibit radial distributions of the three velocity components (u_ϑ, u_r, u_h) in the horizontal impeller discharge plane, i.e. along the lower edge of the impeller blade at $h = 0.2H$. In a similar way to the flow maps discussed above and in the previous chapters, all the velocity plots have been normalised by the impeller tip speed, u_{tip}, for ease of comparison.

As expected, due to the type of agitator used, the dominant velocity component in this plane for all the mixture components is the axial u_h. The tangential velocity component is only significant close to the impeller and falls off to almost zero away from it. The radial component for all phase components is generally relatively small, except at 40 wt% solids where for both solid components it is comparable to the tangential component.

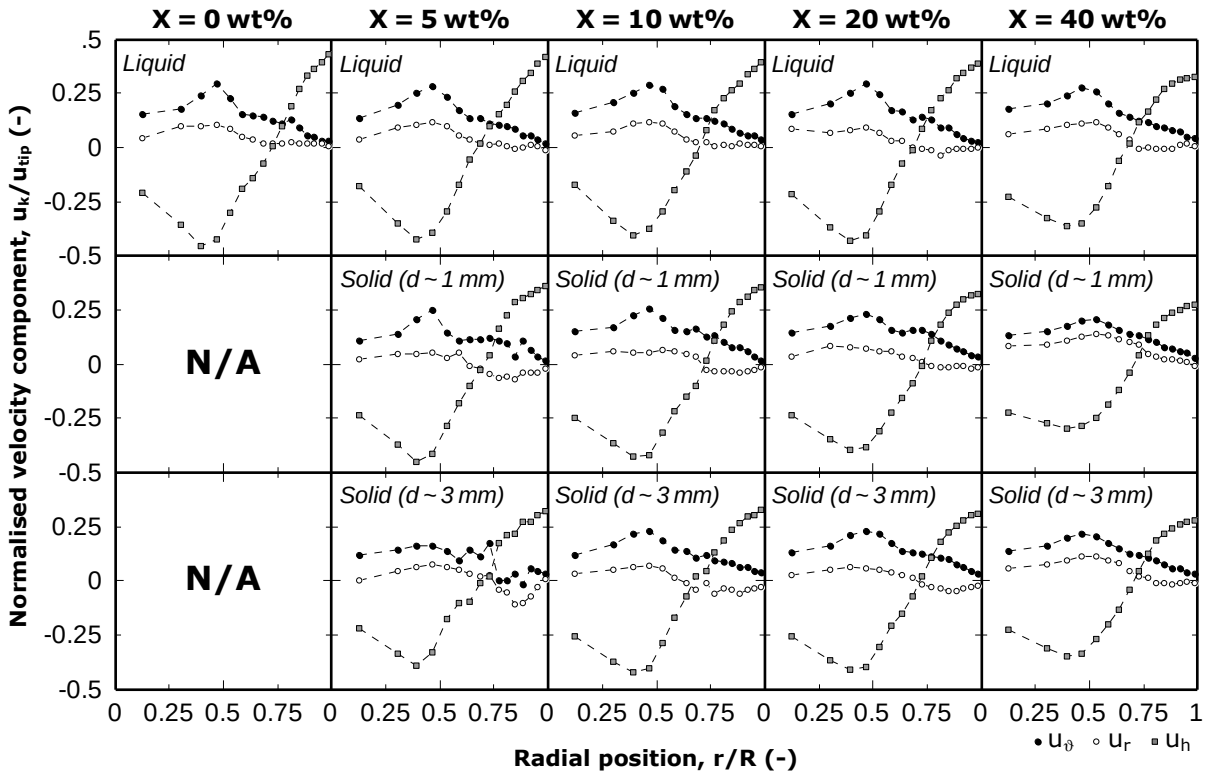

Figure 8.5. Azimuthally-averaged radial profiles of the three velocity components in the horizontal impeller discharge plane at $h = 0.2H$; $N = N_{js}$; PBTD.

8-3.2 Time-averaged slip velocity maps

The primary objectives of solid-liquid mixing are to create and maintain a slurry and/or to promote and enhance the rate of mass or heat transfer between the solid and the liquid phase. Heat and mass transfer coefficients are significantly influenced by the relative velocity between phases, also known as slip velocity. Such an important hydrodynamic variable obviously varies from point to point within a stirred vessel and there are no techniques available for measuring it. Consequently, in practice, the particle settling velocity has often been taken as a guess estimate of the slip velocity (Atiemo-Obeng *et al.*, 2004).

Neglecting any contribution to slip which might arise from possible rotation of a particle about its centre, the magnitude of the local time-averaged slip velocity vector can be determined for each solid component *j*, thus:

$$s_j = \sqrt{\left(u_\vartheta^{(L)} - u_\vartheta^{(j)}\right)^2 + \left(u_r^{(L)} - u_r^{(j)}\right)^2 + \left(u_h^{(L)} - u_h^{(j)}\right)^2} \tag{8.7}$$

In consequence, the radial-axial and tangential velocity data presented in **Figure 8.3** and **Figure 8.4** can be used to map the local time-averaged slip velocity.

The effects of the mean solid concentration on the spatial distribution of the normalised slip velocity for each solid component of the mixture is shown in **Figure 8.6**. The irregularities of the solid flow fields attributed to the scarce presence of solid particles in the upper part of the vessel, as discussed above in relation to **Figure 8.3**, cause analogous effects in the slip velocity maps at $X = 5$ wt% for the smaller particles and up to $X = 10$ wt% for the larger particles.

There are wide variations in the spatial distribution of s_j. As a consequence of Eq. (8.7), which combines radial-axial and tangential contributions, the regions of maximum slip velocity occasionally correspond with the lower tip of the impeller blades (tangential dominance), with the discharge region of the impeller (radial-axial dominance), or with both areas when there is a more balanced contribution of the three cylindrical components of the slip velocity vector. For both particle size fractions, the areas above the impeller and in the upper part of the vessel, i.e. $h > 0.4H$, are characterised by a gradual but significant reduction in the slip velocity with increasing X. A similar reduction is observed in the rest of the vessel for particles with $d \sim 3$ mm.

8-3.3 Spatial solid and liquid distribution

On the basis of Eq. (8.6), in each binary suspension the local occupancy can be obtained for each solid component and the liquid; consequently, the volume concentration of each component can be mapped. The spatial distributions of the three phases can be effectively compared using purposely created maps, where the radial-axial plane is divided into square boxes containing information for every solid and liquid component, as shown in **Figure 8.7a**. Each box contains two shaded bars: the fraction of the box area occupied by each bar is equivalent to the local volume of the corresponding solid component, while the remaining

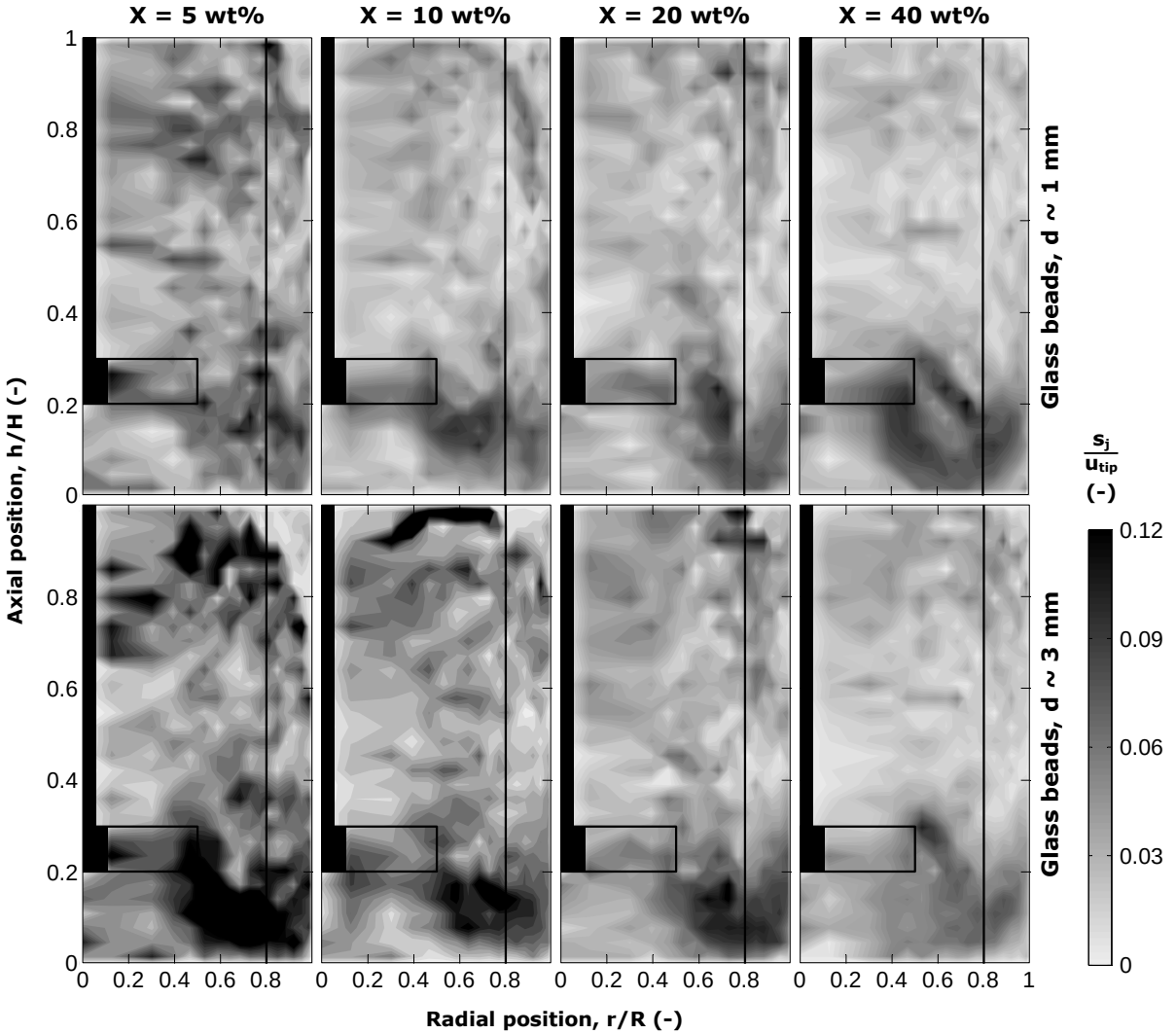

Figure 8.6. Normalised azimuthally-averaged maps of time-averaged slip velocity of the solid components of the suspension at varying X; $N = N_{js}$; PBTD.

white area is equivalent to the local liquid volume. Furthermore, by drawing bars of equal base, their height is also proportional to the local solid volume concentration and, thus, horizontal profiles of solid concentration for each solid component can be represented at each horizontal level as depicted in **Figure 8.7b**.

The spatial distribution of the volume fraction of both particle size classes is shown in **Figure 8.8** for X = 5-40 wt%. Since these 2D maps were obtained from azimuthally averaged data, the area of each square cell is representative of the volume of the related 3D cell (a torus with a square cross-section). A high solid accumulation underneath the impeller is visible for every value of the mean solid concentration. This effect is more pronounced for larger glass particles, so that the local solid volume concentration of the larger particles (d ~ 3 mm) is about twice the concentration of the smaller particles (d ~ 1 mm) up to X = 20 wt%. At X = 40 wt%, the accumulation underneath the impeller is still high compared to the rest of the tank, but overall the solids distribution appears much more uniform than for lower X values, especially in the case of the smaller particles. This result suggests that, at $N = N_{js}$, the accumulation below the turbine reduces for smaller particles and/or higher solids concentrations.

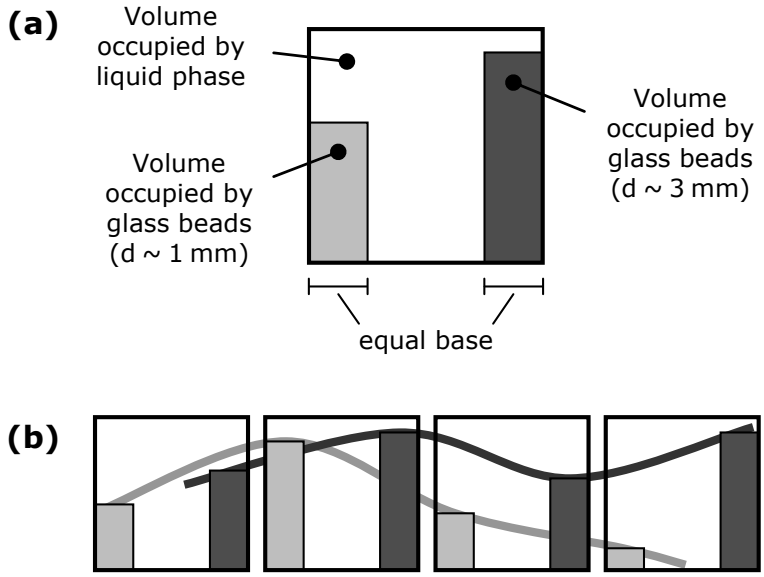

Figure 8.7. Representation of the local concentration of the three suspension components: (a) square box containing information for every solid and liquid component; (b) a sequence of adjacent boxes depicting two horizontal solid volume concentration profiles.

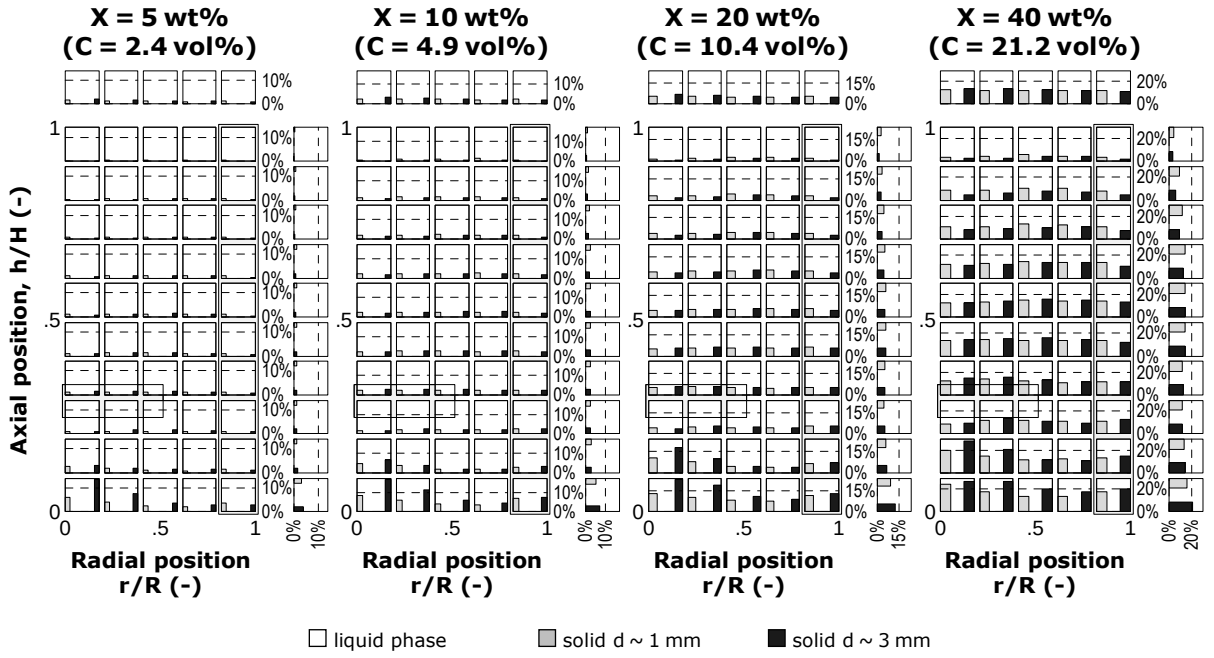

Figure 8.8. Azimuthally-averaged local volume concentrations maps for the three components of the suspension at varying *X*; PBTD. Note that unless otherwise indicated the symbol '%' indicates 'vol%'.

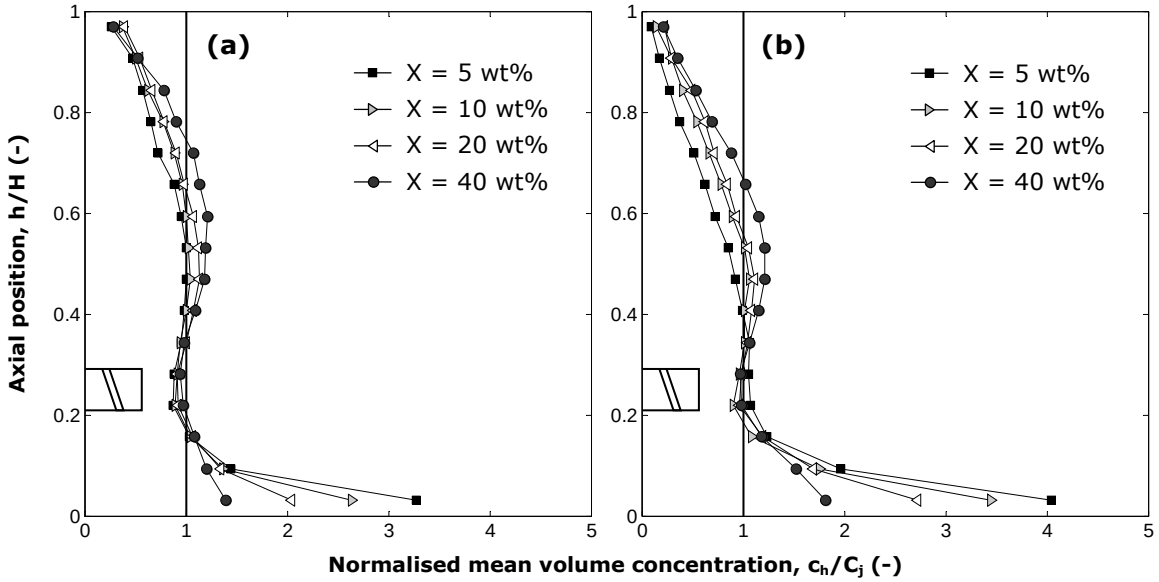

Figure 8.9. Vertical normalised profiles of azimuthally and radially-averaged solid volume concentration at $N = N_{js}$ for PBTD: (a) ~ 1 mm glass beads; (b) ~ 3 mm glass beads.

Moreover, information on the radial and vertical average concentration profiles is also provided in **Figure 8.8**; whilst to the right of each map the vertical profile of the radially-averaged volume concentration is shown, the radial profile of the vertically averaged volume concentration is shown above the map. The average radial profiles are more or less flat for both particle size fractions, whereas the vertical profiles show similar behaviour at every X value. To compare such vertical profiles, normalised values of the azimuthally and radially averaged volume concentration, c_h, of each particle size class are plotted in **Figure 8.9**. The plots highlight the non-uniformity of the solids distribution, with a minimum at the impeller plane and a maximum above it, near the central plane. The proximity of the profiles to the vertical line $c_h / C_j = 1$ for smaller particles and/or higher solids concentrations, corrobates the point previously highlighted that local solids build up diminishes under these conditions.

In a similar way to the monodisperse systems studied in Chapter VII, the shape of the curves in **Figure 8.9** bears a good resemblance to the so-called 'belly-plots' reported in the literature in a number of studies using either a single vertical probe traverse or a withdrawal technique, e.g. Barresi and Baldi, 1987. The results presented here, however, are much more detailed as local solid concentration values are accurately determined on a pointwise 3D grid covering the whole vessel.

8-3.4 Global indices for multi-phase mixing

Flow number

In order to further assess the magnitude of the effect of the presence of particles on the flow field inside the stirred vessel, the dimensionless flow number was estimated. Because of the considerable quantity of solids used, the volumetric flowrate discharged by the agitator needs to be determined separately for each flow component taking into account its local volume concentration. For each component of the mixture, $Q^{(j)}$ was calculated along the horizontal lower edge of the impeller blade corresponding to the impeller discharge plane, by integrating the axial velocity profile weighted by the local volume concentration, i.e. by c_1 and c_2 for the solid components and by c_3 for the liquid phase. Thus, the usual definition of the flow number used to estimate the pumping effectiveness of impellers in single-phase systems, which has already been extended to the two-phase flow number in Chapter VII, was further extended to this three-component problem. The flow number was computed for each component using the following expression:

$$Fl^{(j)} = \frac{Q^{(j)}}{ND^3} = \frac{1}{ND^3} \int_{PBT} c_j u_h^{(j)} dS \tag{8.8}$$

where the integral is evaluated over the horizontal discharge edge of the impeller blade ($h = 0.2H$ and $r \leq 0.5R$). The sum of $Q^{(L)}$, $Q^{(1)}$ and $Q^{(2)}$ represents the total volumetric discharge, Q, and introducing the total two-phase flow number, Fl, it follows that:

$$Fl = \frac{Q}{ND^3} = \frac{Q^{(L)} + Q^{(1)} + Q^{(2)}}{ND^3} = Fl^{(L)} + Fl^{(1)} + Fl^{(2)} \tag{8.9}$$

As shown in **Figure 8.10**, low to moderate solid concentrations up to 10 wt% seem to cause a small reduction in $Fl^{(L)}$ which is not compensated for by the simultaneous increase in $Fl^{(1)}$ and $Fl^{(2)}$ (mainly due to the local rise in c_1 and c_2); thus, the total flow number, Fl, diminishes from 0.86 to 0.77. At higher solid concentrations above 20 wt%, the approximately linear increase in $Fl^{(1)}$ and $Fl^{(2)}$ fails to counterbalance the steep reduction in $Fl^{(L)}$ caused by the presence of solid particles, consequently leading to a substantial fall in Fl. Overall, Fl incurs a reduction of ~ 20 % when X rises from 0 to 40 wt%.

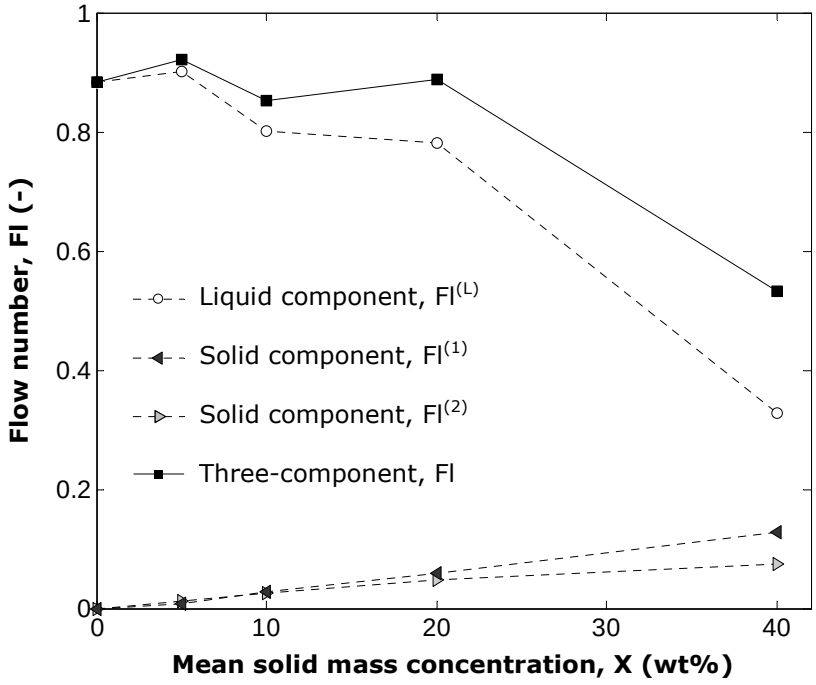

Figure 8.10. Effect of the mean mass concentration of the solid phase on the flow number; PBTD.

Average slip velocity

The qualitative observations noted above in relation to **Figure 8.6** concerning the reduction in slip velocity with an increase in mean solid mass concentration, can be effectively quantified by evaluating an average of the azimuthally-averaged values of normalised slip velocity across the whole radial-axial plane. Using a grid with equal volume cells guarantees that the arithmetic mean of slip velocity coincides with the volume-weighted average. These space-averaged slip velocity values are plotted as a function of X in **Figure 8.11** for both particle size fractions. As expected, for both solid components the normalised average slip velocity, $\bar{s}_j$, decreases with X. Starting at X = 5 wt% with a value of $\bar{s}_2$ 37% higher than $\bar{s}_1$, both $\bar{s}_j$ values rapidly fall off to a similar value (~ 0.034u_{tip}) as X increases to 40 wt%. Hence, it can be concluded that at high solid concentrations the normalised average slip velocity is considerably reduced, but it is not entirely clear whether it loses its dependence on particle size.

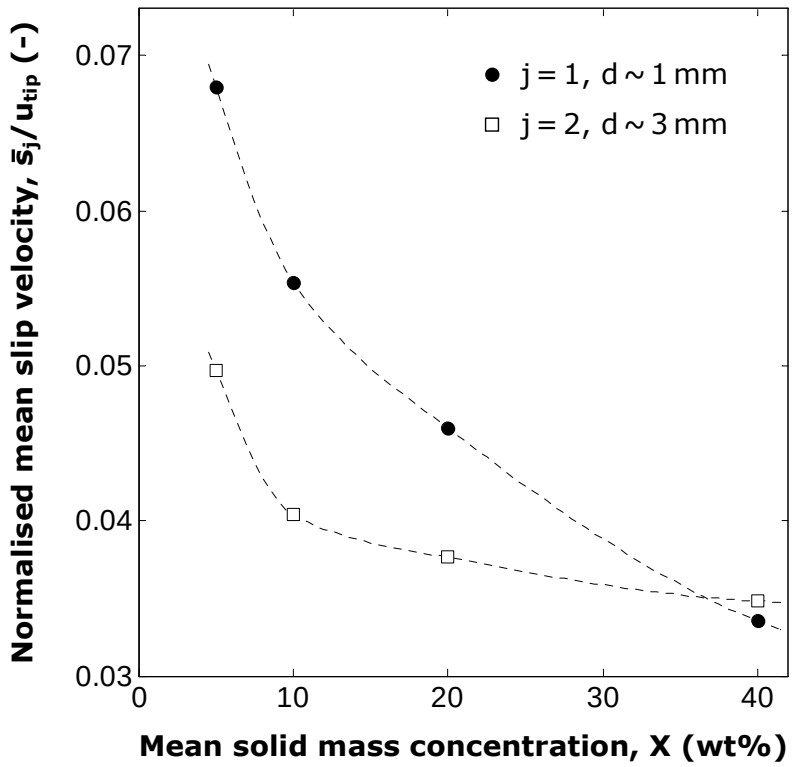

Figure 8.11. Variation of the normalised mean time-averaged slip velocity as a function of the mean solid mass concentration; PBTD.

Uniformity of suspension

The substantial variation of the local solid concentration throughout the vessel, as demonstrated by the maps in **Figure 8.8** and the axial profiles in **Figure 8.9**, warrants the use of a further global index to enable a quantitative description of the spatial uniformity of the solids distribution. Similarly to Chapter VII, for each particle size fraction a uniformity index is defined as:

$$\xi_j = \frac{1}{\sigma_j^2 + 1} = \frac{1}{\frac{1}{n_c}\sum_{i=1}^{n_c}\left(\frac{c_j^{(i)} - C_j}{C_j}\right)^2 + 1} = \frac{C_j^2}{\left\langle c_j^2 \right\rangle} \tag{8.10}$$

where *i* is the cell number within the measurement grid. The index is conveniently defined so that as $\xi_j \to 0$ the uniformity of the *j*-th solid component is at its minimum (condition achieved for a theoretically infinite variance, σ_j^2, of the normalised local concentration); and when $\xi_j = 1$ the solids the *j*-th component are uniformly distributed within the vessel volume, i.e. there are no concentration gradients present and the related local concentration everywhere is equal to the average concentration, C_j, in the vessel (i.e. $\sigma_j^2 = 0$). Values of the index ξ_j at varying average mass concentrations are plotted in **Figure 8.12**, for both particle sizes, showing that ξ_j increases with *X*. This seems to suggest, perhaps counter-intuitively, that as long as the particles are in the 'just suspended' mode more concentrated suspensions

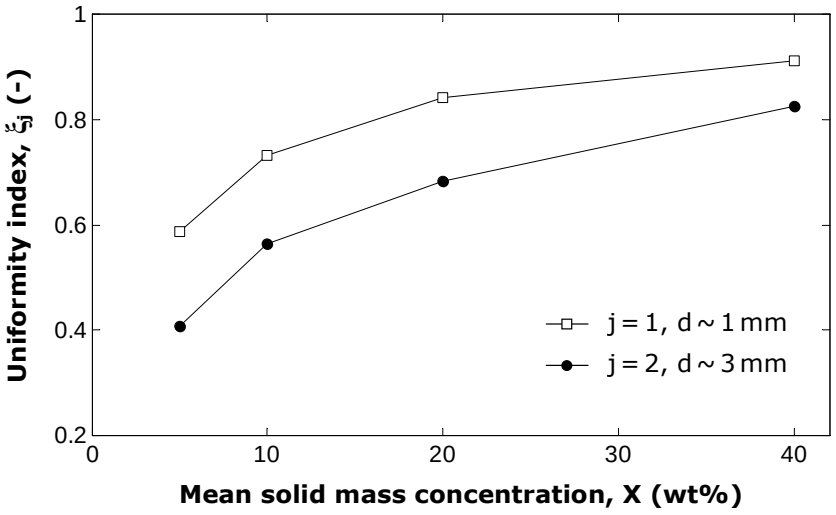

Figure 8.12. Variation of the uniformity index ξ_j as a function of the mean solid mass concentration; PBTD.

will tend towards a homogeneous state by virtue of their increased solids loading. The smaller particles, however, are significantly better dispersed than the larger ones at all the values of X used here.

8-3.5 Verification of mass balance and mass continuity

As already discussed in Chapter VII in the case of monodisperse systems, the pointwise measurements enables the solids mass balance throughout the vessel to be accurately verified, i.e. the measured local values of the two solid volume concentrations balance the experimental parameter $C_j = V_j / V_T$, so that:

$$\frac{1}{n_c}\sum_{i=1}^{n_c} c_j^{(i)} \equiv C_j \tag{8.11}$$

The identity symbol '≡' appears in Eq. (8.11) because the local concentration is obtained from Eq. (8.6) through the measurement of local values of the occupancy O_j whose average value is by definition identically equal to 1.

Another important tool for checking the accuracy and reliability of flow data is mass continuity. The net mass flux through a volume bounded by a closed surface S should be zero, thus

$$\sum_S \mathbf{u}^{(j)} \cdot \Delta\mathbf{S} \cong 0 \tag{8.12}$$

Two types of surfaces S_h and S_r were numerically introduced in the vessel and the continuity test was conducted on all the sets of PEPT data collected in this study. As previously reported in Chapter III, the results which are summarised in **Figure 3.18** showed a very good verification of the mass continuity as the velocity average across the given surface in each case is close to zero, generally less than $0.03u_{tip}$.

8-4 PBTU: results and discussion

In order to expand the results presented in the previous section, the whole set of PEPT experiments was repeated using the same geometrical configuration but with an up-pumping pitched blade turbine. Similarly to the data presented above for the PBTD, results obtained

with the PBTU include three-component flow fields, spatial distributions, slip velocities, flow number and uniformity index values. Finally three-component mass continuity calculations conducted throughout the vessel are also provided.

Both in single and multi-phase conditions, the observed radial-axial flow field with two flow loops is typical of an up-pumping PBT, as shown in **Figures 8.13** and **8.14**. Fluid velocities are relatively high in the impeller region and around the lower flow loop, but low in the upper parts of the tank and in the centre of the main loop. As expected, all the greyscale contours of tangential velocity exhibit their maxima near the upper tip of the impeller blades. Similarly to the PBTD, velocity maps and radial profiles (**Figures 8.13-8.16**) and flow number (**Figure 2.1**) confirm that the increase of mean solid mass concentration produces a damping effect on the local velocities of all the flow components.

Whilst in **Figure 8.6** a single scale (0-0.12 u_{tip}) was adopted, in the case of the PBTU the

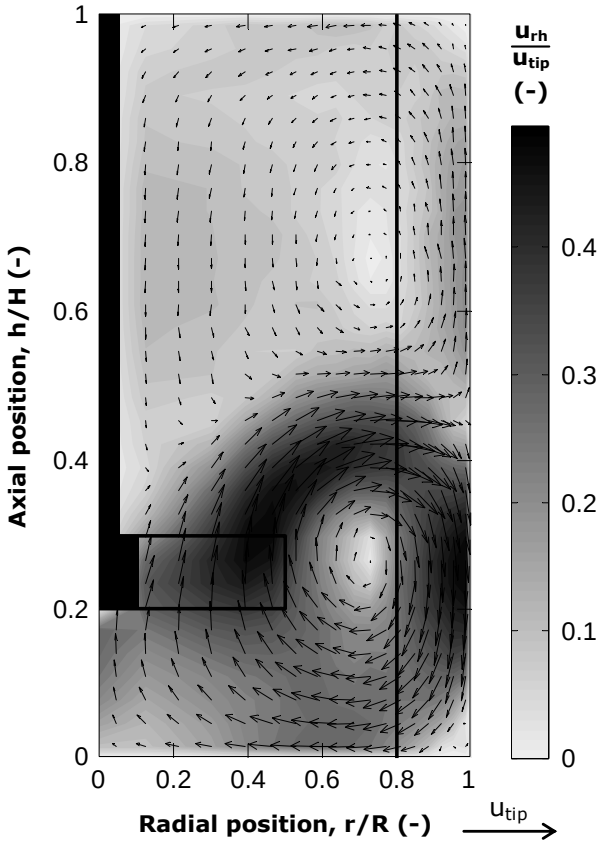

Figure 8.13. Azimuthally-averaged radial-axial velocity map of the liquid phase in the absence of solid particles (X = 0 wt%) at N = 5.0 s^{-1}; PBTU.

larger particles (d ~ 3 mm) presented a consistently higher local time-averaged slip velocity, so that, two different colour scales had to be used, as shown in **Figure 8.17**. Such a difference of the slip velocities between the two particle size fractions is confirmed by **Figure 8.21**, where, at every mean solid concentration, the values of $\bar{s}_2$ are much higher than $\bar{s}_1$. For both particle size fractions, local slip velocity values were generally higher than those generated by the PBTD.

In **Figure 8.18**, a high solid accumulation underneath the impeller is visible for every value of the mean solid concentration. This effect, compared to the case of the PBTD, is more pronounced for the PBTU, and at X = 40 wt%, the local solid volume concentration of the smaller particles (d ~ 1 mm) is surprisingly ~ 50% higher than the concentration of the larger particles (d ~ 3 mm). Overall, however, **Figure 8.19** suggests that smaller particles distribute more uniformly than large particles. This is finally confirmed by the value of the uniformity index reported in **Figure 8.22**.

Finally, mass continuity calculations, conducted as discussed in Section 3-5.2, are shown in **Figure 8.23**. A very good verification of the mass continuity is achieved as the velocity average across the given surface in each case is close to zero, generally less than the $0.03u_{tip}$ for horizontal planes and $0.01u_{tip}$ for cylindrical surfaces.

8-5 Direct 1D comparison PBTD-PBTU

In order to enable a rapid but multifaceted comparison between PBTD and PBTU, the performances of the two agitation modes were compared by using the three global parameters defined above: the three-component flow number, the normalised mean slip velocity and the uniformity index. The three diagrams presented in **Figure 8.24** show the variation of the three indices with the mean solid mass concentration, X, for both pumping modes.

In terms of multi-phase pumping capacity of the impeller, the PBTU performed better than the PBTD up to X = 20 wt%; however, at the maximum mean solid concentration investigated (X = 40 wt%), the three-component flow number for the PBTU is 25 % lower than the one generated by the PBTD.

With regards to the measurements of slip velocity, which strongly influences heat and mass

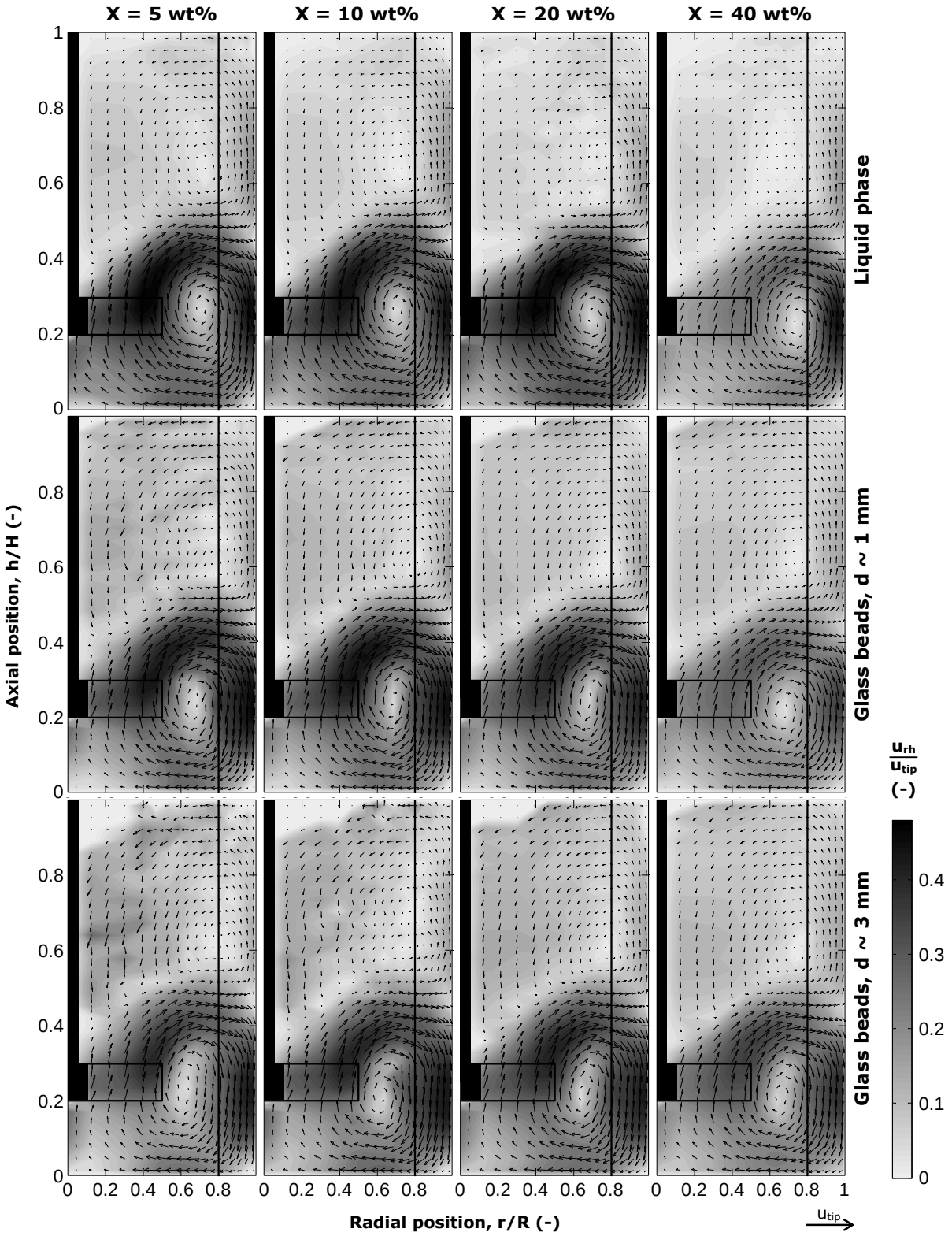

Figure 8.14. Azimuthally-averaged radial-axial velocity maps of the three components of the suspension at varying X; $N = N_{js}$; PBTU.

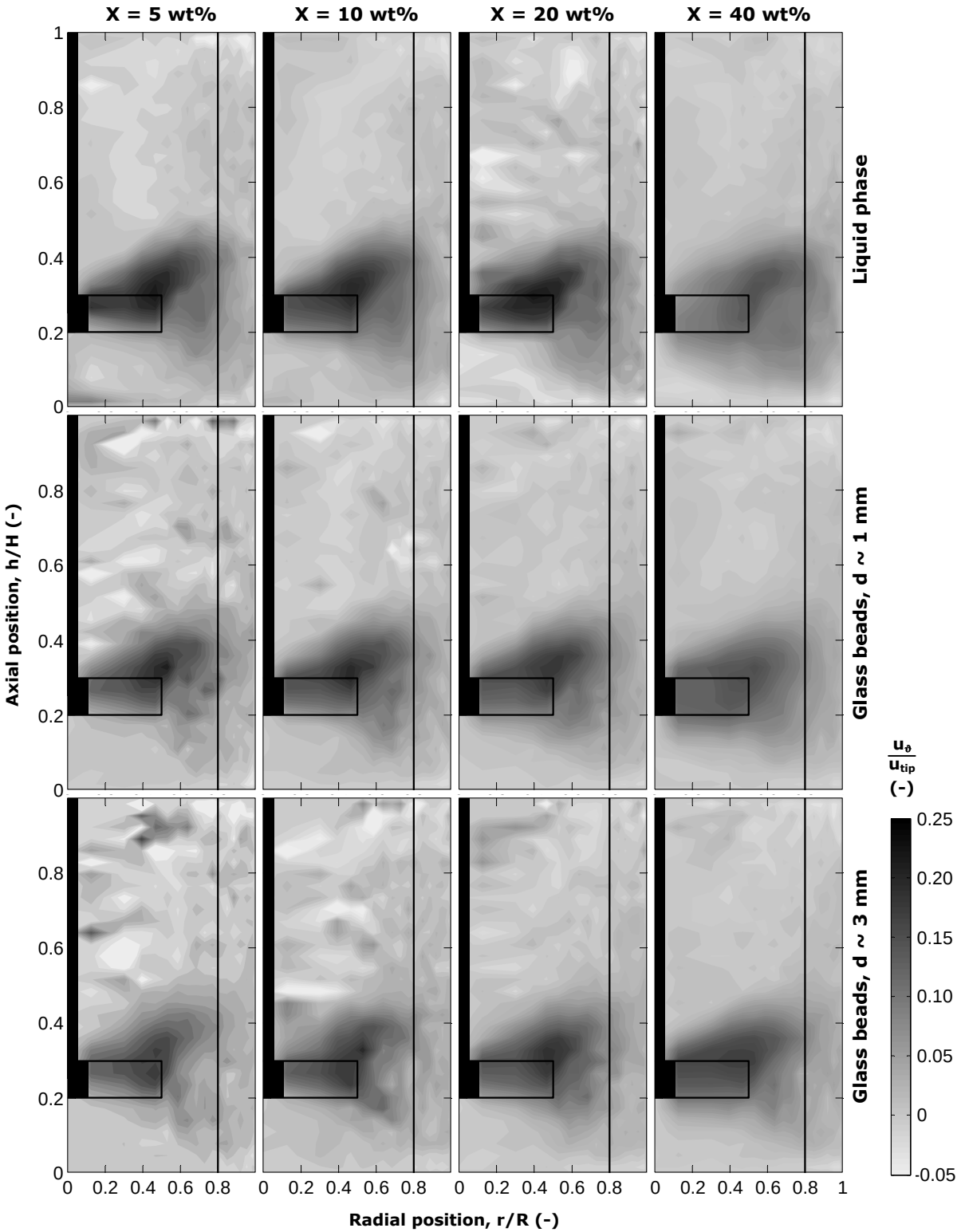

Figure 8.15. Azimuthally-averaged tangential velocity maps of the three components of the suspension at varying X; $N = N_{js}$; PBTU.

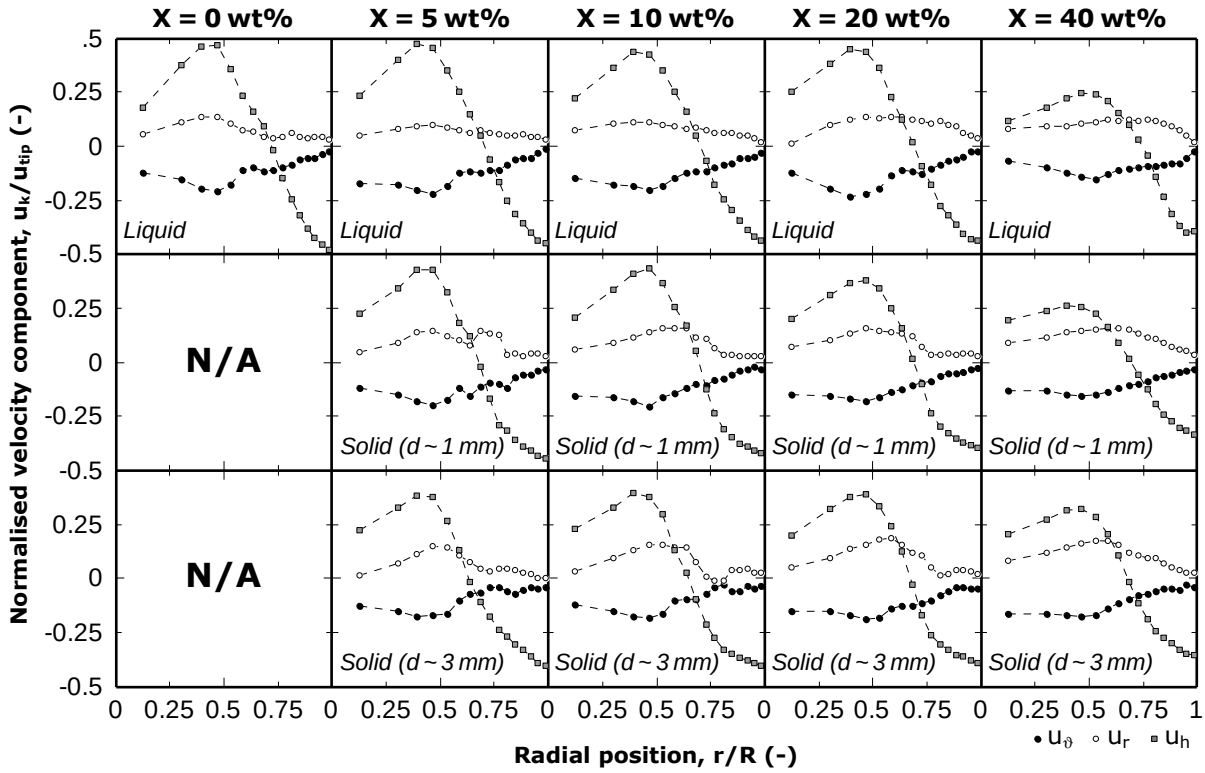

Figure 8.16. Azimuthally-averaged radial profiles of the three velocity components in the horizontal impeller discharge plane at $h = 0.2H$; $N = N_{js}$; PBTU.

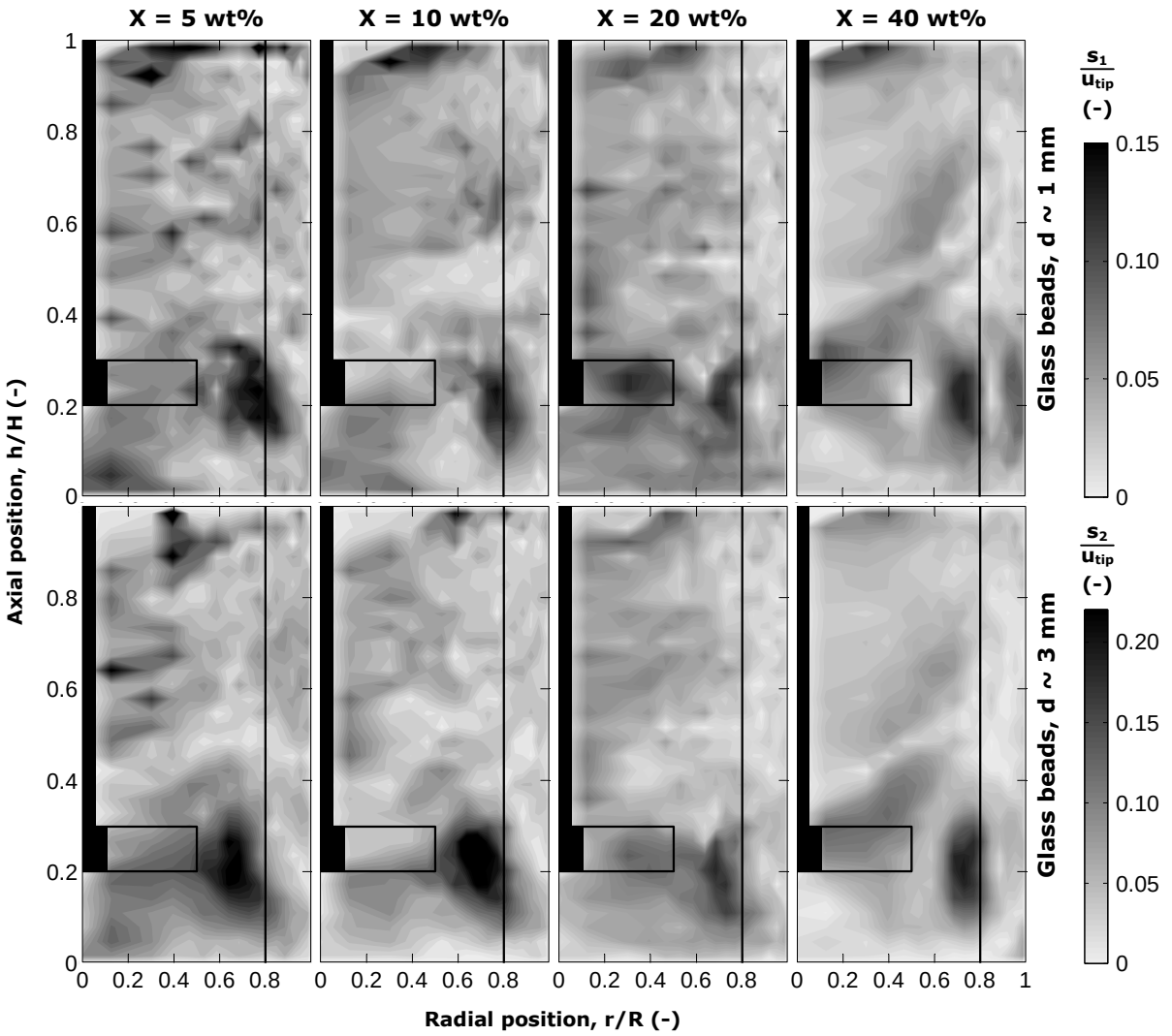

Figure 8.17. Normalised azimuthally-averaged maps of time-averaged slip velocity of the solid components of the suspension at varying X; $N = N_{js}$; PBTU.

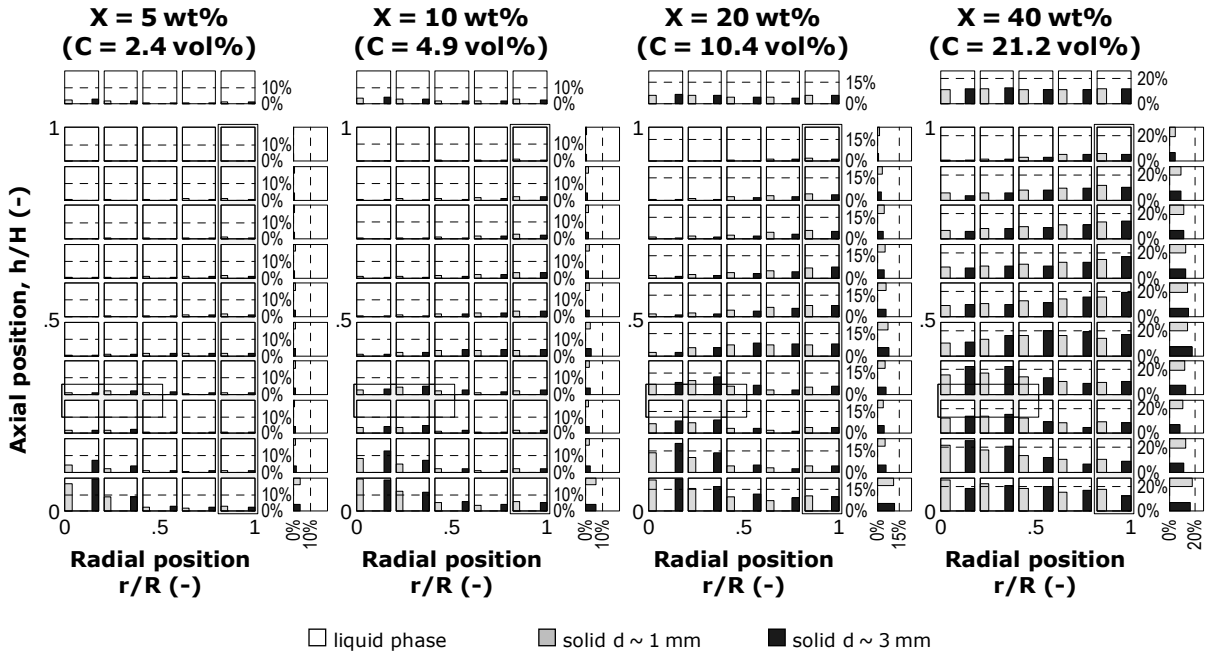

Figure 8.18. Azimuthally-averaged local volume concentrations maps for the three components of the suspension at varying *X*; PBTU. Note that unless otherwise indicated the symbol '%' indicates 'vol%'.

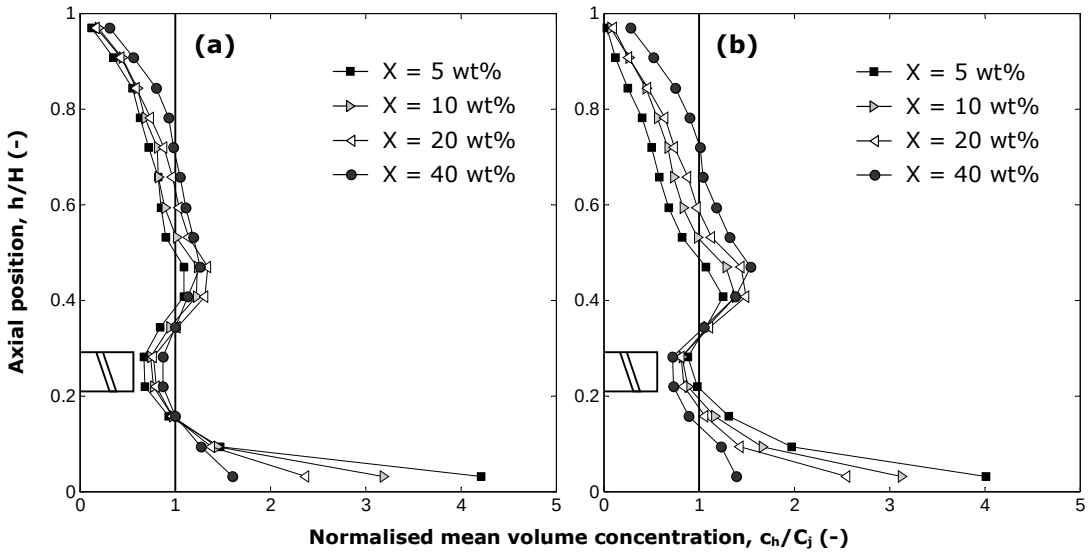

Figure 8.19. Vertical normalised profiles of azimuthally and radially-averaged solid volume concentration at $N = N_{js}$ for PBTU: (a) ~ 1 mm glass beads; (b) ~ 3 mm glass beads.

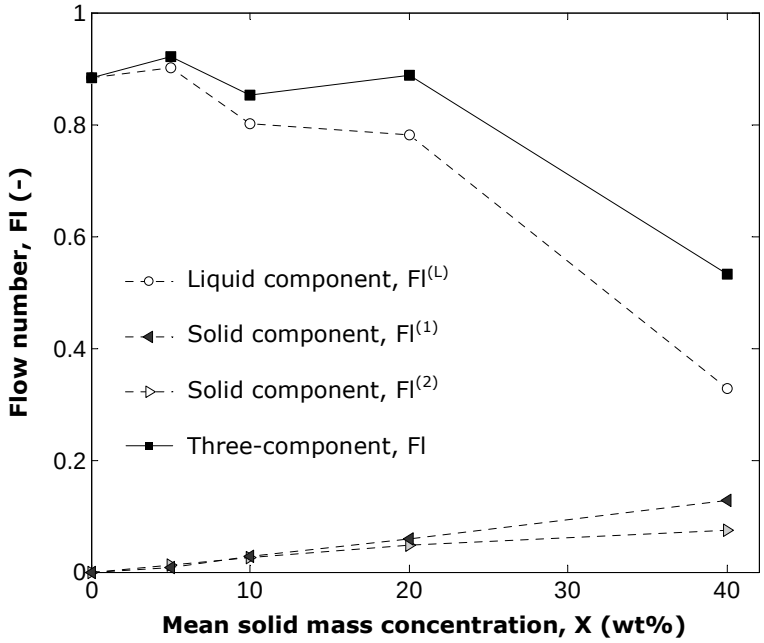

Figure 8.20. Effect of the mean mass concentration of the solid phase on the flow number; PBTU.

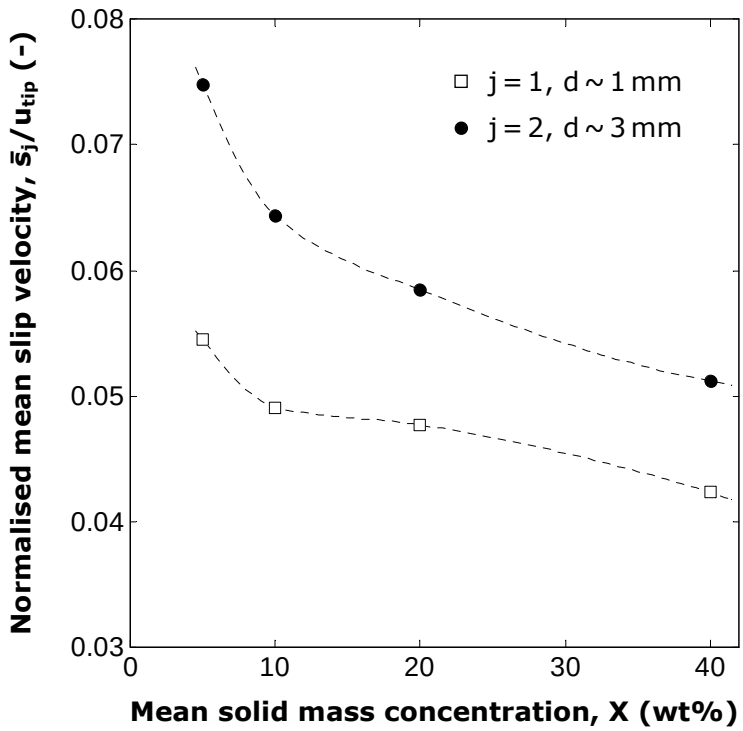

Figure 8.21. Variation of the normalised mean time-averaged slip velocity as a function of the mean solid mass concentration; PBTU.

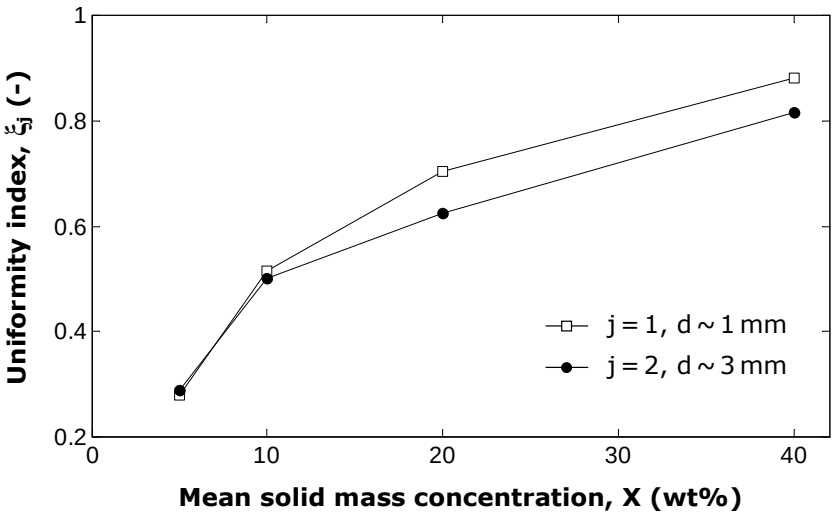

Figure 8.22. Variation of the uniformity index ξ_j as a function of the mean solid mass concentration; PBTU.

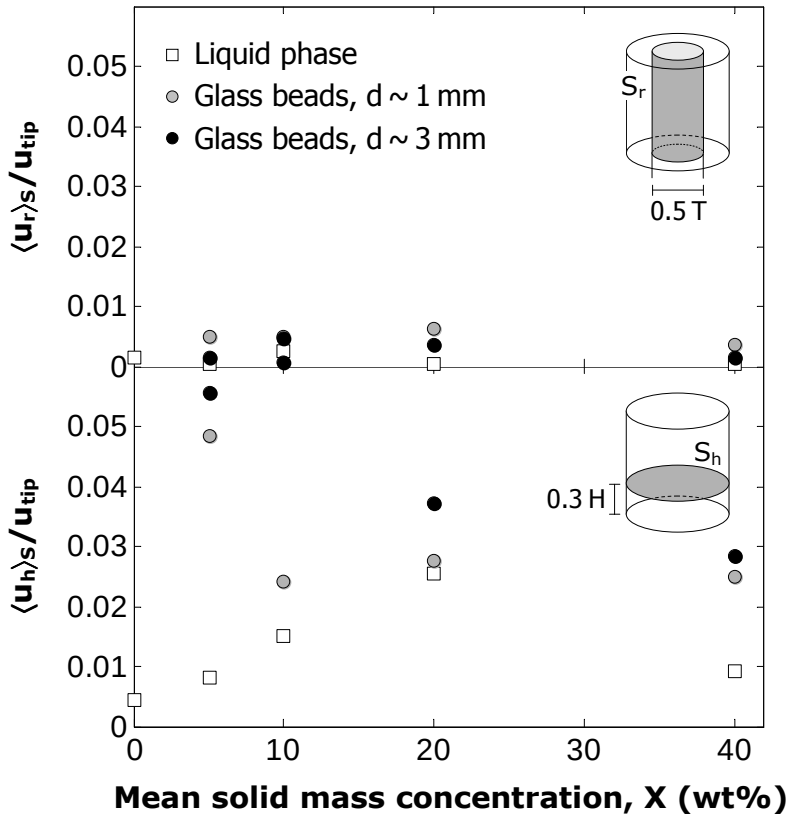

Figure 8.23. Normalised radial and axial velocities averaged on surfaces S_r (of diameter 0.5T) and S_h (0.3H off the base), respectively; PBTU.

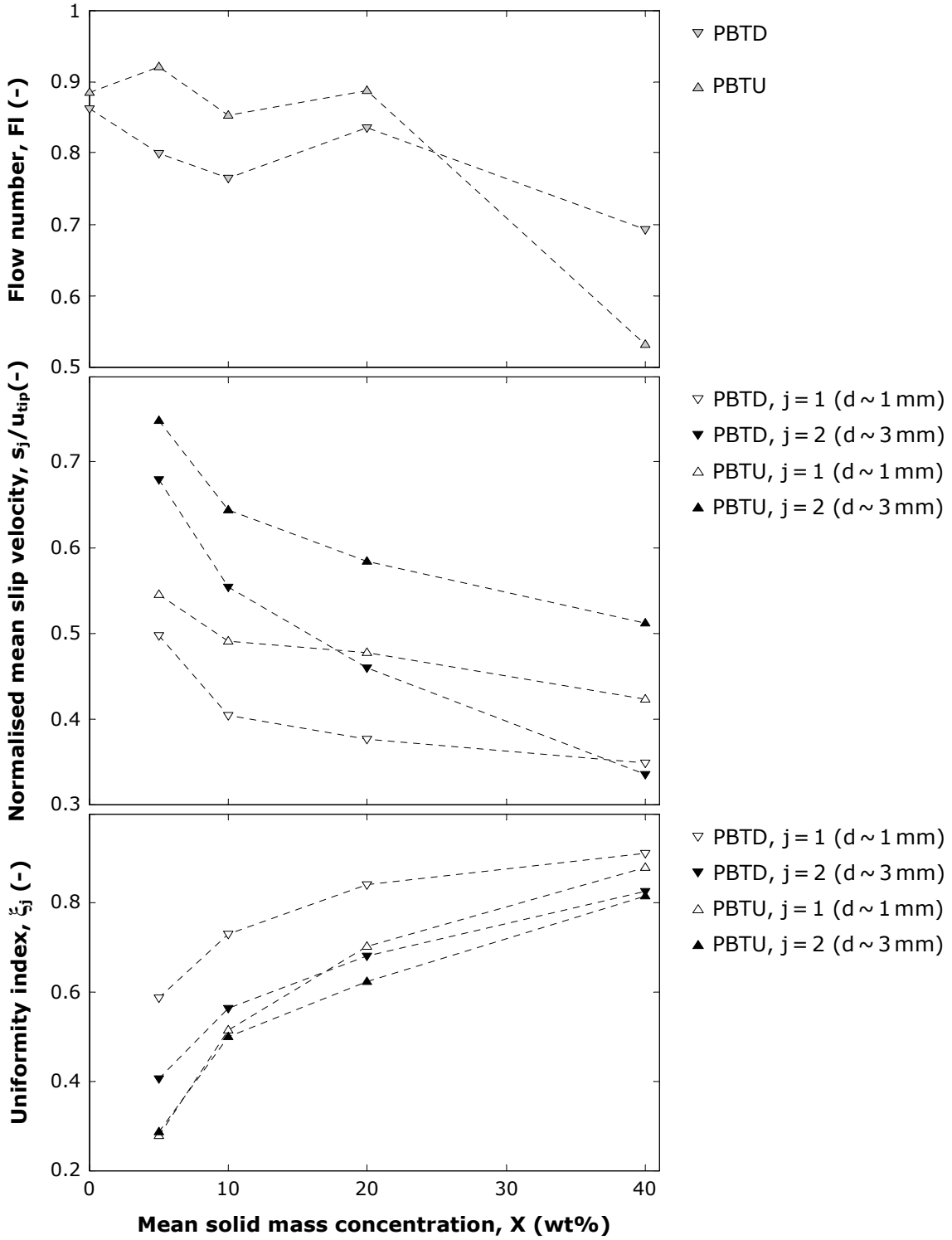

Figure 8.24. Effect of the mean mass concentration of the solid phase on the three-component flow number, the normalised mean time-averaged slip velocity and the uniformity index for both PBTD and PBTU.

transfer between the liquid and the solid components, the PBTU performed much better than the PBTD at every mean solid mass concentration.

For a given solids concentration, a down-pumping PBT achieves a more uniform suspension of both particle size fractions compared to an up-pumping PBT, but the difference between the two modes of impeller operation becomes small at high solids concentrations. The smaller particles are better dispersed than the larger ones when using either a PBTD or a PBTU. Such a difference in behaviour between the two particle sizes is, however, more pronounced with a PBTD.

8-6 Conclusions

The Lagrangian technique of positron emission particle tracking has been successfully applied to the study of dense solid-liquid binary suspensions. The Lagrangian flow data provided by the technique have been converted to give a detailed Eulerian description of each of the three phase components of the flow generated by a pitched blade turbine. For the first time, it has been possible to determine the full 3D velocity field and spatial distribution of the liquid phase and of each particle size fraction within a binary suspension.

In addition, a substantial amount of unique experimental data on local hydrodynamics and homogeneity of suspension have been obtained in solid-liquid flows of such high concentrations reaching 40 wt%. Such detailed results could be used to inform the design of experiments to study mixing phenomena or equipment design to maximise the global or local mixing efficiency of the system. The accuracy of the PEPT measurements has been ascertained through multi-component mass continuity verifications throughout the vessel.

Values of the multi-component flow number indicate that the pumping effectiveness of the PBT agitator is preserved for low to moderate concentrations. At high solid concentrations, however, the multi-component flow number and normalised mean slip velocity for both particle sizes are considerably reduced; such a reduction is accentuated for an up-pumping PBT.

Results on spatial phase distribution have shown how local solids build up diminishes for smaller particles and/or higher solids concentrations, with the maximum uniformity index

being obtained for the smaller particles at 40 wt% solids. Overall, a PBTD achieves a better homogeneity than a PBTU at low and moderate solids concentrations, but the difference in suspension uniformity between the different particle size classes is higher.

The technique can, therefore, be extended to the study of more challenging systems with wider particle size distributions, more complex rheologies and probably even higher concentrations.

Notation

Roman letters

C	Total mean volume concentration of solids	-
c_h	Mean volume concentration at level h	-
c_j	Local volume concentration of component j	-
C_j	Mean volume concentration of component j	-
D	Impeller diameter	m
d d_1 d_2	Particle diameter	m
Fl	Multi-phase flow number	-
$Fl^{(j)}$	Flow number of component j	-
H	Height of the suspension	m
i	Cell number	-
j	Mixture component index	-
k	Cylindrical direction index (ϑ, r or h)	-
N	Impeller rotational speed	s^{-1}
n_c	Number of grid cells	-
n_j	Number of particles of j within the vessel	-
N_{js}	Minimum speed for particle suspension	s^{-1}
O_j	Occupancy	-
$\mathbf{P}$	Tracer location vector	|m|
Q	Total multi-phase impeller pumping rate	$m^3\ s^{-1}$
$Q^{(j)}$	Impeller pumping rate of component j	$m^3\ s^{-1}$
r h	Radial-axial cylindrical coordinates	m
R	Vessel radius	m
Re_{imp}	Impeller Reynolds number ($N_{js}D^2/\nu$)	-
S	Surface area	m^2
S_h	Horizontal planar surface areas	m^2
S_r	Vertical cylindrical surface areas	m^2
s_j	Local slip velocity of component j	$m\ s^{-1}$
$\bar{s}_j$	Mean slip velocity of component j	$m\ s^{-1}$
t	Time	s
T	Vessel diameter	m

t_∞	PEPT runtime	s
t_E	Ergodic time	s
u	3D velocity vector	$\lvert m\ s^{-1} \rvert$
$u_\vartheta\ u_r\ u_h$	Cylindrical velocity components	$m\ s^{-1}$
u_{rh}	2D radial-axial velocity magnitude	$m\ s^{-1}$
u_{tip}	Impeller tip speed	$m\ s^{-1}$
V	Volume	m^3
V_j	Volume of component j in the vessel	m^3
V_{Pj}	Particle volume of component *j*	m^3
V_T	Total suspension volume	m^3
$x\ y\ z$	Cartesian coordinates	m
X	Total mean mass concentration of solids	-
$X_1\ X_2$	Mean mass concentration of solid component	-

Greek letters

ϑ	Azimuthal coordinate	rad
ν	Kinematic liquid viscosity	$m^2\ s^{-1}$
ξ_j	Uniformity index of component *j*	-
σ_j	Standard deviation of normalised c_j	-

Abbreviations

LDV	Laser Doppler velocimetry
PBT	Pitched blade turbine
PBTD	Down-pumping PBT
PBTU	Up-pumping PBT
PEPT	Positron emission particle tracking
PIV	Particle image velocimetry

Chapter IX
Mixing of Polydisperse Solid-Liquid Suspensions

Abstract

The work presented in the previous two chapters has been extended to complex polydisperse systems where solid particles of five different size fractions have been selectively radio-labelled and tracked. Here, the multi-component flow field and spatial phase distribution of polydisperse suspensions of glass beads generated by a pitched blade turbine operating in up-pumping or down-pumping mode have been resolved using the Lagrangian technique of positron emission particle tracking. PEPT multi-component investigations consisted of six successive and distinct experiments to track the liquid phase and the five flow components of the solid phase. Experiments were performed with a total solid concentration varying in the range 0 to 40 wt%. Extensive data were obtained on the local hydrodynamics and phase distribution of each particle size fraction; consequently, in order to enable efficient examination and comparison of data, results are presented in a concise format using composite images judiciously produced by grouping together multiple graphs, greyscale contours, or vector plots. Results include for each liquid and solid component of the mixture, flow fields, spatial distributions, slip velocities, flow number and spatial uniformity index values. Finally, in a similar way to the experimental studies presented in Chapter VI and Chapter VIII, the reliability of the three-dimensional measurements and the related data analysis is assessed via six-component mass continuity calculations.

9-1 Introduction

In industrial operations, the solid phase is often completely suspended but a uniform distribution of solid particles within the suspension is difficult to attain (Micale *et al.*, 2000). This condition is particularly desirable when a continuous and representative flow of solids from the system is required or a uniform concentration of solids must be achieved (e.g. crystallizers, polymerization reactors, heterogeneous photocatalytic reactors, etc.). In crystallization, non-uniform solids concentration may lead to unacceptably high local supersaturation levels and subsequent non-uniformity in crystal growth (Atiemo-Obeng *et al.*, 2004). Therefore, knowledge of the solid concentration and distribution in polydisperse systems, where multiple particle size fraction are suspended in a liquid phase, would be needed for design purposes, process development and scale-up.

As mentioned in Section 2.4.2, uniform suspension is not only characterised by an approximately uniform solid concentration throughout the vessel but also by a uniform particle size distribution. However, the results presented in Chapter VIII for binary suspensions, showed that particles of different size within the same solid suspension exhibit significantly different hydrodynamic and phase distribution behaviours. In a polydisperse system this should lead to similar non-uniformities in the solid concentration field as well as to a significantly different particle size distribution from point to point.

Detailed experimental investigation of these phenomena has remained a major challenge due to a lack of adequate non-optical measurement techniques capable of probing such opaque multiphase systems (Barigou, 2004).

This chapter reports on the use of the PEPT technique to study the mixing of concentrated polydisperse solid-liquid mixtures where glass beads of five different size classes are simultaneously suspended in water. Extensive data for these polydisperse suspensions containing up to 40 wt% solids are presented here. Detailed information is obtained on particle and fluid trajectories which is converted to give a pointwise Eulerian description of the six-component flow field as well as the spatial distribution of each of the liquid and five solid components of the mixture. Global parameters such as flow number, average slip velocity and uniformity index are then compared to assess the different behaviour of each flow component.

9-2 Experimental

9-2.1 Multi-component positron emission particle tracking

In the case of a multi-component system, the full three-dimensional trajectory of each component must be resolved separately using different particle tracers. Currently, PEPT can most accurately track one particle at a time. Therefore, PEPT multi-component investigations consist of multiple successive and separate experiments, i.e. one for a single-phase system, two for a monodisperse suspension, three for a binary suspension and $n_s + 1$ for a polydisperse suspension consisting of a liquid phase and n_s different size fractions. In this work where $n_s = 5$, so that six consecutive PEPT measurements must be performed at each mean solid concentration and agitation mode.

9-2.2 Experimental apparatus and procedure

PEPT experiments were conducted in a flat-base cylindrical vessel of diameter $T = 288$ mm made of Perspex, as shown in **Figure 7.1**. The vessel was fitted with four wall baffles of width $0.1T$ and was agitated by a 6-blade 45º pitched-turbine (PBT) of diameter $D = 0.5T$ and height $0.1T$ as depicted in **Figure 7.2**. The off-bottom clearance of the turbine was set to $0.25T$ to enhance solid suspension, and the height of the suspension in the vessel was set at $H = T$. The suspending liquid used was water whose density was adjusted to 1150 kg m^{-3} by adding NaCl to make the PEPT particle tracer used to track the liquid phase neutrally buoyant. Five nearly-monomodal particle size fractions nearly-spherical glass beads whose characteristics are shown in **Table 9.1** having a density of 2485 kg m^{-3} were used to make a

Table 9.1. Glass particles characteristics.

Diameter			Density (kg m^{-3})
denomination	range (mm)	average (mm)	
d_1	1.0-1.25	1.1	2485
d_2	1.5-1.85	1.7	2485
d_3	2-2.3	2.2	2485
d_4	2.55-2.85	2.7	2485
d_5	2.85-3.3	3.1	2485

two-phase six-component suspension with a mean solid mass concentration, X, varying in the range 0 to 40 wt% (or, equivalently, with the mean solid volume concentration, C, varying in the range 0-23.6 vol%). The five size fractions were mixed in equal proportions, i.e.,

$$X_1 = X_2 = X_3 = X_4 = X_5 = 0.2X \tag{9.1}$$

Experiments were conducted at the minimum rotational speed for particle suspension, N_{js}.

Mixing of the suspension was investigated with the impeller operating in the down-pumping mode (PBTD) and in the up-pumping mode (PBTU). The experimental conditions are summarised in **Table 9.2**. At a given solid fraction, the measured N_{js} values for the PBTD and PBTU in this case are the same within experimental error. It should be noted, however, that while the concept of N_{js} is simple, its accurate measurement is not especially under conditions of high solids concentration. Determination of N_{js} tends to be somewhat subjective and even more so under such turbid conditions, so that accurate measurement of N_{js} using the Zwietering criterion can be difficult.

For a given solid-liquid suspension, PEPT experiments consisted of independently resolving the full three-dimensional trajectories of the fluid phase and of the solid phase in six successive and distinct experiments. A representative glass particle taken alternatively from each of the five solid components radioactively labelled with ^{18}F, by direct irradiation, was used to track each solid component, whilst a neutrally-buoyant resin tracer of 600 μm diameter also labelled with ^{18}F was used to track the liquid phase.

Fore each experiment, the PEPT tracking time, t_∞, in this study was set at 40 min for each

Table 9.2. Experimental conditions for the study of polydisperse solid-liquid suspensions.

X (wt%)	C (vol%)	N *or* N_{js} (s^{-1})		Re_{imp} (-)	
		PBTD	PBTU	PBTD	PBTU
0	0	5.50	5.50	1.31×10^5	1.31×10^5
5.2	2.5	6.33	6.00	1.51×10^5	1.43×10^5
10.6	5.2	7.50	7.00	1.79×10^5	1.67×10^5
20.0	10.4	8.50	8.00	2.03×10^5	1.91×10^5
40.0	23.6	10.17	10.00	2.43×10^5	2.38×10^5

phase, which was long enough to acquire a sufficient amount of data in all regions of the vessel, so that ergodicity could be safely assumed given that in such a system the probability of visit is sufficiently uniform by virtue of the highly turbulent state of the suspension ($\mathrm{Re}_{imp} = N_{js}D^2/\nu > 10^5$), and the open geometry of the vessel where all regions are more or less equally accessible by the tracer. Ergodicity is discussed in more details in Section 3-5.1.

9-3 Results and Discussion

Eulerian data were obtained through Lagrangian tracking of each of the six solid and liquid components of the polydisperse suspensions described above. Results are presented as azimuthally-averaged Eulerian maps which represent the whole flow field including the effect of the baffles. This is an effective way of presenting 3D data in a reduced form. Furthermore, in order to enable efficient examination and comparison of data, results are presented in a concise format using sets of images judiciously produced by grouping together multiple graphs, greyscale contours, or vector plots. Results include for each component of the mixture, flow fields, spatial distributions, slip velocities, flow number and uniformity index values.

Similarly to Chapters VII and VIII, raw data were analysed by defining a cylindrical grid consisting of $n_c = 512$ equal volume cells. The obtained radial-axial velocity vector maps, greyscale contours of tangential velocity, time-averaged slip velocities and volume concentrations and vertical profile of volume concentration are presented in **Figures 9.1-9.9**, for each flow component j and mean solid concentration, X. The index j varies from 1 to 6; however, for clarity purposes $j = 6$, which indicates the only liquid component present in each of the polydisperse systems investigated here is sometimes replaced by L.

All maps reported here present a clear qualitative resemblance with the Eulerian maps presented in Chapters VII and VIII. In quantitative terms, local variations of velocity, slip velocity or concentration can be observed in detail. However, due to the complexity of the system and the large amount of variables involved, it is difficult to identify the exact reasons for the existence of such local variations. Nevertheless, a global assessment approach can be performed using concepts such as the multi-phase flow number, mean time-averaged slip velocity and uniformity index.

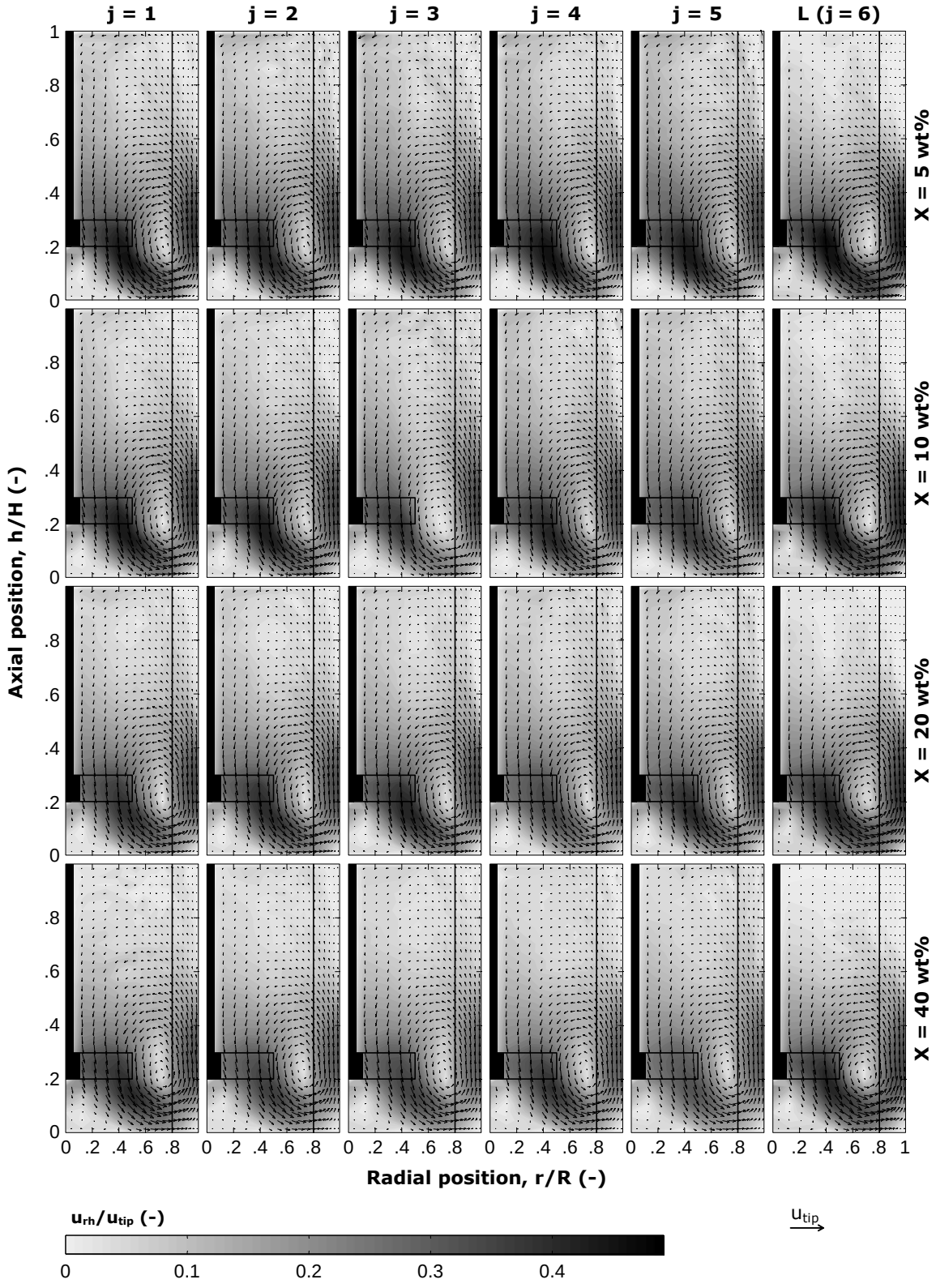

Figure 9.1. Azimuthally-averaged radial-axial velocity maps of the six components of the polydisperse suspension at varying X; $N = N_{js}$; PBTD.

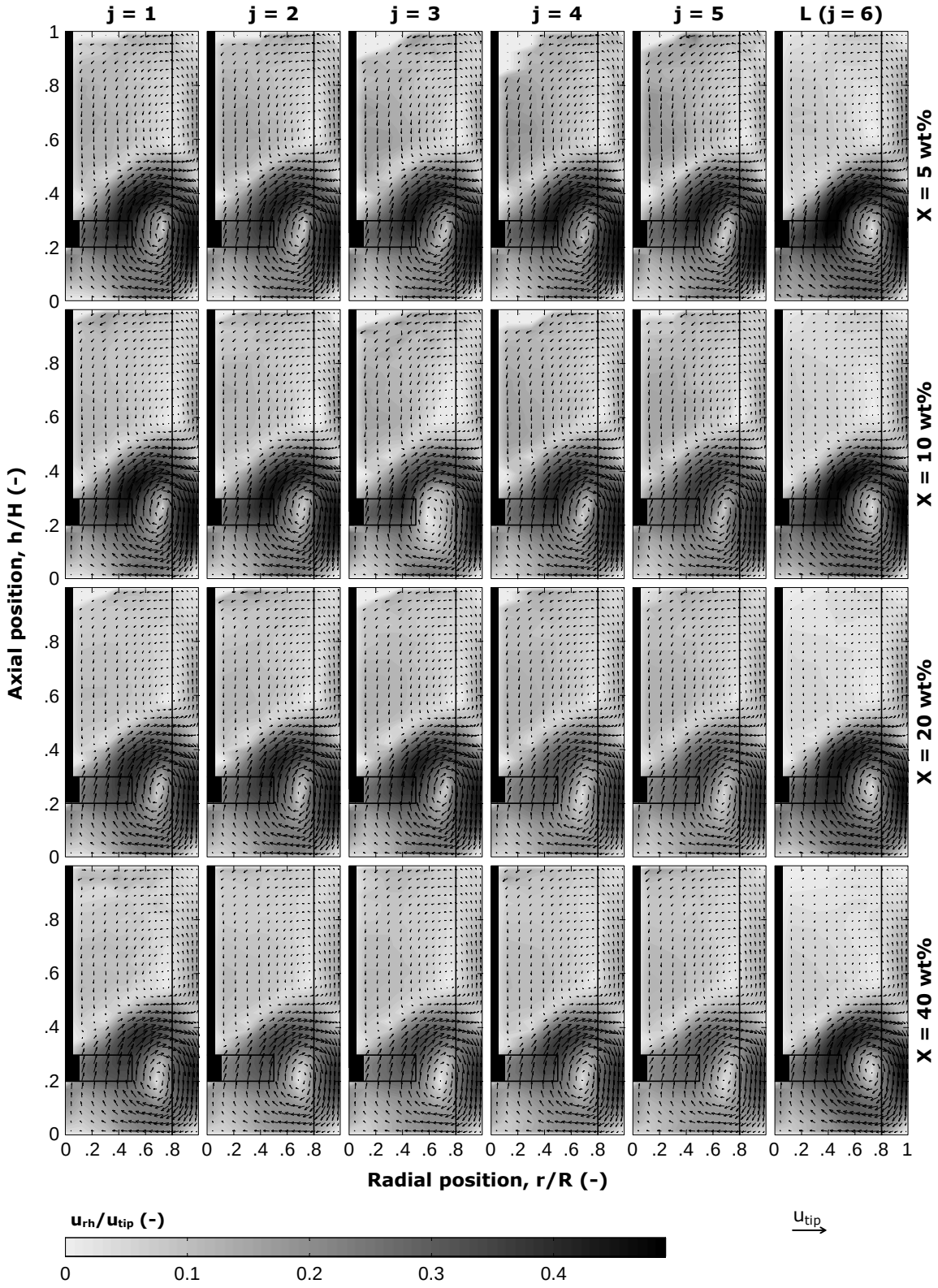

Figure 9.2. Azimuthally-averaged radial-axial velocity maps of the six components of the polydisperse suspension at varying X; $N = N_{js}$; PBTU.

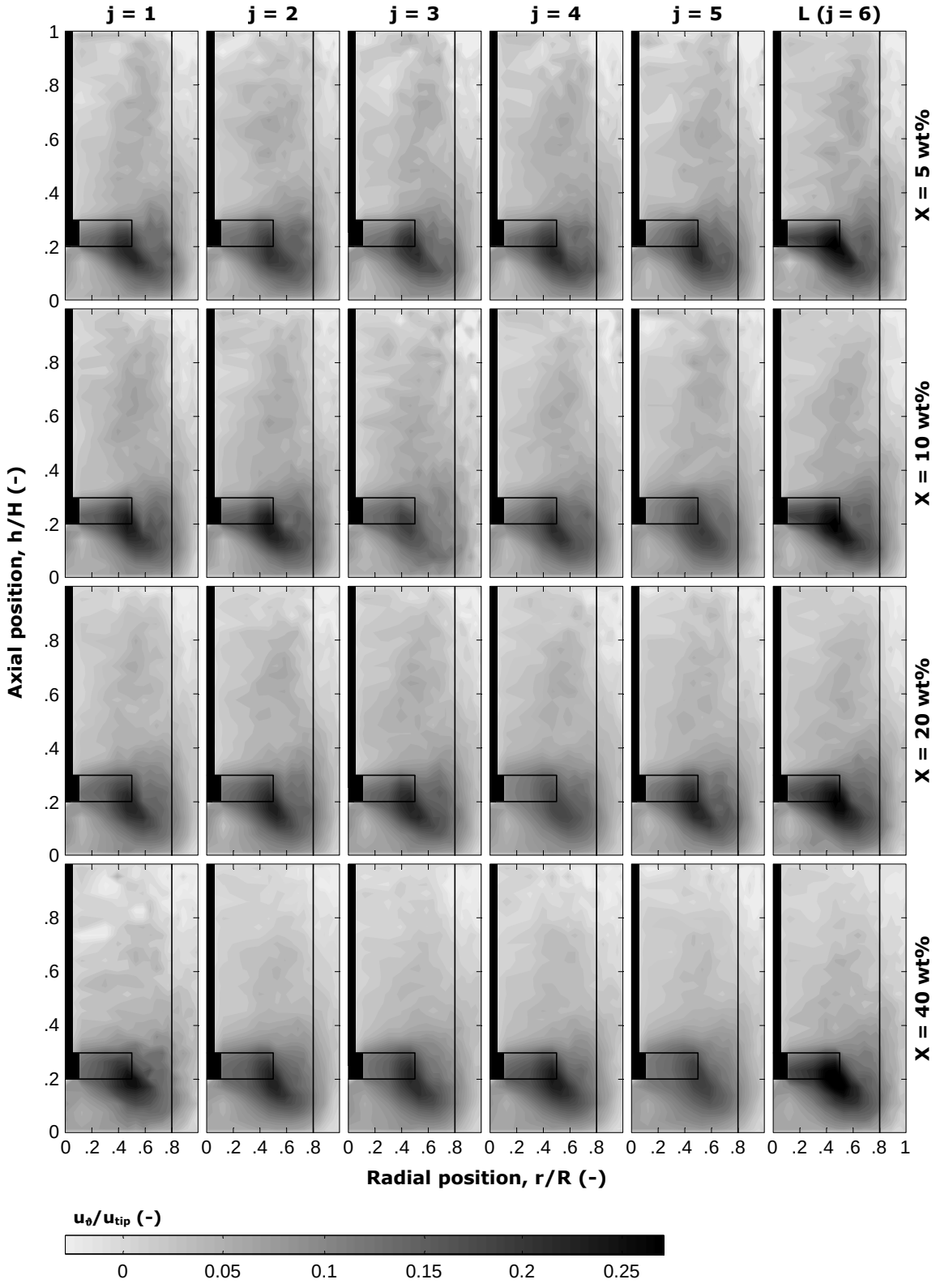

Figure 9.3. Azimuthally-averaged tangential velocity maps of the six components of the polydisperse suspension at varying X; $N = N_{js}$; PBTD.

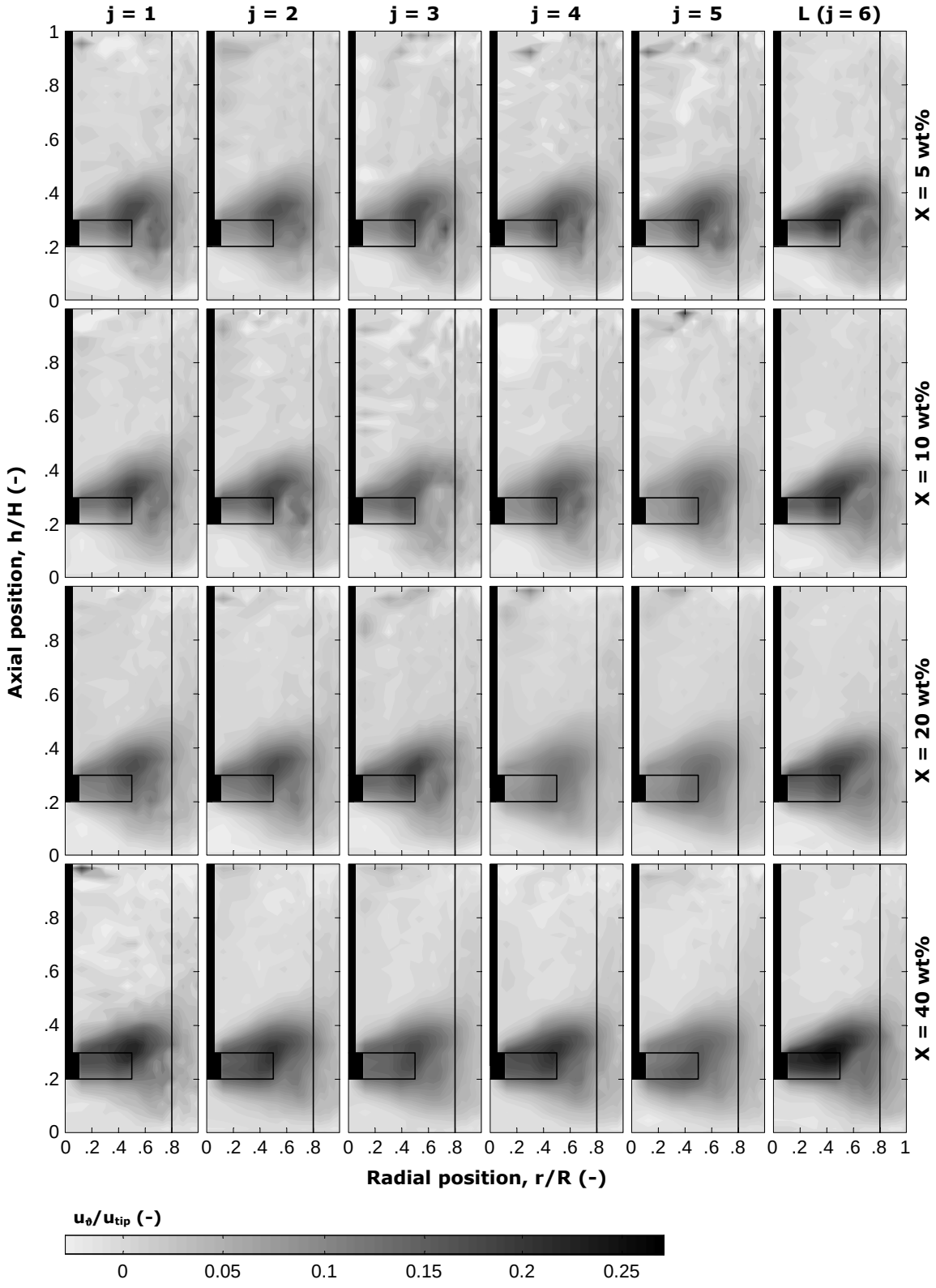

Figure 9.4. Azimuthally-averaged tangential velocity maps of the six components of the polydisperse suspension at varying X; $N = N_{js}$; PBTU.

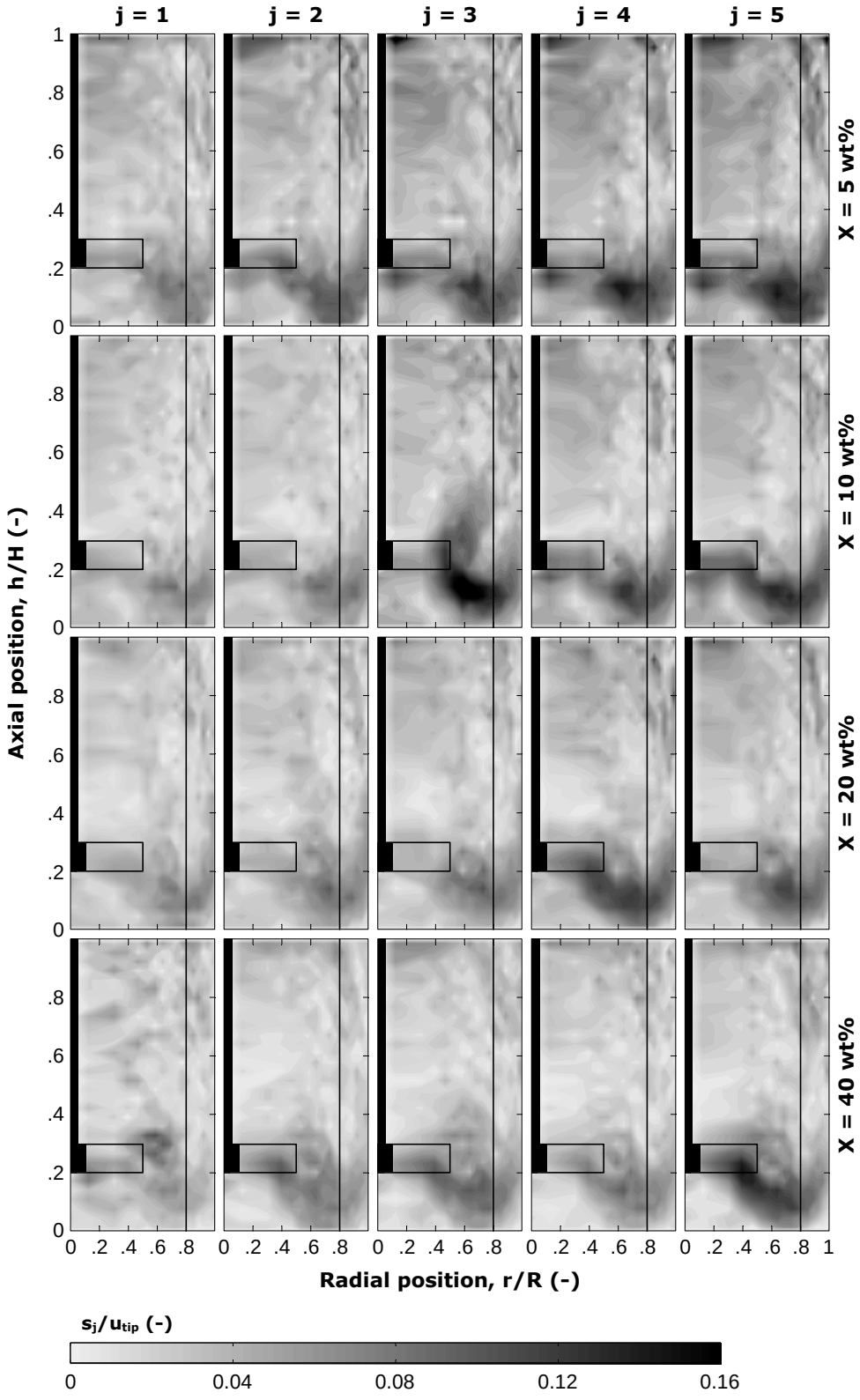

Figure 9.5. Normalised azimuthally-averaged maps of time-averaged slip velocity of the five solid components of the polydisperse suspension at varying X; $N = N_{js}$; PBTD.

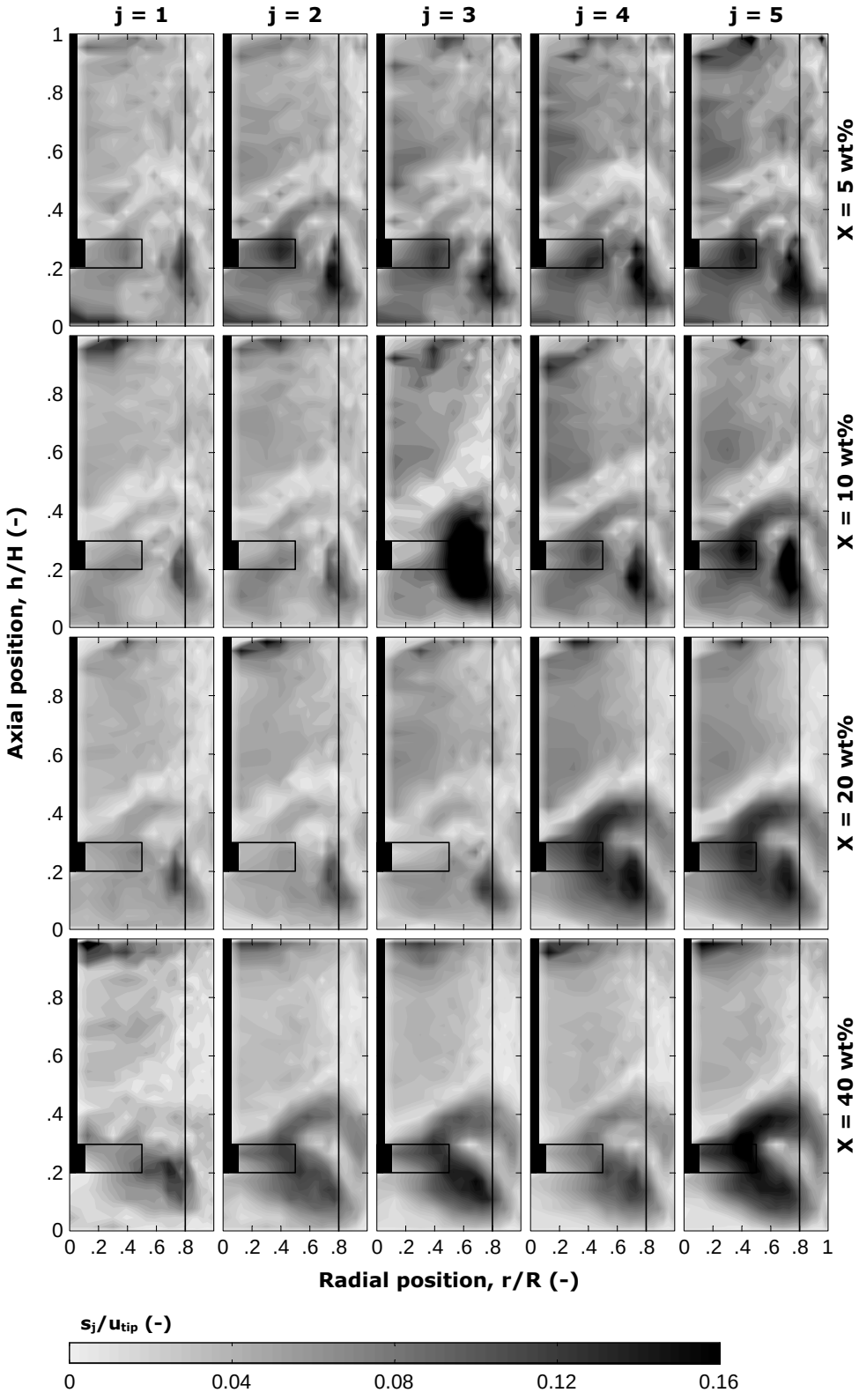

Figure 9.6. Normalised azimuthally-averaged maps of time-averaged slip velocity of the five solid components of the polydisperse suspension at varying X; $N = N_{js}$; PBTU.

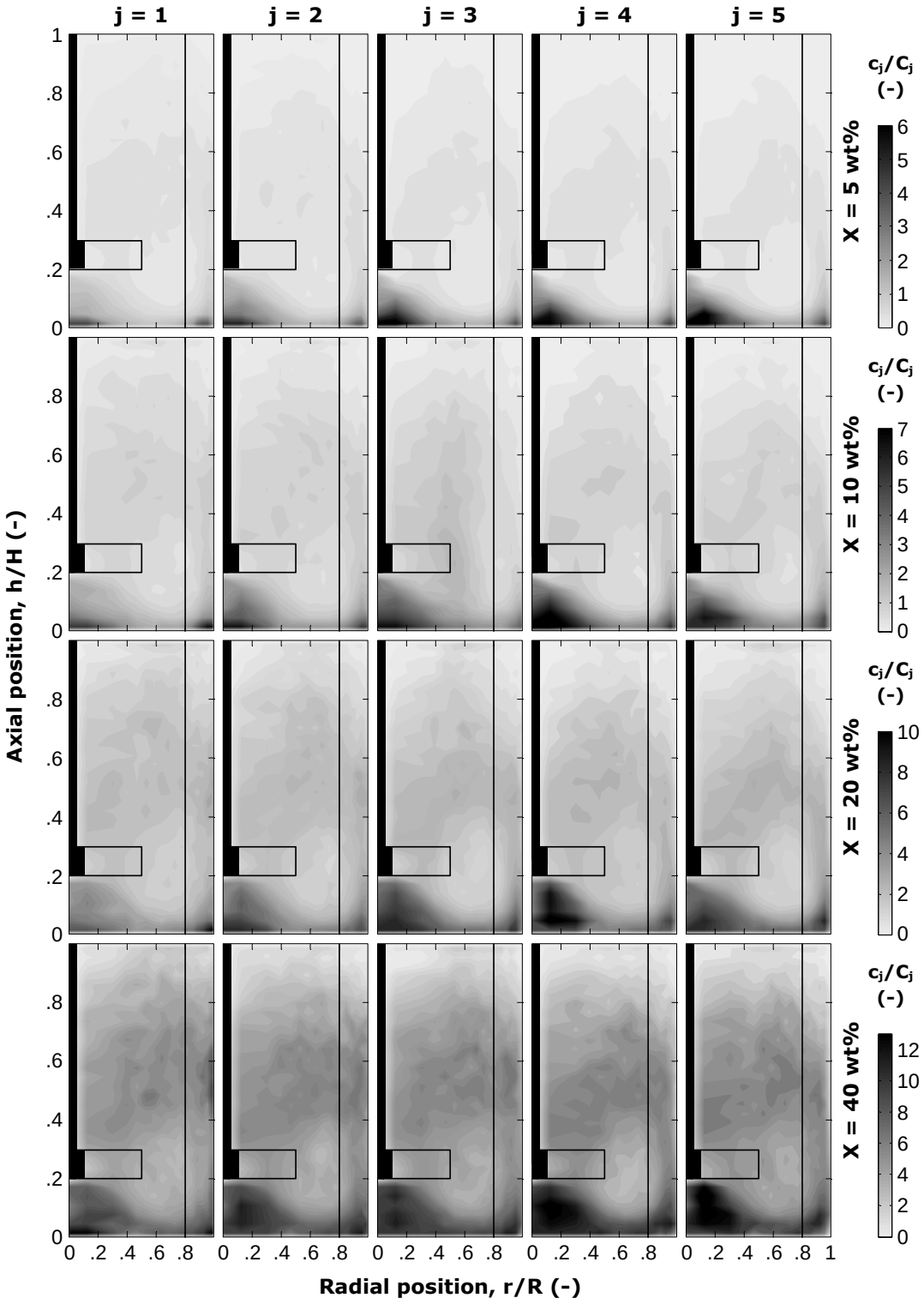

Figure 9.7. Azimuthally-averaged local volume concentrations maps for the five solid components of the polydisperse suspension at varying *X*; PBTD.

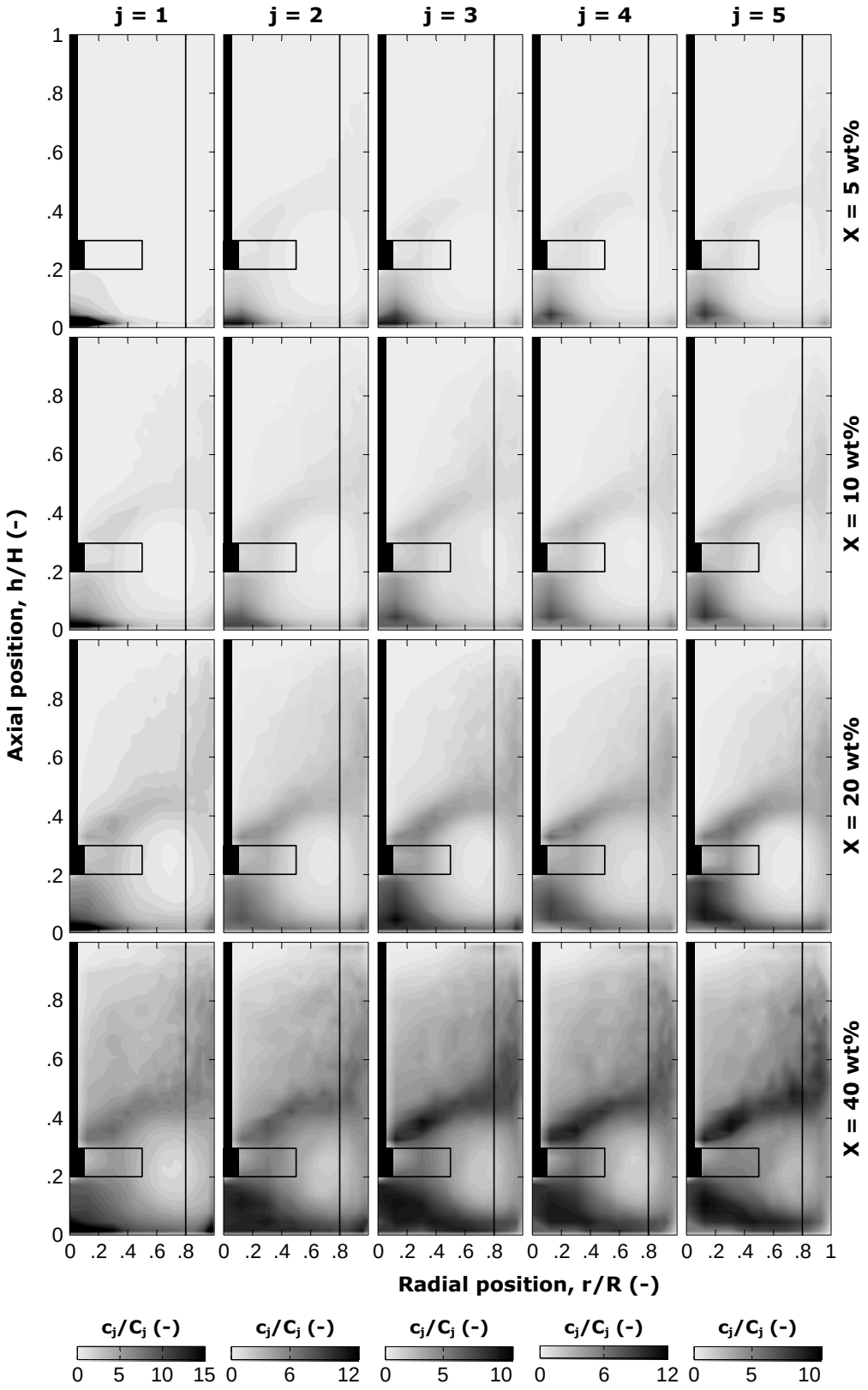

Figure 9.8. Azimuthally-averaged local volume concentrations maps for the five solid components of the polydisperse suspension at varying *X*; PBTU.

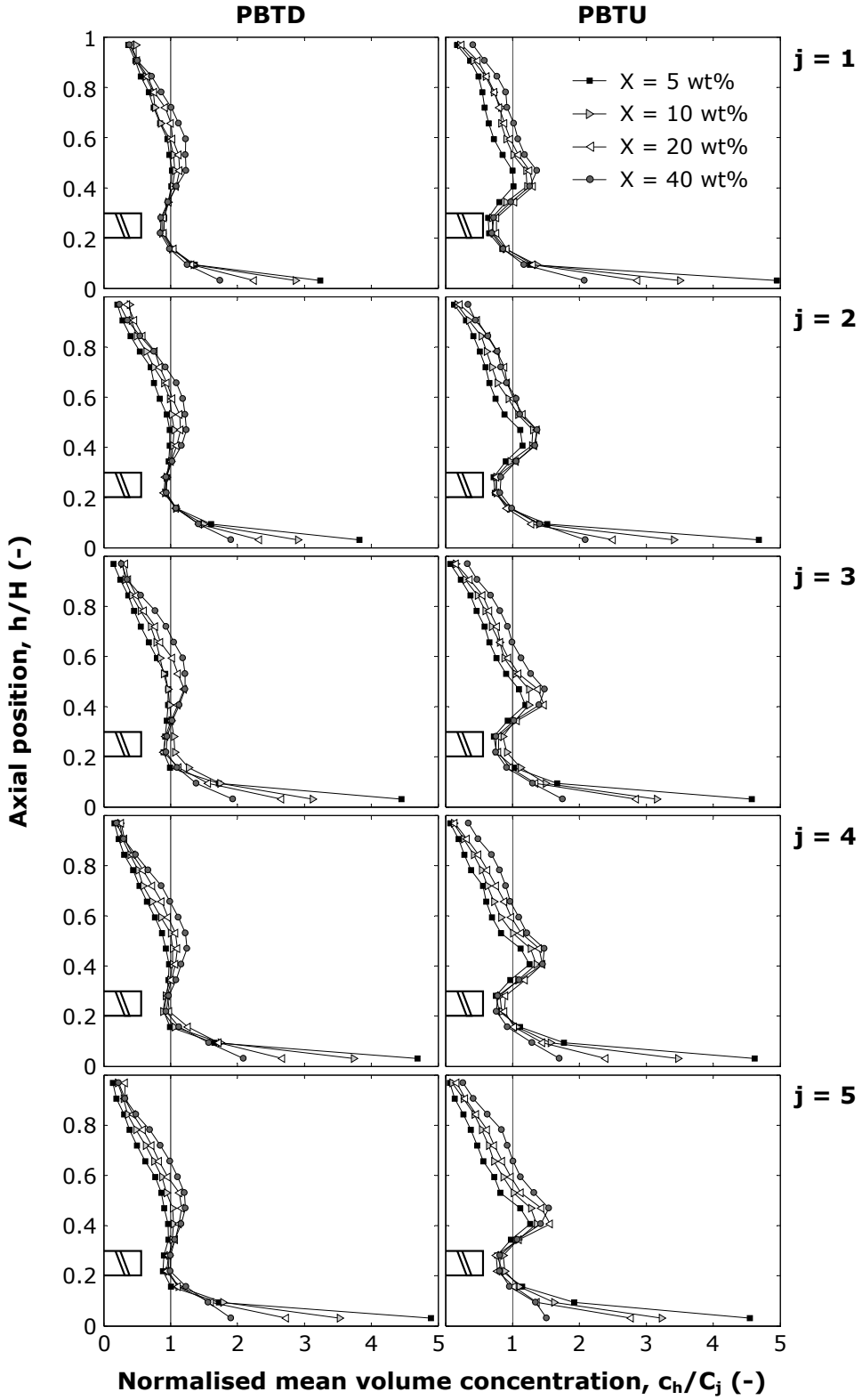

Figure 9.9. Vertical normalised profiles of azimuthally and radially-averaged solid volume concentration at $N = N_{js}$ for both PBTD and PBTU.

Defining the volumetric flow rate discharged by the agitator as in Eq. (8.8), the total volumetric flow rate related to the whole polydisperse mixture is given by

$$Q = Q^{(L)} + \sum_{j=1}^{5} Q^{(j)} \tag{9.2}$$

where the superscript L indicates the liquid phase and $Q^{(j)}$ is the volumetric flow rate of the j-th solid flow component. Consequently, the multi-phase flow number for the present study can be defined as

$$Fl = \frac{Q}{ND^3} = \frac{Q^{(L)} + \sum_{j=1}^{5} Q^{(j)}}{ND^3} = Fl^{(L)} + \sum_{j=1}^{5} Fl^{(j)} = Fl^{(L)} + Fl^{(S)} \tag{9.3}$$

where the superscript S indicates the total solid phase, i.e., the sum of the five solid flow components (j = 1-5).

Defining the uniformity index, ξ_j, for each of the solid component j in the same way as in Eq. (8.10), and calculating $\bar{s}_j$ as an average of the azimuthally-averaged values of normalised slip velocity across the whole radial-axial plane, three global indices can be obtained for each flow component at each mean solid mass concentration.

The three diagrams presented in **Figure 9.10** show the variation of the three indices with the mean solid mass concentration, X, for both pumping modes.

Similarly to Chapter VIII, the PBTU produced a better multi-phase impeller pumping capacity than the PBTD up to X = 10 wt%, as shown in **Figure 9.10a-b**. However, for X = 20 wt% and above, the three-component flow number for the PBTU is lower (up to 15% when X = 40 wt%) than the one generated by the PBTD. This effect seems to be caused by the contribution of the liquid phase which is sensitive to the pumping direction, as $Fl^{(S)}$ appears to be practically unaffected by the agitation mode.

Every particle size fraction presents a higher normalised slip velocity when the agitator is pumping upwards (**Figure 9.10c-d)**. Such an enhancement in the normalised mean slip velocity is more pronounced for larger particles. Surprisingly, when using a PBTU at X = 40 wt%, two of the three medium-sized particle fractions present a non-negligible enhancement in $\bar{s}_j$. This is contrary to the general behaviour of the rest of the particles

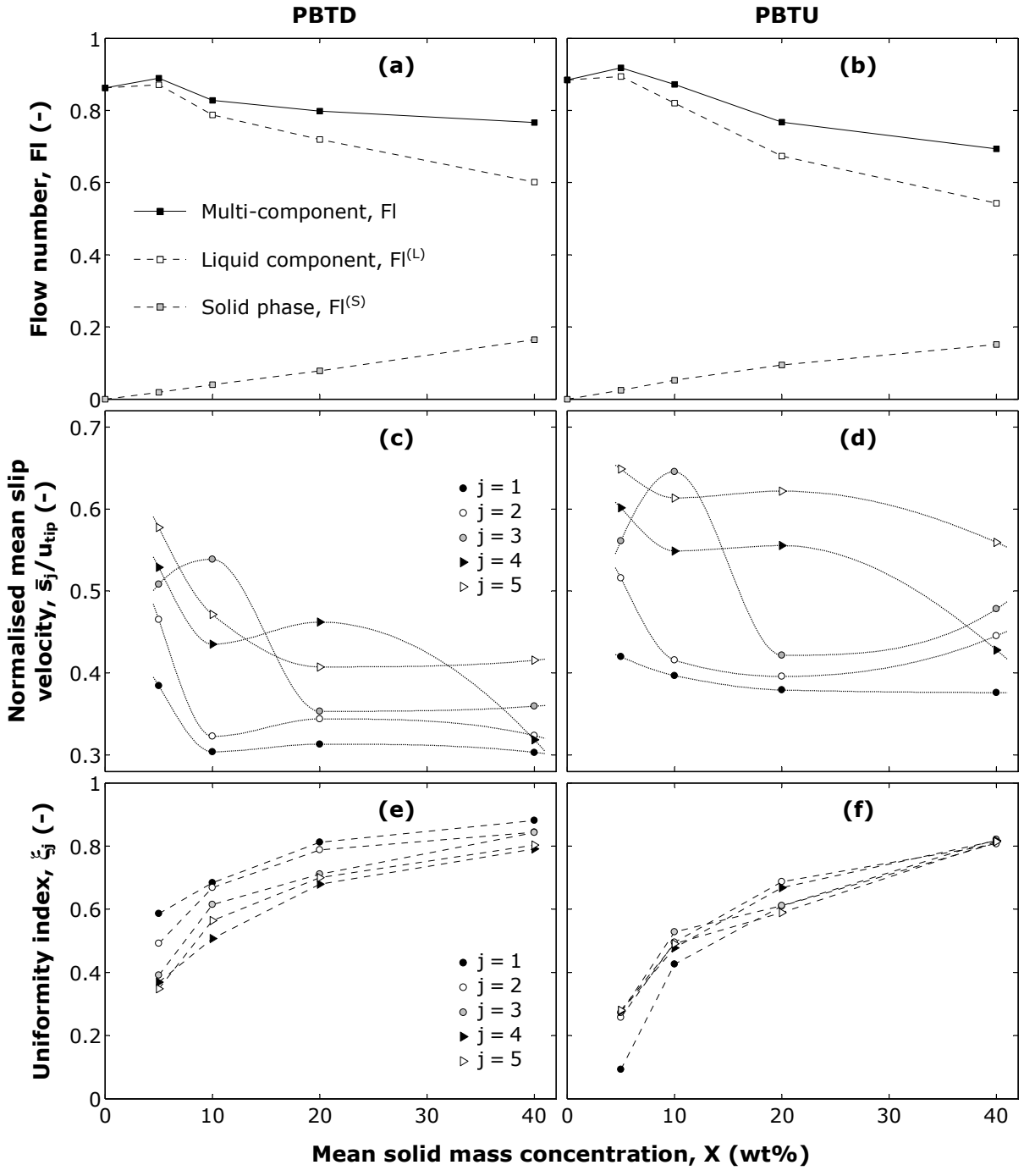

Figure 9.10. Effect of the mean mass concentration of the solid phase on the (a-b) multi-component flow number, (c-d) the normalised mean time-averaged slip velocity, and (e-f) the uniformity index.

which, for both agitation modes, generally present a small diminution in mean slip velocity when X increases.

For a given solids concentration, a down-pumping PBT achieves a more uniform suspension of each particle size fraction compared to an up-pumping PBT, as shown in **Figure 9.10e-f** but the difference between the two modes of impeller operation becomes small at high solids concentrations. Whilst the smaller particles are better dispersed than the larger ones when using a PBTD, at low to moderate mean solid concentrations, the PBTU generates a poor dispersion of the small particles which are probably highly influenced by the presence of other solid components.

For the PEPT velocity fields, calculations, conducted as discussed in Section 3-5.2, gave a velocity average close to zero, generally less than $0.03u_{tip}$ for both PBTD and PBTU, as demonstrated in **Figure 9.11**.

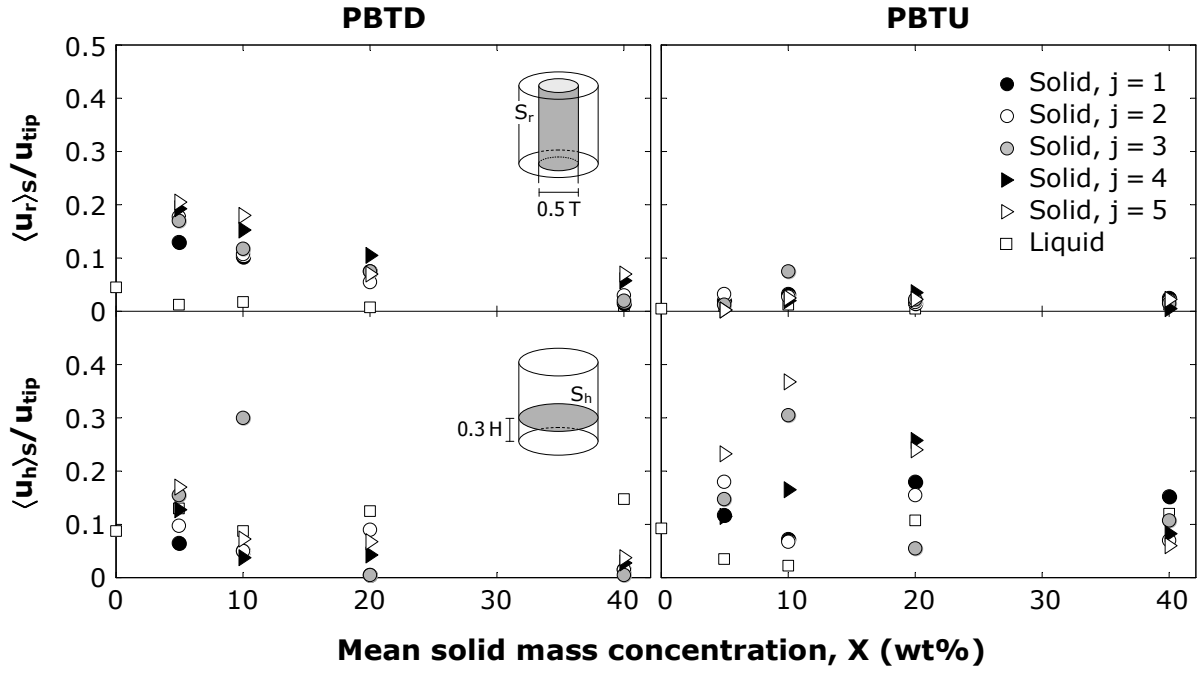

Figure 9.11. Normalised radial and axial velocities averaged on surfaces S_r (of diameter $0.5T$) and S_h ($0.3H$ off the base), respectively.

9-4 Conclusions

The limits of applicability of the Lagrangian technique of positron emission particle tracking have been successfully extended to the study of dense solid-liquid polydisperse suspensions. The Lagrangian flow data provided by the technique have been converted to give a detailed Eulerian description of each of the six liquid and solid components of the flow generated by a pitched blade turbine operating in both up- and down-pumping conditions. For the first time, it has been possible to determine the full 3D velocity field and spatial distribution of the liquid phase and of each particle size fraction within such complex polydisperse suspensions.

Due to the complexity of the system investigated here and the large amount of variables involved, not all local phenomena observe can be explained. However, the effect of the agitation mode and the mean solid mass concentration have been studied via a global assessment approach, involving concepts such as the multi-phase flow number, mean time-averaged slip velocity and uniformity index. Values of the multi-component flow number indicate that the pumping effectiveness of the PBT agitator is preserved for low to moderate concentrations. At high solid concentrations, however, the multi-component flow number is slightly reduced; such a reduction is more accentuated for an up-pumping PBT.

Every particle size fraction presents a higher normalised mean slip velocity when the agitator operates in the up-pumping mode. Such an enhancement in the normalised mean slip velocity is more pronounced for larger particles.

Results on spatial phase distribution have showed how local solids build up generally diminishes for smaller particles and/or higher solids concentrations, with the maximum uniformity index being obtained for the smaller particles at 40 wt% solids. Whilst, a PBTD achieves a better homogeneity than a PBTU at low and moderate solids concentrations, the PBTU generates a poor dispersion of the small particles which are probably highly influenced by the presence of other solid components.

An extensive amount of unique experimental data on local hydrodynamics and suspension homogeneity have been obtained in complex solid-liquid flows of high concentrations reaching 40 wt%. Such detailed results could be used to inform the design of experiments to study mixing phenomena or equipment design to maximise the global or local mixing efficiency of the system. The accuracy of the whole set of PEPT measurements has been ascertained through multi-component mass continuity verifications throughout the vessel.

Notation

Roman letters

C	Total mean volume concentration of solids	-
c_h	Mean volume concentration at level h	-
c_j	Local volume concentration of component j	-
C_j	Mean volume concentration of component j	-
D	Impeller diameter	m
d_j	Particle diameter	m
Fl	Multi-phase flow number	-
$Fl^{(j)}$	Flow number of the component j	-
$Fl^{(L)}$ $Fl^{(S)}$	Flow number of the liquid and solid phase	-
H	Height of the suspension	m
j	Mixture component index	-
N	Impeller rotational speed	s^{-1}
n_c	Number of grid cells	-
n_s	Number of particle size fractions	-
N_{js}	Minimum speed for particle suspension	s^{-1}
Q	Total multi-phase impeller pumping rate	$m^3\ s^{-1}$
$Q^{(L)}$	Impeller pumping rate of the liquid component	$m^3\ s^{-1}$
$Q^{(j)}$	Impeller pumping rate of component j	$m^3\ s^{-1}$
r h	Radial-axial cylindrical coordinates	m
R	Vessel radius	m
Re_{imp}	Impeller Reynolds number ($N_{js}D^2/\nu$)	-
S_h	Horizontal planar surface areas	m^2
S	Surface area	m^2
S_r	Vertical cylindrical surface areas	m^2
s_j	Local slip velocity of component j	$m\ s^{-1}$
$\bar{s}_j$	Mean slip velocity of component j	$m\ s^{-1}$
T	Vessel diameter	m
t_∞	PEPT runtime	s
u_ϑ u_r u_h	Cylindrical velocity components	$m\ s^{-1}$
u_{rh}	2D radial-axial velocity magnitude	$m\ s^{-1}$

u_{tip}	Impeller tip speed	m s^{-1}
X	Total mean mass concentration of solids	-
X_j	Mean mass concentration of solid component j	-

Greek letters

ν	Kinematic liquid viscosity	m^2 s^{-1}
ξ_j	Uniformity index of component j	-

Abbreviations

PBT	Pitched blade turbine
PBTD	Down-pumping PBT
PBTU	Up-pumping PBT
PEPT	Positron emission particle tracking
PIV	Particle image velocimetry

Chapter X
General conclusions and Future Recommendations

Abstract

In-depth conclusions of each of the studies undertaken in this work can be found at the end of each chapter. In addition, this final chapter presents overall concluding remarks and future recommendations.

10-1 Conclusions

Mixing is intrinsically a Lagrangian process and, although Eulerian data are essential, a Lagrangian study is necessary for its complete description. The Lagrangian approach has been used in this work to describe laminar and turbulent mixing, in single- and multi-phase opaque systems.

10-1.1 Data analysis methodology

The main purpose of the first stage of this work was to develop a detailed methodology for the analysis and validation of Lagrangian data obtained from tracer trajectories in fluid mixing systems. Such a methodology has been successfully applied to the analysis of data collected in various mixing systems using position emission particle tracking.

This novel technique is capable of providing unique and accurate Lagrangian flow data within opaque flows. It thus opens up new possibilities for tackling a range of challenging problems in the mixing of opaque single-phase and concentrated multi-phase systems which have remained hitherto unaddressed/unresolved because of a lack of adequate measurement techniques. Thus, it has been possible to visualise the Lagrangian trajectory and the 3D flow structure within the cavern formed around the agitator when mixing a viscoplastic fluid. It has also been possible to analyse Lagrangian multi-phase data to give detailed Eulerian descriptions of various mixing systems including the full 3D velocity field, local occupancy and residence time distributions, and spatial distribution of each phase component. Other features such as the use of hyperplanes and Lagrangian frequency distributions, decorrelation time and Poincaré sections have also been demonstrated.

One of the important tools developed enables the mass continuity of each tracked component within a multi-phase mixture to be accurately tested, which is crucial for the reliability of the measurements.

The structure of the computational code for extracting Eulerian information has been developed on the basis of a set of subroutines containing different algorithms aimed to progressively analyse the initial Lagrangian information and store important intermediate outputs. Due to the variety of mixing systems which can be examined, the code has been created with intrisec flexibility enabling key-parameters to be set and specific subroutines to be activated or deactivated as required. The code was written in MATLAB and examples of

typical input/output files are presented in Appendix A.

10-1.2 Validation of the PEPT technique

In order to study the nature of the axial symmetry within a baffled mechanically agitated vessel, two-dimensional PIV experiments have been successfully conducted in multiple vertical planes passing through the axis of a fully-baffled vessel agitated by a PBT and operating in the turbulent flow regime. By considering flow through horizontal and cylindrical hyperplanes introduced numerically in the vessel, the overall accuracy and reliability of the PIV measurements has been demonstrated by showing that the mass continuity is verified throughout the vessel.

With the laser sheet set at 17 different azimuthal positions, important details of the 3D Eulerian fields of velocity and turbulent kinetic energy have been obtained. Rotation of the laser plane causes a gradual variation of the measured 2D flow properties ultimately leading to considerable transformations in the velocity distribution in the plane, the shape of the primary flow loop, the position of its centre, the flow discharge angle, the velocity magnitude in the impeller suction, the velocities around the secondary flow loop, the direction of the flow in the upper part of the tank, and the turbulent kinetic energy distribution. The measurement planes at 5º either side of a baffle exhibit the largest differences in flow properties, the plane on the windward side of the baffle (85º) containing the highest velocities. The turbulent kinetic energy appears to be more uniformly distributed in this plane, while the highest TKE values are detected in the 5º plane on the leeward side of the baffle around the impeller discharge region and near the wall.

The agitation index proposed in the literature, based on the average (weighted with the volume of the grid cells) of the mean 2D velocity magnitude measured in each plane, appears to be unreliable for describing impeller effectiveness as it can vary by up to 50% between measurement planes. On the other hand, using the 2D approximation of the ϑ-invariant mean velocity for each vertical plane, the obtained flow number $Fl^{(2D)}$ is not significantly affected by the rotation of the laser plane, as it fluctuates around its average value (Fl = 0.67) with a standard error < 5%. The results have shown for the type and size of impeller used here, the importance of including both the axial and radial discharge contributions for an accurate evaluation of the flow number.

The findings of this study suggest, overall, that the ϑ-invariance of the flow field cannot be assumed in a baffled configuration without a considerable loss of information. As a result, instead of using a single vertical plane, most of the results obtained by a technique capable of collecting data in the whole three-dimensional system should always be presented in 3D, plane by plane or as azimuthally averaged Eulerian maps or profiles, which contain the whole 3D information.

Using identical equipment and fluid, three-dimensional Eulerian velocity measurements made by PEPT in a baffled stirred vessel have been compared directly with the above mentioned PIV measurements performed in multiple planes. The study aimed to investigate possible minor local discrepancies and, whether significant, develop an understanding of the reasons of their existence.

A previously performed comparison between the PEPT and an optical technique involving measurements conducted in one single plane and azimuthally-averaged maps obtained from tracking the whole 3D system, showed an overall satisfactory agreement between the two methods. However, since the two-dimensional PIV measurements showed that cylindrical symmetry of the flow field cannot be assumed in a baffled configuration without a considerable loss of information, the comparison was then refined by using azimuthally-averaged Eulerian velocity fields obtained via PEPT and PIV measurements.

Nevertheless, due to the importance of such comparison, a detailed 3D study of the differences in the flow fields obtained with these two techniques in multiple vertical planes is presented here. Eulerian velocity fields in 17 vertical planes obtained by three-dimensional PEPT measurements are compared directly with those performed in each of these planes via PIV using the same equipment and fluid. Excellent overall agreement is obtained between vector plots and contours at each of the 17 planes, and a quantitative assessment based on axial and radial velocity component profiles confirms that.

Moreover, cavern boundaries in a viscoplastic fluid with an apparent yield stress, were visualised via a planar laser induced fluorescence (PLIF) technique and radioactively detected using PEPT. The superimposition of the cavern profiles measured showed no significant difference between these two different methods of measurement.

As a direct consequence, PEPT has now been successfully tested in details in two different

fluids and flow regimes through detailed comparisons with well-established optical techniques. PEPT can now be reliably used to obtain accurate data throughout the entire complex three-dimensional flow field in a range of mechanically agitated, laminar or turbulent, single- or multi-phase opaque systems previously not amenable to quantitative analysis.

10-1.3 Alternative methodology for Lagrangian tracking

A new methodology based on the concept of Shannon entropy has been developed for studying the local and global mixing performance in a batch stirred vessel. The Lagrangian technique of positron emission particle tracking has been used to conduct experiments in the fully turbulent regime.

Three newly defined local entropy mixing times have been proposed which enable rapid identification of the regions within the vessel producing the fastest flow dispersion or reaching the fastest flow diversification, and the regions where both effects are considerably fast. Such detailed results could be used to inform the design of experiments to study mixing phenomena or equipment design to maximise the global or local mixing efficiency of the system.

For the stirred vessel single-phase configuration and pitched blade turbine considered here, the best positions for feeding have been located relatively close to the wall in line with the upper edge of the impeller for a PBTD or slightly above it for a PBTU, whilst the best withdrawal positions are found approximately a baffle-width away from the wall slightly above the central horizontal plane of the vessel regardless of the orientation of the PBT. A better global and local mixing performance is generally obtainable using a PBTD rather than a PBTU; however, for processes where there is a requirement to use a specific feed or withdrawal position, both impeller configurations should be considered as a PBTU might be preferred to a PBTD.

Despite the additional complexity generated when a pipe is placed deep inside the flow (e.g. vortex shedding around the pipe or influence of the feed rate), the common industrial practice of injecting at the surface and extracting at the base should be reconsidered to achieve better mixing efficiency in these systems.

10-1.4 Solid-liquid suspensions

PEPT has been successfully applied to the study of turbulent solid-liquid suspensions in a stirred vessel. For the first time, the flow field in dense suspensions of up to 40 wt% solids has been probed in detail, which serves to demonstrate the exceptional power of PEPT as a non-invasive technique for the analysis of opaque multi-phase systems. It has been possible to obtain the trajectory, the full 3D velocity field and spatial distribution of both the liquid and solid phases, thus, yielding a substantial amount of unique experimental data.

Values of the two-phase flow number indicate that the pumping effectiveness of the PBT agitator is preserved for low to moderate concentrations. At high solid concentrations, however, the flow number is significantly reduced for a PBTD and even much more so for a PBTU.

The azimuthally and radially-averaged vertical solids distributions show qualitative resemblance with the very limited literature data obtained in a number of other studies using either a single vertical probe traverse or a withdrawal technique. A criterion based on the variance of the local solids concentration in the vessel has been used to quantitatively describe the uniformity of the suspension and a PBTD has been shown to achieve in general a significantly more homogeneous suspension than a PBTU.

Furthermore, the detailed pointwise measurements obtained with PEPT have enabled the solids mass balance throughout the vessel and the mass continuity of the two phases to be accurately verified; a unique result which has not been achieved by any other technique.

In a subsequent experimental study, the fluid-dynamic characterisation of stirred binary solid-liquid suspensions at varying solids concentration has been made by using PEPT. The three-component flow field and spatial phase distribution of binary mixtures of glass particles suspended in water in a stirred vessel have been resolved via Lagrangian radioactive tracking. Unique experimental data on local hydrodynamics and homogeneity of suspension have been obtained in solid-liquid flows of such high concentrations reaching 40 wt%. These detailed results could be used to inform the design of experiments to study mixing phenomena or equipment design to maximise the global or local mixing efficiency of the system. The accuracy of the PEPT measurements has been ascertained through multi-component mass continuity verifications throughout the vessel.

Values of the multi-component flow number indicate that the pumping effectiveness of the PBT agitator is preserved for low to moderate concentrations. At high solid concentrations, however, the multi-component flow number and normalised mean slip velocity for both particle sizes are considerably reduced; such a reduction is accentuated for an up-pumping PBT.

Results on spatial phase distribution have shown how local solids build up diminishes for smaller particles and/or higher solids concentrations, with the maximum uniformity index being obtained for the smaller particles at 40 wt% solids. Overall, in these binary suspensions, a PBTD achieves a better homogeneity than a PBTU at low and moderate solids concentrations, but the difference in suspension uniformity between the different particle size classes is higher.

Thanks to a third experimental campaign involving solid-liquid suspensions, the limits of applicability of the Lagrangian technique of positron emission particle tracking have been successfully extended. PEPT has been applied to the study of dense solid-liquid polydisperse suspensions containing a total of five solid components. For the first time, it has been possible to determine the full 3D velocity field and spatial distribution of the liquid phase and of each particle size fraction within such complex six-component polydisperse suspensions.

The effect of the agitation mode and the mean solid mass concentration have been studied via a global assessment approach, involving concepts such as the multi-phase flow number, mean time-averaged slip velocity and uniformity index. Values of the multi-component flow number indicate that the pumping effectiveness of the PBT agitator is preserved for low to moderate concentrations. At high solid concentrations, however, the multi-component flow number is slightly reduced; such a reduction is more accentuated for an up-pumping PBT.

Every particle size fraction presents a higher normalised mean slip velocity when the agitator operates in the up-pumping mode. Such an enhancement in the normalised mean slip velocity is more pronounced for larger particles.

Results on spatial phase distribution have shown, similarly to the binary suspensions, how local solids build up generally diminishes for smaller particles and/or higher solids concentrations, with the maximum uniformity index being obtained for the smaller particles at 40 wt% solids. Whilst, a PBTD achieves a better homogeneity than a PBTU at low and

moderate solids concentrations, the PBTU generates a poor dispersion of the small particles which are probably highly influenced by the presence of other solid components.

10-2 Future recommendations

This work has shown that concentrated solid-liquid suspensions in mechanical agitated systems can be investigated in details by using the technique of positron emission particle tracking. The complexity of the phase distribution and flow data produced highlights the need for further research in this area which can build on the results reported here. Suggestions for further work are provided below.

The whole set of solid-liquid experiments were performed using a 6-blade 45º pitched-turbine (PBT) of diameter $D = 0.5T$ and height $0.1T$, the off-bottom clearance of the PBT was $0.25T$, and the height of the suspension in the vessel was set at $H = T$. As the impeller provides the primary source of turbulence, further research can be conducted to study other impeller designs, changing impeller type or fundamental agitation parameters (number of blades, blade attack angle, D/T ratio, off-bottom impeller clearance). Alternative vessel configurations may also be considered to study their effect on the flow and phase distribution, including the shape of the vessel base, number of baffles and the use a multiple impeller agitated system.

The application of the Shannon Entropy analysis presented in Chapter VI, can certainly be extended to rheologically complex fluids and multi-phase suspensions. The generalisation of these theoretical and experimental procedures to the study of such complex systems is a very challenging exercise and should be investigated further.

Apart from the data collected for the validation of PEPT against the optical techniques of PIV and PLIF, Lagrangian data were usually collected for 30-40 min per experiment which generated an average of 200-250 thousands raw PEPT tracer locations. An in-depth 3D analysis could be conducted (similarly to the multi-plane investigation in Chapter V) for each of the already investigated concentrated solid-liquid suspensions in order to unravel precious details on local phenomena. This could be achieved by simply using a longer PEPT runtime per experiment or, alternatively, by the enhancement of the acquisition rate via, for example, a PEPT tracer capable of containing a higher positron activity concentration or an improved PEPT camera efficiency.

Each solid-liquid experiment was performed at $N = N_{js}$; with a purposely designed experimental program involving $N > N_{js}$, important correlations between the uniformity index and the impeller rotational speed could be empirically determined, so that values of minimum rotational speed for uniform suspension could be predicted at varying solid concentration or vessel/impeller configurations.

Previous research studies have been mainly concerned with the study of suspension of solids in turbulent Newtonian flows. The dispersion of coarse particles in non-Newtonian fluids have received little attention, so that solid-liquid suspensions in rheologically complex fluids could be studied in details using the PEPT technique in conjunction with the set of Lagrangian tools developed here.

Appendix A
Examples of input and output data files

Summary

An example of PEPT data file is presented in this appendix. Due to the large number of pages required, the PEPT data file in **Table A.1** is truncated to the first 60 rows corresponding to the first 43 tracer location in time and space; a full data file can contains millions of rows. As described in Chapter III, such a PEPT data file contains the Lagrangian information and is used as input for the computational code for the Lagrangian-Eulerian analysis. The output file containing the Eulerian information, as discussed in Section 3-3.8, is presented in **Figure A.1**. Finally a typical input file containing the user defined computational parameters necessary to execute the Lagrangian-Eulerian data analysis is reported in **Table A.2**.

Table A.1. Sample of PEPT data file.

```
40%3mmGup580rpm_G

Separation=   530

f(opt) :  0.200      Displacement parameters :    300,   400,  1500


Fixed slices:     60 events/slice,    1 locations/slice
```

5.7	261.9	205.1	237.4	9.7	0.0	0.00	12
22.8	260.6	221.3	229.5	4.7	0.0	0.00	11
35.8	259.2	233.3	237.5	8.8	0.0	0.00	11
53.1	229.2	262.8	265.7	9.9	0.0	0.00	11
61.8	216.6	274.5	267.5	3.4	0.0	0.00	11
69.6	204.5	280.7	270.8	3.4	0.0	0.00	10
76.6	192.6	279.9	279.2	5.9	0.0	0.00	10
83.8	184.6	279.6	289.1	4.1	0.0	0.00	10
89.4	181.9	277.9	287.5	3.2	0.0	0.00	10
95.5	175.2	274.1	294.9	2.8	0.0	0.00	10
100.8	174.2	264.9	291.4	2.6	0.0	0.00	9
108.4	170.7	252.4	305.5	2.6	0.0	0.00	9
113.8	173.1	246.3	302.3	2.3	0.0	0.00	9
118.7	172.0	235.0	295.9	3.0	0.0	0.00	9
125.1	177.9	219.7	303.3	2.5	0.0	0.00	9
130.9	179.0	210.4	312.0	3.1	0.0	0.00	9
139.4	186.6	197.5	304.9	2.4	0.0	0.00	9
148.0	192.8	191.3	301.7	2.4	0.0	0.00	9
154.9	202.3	185.0	296.7	5.3	0.0	0.00	9
167.9	217.3	186.5	285.0	5.1	0.0	0.00	9
179.1	237.7	186.7	283.8	3.9	0.0	0.00	10
191.3	253.5	188.5	279.0	6.6	0.0	0.00	10
203.7	261.4	191.5	272.0	2.5	0.0	0.00	10
214.1	266.6	193.3	282.3	5.5	0.0	0.00	10
226.5	275.1	201.2	274.9	3.8	0.0	0.00	10
239.6	277.7	209.5	274.0	3.7	0.0	0.00	11
250.4	280.7	212.0	274.6	3.3	0.0	0.00	11
262.0	281.4	216.2	271.3	4.9	0.0	0.00	11
272.8	282.2	220.2	278.5	4.8	0.0	0.00	11
311.7	298.9	256.2	313.7	6.0	0.0	0.00	11
356.3	337.8	285.5	343.3	7.6	0.0	0.00	11
366.9	357.3	287.7	343.5	7.7	0.0	0.00	11
384.5	365.6	292.0	351.7	9.6	0.0	0.00	11
407.9	380.7	286.3	347.6	10.0	0.0	0.00	11
435.6	396.7	265.8	350.9	7.3	0.0	0.00	11
451.9	404.5	245.7	382.3	7.7	0.0	0.00	10
470.7	410.9	216.0	348.1	6.4	0.0	0.00	10
489.3	410.0	187.6	354.7	1.9	0.0	0.00	9
509.6	404.4	183.6	356.3	9.1	0.0	0.00	9
529.6	388.9	178.1	329.1	4.7	0.0	0.00	9
546.4	370.7	183.2	337.1	7.6	0.0	0.00	9
560.9	363.4	186.1	320.6	5.1	0.0	0.00	10
574.5	358.8	193.6	312.7	4.3	0.0	0.00	10
.....	.....	.....	.....	....	...	....	..

guida13.a10.csv

	A	B	C	D	E	F	G	H	I	J	K	L	M	N	O	P	Q	R	S	
1	guida13.a10	40%3mmGup580rpm_G											Written on 12-Nov-2009 h15:40							
2																				
3	N [rpm]	580																		
4	vtip [m/s]	4.37																		
5	Flow No.	0.339																		
6																				
7	r/R	z/H	uth/utip	ur/utip	uz/utip	u/utip	urz/utip	s uth/utip	s ur/utip	s uz/utip	s u/utip	s urz/utip	Appearance	Locations	Visits	Occupancy		PARAMETERS		
8	0.125	0.0156	-1.25E-02	-3.48E-02	1.63E-02	4.04E-02	3.85E-02	2.73E-02	2.66E-02	1.52E-02	4.10E-02	3.06E-02	1	371	78	9.76E-01				
9	0.125	0.0469	-1.50E-02	-3.71E-02	3.31E-02	5.20E-02	4.97E-02	3.25E-02	3.19E-02	1.62E-02	4.83E-02	3.58E-02	1	731	214	2.06E+00		%% Folders and files names		
10	0.125	0.0781	-1.47E-02	-3.48E-02	6.00E-02	7.09E-02	6.94E-02	3.65E-02	4.89E-02	2.62E-02	6.64E-02	5.55E-02	1	801	360	2.33E+00		INfolder	'PEPTdata'	
11	0.125	0.1094	-2.68E-02	-2.86E-02	8.78E-02	9.61E-02	9.23E-02	5.48E-02	6.54E-02	3.91E-02	9.38E-02	7.61E-02	1	893	522	2.47E+00		OUTfolder	'csv'	
12	0.125	0.1406	-5.03E-02	-1.38E-02	1.13E-01	1.24E-01	1.14E-01	6.98E-02	5.92E-02	4.64E-02	1.03E-01	7.52E-02	1	995	666	2.53E+00				
13	0.125	0.1719	-9.68E-02	1.10E-02	1.47E-01	1.77E-01	1.48E-01	8.25E-02	6.80E-02	5.76E-02	1.21E-01	8.91E-02	1	955	728	2.16E+00		%% Geometrical parameters		
14	0.125	0.2031	-1.74E-01	3.02E-02	1.86E-01	2.56E-01	1.88E-01	9.81E-02	8.73E-02	5.83E-02	1.44E-01	1.05E-01	1	774	696	1.47E+00		H	288	% V
15	0.125	0.2344	-2.47E-01	6.15E-02	2.11E-01	3.31E-01	2.20E-01	9.81E-02	8.18E-02	5.98E-02	1.41E-01	1.01E-01	1	599	571	9.77E-01		T	288	% V
16	0.125	0.2656	-2.62E-01	1.02E-01	1.93E-01	3.41E-01	2.18E-01	1.22E-01	8.81E-02	7.83E-02	1.69E-01	1.18E-01	1	447	399	7.96E-01		D	144	% Ir
17	0.125	0.2969	-2.32E-01	9.87E-02	9.91E-02	2.71E-01	1.40E-01	1.11E-01	9.06E-02	1.16E-01	1.85E-01	1.48E-01	1	423	267	1.17E+00		H_imp	28	% Ir
18	0.125	0.3281	-1.09E-01	3.90E-02	-1.08E-02	1.16E-01	4.05E-02	8.02E-02	8.73E-02	1.03E-01	1.57E-01	1.35E-01	1	713	289	2.08E+00		imp_cle	0.25	% Ir
19	0.125	0.3594	-5.84E-02	2.23E-03	-5.33E-02	7.91E-02	5.34E-02	8.14E-02	7.49E-02	8.38E-02	1.39E-01	1.12E-01	1	658	337	1.81E+00		w_baff	29	% E
20	0.125	0.3906	-2.47E-02	-2.92E-02	-7.07E-02	8.04E-02	7.65E-02	7.73E-02	5.55E-02	8.20E-02	1.26E-01	9.90E-02	1	576	327	1.46E+00		s_baff	5	% E
21	0.125	0.4219	-8.80E-04	-4.16E-02	-8.30E-02	9.29E-02	9.29E-02	8.81E-02	5.09E-02	8.26E-02	1.31E-01	9.70E-02	1	392	236	9.35E-01		a_baff	0	% E
22	0.125	0.4531	-8.29E-03	-2.91E-02	-9.65E-02	1.01E-01	1.01E-01	1.21E-01	9.35E-02	4.70E-02	1.60E-01	1.05E-01	1	223	140	4.90E-01				
23	0.125	0.4844	2.15E-02	-3.69E-02	-1.05E-01	1.14E-01	1.12E-01	5.96E-02	6.29E-02	4.90E-02	9.95E-02	7.97E-02	1	117	76	2.34E-01		%% Probability function		
24	0.125	0.5156	2.15E-02	-1.39E-02	-1.05E-01	1.08E-01	1.06E-01	4.89E-02	1.19E-01	8.63E-02	1.55E-01	1.47E-01	1	92	52	1.76E-01		Hd	510	% V
25	0.125	0.5469	1.85E-03	-2.28E-02	-1.17E-01	1.20E-01	1.20E-01	6.23E-02	6.96E-02	5.17E-02	1.07E-01	8.66E-02	1	65	41	1.21E-01		Ld	380	% H
26	0.125	0.5781	7.40E-03	-4.63E-02	-1.23E-01	1.32E-01	1.32E-01	5.54E-02	5.64E-02	3.71E-02	8.73E-02	6.75E-02	1	51	27	9.56E-02		Dd	600	% D
27	0.125	0.6094	-7.18E-03	-2.94E-02	-1.13E-01	1.17E-01	1.17E-01	5.61E-02	4.25E-02	2.90E-02	7.62E-02	5.15E-02	1	47	26	8.49E-02		deltaX	5	% H
28	0.125	0.6406	1.01E-02	-4.03E-02	-1.19E-01	1.26E-01	1.26E-01	4.70E-02	5.18E-02	2.94E-02	7.59E-02	5.96E-02	1	31	19	5.57E-02		deltaY	5	% H
29	0.125	0.6719	1.72E-02	-1.47E-02	-1.14E-01	1.16E-01	1.14E-01	8.22E-02	3.90E-02	3.49E-02	9.74E-02	5.23E-02	1	21	13	3.88E-02		deltaZ	5	% H
30	0.125	0.7031	2.02E-02	-3.57E-02	-1.17E-01	1.24E-01	1.22E-01	3.25E-02	4.93E-02	4.10E-02	7.19E-02	6.41E-02	1	15	9	2.77E-02				
31	0.125	0.7344	5.21E-02	-7.61E-04	-1.20E-01	1.31E-01	1.20E-01	1.11E-01	1.31E-01	6.85E-02	1.85E-01	1.48E-01	1	27	8	4.31E-02		%% Filter of data running		
32	0.125	0.7656	-5.49E-02	-4.09E-02	-6.99E-02	9.78E-02	8.10E-02	5.86E-02	3.27E-02	4.23E-02	7.93E-02	5.34E-02	1	8	5	1.34E-02		flag_fi	0	% o
33	0.125	0.7969	-9.37E-03	-3.13E-02	-6.82E-02	7.56E-02	7.51E-02	0.00E+00	0.00E+00	0.00E+00	0.00E+00	0.00E+00	1	2	1	3.95E-03		width_kerne	4	% V
34	0.125	0.8281	-3.37E-02	-5.16E-02	-5.92E-02	8.54E-02	7.85E-02	9.41E-03	5.34E-02	6.69E-03	5.47E-02	5.38E-02	1	4	2	7.86E-03		sigma	3	% S
35	0.125	0.8594	0.00E+00	0.00E+00	0.00E+00	0.00E+00	0.00E+00	0.00E+00	0.00E+00	0.00E+00	0.00E+00	0.00E+00	0	0	0	0.00E+00		k_vtip	1.2	
36	0.125	0.8906	0.00E+00	0.00E+00	0.00E+00	0.00E+00	0.00E+00	0.00E+00	0.00E+00	0.00E+00	0.00E+00	0.00E+00	0	0	0	0.00E+00		c_star	5	
37	0.125	0.9219	0.00E+00	0.00E+00	0.00E+00	0.00E+00	0.00E+00	0.00E+00	0.00E+00	0.00E+00	0.00E+00	0.00E+00	0	0	0	0.00E+00				
38	0.125	0.9531	0.00E+00	0.00E+00	0.00E+00	0.00E+00	0.00E+00	0.00E+00	0.00E+00	0.00E+00	0.00E+00	0.00E+00	0	0	0	0.00E+00		%% Poincare Sections		
39	0.125	0.9844	8.13E-01	3.54E-01	-1.77E-01	9.04E-01	3.95E-01	0.00E+00	0.00E+00	0.00E+00	0.00E+00	0.00E+00	1	2	1	1.55E-03		flag_ps	0	% o
40	0.3018	0.0156	-1.71E-02	-7.36E-02	2.19E-02	7.87E-02	7.68E-02	6.15E-02	5.79E-02	2.77E-02	8.89E-02	6.42E-02	1	659	230	1.71E+00		Ns_r	0	% N
41	0.3018	0.0469	-1.18E-02	-7.68E-02	4.92E-02	9.20E-02	9.12E-02	6.87E-02	5.65E-02	3.15E-02	9.44E-02	6.47E-02	1	872	472	2.35E+00		Ns_z	0	% N
42	0.3018	0.0781	-2.15E-02	-8.44E-02	8.97E-02	1.25E-01	1.23E-01	6.79E-02	7.53E-02	3.61E-02	1.08E-01	8.35E-02	1	919	681	2.36E+00		Sec_r	[.552]	% S
43	0.3018	0.1094	-4.06E-02	-7.17E-02	1.29E-01	1.53E-01	1.48E-01	6.36E-02	7.44E-02	4.10E-02	1.06E-01	8.49E-02	1	1056	912	2.36E+00		Sec_z	[.25]	% S
44	0.3018	0.1406	-6.75E-02	-5.01E-02	1.61E-01	1.82E-01	1.69E-01	9.74E-02	8.23E-02	4.37E-02	1.35E-01	9.32E-02	1	1245	1119	2.39E+00				
45	0.3018	0.1719	-1.26E-01	-9.38E-03	1.98E-01	2.35E-01	1.99E-01	1.13E-01	8.83E-02	5.47E-02	1.54E-01	1.04E-01	1	1337	1244	2.16E+00		%% Centring Parameters		
46	0.3018	0.2031	-2.09E-01	3.50E-02	2.38E-01	3.19E-01	2.41E-01	1.23E-01	9.26E-02	6.07E-02	1.66E-01	1.11E-01	1	1408	1328	1.93E+00		flag_sc	1	% o
47	0.3018	0.2344	-2.61E-01	8.27E-02	2.61E-01	3.78E-01	2.73E-01	1.23E-01	9.97E-02	6.36E-02	1.70E-01	1.18E-01	1	1412	1334	1.71E+00		marginT	5	% R
48	0.3018	0.2656	-2.83E-01	1.32E-01	2.55E-01	4.03E-01	2.87E-01	1.26E-01	9.71E-02	6.61E-02	1.72E-01	1.17E-01	1	1329	1248	1.55E+00		LRT	0.2	% L
49	0.3018	0.2969	-2.74E-01	1.66E-01	2.14E-01	3.86E-01	2.71E-01	1.24E-01	9.98E-02	8.29E-02	1.79E-01	1.30E-01	1	1166	1035	1.58E+00		n_rings	4	% N

guida13.a10

Figure A.1. Typical comma separated values (CSV) output file obtained via Lagrangian-Eulerian analysis.

Table A.2. Typical input file containing computational parameters for the Lagrangian-Eulerian data analysis.

```
% Declare parameters
%% Folders and files names
IN_OUTfolder = 'input-output';
%% Geometrical parameters
H = 288;         % Vessel height [mm]
T = 288;         % Vessel diameter [mm]
D = 144;         % Impeller diameter [mm]
H_imp = 28;      % Impeller height [mm]
imp_cle = .25;   % Impeller clearance [H]
D_shaft = 16;    % Shaft diameter [mm]
D_hub = 28;      % Hub diameter [mm]
H_hub = 30;      % Hub height [mm]
w_baff = 29;     % Baffles width [mm]
s_baff = 5;      % Baffles thickness [mm]
a_baff = 0;      % Baffles-detectors angle [deg]
%% Probability function
Hd = 510;        % Vertical height of the detector rectangle [mm]
Ld = 380;        % Horizontal width of the detector rectangle [mm]
Dd = 600;        % Distance between the detectors [mm]
deltaX = 5;      % Horizontal step [mm]
deltaY = 5;      % Horizontal step [mm]
deltaZ = 5;      % Height step [mm]
%% Filter of data running
flag_fi = 0;        % on=1 off=0
width_kernel = 4;   % Width of the Gaussian kernel
sigma = 3;          % Standard deviation of the Gaussian kernel
k_vtip = 1.2;
c_star = 5;
%% Poincare Sections
flag_ps = 0;        % on=1 off=0
Ns_r = 0;           % Num of sections (r=cost) - 0 for irregular steps
Ns_z = 0;           % Num of sections (z=cost) - 0 for irregular steps
Sec_r = [.552];     % Specify r/R for irregular steps
Sec_z = [.25];      % Specify z/H for irregular steps
%% Centring Parameters
flag_sc = 1;      % on=1 off=0
marginT = 5;      % Radiuses (mm) to scan lower than T/2
LRT = 0.20;       % Locations ratio threshold
n_rings = 4;      % Number of rings (mm) to average the annular density
x0 = 307.0;       % Suggested origin if flag_sc=0
y0 = 167.0;       % Suggested origin if flag_sc=0
z0 = 300.0;       % Suggested origin if flag_sc=0
%% Gostpoints
flag_gp = 1;      % To fill skipped voxels with interpolated locations
%% Fitting and Lagrangian velocities
coo = 'cyl';  % 'cyl' ('car') to fit in cylindrical (Cartesian) coordinates
n_fit = 3;    % Width of the interpolation/fitting interval [locations]
%% Eulerian velocities
flag_fitloc = 1;  % Write 1 (0) to use fitted (original) locations
th4sym = 1;       % To use the cylindrical pseudo-symmetry (4 baffles)
Ntheta = 1;       % Discretization using cylindrical coordinates
Nr = 16;          % Discretization using cylindrical coordinates
Nz = 32;          % Discretization using cylindrical coordinates
%% Plot
flag_lagsave = 0;        % on=1 off=0 to export Lagrangian images
flag_eulsave = 0;        % on=1 off=0 to export Eulerian images
flag_scPL = 1;           % '1' plot the results of centring '0' no plot
flag_gpPL = 0;           % on=1 off=0 to plot images from gostpoints_cyl.m
rangepl = 2400:2600;     % Change to see different trajectory's piece
locplot = 10000;         % Number of location to plot
```

Appendix B
Emulation of multiple particle tracking

Summary

A PEPT runtime of 30 min provided more than 200 thousands tracer locations under the turbulent conditions discussed in Chapter VIII. For each of the three components of the mixture, the tracer trajectory was experimentally determined and computationally partitioned in as many segments as the number of times the tracer visited a selected toroidal small volume above the impeller. This emulates the simultaneous tracking of hundreds of particles as discussed in Section 6-3.5. Using available Lagrangian data collected for the three-component binary system with total solid concentration equal to 10 wt%, as described in Section 8-2.2, the consecutive location in the mixing vessel of hundred of particles is shown in **Figures B.1-B.3**. These consecutive radial-axial projections are separated by a time interval of 0.01 s, short enough to allow the paths of the particles to be discerned.

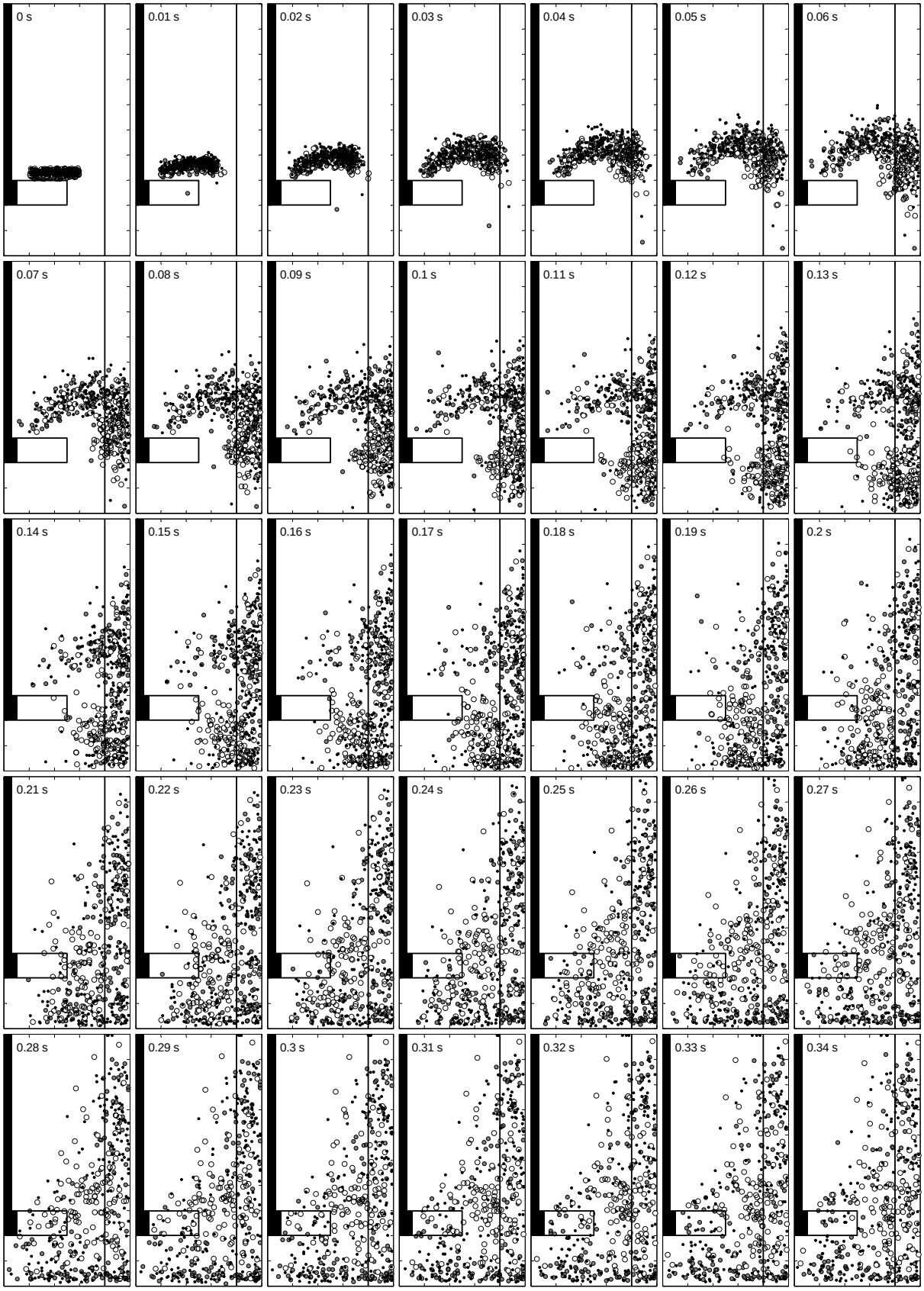

Figure B.1. Emulated multiple particle tracking: t = 0-0.34 s; ● solid (d ~ 1 mm); ◎ solid (d ~ 3 mm); ○ liquid.

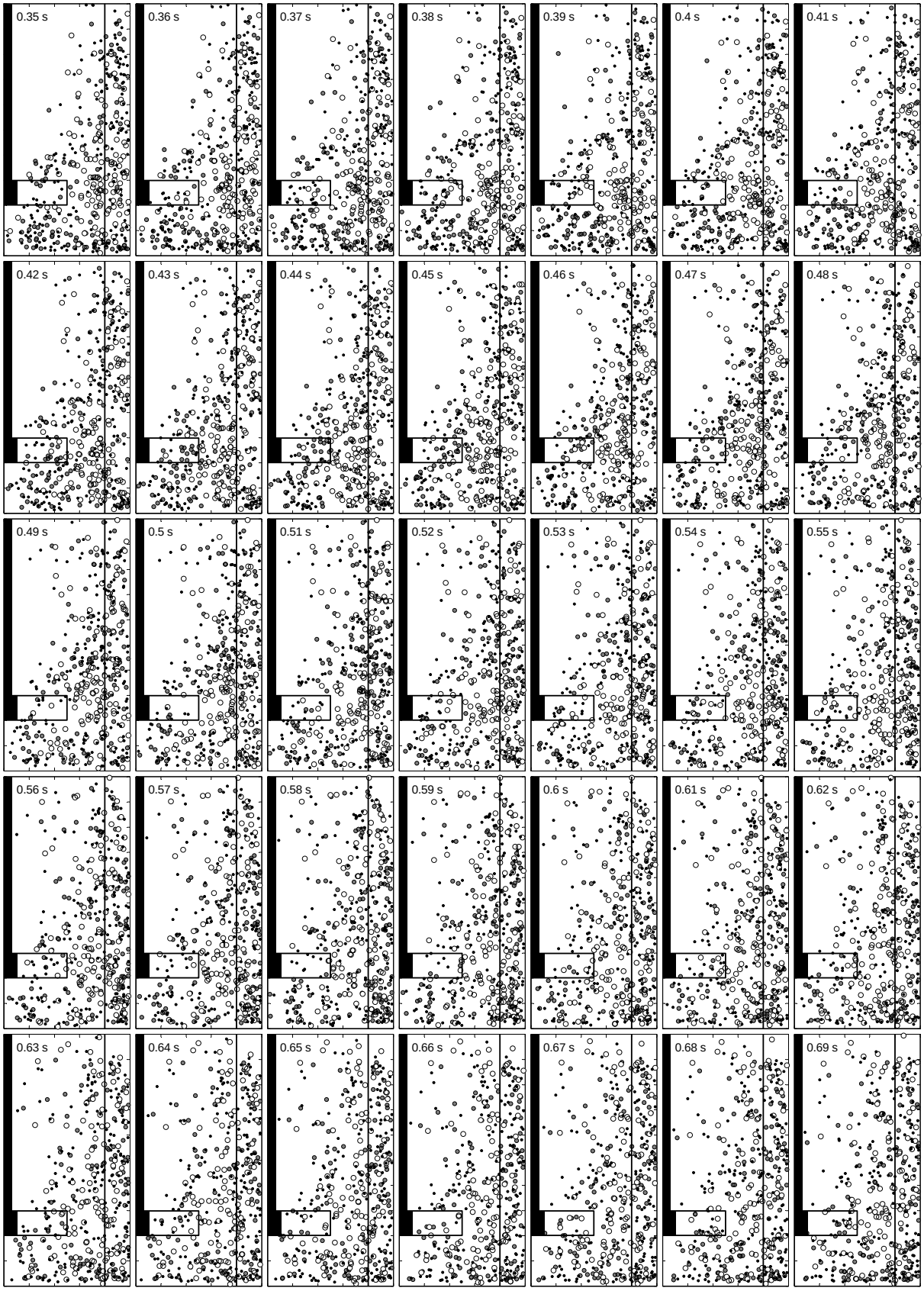

Figure B.2. Emulated multiple particle tracking: $t = 0.35\text{-}0.69$ s; ● solid (d ~ 1 mm); ⊙ solid (d ~ 3 mm); ○ liquid.

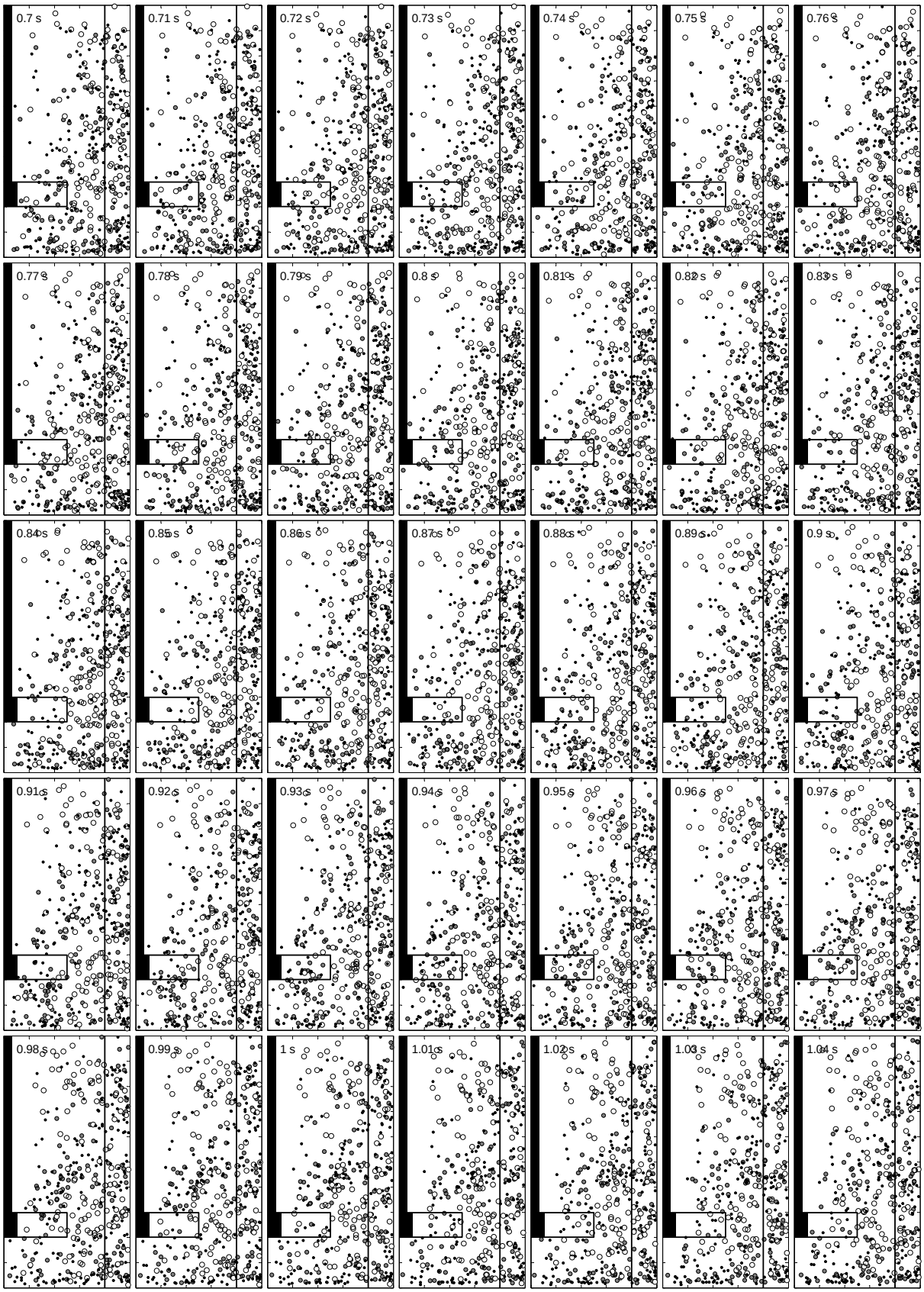

Figure B.3. Emulated multiple particle tracking: $t = 0.7\text{-}1.04$ s; ● solid (d ~ 1 mm); ⊙ solid (d ~ 3 mm); ○ liquid.

References

Adams, L., Chiti, F., Guida, A., Jaffer, S., Nienow, A.W. and Barigou, M. (2008), Positron emission particle tracking inside caverns formed during mixing of an industrial slurry, *Proceedings of International Symposium on Mixing in Industrial Processes VI*, Niagara on the Lake, Niagara Falls, Ontario, Canada, Aug 17-21.

Adams, L.W. (2009), Experimental and computational study of non-turbulent flow regimes and cavern formation of non-Newtonian fluids in a stirred tank, *Ph.D. Thesis*, University of Birmingham.

Adams, L.W. and Barigou, M. (2007), CFD analysis of caverns and pseudo-caverns developed during mixing of non-newtonian fluids, *Chem Eng Res Des*, **85**(A5), 598-604.

Adrian, R.J. (1986), Image shifting technique to resolve directional ambiguity in double-pulsed velocimetry, *Appl Opt*, **25**(21), 3855-3858.

Adrian, R.J. (1991), Particle-Imaging Techniques for Experimental Fluid-Mechanics, *Annu Rev Fluid Mech*, **23**(21), 261-304.

Altway, A., Setyawan, H., Margono and Winardi, S. (2001), Effect of particle size on simulation of three-dimensional solid dispersion in stirred tank, *Chem Eng Res Des*, **79**(A8), 1011-1016.

Alvarez-Hernández, M.M., Shinbrot, T., Zalc, J. and Muzzio, F.J. (2002), Practical chaotic mixing, *Chem Eng Sci*, **57**(17), 3749-3753.

Aref, H. (1984), Stirring by Chaotic Advection, *J Fluid Mech*, **143**(Jun), 1-21.

Aref, H. and El Naschie, M.S. (1995), *Chaos applied to fluid mixing*, Pergamon: Oxford.

Armenante, P.M., Luo, C.G., Chou, C.C., Fort, I. and Medek, J. (1997), Velocity profiles in a closed, unbaffled vessel: comparison between experimental LDV data and numerical CFD predictions, *Chem Eng Sci*, **52**(20), 3483-3492.

Armenante, P.M., Nagamine, E.U. and Susanto, J. (1998), Determination of correlations to predict the minimum agitation speed for complete solid suspension in agitated vessels, *Can J Chem Eng*, **76**(3), 413-419.

Assirelli, M., Bujalski, W., Eaglesham, A. and Nienow, A.W. (2005), Intensifying micromixing in a semi-batch reactor using a Rushton turbine, *Chem Eng Sci*, **60**(8-9), 2333-2339.

Atiemo-Obeng, V.A., Penney, R.W. and Armenante, P. (2004), Solid–Liquid mixing, in: Paul, E.L., Atiemo-

Obeng, V.A. and Kresta, S.M. (Eds), *Handbook of industrial mixing: Science and practice*, Wiley-Interscience: Hoboken, NJ. Chapter 10, 543-584.

Aubin, J., Le Sauze, N., Bertrand, J., Fletcher, D.F. and Xuereb, C. (2004), PIV measurements of flow in an aerated tank stirred by a down- and an up-pumping axial flow impeller, *Exp Therm Fluid Sci*, **28**(5), 447-456.

Aubin, J., Mavros, P., Fletcher, D.F., Bertrand, J. and Xuereb, C. (2001), Effect of axial agitator configuration (up-pumping, down-pumping, reverse rotation) on flow patterns generated in stirred vessels, *Chem Eng Res Des*, **79**(A8), 845-856.

Bakker, A. and van den Akker, H.E.A. (1990), The Use of Profiled Axial Flow Impellers in Gas-Liquid Reactors, *Proceedings of Fluid Mixing IV, IChemE Symposium Series No 121*, Bradford, UK, Sep 11-13.

Baldi, S. and Yianneskis, M. (2004), On the quantification of energy dissipation in the impeller stream of a stirred vessel from fluctuating velocity gradient measurements, *Chem Eng Sci*, **59**(13), 2659-2671.

Barigou, M. (2004), Particle tracking in opaque mixing systems: An overview of the capabilities of PET and PEPT, *Chem Eng Res Des*, **82**(A9), 1258-1267.

Barigou, M., Chiti, F., Pianko-Oprych, P., Guida, A., Adams, L., Fan, X., Parker, D.J. and Nienow, A.W. (2009), Using Positron Emission Particle Tracking (PEPT) to Study Mixing in Stirred Vessels: Validation and Tackling Unsolved Problems in Opaque Systems, *J Chem Eng Jpn*, **42**(11), 839-846.

Barresi, A. and Baldi, G. (1987), Solid dispersion in an agitated vessel, *Chem Eng Sci*, **42**(12), 2949-2956.

Broadbent, C.J., Bridgwater, J., Parker, D.J., Keningley, S.T. and Knight, P. (1993), A Phenomenological Study of a Batch Mixer Using a Positron Camera, *Powder Technol*, **76**(3), 317-329.

Brown, D.A.R., Jones, P.N. and Middleton, J.C. (2004), Experimental Methods: Measuring Tools and Techniques for Mixing and Flow Visualization Studies, in: Paul, E.L., Atiemo-Obeng, V.A. and Kresta, S.M. (Eds), *Handbook of industrial mixing: Science and practice*, Wiley-Interscience: Hoboken, NJ. Chapter 4A, 145-202.

Brucato, A., Ciofalo, M., Grisafi, F. and Micale, G. (1998), Numerical prediction of flow fields in baffled stirred vessels: A comparison of alternative modelling approaches, *Chem Eng Sci*, **53**(21), 3653-3684.

Brujes, L., Legrand, J. and Carnelle, G. (1998), Complete suspension of microcapsules in baffled and unbaffled stirred tanks, *Chem Eng Technol*, **21**(9), 735-744.

Brunazzi, E., Galletti, C., Paglianti, A. and Pintus, S. (2004), An impedance probe for the measurements of flow characteristics and mixing properties in stirred slurry reactors, *Chem Eng Res Des*, **82**(A9), 1250-1257.

Buckingham, E. (1914), On physically similar systems, illustrations of the use of dimensional equations, *Phys Rev*, **4**(4), 345-376.

Bujalski, W., Nienow, A.W. and Liu, H.X. (1990), The Use of Upward Pumping 45-Degrees Pitched Blade Turbine Impellers in 3-Phase Reactors, *Chem Eng Sci*, **45**(2), 415-421.

Cabaret, F., Bonnot, S., Fradette, L. and Tanguy, P.A. (2007), Mixing time analysis using colorimetric methods and image processing, *Ind Eng Chem Res*, **46**(14), 5032-5042.

Cassanello, M., Larachi, F., Marie, M.N., Guy, C. and Chaouki, J. (1995), Experimental Characterization of the Solid Phase Chaotic Dynamics in Three-Phase Fluidization, *Ind Eng Chem Res*, **34**(9), 2971-2980.

Chandrasekaran, M., Marcroft, H., Bakalis, S. and Karwe, M.V. (1997), Applications of laser Doppler anemometry in understanding food processing operations, *Trends Food Sci Technol*, **8**(11), 369-375.

Chang, T.P.K., Watson, A.T. and Tatterson, G.B. (1985a), Image Processing of Tracer Particle Motions as Applied to Mixing and Turbulent Flow: I. The Technique, *Chem Eng Sci*, **40**(2), 269-275.

Chang, T.P.K., Watson, A.T. and Tatterson, G.B. (1985b), Image Processing of Tracer Particle Motions as Applied to Mixing and Turbulent Flow: II. Results and Discussion, *Chem Eng Sci*, **40**(2), 277-285.

Chung, K.H.K. (2008), Mixing in high throughput experimentation reactors, *Ph.D. Thesis*, University of Birmingham.

Chung, K.H.K., Barigou, M. and Simmons, M.J.H. (2007), Reconstruction of 3-D flow field inside miniature stirred vessels using a 2-D PIV technique, *Chem Eng Res Des*, **85**(A5), 560-567.

Chung, K.H.K., Simmons, M.J.H. and Barigou, M. (2009), Angle-resolved Particle Image Velocimetry measurements of flow and turbulence fields in small-scale stirred vessels of different mixer configurations, *Ind Eng Chem Res*, **48**(2), 1008-1018.

Ciofalo, M., Brucato, A., Grisafi, F. and Torraca, N. (1996), Turbulent flow in closed and free-surface unbaffled tanks stirred by radial impellers, *Chem Eng Sci*, **51**(14), 3557-3573.

Cronin, D.G., Nienow, A.W. and Moody, G.W. (1994), An experimental study of the mixing in a proto-fermenter agitated by dual Rushton turbines, *Food Bioprod Process*, **72**(C1), 35-40.

Doucet, J., Bertrand, F. and Chaouki, J. (2008a), An extended radioactive particle tracking method for systems with irregular moving boundaries, *Powder Technol*, **181**(2), 195-204.

Doucet, J., Bertrand, F. and Chaouki, J. (2008b), A measure of mixing from Lagrangian tracking and its application to granular and fluid flow systems, *Chem Eng Res Des*, **86**(12A), 1313-1321.

Doulgerakis, Z., Yianneskis, M. and Ducci, A. (2009), On the interaction of trailing and macro-instability vortices in a stirred vessel-enhanced energy levels and improved mixing potential, *Chem Eng Res Des*, **87**(4A), 412-420.

Ducci, A. and Yianneskis, M. (2006), Turbulence kinetic energy transport processes in the impeller stream of

stirred vessels, *Chem Eng Sci*, **61**(9), 2780-2790.

Ducci, A. and Yianneskis, M. (2007a), Vortex identification methodology for feed insertion guidance in fluid mixing processes, *Chem Eng Res Des*, **85**(A5), 543-550.

Ducci, A. and Yianneskis, M. (2007b), Vortex tracking and mixing enhancement in stirred processes, *AIChE J*, **53**(2), 305-315.

Edwards, I., Axon, S.A., Barigou, M. and Stitt, E.H. (2009), Combined use of PEPT and ERT in the study of aluminum hydroxide precipitation, *Ind Eng Chem Res*, **48**(2), 1019-1028.

Edwards, M.F., Baker, M.R. and Godfrey, J.C. (1997), Mixing of liquids in stirred tanks, in: Harnby, N., Edwards, M.F. and Nienow, A.W. (Eds), *Mixing in the process industries*, Butterworth-Heinemann: Oxford. Chapter 8, 137-158.

Eesa, M. and Barigou, M. (2008), Horizontal laminar flow of coarse nearly-neutrally buoyant particles in non-Newtonian conveying fluids: CFD and PEPT experiments compared, *Int J Multiphase Flow*, **34**(11), 997-1007.

Eesa, M. and Barigou, M. (2009), CFD investigation of the pipe transport of coarse solids in laminar power law fluids, *Chem Eng Sci*, **64**(2), 322-333.

Elson, T.P. (1990), The Growth of Caverns Formed around Rotating Impellers during the Mixing of a Yield Stress Fluid, *Chem Eng Commun*, **96**(1), 303-319.

Fan, X., Parker, D.J. and Smith, M.D. (2006a), Enhancing F-18 uptake in a single particle for positron emission particle tracking through modification of solid surface chemistry, *Nucl Instrum Methods Phys Res A*, **558**(2), 542-546.

Fan, X., Parker, D.J. and Smith, M.D. (2006b), Labelling a single particle for positron emission particle tracking using direct activation and ion-exchange techniques, *Nucl Instrum Methods Phys Res A*, **562**(1), 345-350.

Fangary, Y.S., Barigou, M., Seville, J.P.K. and Parker, D.J. (2000), Fluid trajectories in a stirred vessel of non-newtonian liquid using positron emission particle tracking, *Chem Eng Sci*, **55**(24), 5969-5979.

Fangary, Y.S., Barigou, M., Seville, J.P.K. and Parker, D.J. (2002), A Langrangian study of solids suspension in a stirred vessel by Positron Emission Particle Tracking (PEPT), *Chem Eng Technol*, **25**(5), 521-528.

Fishwick, R.P., Winterbottom, J.M. and Stitt, E.H. (2003), Explaining mass transfer observations in multiphase stiffed reactors: particle-liquid slip velocity measurements using PEPT, *Catal Today*, **79**(1-4), 195-202.

Forrest, S., Bridgwater, J., Mort, P.R., Litster, J. and Parker, D.J. (2003), Flow patterns in granulating systems, *Powder Technol*, **130**(1-3), 91-96.

Gabriele, A., Nienow, A.W. and Simmons, M.J.H. (2009), Use of angle resolved PIV to estimate local specific energy dissipation rates for up- and down-pumping pitched blade agitators in a stirred tank, *Chem Eng Sci*,

64(1), 126-143.

Geisler, R.K., Buurman, C. and Mersmann, A.B. (1993), Scale-up of the Necessary Power Input in Stirred Vessels with Suspensions, *Chem Eng J*, **51**(1), 29-39.

Grenville, R.K. and Nienow, A.W. (2004), Blending of miscible liquids, in: Paul, E.L., Atiemo-Obeng, V.A. and Kresta, S.M. (Eds), *Handbook of industrial mixing: Science and practice*, Wiley-Interscience: Hoboken, NJ. Chapter 9, 507-542.

Guha, D., Ramachandran, P.A. and Dudukovic, M.P. (2007), Flow field of suspended solids in a stirred tank reactor by Lagrangian tracking, *Chem Eng Sci*, **62**(22), 6143-6154.

Guida, A., Fan, X., Parker, D.J., Nienow, A.W. and Barigou, M. (2009), Positron Emission Particle Tracking in a mechanically agitated solid-liquid suspension of coarse particles, *Chem Eng Res Des*, **87**(4A), 421-429.

Guida, A., Nienow, A.W. and Barigou, M. (2010a), PEPT measurements of solid-liquid flow field and spatial phase distribution in concentrated monodisperse stirred suspensions, *Chem Eng Sci*, **65**(6), 1905-1914.

Guida, A., Nienow, A.W. and Barigou, M. (2010b), The effects of the azimuthal position of the measurement plane on the flow parameters determined by PIV within a stirred vessel, *Chem Eng Sci*, **65**(8), 2454-2463.

Guida, A., Nienow, A.W. and Barigou, M. (2010c), Shannon entropy for local and global description of mixing by Lagrangian particle tracking, *Chem Eng Sci*, **65**(10), 2865-2883.

Guillard, F. and Tragardh, C. (2003), Mixing in industrial Rushton turbine-agitated reactors under aerated conditions, *Chem Eng Process*, **42**(5), 373-386.

Haam, S.J., Brodkey, R.S., Fort, I., Klaboch, L., Placnik, M. and Vanecek, V. (2000), Laser Doppler anemometry measurements in an index of refraction matched column in the presence of dispersed beads - Part I, *Int J Multiphase Flow*, **26**(9), 1401-1418.

Hall, J.F., Barigou, M., Simmons, M.J.H. and Stitt, E.H. (2004), Mixing in unbaffled high-throughput experimentation reactors, *Ind Eng Chem Res*, **43**(15), 4149-4158.

Hall, J.F., Barigou, M., Simmons, M.J.H. and Stitt, E.H. (2005a), Just because it's small doesn't mean it's well mixed: Ensuring good mixing in mesoscale reactors, *Ind Eng Chem Res*, **44**(25), 9695-9704.

Hall, J.F., Barigou, M., Simmons, M.J.H. and Stitt, E.H. (2005b), Comparative study of different mixing strategies in small high throughput experimentation reactors, *Chem Eng Sci*, **60**(8-9), 2355-2368.

Hankerson, D.R., Harris, G.A. and Johnson, P.D.J. (2003), *Introduction to information theory and data compression*, CRC Press: New York.

Hemrajani, R.R. and Tatterson, G.B. (2004), Mechanically Stirred Vessels, in: Paul, E.L., Atiemo-Obeng, V.A. and Kresta, S.M. (Eds), *Handbook of industrial mixing: Science and practice*, Wiley-Interscience: Hoboken, NJ.

Chapter 6, 345-390.

Hiseman, M.J.P., Laurent, B.F.C., Bridgwater, J., Wilson, D.I., Parker, D.J., North, N. and Merrifield, D.R. (2002), Granular flow in a planetary mixer, *Chem Eng Res Des*, **80**(A5), 432-440.

Holden, P.J., Wang, M., Mann, R., Dickin, F.J. and Edwards, R.B. (1998), Imaging stirred-vessel macromixing using electrical resistance tomography, *AIChE J*, **44**(4), 780-790.

Incropera, F.P. and DeWitt, D.P. (1996), *Fundamentals of heat and mass transfer*, Wiley: New York.

Jaworski, Z., Dyster, K.N. and Nienow, A.W. (2001), The effect of size, location and pumping direction of pitched blade turbine impellers on flow patterns: LDA measurements and CFD predictions, *Chem Eng Res Des*, **79**(A8), 887-894.

Jaworski, Z., Nienow, A.W. and Dyster, K.N. (1996), An LDA study of the turbulent flow field in a baffled vessel agitated by an axial, down-pumping hydrofoil impeller, *Can J Chem Eng*, **74**(1), 3-15.

Jones, J.R. and Bridgwater, J. (1998), A case study of particle mixing in a ploughshare mixer using Positron Emission Particle Tracking, *Int J Miner Process*, **53**(1-2), 29-38.

Jüsten, P., Paul, G.C., Nienow, A.W. and Thomas, C.R. (1996), Dependence of mycelial morphology on impeller type and agitation intensity, *Biotechnol Bioeng*, **52**(6), 672-684.

Kagoshima, M. and Mann, R. (2006), Development of a networks-of-zones fluid mixing model for an unbaffled stirred vessel used for precipitation, *Chem Eng Sci*, **61**(9), 2852-2863.

Khan, F.R., Rielly, C.D. and Brown, D.A.R. (2006), Angle-resolved stereo-PIV measurements close to a down-pumping pitched-blade turbine, *Chem Eng Sci*, **61**(9), 2799-2806.

Khan, F.R., Rielly, C.D. and Hargrave, G.K. (2004), A multi-block approach to obtain angle-resolved PIV measurements of the mean flow and turbulence fields in a stirred vessel, *Chem Eng Technol*, **27**(3), 264-269.

Khazam, O. and Kresta, S.M. (2008), Mechanisms of solids drawdown in stirred tanks, *Can J Chem Eng*, **86**(4), 622-634.

Khazam, O. and Kresta, S.M. (2009), A novel geometry for solids drawdown in stirred tanks, *Chem Eng Res Des*, **87**(3A), 280-290.

Kresta, S.M. and Brodkey, R.S. (2004), Turbulence in Mixing Applications, in: Paul, E.L., Atiemo-Obeng, V.A. and Kresta, S.M. (Eds), *Handbook of industrial mixing: Science and practice*, Wiley-Interscience: Hoboken, NJ. Chapter 2, 19-87.

Kresta, S.M., Mao, D.M. and Roussinova, V. (2006), Batch blend time in square stirred tanks, *Chem Eng Sci*, **61**(9), 2823-2825.

Kresta, S.M. and Wood, P.E. (1993a), The flow field produced by a pitched blade turbine: Characterization of

the turbulence and estimation of the dissipation rate, *Chem Eng Sci*, **48**(10), 1761-1774.

Kresta, S.M. and Wood, P.E. (1993b), The mean flow field produced by a 45-degrees pitched blade turbine: Changes in the circulation pattern due to off bottom clearance, *Can J Chem Eng*, **71**(1), 42-53.

Kuo, H.P., Knight, P.C., Parker, D.J. and Seville, J.P.K. (2005), Solids circulation and axial dispersion of cohesionless particles in a V-mixer, *Powder Technol*, **152**(1-3), 133-140.

Kuo, H.P., Knight, R.C., Parker, D.J., Adams, M.J. and Seville, J.P.K. (2004), Discrete element simulations of a high-shear mixer, *Advanced Powder Technology*, **15**(3), 297-309.

Larachi, F., Cassanello, M., Chaouki, J. and Guy, C. (1996), Flow structure of the solids in a 3-D gas-liquid-solid fluidized bed, *AIChE J*, **42**(9), 2439-2452.

Larachi, F., Chaouki, J. and Kennedy, G. (1995), 3-D Mapping of Solids Flow Fields in Multiphase Reactors with Rpt, *AIChE J*, **41**(2), 439-443.

Larachi, F., Kennedy, G. and Chaouki, J. (1994), A Gamma-Ray Detection System for 3-D Particle Tracking in Multiphase Reactors, *Nucl Instrum Methods Phys Res A*, **338**(2-3), 568-576.

LaRoche, R.D. (2005), Evolution of CFD as a tool for chemical engineering, *Proceedings of CFD in Chemical Reaction Engineering IV*, Barga, Italy, Jun 19-24.

Laurent, B.F.C. and Bridgwater, J. (2002), Dispersive granular flow in a horizontal drum stirred by a single blade, *AIChE J*, **48**(1), 50-58.

Lavezzo, V., Verzicco, R. and Soldati, A. (2009), Ekman pumping and intermittent particle resuspension in a stirred tank reactor, *Chem Eng Res Des*, **87**(4A), 557-564.

Lee, K.C. and Yianneskis, M. (1997), A liquid crystal thermographic technique for the measurement of mixing characteristics in stirred vessels, *Chem Eng Res Des*, **75**(A8), 746-754.

Lee, K.C. and Yianneskis, M. (1998), Turbulence properties of the impeller stream of a Rushton turbine, *AIChE J*, **44**(1), 13-24.

Limtrakul, S., Chen, J.W., Ramachandran, P.A. and Dudukovic, M.P. (2005), Solids motion and holdup profiles in liquid fluidized beds, *Chem Eng Sci*, **60**(7), 1889-1900.

Lourenco, L.M., Krothopalli, A. and Smith, C.A. (1989), Particle image velocimetry, in: Gad-el-Hak, M. (Ed), *Advances in fluid mechanics measurement*, Springer-Verlag: Berlin. Chapter 4, 128-199.

Martin, T.W., Seville, J.P.K. and Parker, D.J. (2007), A general method for quantifying dispersion in multiscale systems using trajectory analysis, *Chem Eng Sci*, **62**(13), 3419-3428.

Mavros, P. (2001), Flow visualization in stirred vessels: A review of experimental techniques, *Chem Eng Res Des*, **79**(A2), 113-127.

Mavros, P. and Baudou, C. (1997), Quantification of the performance of agitators in stirred vessels: Definition and use of an agitation index, *Chem Eng Res Des*, **75**(A8), 737-745.

Mavros, P., Xuereb, C. and Bertrand, J. (1996), Determination of 3-D flow fields in agitated vessels by laser-Doppler velocimetry: Effect of impeller type and liquid viscosity on liquid flow patterns, *Chem Eng Res Des*, **74**(A6), 658-668.

Mavros, P., Xuereb, C. and Bertrand, J. (1998), Determination of 3-D flow fields in agitated vessels by laser-Doppler velocimetry: Use and interpretation of RMS velocities, *Chem Eng Res Des*, **76**(A2), 223-233.

McNaught, A.D. and Wilkinson, A. (1997), *Compendium of chemical terminology: IUPAC recommendations*, Blackwell Science: Oxford.

Melton, L.A., Lipp, C.W., Spradling, R.W. and Paulson, K.A. (2002), DISMT - Determination of mixing time through color changes, *Chem Eng Commun*, **189**(3), 322-338.

Mersmann, A., Werner, F., Maurer, S. and Bartosch, K. (1998), Theoretical prediction of the minimum stirrer speed in mechanically agitated suspensions, *Chem Eng Process*, **37**(6), 503-510.

Metzner, A.B. and Otto, R.E. (1957), Agitation of Non-Newtonian Fluids, *AIChE J*, **3**(1), 3-10.

Micale, G., Montante, G., Grisafi, F., Brucato, A. and Godfrey, J. (2000), CFD simulation of particle distribution in stirred vessels, *Chem Eng Res Des*, **78**(A3), 435-444.

Molerus, O. and Latzel, W. (1987a), Suspension of Solid Particles in Agitated Vessels .1. Archimedes Numbers Less-Than-or-Equal-to 40, *Chem Eng Sci*, **42**(6), 1423-1430.

Molerus, O. and Latzel, W. (1987b), Suspension of Solid Particles in Agitated Vessels .2. Archimedes Numbers Greater-Than 40, Reliable Prediction of Minimum Stirrer Angular Velocities, *Chem Eng Sci*, **42**(6), 1431-1437.

Nienow, A.W. (1968), Suspension of Solid Particles in Turbine Agitated Baffled Vessels, *Chem Eng Sci*, **23**(12), 1453-1459.

Nienow, A.W. (1997a), On impeller circulation and mixing effectiveness in the turbulent flow regime, *Chem Eng Sci*, **52**(15), 2557-2565.

Nienow, A.W. (1997b), The suspension of solid particles, in: Harnby, N., Edwards, M.F. and Nienow, A.W. (Eds), *Mixing in the process industries*, Butterworth-Heinemann: Oxford. Chapter 16, 364-394.

Nienow, A.W. and Elson, T.P. (1988), Aspects of Mixing in Rheologically Complex Fluids, *Chem Eng Res Des*, **66**(1), 5-15.

Nienow, A.W., Harnby, N. and Edwards, M.F. (1997), Introduction to mixing problems, in: Harnby, N., Edwards, M.F. and Nienow, A.W. (Eds), *Mixing in the process industries*, Butterworth-Heinemann: Oxford. Chapter 1, 1-24.

Nienow, A.W., Langheinrich, C., Stevenson, N.C., Emery, A.N., Clayton, T.M. and Slater, N.K.H. (1996), Homogenisation and oxygen transfer rates in large agitated and sparged animal cell bioreactors: Some implications for growth and production, *Cytotechnology*, **22**(1-3), 87-94.

Ogawa, K. (2007), *Chemical engineering: A new perspective*, Elsevier: Amsterdam.

Ogawa, K., Ito, S. and Matsumura, Y. (1980), Mixing rate in a stirred vessel, *J Chem Eng Jpn*, **13**(4), 324-326.

Ottino, J.M. (1989), *The kinematics of mixing: stretching, chaos, and transport*, Cambridge University Press: Cambridge.

Papadopoulos, G. and Arik, E.B. (2004), Experimental Methods: Fundamental Flow Measurement, in: Paul, E.L., Atiemo-Obeng, V.A. and Kresta, S.M. (Eds), *Handbook of industrial mixing: Science and practice*, Wiley-Interscience: Hoboken, NJ. Chapter 4B, 202-256.

Parker, D.J., Broadbent, C.J., Fowles, P., Hawkesworth, M.R. and Mcneil, P. (1993), Positron Emission Particle Tracking - A technique for studying flow within engineering equipment, *Nucl Instrum Methods Phys Res A*, **326**(3), 592-607.

Parker, D.J., Forster, R.N., Fowles, P. and Takhar, P.S. (2002), Positron Emission Particle Tracking using the new Birmingham positron camera, *Nucl Instrum Methods Phys Res A*, **477**(1-3), 540-545.

Parker, D.J., Leadbeater, T.W., Fan, X., Hausard, M.N., Ingram, A. and Yang, Z. (2008), Positron imaging techniques for process engineering: recent developments at Birmingham, *Meas Sci Technol*, **19**(9), 094004.

Parkinson, D. (1951), The Reinforcement of Rubber by Carbon Black, *Br J Appl Phys*, **2**(10), 273-280.

Paul, E.L., Atiemo-Obeng, V.A. and Kresta, S.M. (2004), Blending of miscible liquids, in: Paul, E.L., Atiemo-Obeng, V.A. and Kresta, S.M. (Eds), *Handbook of industrial mixing: Science and practice*, Wiley-Interscience: Hoboken, NJ. Chapter 0, xxxiii-lxi.

Pianko-Oprych, P., Nienow, A.W. and Barigou, M. (2009), Positron emission particle tracking (PEPT) compared to particle image velocimetry (PIV) for studying the flow generated by a pitched-blade turbine in single phase and multi-phase systems, *Chem Eng Sci*, **64**(23), 4955-4968.

Pineault, G. and Cloutier, L. (1972), Transfer-Function of Continuous Stirred Tank .1. Determination by Fluorescent Tracer, *Can J Chem Eng*, **50**(6), 736-742.

Raffel, M., Willert, C.E. and Kompenhans, J.r. (1998), *Particle image velocimetry: a practical guide*, Springer: Berlin.

Raghava Rao, K.S.M.S., Rewatkar, V.B. and Joshi, J.B. (1988), Critical Impeller Speed for Solid Suspension in Mechanically Agitated Contactors, *AIChE J*, **34**(8), 1332-1340.

Rammohan, A.R., Kemoun, A., Al-Dahhan, M.H. and Dudukovic, M.P. (2001), A Lagrangian description of

flows in stirred tanks via computer-automated radioactive particle tracking (CARPT), *Chem Eng Sci*, **56**(8), 2629-2639.

Rayleigh, J.W.S. (1877), *The theory of sound*, Dover Pubblications: New York.

Roussinova, V.T., Grgic, B. and Kresta, S.M. (2000), Study of macro-instabilities in stirred tanks using a velocity decomposition technique, *Chem Eng Res Des*, **78**(A7), 1040-1052.

Rubinovitch, M. and Mann, U. (1983a), Single-Particle Approach for Analyzing Flow Systems .1. Visits to Flow Regions, *AIChE J*, **29**(4), 658-662.

Rubinovitch, M. and Mann, U. (1983b), Single-Particle Approach for Analyzing Flow Systems .2. Regional Residence Times and Local Flow-Rates, *AIChE J*, **29**(4), 663-668.

Ruszkowski, S. (1994), A rational method for measuring blending performance, and comparison of different impeller types, *Proceedings of 8th European Conference on Mixing*, Cambridge, UK, Sep 21-23.

Saarenrinne, P., Piirto, M. and Eloranta, H. (2001), Experiences of turbulence measurement with PIV, *Meas Sci Technol*, **12**(11), 1904-1910.

Sahu, A.K. and Joshi, J.B. (1995), Simulation of Flow in Stirred Vessels with Axial-Flow Impellers - Effects of Various Numerical Schemes and Turbulence Model Parameters, *Ind Eng Chem Res*, **34**(2), 626-639.

Schafer, M., Yianneskis, M., Wachter, P. and Durst, F. (1998), Trailing vortices around a 45 degrees pitched-blade impeller, *AIChE J*, **44**(6), 1233-1246.

Shamlou, P.A. (1993), *Processing of solid-liquid suspensions*, Butterworth-Heinemann: Oxford.

Shannon, C.E. (1948), A mathematical theory of communication, *Bell Syst Tech J*, **27**(3), 379-423.

Sharp, K.V. and Adrian, R.J. (2001), PIV study of small-scale flow structure around a Rushton turbine, *AIChE J*, **47**(4), 766-778.

Sheng, J., Meng, H. and Fox, R.O. (2000), A large eddy PIV method for turbulence dissipation rate estimation, *Chem Eng Sci*, **55**(20), 4423-4434.

Shervin, C.R., Studeny, J.E. and Romaszewski, R.A. (1992), Use of dielectric loss to determine blend time for organic polymer solutions, *AIChE J*, **38**(9), 1395-1398.

Skelland, A.H.P. (1967), *Non-Newtonian flow and heat transfer*, Wiley: New York.

Smith, J.M. (1990), Industrial needs for mixing research, *Chem Eng Res Des*, **68**(1), 3-6.

Špidla, M., Sinevič, V., Jahoda, M. and Machoň, V. (2005), Solid particle distribution of moderately concentrated suspensions in a pilot plant stirred vessel, *Chem Eng J*, **113**(1), 73-82.

Tamburini, A., Cipollina, A., Micale, G., Ciofalo, M. and Brucato, A. (2009), Dense solid-liquid off-bottom

suspension dynamics: Simulation and experiment, *Chem Eng Res Des*, **87**(4A), 587-597.

Tang, L., Wen, F., Yang, Y., Crowe, C.T., Chung, J.N. and Troutt, T.R. (1992), Self-organizing particle dispersion mechanism in a plane wake, *Phys Fluids A*, **4**(10), 2244-2251.

Toschi, F. and Bodenschatz, E. (2009), Lagrangian Properties of Particles in Turbulence, *Annu Rev Fluid Mech*, **41**(1), 375-404.

Tribus, M. (1961), *Thermostatics and thermodynamics: An introduction to energy, information and states of matter, with engineering applications*, Van Nostrand: London.

Tsallis, C. (1988), Possible generalization of Boltzmann-Gibbs statistics, *J Stat Phys*, **52**(1-2), 479-487.

Unadkat, H., Rielly, C.D., Hargrave, G.K. and Nagy, Z.K. (2009), Application of fluorescent PIV and digital image analysis to measure turbulence properties of solid-liquid stirred suspensions, *Chem Eng Res Des*, **87**(4A), 573-586.

Villermaux, J. (1996), Trajectory Length Distribution (TLD), a novel concept to characterize mixing in flow systems, *Chem Eng Sci*, **51**(10), 1939-1946.

Virdung, T. and Rasmuson, A. (2007), Measurements of continuous phase velocities in solid-liquid flow at elevated concentrations in a stirred vessel using LDV, *Chem Eng Res Des*, **85**(A2), 193-200.

Wang, M., Dorward, A., Vlaev, D. and Mann, R. (2000), Measurements of gas-liquid mixing in a stirred vessel using electrical resistance tomography (ERT), *Chem Eng J*, **77**(1-2), 93-98.

Willert, C.E. and Gharib, M. (1991), Digital Particle Image Velocimetry, *Exp Fluids*, **10**(4), 181-193.

Wittmer, S., Falk, L., Pitiot, P. and Vivier, H. (1998), Characterization of stirred vessel hydrodynamics by three dimensional trajectography, *Can J Chem Eng*, **76**(3), 600-610.

Yianneskis, M. and Whitelaw, J.H. (1993), On the Structure of the Trailing Vortices around Rushton Turbine-Blades, *Chem Eng Res Des*, **71**(A5), 543-550.

Zlokarnik, M. (2001), *Stirring: Theory and practice*, Wiley-VCH: Weinheim.

Zwietering, T.N. (1958), Suspending of solid particles in liquid by agitators, *Chem Eng Sci*, **8**(3-4), 244-253.